frontiers | Research Topics

Updates in ocular therapeutics and surgery, volume IV

Edited by
Georgios D. Panos and Horace Massa

Published in
Frontiers in Medicine

ISSN 1664-8714
ISBN 978-2-8325-6906-1
DOI 10.3389/978-2-8325-6906-1

Generative AI statement
Any alternative text (Alt text) provided alongside figures in the articles in this ebook has been generated by Frontiers with the support of artificial intelligence and reasonable efforts have been made to ensure accuracy, including review by the authors wherever possible. If you identify any issues, please contact us.

About Frontiers

Frontiers is more than just an open access publisher of scholarly articles: it is a pioneering approach to the world of academia, radically improving the way scholarly research is managed. The grand vision of Frontiers is a world where all people have an equal opportunity to seek, share and generate knowledge. Frontiers provides immediate and permanent online open access to all its publications, but this alone is not enough to realize our grand goals.

Frontiers journal series

The Frontiers journal series is a multi-tier and interdisciplinary set of open-access, online journals, promising a paradigm shift from the current review, selection and dissemination processes in academic publishing. All Frontiers journals are driven by researchers for researchers; therefore, they constitute a service to the scholarly community. At the same time, the *Frontiers journal series* operates on a revolutionary invention, the tiered publishing system, initially addressing specific communities of scholars, and gradually climbing up to broader public understanding, thus serving the interests of the lay society, too.

Dedication to quality

Each Frontiers article is a landmark of the highest quality, thanks to genuinely collaborative interactions between authors and review editors, who include some of the world's best academicians. Research must be certified by peers before entering a stream of knowledge that may eventually reach the public - and shape society; therefore, Frontiers only applies the most rigorous and unbiased reviews. Frontiers revolutionizes research publishing by freely delivering the most outstanding research, evaluated with no bias from both the academic and social point of view. By applying the most advanced information technologies, Frontiers is catapulting scholarly publishing into a new generation.

What are Frontiers Research Topics?

Frontiers Research Topics are very popular trademarks of the *Frontiers journals series*: they are collections of at least ten articles, all centered on a particular subject. With their unique mix of varied contributions from Original Research to Review Articles, Frontiers Research Topics unify the most influential researchers, the latest key findings and historical advances in a hot research area.

Find out more on how to host your own Frontiers Research Topic or contribute to one as an author by contacting the Frontiers editorial office: frontiersin.org/about/contact

Updates in ocular therapeutics and surgery, volume IV

Topic editors

Georgios D. Panos — Aristotle University of Thessaloniki, Greece

Horace Massa — Hôpitaux universitaires de Genève (HUG), Switzerland

Citation

Panos, G. D., Massa, H., eds. (2025). *Updates in ocular therapeutics and surgery, volume IV*. Lausanne: Frontiers Media SA. doi: 10.3389/978-2-8325-6906-1

Table of contents

05 Editorial: Updates in ocular therapeutics and surgery, volume IV
Georgios D. Panos and Horace Massa

08 Treatment of neovascular age-related macular degeneration: one year real-life results with intravitreal Brolucizumab
Settimio Rossi, Carlo Gesualdo, Ernesto Marano, Raffaele Perrotta, Maria Consiglia Trotta, Antonio Del Giudice and Francesca Simonelli

18 The influence of amniotic membrane proteins on corneal regeneration when delivered directly or using hydrogel platforms
Ayla Basasoro, Javier Mendicute, Marta Rezola, Jorge Burgos, Mercedes Fernández, David Esporrín-Ubieto, Ana Sonzogni, Marcelo Calderón, Itxaso Calafel, Aitor Díaz, Juliana De Souza, Ana Aiastui, Mikel Azkargorta, Félix Elortza, Elena Vecino and Arantxa Acera

31 Intravitreal aflibercept for diabetic macular edema: structural and functional improvements
Chuanhe Zhang, Tianyu Chen, Ru Jia, Di Gong, Zhigao Liu, Changlong Wu, Xiangwen Shu, Fangju Han and Bin Gong

40 Levitation of posteriorly dislocated intraocular lens: I.V. catheter connected to the vitreotome aspiration
Ruiping Gu, Yue Guo, Yuan Zong, Rui Jiang and Zhongcui Sun

46 Localization of fluorescent gold nanoparticles throughout the eye after topical administration
Gabrielle Raîche-Marcoux, Sébastien Méthot, Ange Tchatchouang, Camille Bettoli, Cloé Maranda, Alexis Loiseau, Stéphanie Proulx, Patrick J. Rochette, Emilie Genin and Élodie Boisselier

67 Treatment of traumatic subluxation of the crystalline lens with custom-made capsular hook
Ning Li, Jie Dong, Jianfeng Wang, Xiaohui Ren, Juanjuan Guo, Juan Li and Ziqing Gao

77 Clinical outcomes of DMEK comparing endothelium-out injector and endothelium-in pull-through techniques in Asian eyes
Ezekiel Ze Ken Cheong, Clarissa Ng Yin Ling, Qiu Ying Wong, Chloe Si Qi Chua, Hla Myint Htoon and Marcus Ang

86 Corrigendum: Clinical outcomes of DMEK comparing endothelium-out injector and endothelium-in pull-through techniques in Asian eyes
Ezekiel Ze Ken Cheong, Clarissa Ng Yin Ling, Qiu Ying Wong, Chloe Si Qi Chua, Hla Myint Htoon and Marcus Ang

88 Unveiling the molecular mechanisms of stigmasterol on diabetic retinopathy: BNM framework construction and experimental validation
Hongrong Zhang, Yufan Li, Qi Xu and Zhaohui Fang

106 Lutein-based dye vitrectomy for idiopathic epiretinal membrane: a pilot study
Settimio Rossi, Carlo Gesualdo, Michele Della Corte, Antonio Del Giudice, Andrea Rosolia, Maria Consiglia Trotta and Francesca Simonelli

frontiers | Frontiers in Medicine

TYPE Editorial
PUBLISHED 04 September 2025
DOI 10.3389/fmed.2025.1685404

OPEN ACCESS

EDITED AND REVIEWED BY
Jodhbir Mehta,
Singapore National Eye Center, Singapore

*CORRESPONDENCE
Georgios D. Panos
✉ gdpanos@gmail.com

RECEIVED 13 August 2025
ACCEPTED 18 August 2025
PUBLISHED 04 September 2025

CITATION
Panos GD and Massa H (2025) Editorial: Updates in ocular therapeutics and surgery, volume IV. *Front. Med.* 12:1685404. doi: 10.3389/fmed.2025.1685404

Editorial: Updates in ocular therapeutics and surgery, volume IV

Georgios D. Panos[1,2]* and Horace Massa[3]

[1]First Department of Ophthalmology, AHEPA University Hospital, School of Medicine, Aristotle University of Thessaloniki, Thessaloniki, Greece, [2]Division of Ophthalmology and Visual Sciences, School of Medicine, University of Nottingham, Nottingham, United Kingdom, [3]Department of Ophthalmology, Geneva University Hospitals, Geneva, Switzerland

KEYWORDS

cornea, ocular therapeutics, ophthalmic surgery, drug delivery, keratoplasty, vitreoretinal surgery, anti-VEGF, network pharmacology

Editorial on the Research Topic
Updates in ocular therapeutics and surgery, volume IV

1 Introduction

The fourth volume of *Updates in ocular therapeutics and surgery, volume IV* showcases how our field is advancing along three converging fronts: (i) surgical techniques and visualisation, (ii) biomaterials and drug delivery, and (iii) pharmacotherapy informed by real-world evidence and data-driven discovery. Together, the nine articles in this Research Topic—spanning the cornea, lens and retina and including one surgical methods article—highlight pragmatic solutions to persistent clinical bottlenecks and point to platforms with cross-disease applicability. A Corrigendum in this Research Topic also underscores the value of transparent corrections without altering scientific conclusions.

2 Surgery and visualisation

2.1 Refining corneal endothelial surgery

Cheong (a) et al. directly compared Descemet membrane endothelial keratoplasty (DMEK) insertion techniques in an Asian cohort—"injector" (endothelium-out) vs. "pull-through" (endothelium-in). Adjusted analyses showed comparable overall clinical outcomes, with surgical indication (not technique) chiefly driving graft failure, and pseudophakic bullous keratopathy faring worse than Fuchs dystrophy. A linked Corrigendum corrected the order of the panels in a figure and did not change the conclusions. These data will help surgeons choose instruments and manoeuvres based on ocular context rather than fashion, and will set expectations for case selection and training.

2.2 Stabilising the capsular bag after trauma

Li et al. reported on the long-term outcomes of using heat-shaped polypropylene "capsular hooks" to secure zonular-deficient capsular bags in cases of traumatic crystalline lens subluxation. Visual acuity improved markedly with well-centred IOLs and no device dislodgement over a mean follow-up of ~10-month. In settings without commercial fixation devices, this customisable, low-cost approach is both elegant and scalable.

2.3 Retrieving posteriorly dislocated IOLs—simple, safe, reproducible

Gu et al. (Methods article) describe a technique for elevating posteriorly dislocated intraocular lenses by connecting a 22-gauge intravenous catheter to the vitreotome aspiration line, thereby providing controlled suction that lifts the IOL optic away from the retinal surface for safe grasping. In four consecutive cases, the IOL never fell back, and no intraoperative complications occurred. This technique avoids perfluorocarbon liquid (PFCL)-related risks and illustrates how incremental engineering can mitigate risk during delicate vitreoretinal manoeuvres.

2.4 A safer way to see: a lutein-based vital dye

Rossi, Gesualdo, Corte et al. piloted the use of a lutein-based vitreous dye in idiopathic epiretinal membrane surgery. The dye selectively stains the vitreous/posterior hyaloid, facilitates key manoeuvres, and is associated with improved visual acuity and reduced central retinal thickness at 4–6 months without IOP penalty. As visualisation increasingly relies on adjuncts with favourable safety profiles, lutein-based dyes may offer a thoughtful alternative to triamcinolone or indocyanine green.

3 Biomaterials and delivery

3.1 Nanoparticles that can be seen—and deliver

Raîche-Marcoux et al. synthesised fluorescent gold nanoparticles with properties comparable to those of their non-fluorescent counterparts and tracked their localisation across ocular tissues after topical application in *ex vivo* rabbit eyes. The work is a step towards non-invasive delivery systems that can be imaged end-to-end—from the corneal surface to the posterior segment—supporting rational formulation and pharmacokinetic studies.

3.2 Harnessing amniotic membrane proteins via smart hydrogels

Basasoro et al. tested two hydrogel platforms loaded with amniotic membrane protein extract in a rabbit model of severe alkali burn. Treated corneas showed more frequent wound closure by day 14 and histologic signals of modulated inflammation. The message is pragmatic: biocompatible, muco-adhesive hydrogels can turn a proven biological milieu (AM proteins) into a controllable, residence-time-enhancing therapy.

4 Pharmacotherapy and data-driven discovery

4.1 Real-world anti-VEGF: structure–function matters

Zhang C. et al. evaluated aflibercept for diabetic macular oedema with both OCT/OCTA and microperimetry. Short-term treatment reduced central retinal thickness and improved best-corrected visual acuity and fixation stability, while FAZ area/density metrics remained unchanged—reminding us that functional endpoints can move even when angiographic surrogates do not, and supporting the use of microperimetry as a sensitive complement to routine care.

4.2 Brolucizumab in practise

Rossi, Gesualdo, Marano et al. presented 1-year, real-world results for brolucizumab in the treatment of neovascular AMD, reporting improved visual acuity and central retinal thickness with relatively few injections and only one intraocular drug-related adverse event. These pragmatic data will help clinicians balance the potency, durability and safety when individualising anti-VEGF regimens.

4.3 Data-driven discovery meets traditional medicine

Zhang H. et al. constructed an integrated bioinformatics-network pharmacology-machine-learning framework to investigate three traditional Chinese medicines for diabetic retinopathy. They identified a stigmasterol–PPARG axis and validated this *axis in vivo*. In addition to the specific candidates, their blueprint is noteworthy: AI-assisted target/component prioritisation funnelled into experimental confirmation can accelerate hypothesis generation for complex polypharmacy systems.

5 Where do we go from here?

Three priorities emerge. First, we must *standardise* technique-sensitive procedures (e.g., DMEK) alongside indication-aware pathways and training metrics. Second, we need to *translate* biomaterials with imageable, muco-adhesive, and tissue-specific properties from bench to clinic via pharmacokinetics and manufacturability studies. Third, we must *enrich* routine outcomes with function (e.g., microperimetry, fixation stability), not just structure, and continue to develop data-science pipelines that triage candidates before costly trials. The articles assembled here

exemplify clinically grounded innovation—small changes that make surgery safer, smarter matrices that keep drugs where they matter, and pragmatic evidence that helps us to treat the right patient with the right tool at the right time.

Author contributions

GP: Formal analysis, Supervision, Validation, Writing – original draft, Writing – review & editing. HM: Data curation, Validation, Writing – review & editing.

Acknowledgments

We thank all contributing authors and reviewers for their rigorous work and the Frontiers editorial team for their support.

Conflict of interest

The authors declare that the research was conducted in the absence of any commercial or financial relationships that could be construed as a potential conflict of interest.

The author(s) declared that they were an editorial board member of Frontiers, at the time of submission. This had no impact on the peer review process and the final decision.

Generative AI statement

The author(s) declare that no Gen AI was used in the creation of this manuscript.

Any alternative text (alt text) provided alongside figures in this article has been generated by Frontiers with the support of artificial intelligence and reasonable efforts have been made to ensure accuracy, including review by the authors wherever possible. If you identify any issues, please contact us.

Publisher's note

frontiers | Frontiers in Medicine

TYPE Original Research
PUBLISHED 15 January 2025
DOI 10.3389/fmed.2024.1467160

OPEN ACCESS

EDITED BY
Georgios D. Panos,
Aristotle University of Thessaloniki, Greece

REVIEWED BY
Prasanna Srinivasan Ramalingam,
Vellore Institute of Technology, India
Xiangjun She,
Wenzhou Medical University, China

*CORRESPONDENCE
Carlo Gesualdo
✉ carlo.gesualdo@unicampania.it

RECEIVED 19 July 2024
ACCEPTED 04 December 2024
PUBLISHED 15 January 2025

CITATION
Rossi S, Gesualdo C, Marano E, Perrotta R, Trotta MC, Del Giudice A and Simonelli F (2025) Treatment of neovascular age-related macular degeneration: one year real-life results with intravitreal Brolucizumab. *Front. Med.* 11:1467160. doi: 10.3389/fmed.2024.1467160

Treatment of neovascular age-related macular degeneration: one year real-life results with intravitreal Brolucizumab

Settimio Rossi[1], Carlo Gesualdo[1]*, Ernesto Marano[1], Raffaele Perrotta[2], Maria Consiglia Trotta[3], Antonio Del Giudice[1] and Francesca Simonelli[1]

[1]Eye Clinic, Multidisciplinary Department of Medical, Surgical and Dental Sciences University of Campania "Luigi Vanvitelli", Naples, Italy, [2]Eye Unit, G. Rummo Hospital, Benevento, Italy, [3]Department of Experimental Medicine, University of Campania "Luigi Vanvitelli", Naples, Italy

Background: Age-related macular degeneration (AMD) is a prevalent cause of irreversible vision loss worldwide, particularly among the elderly population. Two forms of late AMD are described: neovascular AMD (nAMD), characterized by abnormal choroidal blood vessel growth, and atrophic (dry) AMD, involving retinal cell degeneration. Intravitreal anti-vascular endothelial growth factor (anti-VEGF) agents have transformed nAMD treatment, with Brolucizumab emerging as a promising therapy. The aim of this study is to provide the real-life anatomical-functional and safety results, after 1 year of treatment experience with Brolucizumab.

Methods: This is a retrospective observational real-life study in which 44 patients (44 eyes) diagnosed with nAMD and treated with Brolucizumab were enrolled. We identified two groups: group 1 (24 treatment-naïve eyes) that received a loading dose of 3 monthly intravitreal injections of Broluciziumab 6 mg (0.05 mL solution) + Q8w/Q12w regimen, and a Group 2 (20 non-naïve eyes) which performed 1 injection + ProReNata (PRN) scheme. Monthly, all participants underwent comprehensive ophthalmological evaluation until 12 months follow-up.

Results: We observed a significant improvement in best corrected visual acuity (39 ± 15 L vs. 30 ± 17 L; $p < 0.01$) and central retinal thickness (265 ± 89 μ vs. 360 ± 129 µ; $p < 0.0001$) at the end of follow-up without any differences between treatment-naïve and non-naïve patients. These results were obtained with a low number of injections (3.7 ± 1.9) with only one case of intraocular drug-related adverse event. Finally, the presence of subretinal hyperreflective material correlates with lower visual recovery.

Discussion: Our findings highlight the efficacy of Brolucizumab in managing wet-AMD and suggest its role for long-term efficacy in stabilizing retinal exudation and fluid accumulation, resulting in improved visual prognosis.

KEYWORDS

age-related macular degeneration, intravitreal injection, brolucizumab, real-life, neovascularization

1 Introduction

Age-related macular degeneration (AMD) is a multifactorial, progressive, and debilitating disease predominantly affecting the elderly population, representing a significant public health concern worldwide (1). It stands as one of the leading causes of irreversible blindness in industrialized nations, imposing substantial socioeconomic burdens on healthcare systems and individuals alike (2, 3). AMD causes a progressive threat to visual function, particularly in its advanced stages, where it manifests as a degenerative condition primarily affecting the macula, the central region of the retina responsible for distinct vision (1). AMD is clinically stratified into three main stages: early, intermediate, and late (4). The early and intermediate stages are often asymptomatic or associated with mild visual symptoms, characterized by the presence of typical hallmarks such as drusen deposits and pigmentary changes within the macula (5). These stages are marked by progressive neuroretinal degeneration. Late-stage AMD, on the other hand, presents a more advanced and debilitating clinical picture, with two primary phenotypic manifestations: neovascular (wet) AMD and atrophic (dry) AMD. Neovascular AMD is characterized by the aberrant growth of choroidal blood vessels into retinal layers or below them, leading to the formation of abnormal vascular networks in the macular region (6). That process compromises retinal integrity and function, resulting in profound visual impairment. Conversely, atrophic AMD is distinguished by progressive degeneration of retinal pigment epithelial cells and photoreceptors, resulting in geographic atrophy within the macular area (7). Both forms of late AMD contribute significantly to vision loss and pose considerable challenges for effective management and treatment.

Historically, the therapeutic landscape for wet AMD has evolved considerably, with treatment paradigms transitioning from conventional modalities such as thermal laser photocoagulation and photodynamic therapy to the advent of intravitreally anti-vascular endothelial growth factor (anti-VEGF) agents (8). The introduction of intravitreal anti-VEGF therapy heralded a paradigm shift in AMD management, offering unprecedented efficacy in preserving visual function and improving quality of life, delaying disease progression (9, 10). Notably, numerous landmark clinical trials have demonstrated the efficacy and safety of anti-VEGF agents, consolidating their position as first-line treatments for neovascular AMD (11). Currently approved anti-VEGF agents include ranibizumab, aflibercept, brolucizumab, and faricimab (bispecific antibody). Bevacizumab is also an anti-VEGF agent used off-label to manage neovascular AMD (nAMD). However, there are no direct comparison studies that show the superiority of one drug over another, but only noninferiority trials that compare different anti-VEGF agents. For example, in a large noninferiority trial by the CATT (Center for Preventive Ophthalmology and Biostatistics) research group with a large number of patients enrolled (1208), Bevacizumab and Ranibizumab, both administered monthly, showed the same results after 1 year follow-up (8.0 and 8.5 letters gained, respectively). Moreover, authors highlighted also how Bevacizumab as needed was equivalent to Ranibizumab as needed with +5.9 and + 6.8 letters gained, respectively (12). Authors also analyzed the results of re-randomizing the same patients into continuous monthly treatment and as-needed treatment at year 2, discovering that the as-needed group lost −1.8 letters compared with those undergoing monthly treatment (13). Those two studies highlighted how monthly treatment approach, even being more expensive for healthcare systems and stressful for patients, is more effective in maintaining visual acuity in time.

However, despite the remarkable therapeutic advancements achieved with anti-VEGF therapy, several challenges persist in the management of AMD, particularly in the context of real-world clinical practice (14). The burden of frequent intravitreal injections, the need for long-term monitoring, and possible treatment-related complications pose significant challenges for both patients and healthcare systems to optimize AMD treatment strategies. In recent years, efforts have focused on optimizing treatment protocols and exploring novel therapeutic modalities aimed at enhancing treatment efficacy and reducing treatment burden (15). Brolucizumab, a novel anti-VEGF agent, has gained significant attention as a potential candidate for advancing the treatment paradigm in neovascular AMD (16–18). As a single-chain antibody fragment targeting all isoforms of VEGF-A, Brolucizumab offers the potential for enhanced potency and sustained therapeutic effect (19). Its small molecular size facilitates higher drug concentrations within the vitreous cavity following intravitreal administration, thereby optimizing retinal bioavailability, and minimizing treatment frequency (20). Dealing with its small molecular size, some authors have hypothesized that, even if brolucizumab should be less immunogenic because of an Fc portion missing in its biomolecular anatomy, actually it can be more immunogenic because of its size and potentiality to unfold and consequently expose epitopes that may not be identified by the immune system (21).

Clinical trials evaluating the efficacy and safety of Brolucizumab have yielded promising results, demonstrating non-inferiority to existing anti-VEGF agents in terms of visual acuity outcomes and anatomical improvements (22). Notably, Brolucizumab has shown favorable outcomes in reducing central retinal thickness and extending treatment intervals, offering the prospect of reduced treatment burden and improved patient convenience (23). In fact, in HAWK and HARRIER trials, treatment regimen was made up by a loading phase of 3 monthly injections followed by a q8w/q12w re-treatment scheme based on disease activity. Notably, the authors reported that a high percentage of patients, 55.6% in HAWK and 51.0% in HARRIER, maintained q12w dosing after loading until the end of the follow-up (48 week). Furthermore, authors observed that in patients without disease activity in the first 12 weeks, the probability of maintaining q12w scheme thought-out 48 weeks was very high: 85.4% in HAWK and 81.7% in HARRIER (16). Interestingly, authors have also reported that in patients with nAMD characterized by refractory residual retinal fluid despite undergoing repeated intravitreal injections of anti-VEGF, switching from other drugs to Brolucizumab can help in obtaining both functional and anatomical improvement (24).

Another relevant consideration regarding visual recovery and treatment scheme after loading phase is the evaluation of a new optical coherence tomography (OCT) biomarker highlighted by Sadda et al. in a recent post-hoc analysis (25), that is the subretinal hyperreflective material (SHRM), corresponding to the accumulation of blood, fibrin and fibro-scar tissue in the subretinal space. SHRM creates a mechanical barrier between the retina and retinal pigment epithelium (RPE), thus interfering with metabolic exchanges and normal functionality of the photoreceptors, causing worse functional

Abbreviations: CATT, Center for Preventive Ophthalmology and Biostatistics; IOI, Intraocular Inflammation; PRN, ProReNata; SHRM, Subretinal Hyperreflective Material.

improvement during anti-VEGF intravitreal therapy. On this regard, Sadda et al. observed that high SHRM thickness postloading and high SHRM thickness variability over time are negative predictive factors in patients with nAMD. Moreover, the authors described an higher percentage SHRM thickness reductions from baseline in patients treated with Brolucizumab versus Aflibercept (25).

However, concerns regarding the incidence of treatment-related adverse events, including intraocular inflammation and retinal vasculitis, have been raised, necessitating careful consideration of safety profiles in clinical practice (26). In a *post hoc* review of the HAWK and HARRIER study authors analyzed the incidence of adverse events correlated with intravitreal administration of Brolucizumab, carefully excluding forms of intraocular inflammation (IOI) or endophthalmitis not related to the drug. They found out that the incidence of definite/probable IOI was 4.6, IOI + retinal vasculitis was 3.3%, and IOI + retinal vasculitis + retinal occlusion was 2.1%. In brolucizumab-treated eyes with definite/probable IOI, the risk of at least moderate visual acuity loss was 22.2% in eyes with signs of retinal vasculitis and 30.4% in eyes with signs of retinal vasculitis + retinal occlusion; the risk of severe visual acuity loss was 13.9% in eyes with signs of retinal vasculitis and 21.7% in eyes with signs of retinal vasculitis + retinal occlusion (27). In a large retrospective analysis (432,794 injections) is reported that severe IOI occurred at a rate of 1.06/1000 aflibercept injections and 0.64/1000 ranibizumab injections (28). However, despite these data, authors reported that overall rates of moderate or severe visual acuity loss (including that associated with definite/probable IOI, retinal vasculitis and/or retinal occlusion) were similar for brolucizumab and aflibercept (7.4 and 7.7%, respectively). Based on these findings authors suggest accurate slit-lamp examination and ophthalmoscopy when treating patients with Brolucizumab, looking for subtle vasculitis and/or occlusive disease and/or signs of inflammation in the OCT scans (27). Furthermore, in a recent Japanese study, authors reported an association of macular atrophy and SHRM with the development of intravitreal injection-related IOI (21). Another aspect about Brolucizumab analyzed in recent literature is its relevant effect in reducing ocular blood flow in the 30 min following the injection. This reaction is provoked by other anti-VEGF as well and it is already clearly described in literature even with OCT evidence on the choroidal thickness (29) and it is thought to be caused by the activation of endothelial nitric oxide synthase (30). However, in a recent work by Kato et al., in 3 out of 10 patients studied, Brolucizumab decreased ocular blood flow at choroid of more than 30% and this reaction was not present in patients receiving intravitreal aflibercept, even if this finding was not correlated with any clinical significant variation (31).

Real-world evidence, especially Italian, relating to the long-term efficacy and safety of Brolucizumab remains limited, highlighting the need for further research and post-marketing surveillance to elucidate its clinical utility and risk–benefit profile (32, 33). Therefore, the aim of this study is to provide the real-life anatomical-functional and safety results, after 1 year of treatment experience with Brolucizumab.

2 Materials and methods

This is a retrospective observational study in which 44 patients (44 eyes) diagnosed with neovascular age-related macular degeneration (nAMD) were enrolled and treated. Patients were followed both at the Ophthalmology Clinic of the University of Campania "Luigi Vanvitelli," Naples, Italy, and at the Ophthalmology Unit of the "Rummo" Hospital in Benevento, Italy. Table 1 summarizes the demographic and clinical data of the included subjects. The study adhered to the principles outlined in the Declaration of Helsinki and received the approval of the Institutional Board of Auditors of the University of Campania "Luigi Vanvitelli" (Prot. 0003239/I, 01/02/2023). Informed consent to participate in the study was obtained from all participants. We adopted the following exclusion criteria: previous treatments with Brolucizumab; concomitant ocular pathologies like diabetic retinopathy, hereditary retinal dystrophies, retinal vascular occlusions, uveitis; laser photocoagulation and/or vitrectomy performed in the study eye in the last 6 months.

2.1 Study design

We divided the entire cohort into two groups: group 1 (24 treatment-naïve eyes), which underwent a loading dose of 3 monthly intravitreal injections of Broluciziumab 6 mg (0.05 mL solution) + Q8w/Q12w regimen, and a Group 2 (20 non-naïve eyes) which underwent a treatment regimen of 1 injection + ProReNata (PRN) scheme. Monthly, all participants underwent comprehensive ophthalmological evaluation, including: Best-Corrected Visual Acuity (BCVA) assessment using Early Treatment Diabetic Retinopathy Study (ETDRS) chart at 2 m; anterior segment biomicroscopy and binocular indirect ophthalmoscopy performed with Haag-Streit slit lamp; Spectral-Domain Optical Coherence Tomography (SD-OCT) and Angiography-OCT (OCTA). SD-OCT imaging was conducted using Cirrus 6,000 Zeiss Engineering, employing the protocol Macular Cube 512 × 128. Central retinal thickness (CRT) was measured at the foveal center as the distance between the retinal surface and retinal pigment epithelium (RPE). The OCTA was also performed with Cirrus 6,000 Zeiss Engineering.

2.2 Study endpoints

The primary endpoints were: change in BCVA and CRT at 6 and 12 months. We also evaluated the incidence of adverse events such as

TABLE 1 Demographic and clinical ophthalmic data of the enrolled patients.

Characteristics		Naïve	Non naïve
Age-mean (SD)	Years – 77 ± 5.3	76 (±5.2)	78 (±4.3)
Gender	Male: 25 (56.8%)	16 (64%)	9 (36%)
	Female: 19 (43.2%)	10 (43%)	9 (47%)
Systemic risk factors			
Hypertension		17	20
Smoking		11	14
Alcohol		3	4
Number of eyes		24 (55%)	20 (45%)
Lens status	Phakic: 16 (34%)		
	Pseudophakic: 28 (66%)		
MNV type	Type 1 (n. 28) (64%)	16 (57%)	12 (43%)
	Type 2 (n.12) (27%)	5 (41.7%)	7 (58.3%)
	Type 3 (n.4) (9%)	3 (75%)	1 (25%)

vitreitis and/or vasculitis related to therapy with Brolucizumab. Additionally, patients were stratified on the basis of intraretinal (IR), subretinal (SR) and sub-RPE (SRPE) fluid distribution at baseline, in order to evaluate the visual change during follow-up for each subgroup analyzed.

Moreover, we analyzed the anatomical and functional outcomes considering also the type of macular neovascular membrane (MNV), classificating it as already widely described in literature (34):

- MNV type 1: characterized by a sub-RPE fibrovascular complex grown from the choriocapillaris into the sub-RPE space.
- MNV type 2: characterized by the presence of hyperreflective material originating for choriocapillaris, penetrating through the RPE and spreading subretinally.
- MNV type 3: characterized by proliferating vessels that extend from deep retinal capillary plexus towards the outer retina.

Finally, we evaluated the influence of SHRM on BCVA and its anatomical evolution during the 12 months follow up, as already described in a recent work by Sadda et al. (25).

Baseline and follow-up images were independently graded by two investigators (E.M., R.P.) and verified by a senior colleague (C.G).

2.3 Statistical analysis

Data distribution and homogeneity were assessed by using, respectively, Shapiro–Wilk test and Levene's test. Student's T-test was performed to compare 2 groups (for example, in the evaluation of injection number between naïve and non- naïve). Variables based on repeated observations were analyzed by Friedman's test followed by Dunn's *post hoc* test, or by repeated measures analysis of variance (RM-ANOVA) followed by Bonferroni's multiple comparison test. Particularly, Mauchly's test was performed to assess sphericity for RM-ANOVA, and if violated, Greenhouse–Geisser or Huynh-Feldt correction was applied. Pearson correlation analysis was performed to assess the strength of association between 2 variables, confirmed by a linear regression analysis. Data were reported as mean ± SD and a p value <0.05 was considered statistically significant.

3 Results

A collective of 44 eyes from a total sample size of 44 patients (effect size = 0.25; α value = 0.05, 1-β value = 0.95), comprising 25 males (56.8%) and 19 females (43.2%), affected by wet-AMD, were retrospectively included in this investigation. The mean age was 77 +/− 5.3 years. Notably, no substantial distinctions were highlighted between the two subgroups (naïve vs. non naïve) in terms of age and gender distribution. Regarding the type of MNV, patients were classified as follows: 64% type 1 MNV (n. 28); 27% type 2 MNV (n. 12); 9% type 3 MNV (n. 4). A comprehensive overview of systemic, functional and morphological features of the entire cohort is presented in Table 1.

An average number of 3.7 + 1.9 injections (IVTs) was performed in the entire cohort. Analyzing the 2 subgroups (Levene's test: F statistic = 1.4222; p value = 0.2396), in naïve patients an average number of 3.4 + 1.3 IVTs was performed, while in non-naïve patients the average number of IVTs was 4.1 + 1.3 IVTs, without significant differences between the two subgroups in terms of number of IVTs ($p = 0.30$). Among naïve patients, 24 subjects (96%) maintained a Q12 regimen, performing a maximum of 2 IVTs after the initial loading dose, until the end of follow-up. However, among non-naïve patients, most patients (65%; 13 patients) performed 2 injections after the initial IVT.

3.1 Best-corrected visual acuity and optical coherence tomography results

At the 6-month time point we observe a significant improvement in BCVA compared to baseline in the entire cohort (35 ± 16 letters (L) vs. 30 ± 17 L; $p < 0.01$) (Figure 1A), without significant differences between the 2 groups (38 ± 17 and 32 ± 15 L; $p > 0.05$) (Figure 1B). Instead, remarkably, the complete cohort exhibited statistically significant enhancements in BCVA at the 12-month follow-up relative

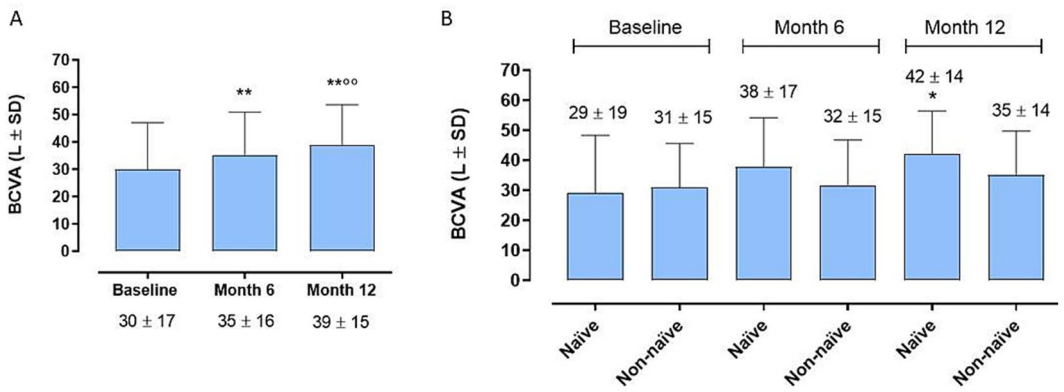

FIGURE 1
(A) Enhancements in best-corrected visual acuity (BCVA) at the 12-month follow-up relative to 6-month follow-up and to baseline [6-month mean difference (MD)]. ** $p < 0.01$ vs. Baseline; °° $p < 0.01$ vs. Month 6 (RM-ANOVA followed by Bonferroni's test, Huynh-Feldt correction). **(B)** Best corrected visual acuity (BCVA) trends between naïve and non-naïve groups during the follow-up. * $p < 0.01$ vs. Baseline, same group; (RM-ANOVA, Greenhouse–Geisser correction).

to baseline (Figure 1A) (39 ± 15 L vs. 30 ± 17 L; $p < 0.01$). Interestingly, the disparity in BCVA improvement between Group 1 and Group 2 failed to obtain statistical significance at 12 months (42 ± 14 L vs. 35 ± 14 L; $p > 0.005$) (Figure 1B). Regarding CRT, marked improvements were observed in both groups, both at 6 and 12 months (281 ± 117 μ vs. 360 ± 129 µ, $p < 0.05$; 265 ± 89 µ vs. 360 ± 129 µ; $p < 0.001$) (Figure 2A), without significant variations between two groups at 6 and 12 months ($p > 0.05$) (Figure 2B).

3.2 Adverse events

Notably, our study reported only one case of acute-onset intermediate uveitis in a treatment-naïve male, whereas non-naïve patients remained free of adverse events throughout the follow-up period. The complete resolution of symptoms was reached with a treatment regimen involving local and systemic steroids and with mydriatic eye drop.

3.3 Best-corrected visual acuity changes and fluid distribution

By evaluating BCVA improvement in relation to the fluid distribution at baseline (IR, SR and SRPE), we did not observe a significant correlation between the localization of the fluids and the visual recovery at the various time points, without significant differences between the two groups of patients analyzed ($p > 0.05$) (Figure 3).

3.4 Visual and optical coherence tomography changes related to the type of macular neovascular membrane

Furthermore, the analysis of BVCA in relation to MNV type (type 1, 2 and 3) did not show substantial changes between groups at baseline and after 6 months ($p > 0.05$), while a significant BVCA improvement was evident in MNV type 1 compared to MNV type 2

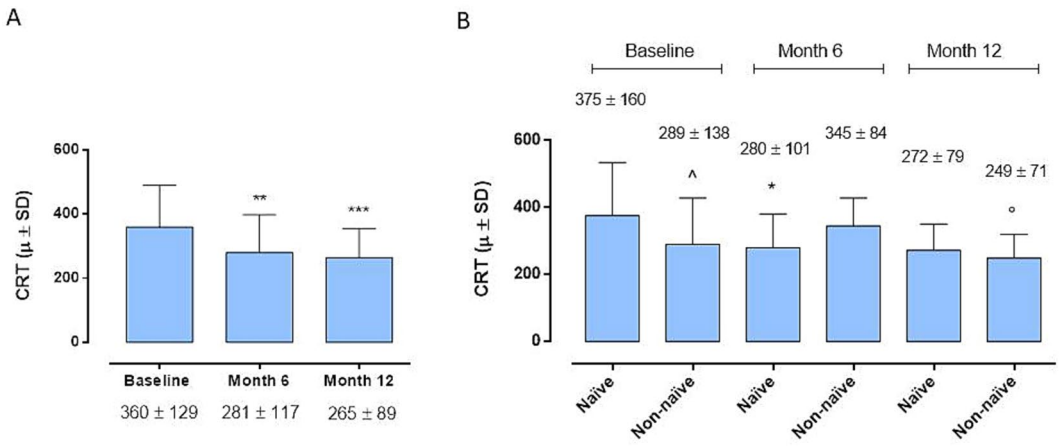

FIGURE 2
(A) Central retinal thickness (CRT) changes in the whole cohort. *$p < 0.01$ and ***$p < 0.001$ vs. Baseline (Friedman's test, followed by Dunn's test). **(B)** Central retinal thickness (CRT) changes between naïve and non-naïve groups during the follow-up (Friedman's test, followed by Dunn's test). *$p < 0.05$ vs Baseline, same group; °$p < 0.05$ vs Month 6, same group; ^$p < 0.05$ vs. naive at Baseline.

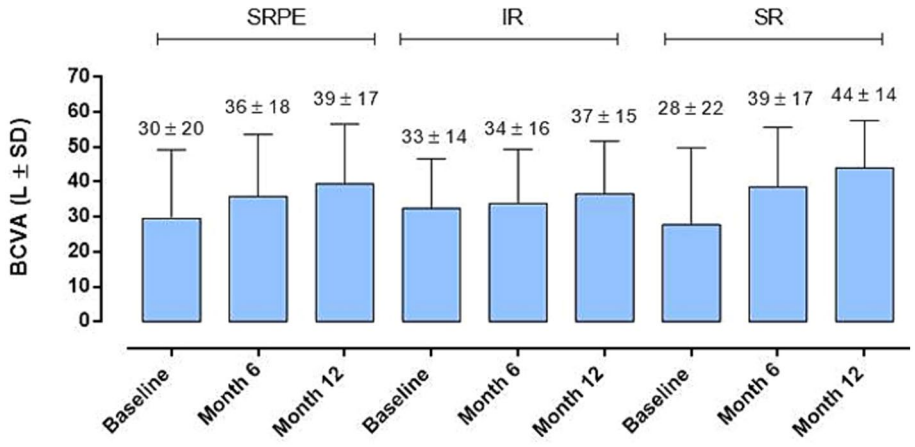

FIGURE 3
Best corrected visual acuity (BCVA) changes in relation to baseline fluid distribution. No significant difference was observed (RM-ANOVA, followed by Bonferroni's test, Greenhouse–Geisser correction); intraretinal (IR), subretinal (SR) and sub- retinal pigment epithelium (SRPE).

($p < 0.05$) after 12 months (Figure 4A). Moreover, the three MNV groups did not show any CRT modifications at all time points considered ($p > 0.05$) (Figure 4B).

3.5 Changes of subretinal hyperreflective material during follow-up

Regarding the SHRM analysis, we observed: (a) the presence of SHRM at baseline was correlated with a lower BCVA after 12 months ($p < 0.05$) (Figure 5A); (b) patients with SHRM at baseline and who performed a greater number of IVTs (equal to or greater than 4 IVTs), showed the persistence of thicker SHRM at the end of follow-up (Figure 5B). In the exemplificative Figure 6, it is possible to observe a case of a naïve patient who presented SHRM at baseline, and despite undergoing 5 injections of Brolucizumab, showed a progressive increase in the SHRM thickness, with concomitant BCVA worsening during the follow-up (Figure 6).

4 Discussion

In this investigation, the morphological and functional changes observed in real life in 45 eyes with nAMD treated with Brolucizumab, after 1 year of follow-up were analyzed.

This study included two cohorts: treatment naïve (Group 1) subjected to a monthly loading phase of 3 injections of Brolucizumab + Q8/Q12; non-naïve (Group 2), who received a single intravitreal injection followed by a PRN treatment regimen. Both groups analyzed demonstrated significant improvements in retinal function (BCVA) and morphology (CRT) at 12 months, with an average improvement of approximately 10 L ETDRS at the end of the follow-up, and with a significant reduction in fluid accumulation in the various compartments (IR, SR, SRPE) at both 6 and 12 months.

The efficacy of Brolucizumab in BCVA enhancement has been previously explored, with reported outcomes displaying variability across studies (33, 35). Notably, the findings of our investigation align more closely with a real-world study conducted by Bilgic et al., which reported BCVA gains in treatment-naïve patients comparable to ours (36). A visual improvement similar to what was observed in our paper has been described by Scupola A. et al., which however describe a greater visual recovery in naïve patients compared to non-naïve patients (+16.0 ± 4.9 L vs. 10.7 ± 5.9 L), associated with a concomitant greater reduction in macular thickness at the end of follow-up (37). Instead, in the BREW study (35), another real-life study, the safety and efficacy of Brolucizumab in determining a stabilization of vision, and not an improvement, was demonstrated only in a cohort of non-naive patients, and after a rather short follow-up of approximately 4 months.

Our findings underscore the effectiveness of Brolucizumab in managing wet-AMD and suggest its potential for long-term efficacy in stabilizing retinal exudation and fluid accumulation, resulting in improved visual prognosis. As proof of the long-lasting action of the drug, in our cohort we achieved good visual recovery after 1 year of follow-up, performing an average small number of 3.9 + 1.9 IVT (on average 2 IVT after the loading phase), and applying a relaxed loading dose in naïve patients (every 45 days), or a single injection + PRN in non-naïve patients. These data suggest a long-lasting effect of the drug, with good anatomical-functional results obtainable even with a

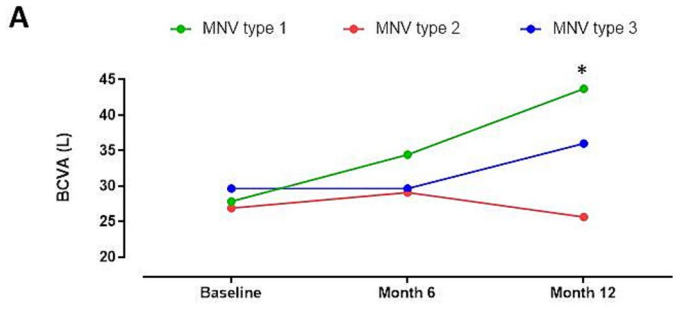

	BCVA (L ± SD)		
MNV type 1	28 ± 18	34 ± 19	44 ± 11 *
MNV type 2	27 ± 23	29 ± 22	26 ± 19
MNV type 3	30 ± 13	30 ± 11	36 ± 13
	Baseline	Month 6	Month 12

* P < 0.05 MNV type 1 vs MNV type 2 at Month 12

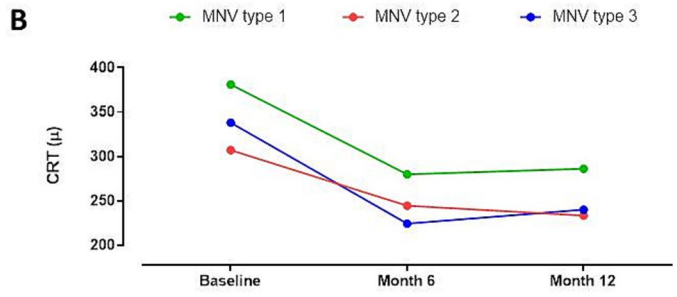

	CRT (µ ± SD)		
MNV type 1	380 ± 149	280 ± 134	285 ± 132
MNV type 2	307 ± 67	244 ± 66	233 ± 46
MNV type 3	338 ± 48	224 ± 68	240 ± 16
	Baseline	**Month 6**	**Month 12**

FIGURE 4
(A) Best corrected visual activity (BCVA) changes in patients with macular neovascular membranes (MNV) type 1, 2 and 3 during follow-up. *$p < 0.05$ MNV type 1 vs. MNV type 2 at Month 12 (RM-ANOVA, followed by Bonferroni's test). **(B)** Central retinal thickness (CRT) changes in patients classified in MNV type 1, 2 and 3 during follow-up (RM-ANOVA, followed by Bonferroni's test).

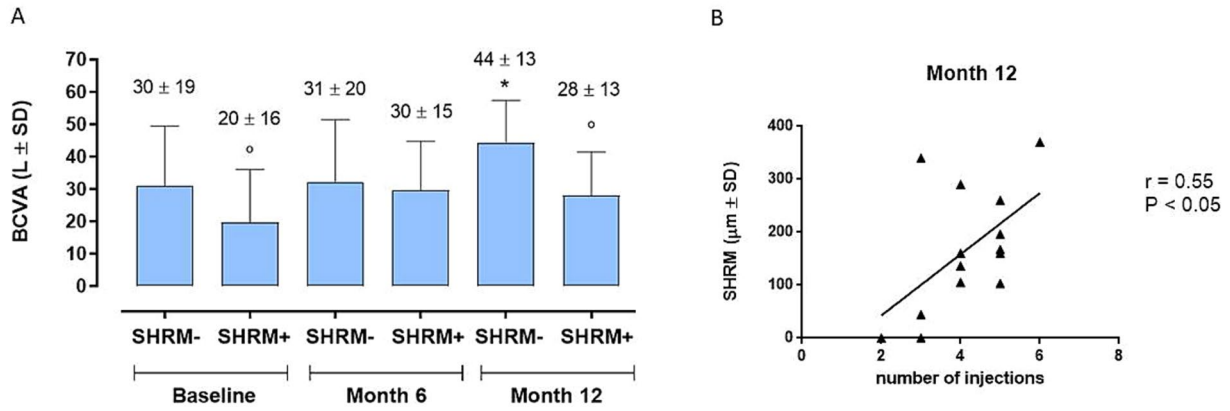

FIGURE 5
(A) Best corrected visual acuity (BCVA) changes in patients with or without baseline subretinal hyperreflective material (SHRM) (SHRM- and SHRM+, respectively) during follow-up. *$p < 0.05$ vs. Baseline, same group; ° $p < 0.05$ vs. SHRM-, same time point (RM-ANOVA, followed by Bonferroni's test, Greenhouse–Geisser correction). **(B)** Significant positive correlation ($p < 0.05$) between subretinal hyperreflective material (SHRM) and number of injections at Month 12, confirmed by a significant linear regression analysis ($p = 0.0429$). r = Pearson's coefficient.

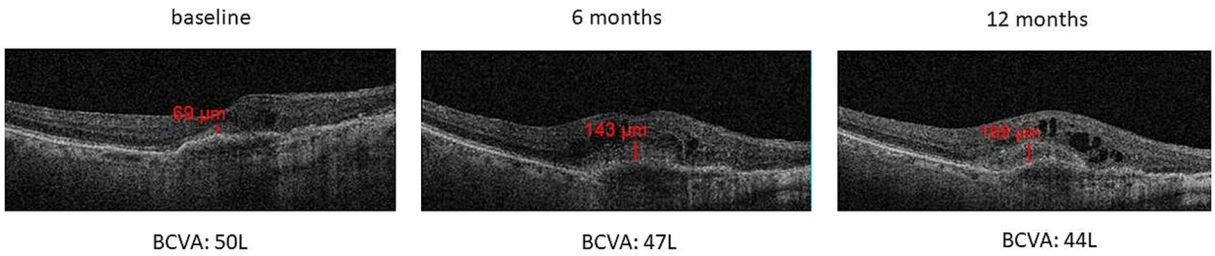

FIGURE 6
Increase of SHRM thickness with concomitant BCVA decrease during 12-months follow-up in a naïve patient that performed 5 intravitreal injections of Brolucizumab.

limited number of injections not too close together, thus reducing the risk of intraocular inflammatory phenomen in this regard, in light of the exponential increase in the prevalence of AMD in the coming years as described in multiple studies (1–3), with consequent increase in the global burden of managing AMD itself (1), and in particular of the advanced form (neovascular), our study, although conducted on a small sample, underlines the importance of using long-acting drugs in real life, such as Brolucizumab, in order to reduce the burden through a smaller number of both injections and check-ups.

Another interesting observation arises from the PROBE study, wherein authors demonstrated the potential efficacy of an initial PRN regimen for Brolucizumab therapy, without loading dose. In fact, the authors observed a significant outcome in terms of both BCVA and CRT at the end of the 11-month follow-up, with a mean of 2.2 ± 0.9 injections (38).

It's conceivable that the smaller size of the Brolucizumab molecule could lead to higher intraocular concentrations, resulting in greater efficacy and duration of pharmacological action (38). However, this characteristic of the drug can determine an increased formation of immune complexes which are the basis of the drug-related immuno-inflammatory reactions, described in multiple studies.

Interesting to note, that however in our study, only one treatment-naïve male patient developed intermediate uveitis. This patient promptly underwent both systemic and topical steroid therapy, with the addition of local mydriatics, showing a rapid and complete visual recovery, demonstrating the importance of early recognition of the initial signs of intraocular inflammation and the consequent timely initiation of the right therapy. An interesting fact that we observed in the management of this patient is the prompt response to steroid therapy with rapid improvement of both the objective and tomographic (OCT) picture, with progressive reduction of the intraretinal edema associated with the neovascular membrane, probably attributable to the decrease in inflammatory component of the disease following the established therapy.

Moreover, at the 12-month follow-up, we observed a significant BCVA improvement in patients with MNV type 1 compared to patients with MNV type 2, without significant differences in terms of CRT. These results are in line with the previous literature data, supporting the evidence that type 1 MNVs are associated with better long term outcomes respect to type 2 MNVs that typically respond quickly to anti-VEGF therapy but are more prone to develop a fibrotic scar (39).

Furthermore, in our study, we observed a significant reabsorption of fluid accumulation in the different retinal compartments (IR, SR, SRPE) during the 12-month follow-up, as already reported in the Hawk and Harrier pivotal studies, and in other real-world studies (16, 23, 40, 41).

Finally, we analyzed the role of a new OCT biomarker, namely SHRM, corresponding to the presence of hyperreflective material in the subretinal space, in relation to the variations in BCVA detected during follow-up. Similarly, to a post-hoc analysis of the Hawk and

Harrier trials (25), and what was stated in a recent long-term study by Fang et al. (42), our study confirmed the negative prognostic role of SHRM, being correlated to a lesser or absent visual recovery in patients (both naïve and non-naïve), who showed greater SHRM thickness at baseline. These results are in agreement with the hypothesis that SHRM, corresponding to the accumulation of blood, fibrin and fibro-scar tissue, creates a mechanical barrier between the retina and RPE, thus interfering with metabolic exchanges and normal functionality of the photoreceptors (43).

At the end of our 12-month analysis, we observed that the patients with SHRM at baseline and who performed a greater number of IVTs (equal to or greater than 4 IVTs), showed the persistence of thicker SHRM at the end of follow-up. The progressive increase in the thickness of the SHRM during follow-up could represent a progressive fibro-cicatricial reaction related to the evolution of the disease itself, and which could also be partially accentuated by antiangiogenic therapy with Brolucizumab. In fact, Brolucizumab is a molecule that shows very innovative and particular structural characteristics such as: small dimensions with a molecular mass of only 26 kDa (smaller than other anti-VEGFs), which allow the achievement of a high concentration, bioavailability and persistence at retinal level, resulting in a high VEGF binding capacity which is 11–22 times greater than aflibercept or ranibizumab (44). All this translates into a very rapid and powerful anti-exudative and anti-hemorrhagic action of Brolucizumab, which could on the other hand also determine a more rapid and marked fibrotic reaction. This result suggests that, especially in the more advanced stages of wet AMD, a very careful selection of patients who can actually benefit from further injections is necessary, especially in real-life where we often encounters problems of an economic and organizational nature.

Since a high number of IVT could also lead to the development of extensive subretinal fibrosis. In this regard, it has been widely demonstrated that even during treatment with anti-VEGF drugs, the development of progressive subretinal fibrosis in the sub-foveal area can occur, representing an important unmet clinical need. For example, the CATT study describes the development of fibrotic scars in 24.7% of all treated eyes, regardless of treatment regimen. Particularly, in the CATT, an average growth in size of the neovascular lesion measured at fluorescein angiography (FA) of approximately: +1.6, +1.9 and + 3.0 mm^2 was observed for monthly bevacizumab, ranibizumab PRN and bevacizumab PRN respectively, therefore showing a continuous growth of fibrovascular tissue. Daniel et al. have observed that the greater risk of developing fibrosis is associated with some basic characteristics of neovascular membrane (NVM), such as: type 2 (predominantly classic) NVM; a larger lesion; increase in foveal retinal thickness; the presence of SF and/or SHRM on OCT (45).

Although this real-life study provides interesting data derived from the daily management of nAMD, it is characterized by some limitations to underline such as: the retrospective design, the relatively small size of the cohort and the short-term follow-up.

5 Conclusion

In conclusion, despite the limitations of the study, our analysis highlights the efficacy and prolonged effect of Brolucizumab therapy in the treatment of nAMD, both in naïve and non-naïve patients, with a good safety profile. Furthermore, this paper underlines the importance of careful selection of the patient to be treated, also considering the negative prognostic role of the possible presence of SHRM at baseline. However, prospective studies with longer follow-up and larger cohorts are needed to better study the long-term effects and any adverse reactions attributable to Brolucizumab therapy.

Data availability statement

The original contributions presented in the study are included in the article/supplementary material, further inquiries can be directed to the corresponding author.

Ethics statement

The studies involving humans were approved by the Ethics Committee of University of Campania "Luigi Vanvitelli", (protocol: 0003239/I, 01/02/2023). The studies were conducted in accordance with the local legislation and institutional requirements. The participants provided their written informed consent to participate in this study.

Author contributions

SR: Conceptualization, Project administration, Supervision, Writing – original draft, Writing – review & editing. CG: Conceptualization, Data curation, Methodology, Writing – original draft, Writing – review & editing. EM: Conceptualization, Data curation, Methodology, Visualization, Writing – original draft, Writing – review & editing. RP: Data curation, Writing – original draft, Writing – review & editing, Methodology, Validation. MT: Data curation, Methodology, Supervision, Validation, Visualization, Writing – original draft, Writing – review & editing. AG: Data curation, Methodology, Writing – original draft, Writing – review & editing. FS: Funding acquisition, Project administration, Resources, Supervision, Validation, Writing – original draft, Writing – review & editing.

Funding

The author(s) declare financial support was received for the research, authorship, and/or publication of this article. This research and the APC were funded by Italian Ministry of Education, University and Research, grant number PRIN 2020FR7TCL_002.

Conflict of interest

The authors declare that the research was conducted in the absence of any commercial or financial relationships that could be construed as a potential conflict of interest.

Publisher's note

References

1. Friedman D, et al. Prevalence of age-related macular degeneration in the United States. *Arch Ophthalmol*. (2004) 122:564. doi: 10.1001/archopht.122.4.564

2. Klaver CC, Assink JJ, van Leeuwen R, Wolfs RC, Vingerling JR, Stijnen T, et al. Incidence and progression rates of age-related maculopathy: the Rotterdam study. *Invest Ophthalmol Vis Sci*. (2001) 42:2237–41.

3. Wong WL, Su X, Li X, Cheung CMG, Klein R, Cheng CY, et al. Global prevalence of age-related macular degeneration and disease burden projection for 2020 and 2040: a systematic review and meta-analysis. *Lancet Glob Health*. (2014) 2:e106–16. doi: 10.1016/S2214-109X(13)70145-1

4. Ferris F, Davis MD, Clemons TE, Lee LY, Chew EY, Lindblad AS, et al. A simplified severity scale for age-related macular degeneration: AREDS report no. 18. *Arch Ophthalmol*. (2005) 123:1570–4. doi: 10.1001/archopht.123.11.1570

5. Wong T, Chakravarthy U, Klein R, Mitchell P, Zlateva G, Buggage R, et al. The natural history and prognosis of Neovascular age-related macular degeneration. *Ophthalmology*. (2008) 115:116–126.e1. doi: 10.1016/j.ophtha.2007.03.008

6. Pauleikhoff D. Neovascular age-related macular degeneration: natural history and treatment outcomes. *Retina*. (2005) 25:1065–84. doi: 10.1097/00006982-200512000-00016

7. Fleckenstein M, Mitchell P, Freund KB, Sadda SV, Holz FG, Brittain C, et al. The progression of geographic atrophy secondary to age-related macular degeneration. *Ophthalmology*. (2018) 125:369–90. doi: 10.1016/j.ophtha.2017.08.038

8. Moutray T, Chakravarthy U. Age-related macular degeneration: current treatment and future options. *Therap Adv Chronic Dis*. (2011) 2:325–31. doi: 10.1177/2040622311415895

9. Fleckenstein M, Schmitz-Valckenberg S, Chakravarthy U. Age-related macular degeneration: a review. *JAMA*. (2024) 331:147. doi: 10.1001/jama.2023.26074

10. Ricci F, Bandello F, Navarra P, Staurenghi G, Stumpp M, Zarbin M. Neovascular age-related macular degeneration: therapeutic management and new-upcoming approaches. *Int J Mol Sci*. (2020) 21:8242. doi: 10.3390/ijms21218242

11. Rosenfeld PJ, Brown DM, Heier JS, Boyer DS, Kaiser PK, Chung CY, et al. Ranibizumab for Neovascular age-related macular degeneration. *N Engl J Med*. (2006) 355:1419–31. doi: 10.1056/NEJMoa054481

12. Schmidt-Erfurth U, Chong V, Loewenstein A, Larsen M, Souied E, Schlingemann R, et al. Guidelines for the management of neovascular age-related macular degeneration by the European Society of Retina Specialists (EURETINA). *Br J Ophthalmol*. (2014) 98:1144–67. doi: 10.1136/bjophthalmol-2014-305702

13. Martin DF, et al. Ranibizumab and bevacizumab for treatment of Neovascular age-related macular degeneration. *Ophthalmology*. (2012) 119:1388–98. doi: 10.1016/j.ophtha.2012.03.053

14. Chakravarthy U, Armendariz BG, Fauser S. 15 years of anti-VEGF treatment for nAMD: success or failure or something in between? *Eye*. (2022) 36:2232–3. doi: 10.1038/s41433-022-02153-9

15. Lanzetta P, Loewenstein A. Fundamental principles of an anti-VEGF treatment regimen: optimal application of intravitreal anti–vascular endothelial growth factor therapy of macular diseases. *Graefes Arch Clin Exp Ophthalmol*. (2017) 255:1259–73. doi: 10.1007/s00417-017-3647-4

16. Dugel PU, Koh A, Ogura Y, Jaffe GJ, Schmidt-Erfurth U, Brown DM, et al. HAWK and HARRIER: phase 3, multicenter, randomized, double-masked trials of Brolucizumab for Neovascular age-related macular degeneration. *Ophthalmology*. (2020) 127:72–84. doi: 10.1016/j.ophtha.2019.04.017

17. Finger RP, Dennis N, Freitas R, Quenéchdu A, Clemens A, Karcher H, et al. Comparative efficacy of Brolucizumab in the treatment of Neovascular age-related macular degeneration: a systematic literature review and network Meta-analysis. *Adv Ther*. (2022) 39:3425–48. doi: 10.1007/s12325-022-02193-3

18. Gesualdo C, Rossi S, Iodice CM, Guarino F, Petrella M, D'Agostino FA, et al. Brolucizumab Intravitreal injections for wet age-related macular degeneration: real-life study on a cohort of Italian patients. *Medicina*. (2023) 59:1110. doi: 10.3390/medicina59061110

19. Ferro Desideri L, Traverso CE, Nicolò M. Brolucizumab: a novel anti-VEGF humanized single-chain antibody fragment for treating w-AMD. *Expert Opin Biol Ther*. (2021) 21:553–61. doi: 10.1080/14712598.2021.1915278

20. Kim HM, Woo SJ. Ocular drug delivery to the retina: current innovations and future perspectives. *Pharmaceutics*. (2021) 13:108. doi: 10.3390/pharmaceutics13010108

21. Sotani R, Matsumiya W, Kim KW, Miki A, Yasuda E, Maeda Y, et al. Correction: clinical features and associated factors of intraocular inflammation following intravitreal brolucizumab as switching therapy for neovascular age-related macular degeneration. *Graefes Arch Clin Exp Ophthalmol*. (2024) 262:671–1. doi: 10.1007/s00417-023-06339-z

22. Dugel PU, Jaffe GJ, Sallstig P, Warburton J, Weichselberger A, Wieland M, et al. Brolucizumab versus Aflibercept in participants with Neovascular age-related macular degeneration: a randomized trial. *Ophthalmology*. (2017) 124:1296–304. doi: 10.1016/j.ophtha.2017.03.057

23. Montesel A, Bucolo C, Sallo FB, Eandi CM. Short-term efficacy and safety outcomes of Brolucizumab in the real-life clinical practice. *Front Pharmacol*. (2021) 12:720345. doi: 10.3389/fphar.2021.720345

24. Cavalleri M, Tombolini B, Sacconi R, Gatta G, Valeri R, Bandello F, et al. Real-life experience and predictors of visual outcomes with Intravitreal Brolucizumab switch for treatment of Neovascular age-related macular degeneration. *Ophthalmologica*. (2023) 246:158–68. doi: 10.1159/000530544

25. Sadda S, Sarraf D, Khanani AM, Tadayoni R, Chang AA, Saffar I, et al. Comparative assessment of subretinal hyper-reflective material in patients treated with brolucizumab versus aflibercept in HAWK and HARRIER. *Br J Ophthalmol*. (2024) 108:852–8. doi: 10.1136/bjo-2023-323577

26. Khanani AM, Zarbin MA, Barakat MR, Albini TA, Kaiser PK, B G, et al. Safety outcomes of Brolucizumab in Neovascular age-related macular degeneration: results from the IRIS registry and komodo healthcare map. *JAMA Ophthalmol*. (2022) 140:20–8. doi: 10.1001/jamaophthalmol.2021.4585

27. Monés J, Srivastava SK, Jaffe GJ, Tadayoni R, Albini TA, Kaiser PK, et al. Risk of inflammation, retinal Vasculitis, and retinal occlusion–related events with Brolucizumab. *Ophthalmology*. (2021) 128:1050–9. doi: 10.1016/j.ophtha.2020.11.011

28. Souied EH, Dugel PU, Ferreira A, Hashmonay R, Lu J, Kelly SP. Severe ocular inflammation following Ranibizumab or Aflibercept injections for age-related macular degeneration: a retrospective claims database analysis. *Ophthalmic Epidemiol*. (2016) 23:71–9. doi: 10.3109/09286586.2015.1090004

29. Pellegrini M, Bernabei F, Mercanti A, Sebastiani S, Peiretti E, Iovino C, et al. Short-term choroidal vascular changes after aflibercept therapy for neovascular age-related macular degeneration. *Graefes Arch Clin Exp Ophthalmol*. (2021) 259:911–8. doi: 10.1007/s00417-020-04957-5

30. Fontaine O, Olivier S, Descovich D, Cordahi G, Vaucher E, Lesk MR. The effect of Intravitreal injection of bevacizumab on retinal circulation in patients with Neovascular macular degeneration. *Invest Opthalmol Visual Sci*. (2011) 52:7400. doi: 10.1167/iovs.10-6646

31. Kato N, Haruta M, Furushima K, Arai R, Matsuo Y, Yoshida S. Decrease in ocular blood flow thirty minutes after Intravitreal injections of Brolucizumab and Aflibercept for Neovascular age-related macular degeneration. *Clin Ophthalmol*. (2023) 17:1187–92. doi: 10.2147/OPTH.S407249

32. Holz FG, Iida T, Maruko I, Sadda SVR. A consensus on risk mitigation for Brolucizumab in Neovascular age-related macular degeneration: patient selection, evaluation, and treatment. *Retina*. (2022) 42:1629–37. doi: 10.1097/IAE.0000000000003556

33. Yeom H, Kwon HJ, Kim YJ, Lee J, Yoon YH, Lee JY. Real-world study to evaluate the efficacy and safety of intravitreal brolucizumab for refractory neovascular age-related macular degeneration. *Sci Rep*. (2023) 13:11400. doi: 10.1038/s41598-023-38173-y

34. Faatz H, Rothaus K, Ziegler M, Book M, Heimes-Bussmann B, Pauleikhoff D, et al. Vascular analysis of type 1, 2, and 3 macular neovascularization in age-related macular degeneration using swept-source optical coherence tomography angiography shows new insights into differences of pathologic vasculature and may Lead to a more personalized understanding. *Biomedicines*. (2022) 10:694. doi: 10.3390/biomedicines10030694

35. Sharma A, Kumar N, Parachuri N, Sadda SR, Corradetti G, Heier J, et al. Correction: Brolucizumab—early real-world experience: BREW study. *Eye*. (2021) 35:1286–6. doi: 10.1038/s41433-020-01351-7

36. Bilgic A, Kodjikian L, Srivastava S, Dwivedi S, Banker AS, Abukashabah A, et al. Initial pro re Nata Brolucizumab for exudative AMD: the PROBE study. *J Clin Med*. (2021) 10:4153. doi: 10.3390/jcm10184153

37. Scupola A, Carlà MM, Boselli F, Giannuzzi F, de Filippis A, Fossataro C, et al. Brolucizumab for wet age-related macular degeneration: one-year real-world experience from a tertiary center. *Ophthalmologica*. (2023) 246:58–67. doi: 10.1159/000529817

38. Bilgic A, Kodjikian L, March De Ribot F, et al. Real-world experience with Brolucizumab in wet age-related macular degeneration: the REBA study. *J Clin Med*. (2021) 10:2758. doi: 10.3390/jcm10132758

39. Mathis T, Holz FG, Sivaprasad S, Yoon YH, Eter N, Chen LJ, et al. Characterisation of macular neovascularisation subtypes in age-related macular degeneration to optimise treatment outcomes. *Eye*. (2023) 37:1758–65. doi: 10.1038/s41433-022-02231-y

40. Matsumoto H, Hoshino J, Mukai R, Nakamura K, Akiyama H. Short-term outcomes of intravitreal brolucizumab for treatment-naïve neovascular age-related macular degeneration with type 1 choroidal neovascularization including polypoidal choroidal vasculopathy. *Sci Rep*. (2021) 11:6759. doi: 10.1038/s41598-021-86014-7

41. Toto L, Ruggeri ML, D'Aloisio R, de Nicola C, Trivigno C, Cerino L, et al. Brolucizumab Intravitreal injection in macular neovascularization type 1: VA, SD-OCT, and OCTA parameter changes during a 16-week follow-up. *Ophthalmic Res*. (2023) 66:218–27. doi: 10.1159/000526851

42. Fang M, Chanwimol K, Maram J, Datoo O'Keefe GA, Wykoff CC, Sarraf D, et al. Morphological characteristics of eyes with neovascular age-related macular degeneration and good long-term visual outcomes after anti-VEGF therapy. *Br J Ophthalmol*. (2023) 107:399–405. doi: 10.1136/bjophthalmol-2021-319602

43. Feo A, Stradiotto E, Sacconi R, Menean M, Querques G, Romano MR. Subretinal hyperreflective material in retinal and chorioretinal disorders: a comprehensive review. *Surv Ophthalmol*. (2024) 69:362–77. doi: 10.1016/j.survophthal.2023.10.013

44. Nguyen QD, das A, do DV, Dugel PU, Gomes A, Holz FG, et al. Brolucizumab: evolution through preclinical and clinical studies and the implications for the management of Neovascular age-related macular degeneration. *Ophthalmology*. (2020) 127:963–76. doi: 10.1016/j.ophtha.2019.12.031

45. Daniel E, Toth CA, Grunwald JE, Jaffe GJ, Martin DF, Fine SL, et al. Risk of scar in the comparison of age-related macular degeneration treatments trials. *Ophthalmology*. (2014) 121:656–66. doi: 10.1016/j.ophtha.2013.10.019

frontiers | Frontiers in Medicine

TYPE Original Research
PUBLISHED 18 February 2025
DOI 10.3389/fmed.2025.1498319

OPEN ACCESS

EDITED BY
Horace Massa,
Hôpitaux Universitaires de Genève (HUG), Switzerland

REVIEWED BY
Charanya Ramachandran,
LV Prasad Eye Institute, India
Ratnakar Tripathi,
University of Missouri, United States

*CORRESPONDENCE
Arantxa Acera
✉ mariaaranzazu.acera@ehu.eus

RECEIVED 18 September 2024
ACCEPTED 03 February 2025
PUBLISHED 18 February 2025

CITATION
Basasoro A, Mendicute J, Rezola M, Burgos J, Fernández M, Esporrín-Ubieto D, Sonzogni A, Calderón M, Calafel I, Díaz A, De Souza J, Aiastui A, Azkargorta M, Elortza F, Vecino E and Acera A (2025) The influence of amniotic membrane proteins on corneal regeneration when delivered directly or using hydrogel platforms.
Front. Med. 12:1498319.
doi: 10.3389/fmed.2025.1498319

The influence of amniotic membrane proteins on corneal regeneration when delivered directly or using hydrogel platforms

Ayla Basasoro[1,2], Javier Mendicute[1,2], Marta Rezola[1], Jorge Burgos[3], Mercedes Fernández[4], David Esporrín-Ubieto[5], Ana Sonzogni[6], Marcelo Calderón[5,7], Itxaso Calafel[4], Aitor Díaz[8], Juliana De Souza[8], Ana Aiastui[2], Mikel Azkargorta[9], Félix Elortza[9], Elena Vecino[10] and Arantxa Acera[2,7,10]*

[1]Hospital Universitario Donostia, Donostia-San Sebastián, Spain, [2]Biogipuzkoa Health Research Institute, Donostia-San Sebastián, Spain, [3]Hospital Universitario Cruces, Barakaldo, Spain, [4]POLYMAT, Department of Polymers and Advanced Materials: Physics, Chemistry and Technology, Faculty of Chemistry, University of the Basque Country UPV/EHU, Donostia-San Sebastián, Spain, [5]POLYMAT, Applied Chemistry Department, Faculty of Chemistry, University of the Basque Country UPV/EHU, Donostia-San Sebastián, Spain, [6]NTEC (UNL-CONICET), Güemes 3450, Santa Fe, Argentina, [7]IKERBASQUE, Basque Foundation for Science, Bilbao, Spain, [8]CIDETEC, Basque Research and Technology Alliance (BRTA), Donostia-San Sebastián, Spain, [9]Proteomics Platform, CIC bioGUNE, Basque Research and Technology Alliance (BRTA), CIBERehd, Derio, Spain, [10]Department of Cell Biology and Histology, Experimental Ophthalmo-Biology Group (GOBE), University of the Basque Country UPV/EHU, Leioa, Spain

Background/aims: Chemical burns to the eye cause extensive ocular surface damage, often resulting in permanent visual impairment. The amniotic membrane (AM), with its regenerative properties, has shown great potential in treating such injuries. Recent innovations, including hydrogel-based delivery systems, have been developed to improve drug retention and promote corneal healing. This study aimed to evaluate whether hydrogels loaded with proteins from human AM could enhance corneal wound healing effectively.

Methods: Alkaline burns (8 mm diameter) were induced in the cornea of anesthetized male New Zealand White rabbits (n = 44) by placing filter paper soaked in 1M NaOH on them for 60 s. After rinsed the corneas immediately with a balanced salt solution, the wounds then received: (1) no treatment; (2) AM transplantation; or (3) a dynamic hyaluronic acid hydrogel based on gold thiolate loaded with an AM protein extract (AME); or (4) a physically cross-linked ocular hydrogel insert loaded with the same AME. The contralateral uninjured eye served as a control. The wound area and proportion of healed corneas was assessed in microphotographs. In addition, corneal histology was evaluated by hematoxylin–eosin and Masson's trichrome staining, examining epithelial and stromal thickness, the endothelial layer, and inflammatory infiltration in the early (day 2) and late (day 28) phases of healing.

Results: There was more frequent corneal wound closure in animals treated with the hydrogels (treatments 3 and 4) on day 14 (44.4 and 55.5%, respectively) than in the untreated controls (33.3%). Histologically, abnormal re-epithelialization and altered epithelial junctions were observed, with no significant differences in epithelial thickness. Endothelial damage correlated with significant thinning (p = 0.001), with treatments 2 and 3 producing significant differences in the inflammatory infiltrate (p = 0.01).

Conclusion: Applying new biocompatible hydrogels to the ocular surface that release AM proteins may help close corneal wounds caused by caustic burns. The aggressive nature of burns hinders the detection of differences in the wound area between treatments 28 days after injury. However, improving the adhesion of a solid hydrogel to the mucosa of the ocular surface could enhance these outcomes by keeping the implant in contact with the wound for a longer period.

KEYWORDS

hydrogel inserts, cornea, wound healing, rabbit, amniotic membrane

1 Introduction

Chemical eye burns produce considerable damage to the ocular surface epithelium, cornea and anterior segment, provoking permanent unilateral or bilateral visual impairment (1). These injuries may be caused by direct exposure of the eye to corrosive chemicals, and they may have severe consequences on the structure and function of the eyeball, and/or its surrounding tissues. The severity of an ocular chemical burn depends on various factors, including the nature of the chemical agent, the duration of exposure, the area exposed, the concentration of the agent and the promptness of treatment (2). Proper management of chemical eye burns requires a rapid and accurate initial assessment, followed by therapeutic interventions that minimize tissue damage, preventing the progression of the injury and promoting healing of the ocular surface (2). In this sense, the amniotic membrane (AM) has been proposed as a promising tool due to its unique composition and regenerative properties (3). This tissue is derived from the inner layer of the amniotic sac and its unique characteristics make it ideal for various therapeutic applications related to ocular conditions (4). There is clinical evidence that AM transplantation promotes corneal epithelial healing (5), reduces scar formation (6), suppresses inflammation (7) and inhibits angiogenesis (8, 9). Many of these effects have been attributed to the protein content of the AM, which includes growth factors (10), cytokines and structural proteins (11) that can modulate immune responses and promote tissue regeneration. The proteins obtained from AM preparations are influenced by several factors, including gestational and donor age (12), the method of preservation employed (13), as well as the filtration and centrifugation protocols used to prepare eye drops. Previously, our group characterized some growth factors in the AM known to be involved in re-epithelialization, such as beta-Fibroblast Growth Factor (bFGF), Endothelial Growth Factor (EGF), Hepatocyte Growth Factor (HGF), Nerve Growth Factor (NGF) and the endogenous anti-angiogenic factor endostatin (14). However, considering the potential of the AM in this process, it would be of interest to obtain a more comprehensive understanding of its protein profile.

Corneal ulcers are generally treated using eye drops, which requires frequent administration as the active ingredient only remains in contact with the ocular surface briefly due to the constant flushing by tears through blinking. Over the past decade, novel approaches to overcome this limitation have been developed, improving drug residence times on the cornea. These include the use of nanoparticles (15), liposomes (16), micro emulsions (17), Nano suspensions (18), polymeric micelles (19, 20) and hydrogel-based delivery systems (21). Hydrogels are three-dimensional polymeric structures made up of water embedded in polymeric chains that are designed to retain the cohesive properties of solids and the transport properties of liquids (22). Hydrogels can be broadly categorized into physical and chemical hydrogels based on the interactions establishing their network structure. Physical Hydrogels are mainly formed through physical interactions like hydrogen bonding, hydrophobic interactions or physical entanglement of polymer chains. These interactions are reversible and can be disrupted by altering environmental conditions, such as temperature, pH or ionic strength (23). Of these, hydrogels based on Eudragits® are of particular interest as combining this polymer with other biocompatible polymers (e.g., polyvinylpyrrolidone (PVP), polyvinyl alcohol (PVA), or polyethylene glycol (PEG)) enables some properties of the hydrogels to be modulated, such as their porosity, stability and cargo release capacity (24, 25). Significantly, the use of Eudragits has been explored in physically cross-linked hydrogels designed for ophthalmic applications (26–29).

Covalently crosslinking polymer chains, stabilizing the bonds in the hydrogel network, form chemical hydrogels. Such crosslinking typically involves chemical reactions like polymerization, crosslinking agents or enzymatic reactions (23). As a result, chemical hydrogels have stable lattice structures that are irreversible under normal conditions. However, modulating the degree of entanglement/cross-linking in these hydrogels can yield soft, degradable and permeable structures, with mechanical properties similar to those of tissues, thereby offering a promising solution for prolonged drug delivery and tissue engineering applications (25). Another key factor that enhances the potential for hydrogels to be used in clinical applications is their mucoadhesivity. The water content and the soft, flexible nature of hydrogels make them suitable to associate with mucin, through either electrostatic interaction, hydrogen bonding, hydrophobic interactions or Van der Waals forces. As a result, there have been efforts to develop hydrogels that adhere to mucous membranes with the potential to extend drug residence times (30). Recent years have seen the development of the next generation of hydrogels based on reversible bonds, namely dynamic hydrogels, offering the promise of being more adaptable and of inducing self-healing in natural tissues. These hydrogels possess a network of polymer chains that can form dynamic bonds that enable the material to reorganize its structure in response to external stimuli (31). Of particular interest are those gels based on interactions established between Au (I) or Ag (I) ions and thiolate polymers. These reversible interactions, namely, metal-thiolate (M-S) and disulphide (S-S) bonds provide gels that adopt features of an injectable material with permanent exchange ratios and self-healing capacities. In addition, if thiolate hyaluronic acid (HA-SH) is used, better mucoadhesivity to the cornea is expected thanks to the ability of thiol groups to react with the thiol groups of cysteine residues in the tear film's mucin (30, 32).

This study set out to evaluate the efficacy of two hydrogel formulations for the treatment of corneal ulcers: one dynamic and injectable; and the other based on Eudragit combined with biocompatible polymers. This is a preliminary study in which, after optimizing the corresponding formulations, biocompatible hydrogels were obtained that could establish a baseline on which further improvements can be made. AM proteins were incorporated into the hydrogels to compare the rate of corneal ulcer closure between them, comparing their effects with the more traditional transplantation of AM fragments using sutures (AMT). Indeed, the AM protein extracts (AMEs) were analyzed out with a view to obtain new insights into the key molecules responsible for the therapeutic effects of the AM. This information may well aid the selection of specific proteins to be included in hydrogels, enhance current formulations and develop new, more effective treatment strategies.

2 Materials and methods

2.1 Amniotic membrane protein extraction

AMs were obtained from the Gynaecology and Obstetrics Department at Cruces University Hospital (Barakaldo, Spain), their use in this study was approved by the Cruces Ethics Committee (CEIC code E20/05). All human tissues were handled in accordance with the tenets of the Declaration of Helsinki regarding medical research involving human subjects. The patient selection process followed the same criteria established for AM donation intended for ocular surface surgery. The inclusion criteria required participants to be between 18 and 42 years of age, seronegative for human immunodeficiency virus (HIV), hepatitis B and C, and syphilis, and to have experienced full-term pregnancies (38–42 weeks). Exclusion criteria ruled out individuals with gestational or fetal diseases.

Human placentas were managed in alignment with the principles outlined in the Declaration of Helsinki. Following the acquisition of informed consent, four human placentas from Caucasian women were collected following elective caesarean deliveries and promptly processed under sterile conditions. First, the placentas were rinsed with sterile saline solution to eliminate blood clots. The AM was then meticulously detached from the chorion using blunt dissection and thoroughly rinsed several times in a saline solution enriched with antibiotics and antifungal agents (penicillin 10,000 U/mL, streptomycin 50 mg/mL, and amphotericin B 2.5 mg/mL). Subsequently, each AM was transferred to a sterile container containing a 1:1 mixture of Dulbecco's Modified Eagle's Medium (DMEM) and glycerol (Gibco®, USA) and preserved at −80°C until required for use.

The protocol for extracting proteins from the AM was carried out as established previously (14).

2.2 Proteomic analysis of the AM

Label-free protein identification based on liquid chromatography-mass spectrometry (LC–MS) was performed to assess the differences in the proteome of the AM tissue used for transplantation (directly in contact with the corneal epithelium) and the AME obtained by sonication and incorporated into the hydrogels studied. For AME, a previously described mild homogenization protocol was used (14). This method is based on a gentle approach designed to preserve the functionality and biological activity of the extracted proteins. In contrast, protein extraction from the AM tissue was obtained through Precellys (Bertin Technologies, Montagne-le-Bretonneux, France) homogenization of the AM extract in a buffer containing 7 M urea, 2 M thiourea and 4% CHAPS. The proteins obtained by the two methods were digested with trypsin (Sigma Aldrich, St. Louis, MO, USA) following the FASP protocol described previously (33). The trypsin was prepared in 50 mM ammonium bicarbonate and added to the protein at a trypsin: protein ratio of 1:10, incubating the mixture overnight (ON) at 37°C. The resulting peptides were dried in a RVC2 25 speedvac concentrator (Christ, Vienna, Austria), resuspended in 0.1% Formic Acid (FA) (Sigma Aldrich, St. Louis, MO, USA), desalted and again resuspended in 0.1% FA using C18 stage tips (Millipore, St. Louis, MO, USA). The peptides recovered were then loaded onto an EvoSep One (EvoSep, Odense, Denmark) chromatograph coupled on-line to a TIMS ToF Pro mass spectrometer (Bruker, Coventry, UK), using Parallel Accumulation Serial Fragmentation (PASEF) acquisition to rapidly achieve a highly sensitive analysis following the 30 SPD protocol (approx. 44 min runs) under default Evosep settings. Data-dependent acquisition (DDA) was used and the data was processed with MaxQuant software (Max Planck Institute of Biochemistry, Martinsried, Germany) using default parameters (34).

Searches were carried out against a database consisting of human protein entries from Uniprot/SWISSPROT [UniProt Consortium, European Bioinformatics Institute (EMBL-EBI), Hinxton, UK; Swiss Institute of Bioinformatics (SIB), Geneva, Switzerland; and Protein Information Resource (PIR), Georgetown University, Washington, DC, USA]. Carbamidomethylation of cysteines was considered as a fixed modification and the oxidation of methionines as a variable modification. Proteins passing a false detection rate (FDR) filter of <1% at the protein level were considered for further analysis. Spectral Count data was used to compare the different conditions, specifically using a modified spectral counting method named Normalized Spectral Abundance Factor (NSAF) (35). Briefly, protein spectral counts (the sum of all peptide identifications obtained for a given protein) were corrected by protein length, obtaining the Spectral Abundance Factor (SAF) for each protein. These SAF values were further normalized against the sum of all SAF values in a specific sample and expressed as a percentage of the total.

The mass spectrometry proteomics data have been deposited to the ProteomeXchange Consortium via the PRIDE (36) partner repository with the dataset identifier PXD055969.

Gene Ontology (GO) enrichment analysis was carried out using the DAVID online tool (http://david.abcc.ncifcrf.gov/summary.jsp, Accessed 7 October 2020) (37). DAVID is a GO Term annotation and enrichment analysis tool used to highlight the most relevant GO terms associated with a given gene list.

2.3 Hydrogel synthesis

Two hydrogels were synthesized, designated as hydrogel A (treatment 3) and B (treatment 4), each with distinct formulations but encapsulating the same AME proteins.

2.3.1 Hydrogel A

Hydrogel A is an injectable dynamic hydrogel prepared using HA-SH as described below (Figures 1A,B). Initially, HA-SH (20 mg) with a molecular weight (MW) of 250 kDa and with 3.6 μmol thiol groups (Haworks, USA) was dissolved in 500 μL of deionized water (solution A). Subsequently, solution B was obtained by diluting 3.6 μL of an aqueous solution of HAuCl4 (0.01 M, 99% purity: Aldrich, USA) in 686.4 μL of deionized water. Both solutions (A and B) were shielded under nitrogen to prevent oxidation of the free thiols until solution B was slowly added to solution A with continuous magnetic stirring. Phenol red (10 μL, 0.07%wt: Aldrich, USA) was introduced as a pH indicator and the pH of the hydrogel was adjusted to approximately 7.5 using an aqueous 5 M solution of NaOH (Aldrich, USA), after which 100 μL of 10X PBS (Merck, Germany) was added to buffer the samples. The remaining free thiolates were left as oxidized until no variation in the rheological properties (loss and storage moduli) were observed after approximately 48 h at 4°C. AM proteins were incorporated into the hydrogel during the buffering step, resulting in a final protein concentration of 1 mg/mL when determined using the Bradford assay (Thermo Fisher Scientific, USA).

2.3.2 Hydrogel B

Hydrogel B, a physical hydrogel, was prepared as a film using different polymers in its formulation, all of them FDA approved (Figures 1C,D). Hydrogel B is composed of 50 kDa MW PVP, 100 kDa MW PVA, 2 kDa PEG, 125 kDa Eudragit S100, HA with a MW of 750 kDa and glycerol. The incorporation of HA to what was a previously described formulation was aimed at improving ocular mucoadhesion (38). Films were prepared using the solvent-casting technique, whereby PVA and PVP were mixed for 2 h in water at 90°C (39) and after cooling. PEG, Eudragit S100 and HA were added to the mixture, and the pH was adjusted to 7.4 using 10 mM PBS and NaOH/HCl 1 M. AM proteins were incorporated prior to evaporation of the solvent at a constant temperature of 37°C. Finally, the resulting film was cut into 0.4 × 0.4 cm fragments with an average thickness of 1 mm, each containing 1 mg/mL of AM protein.

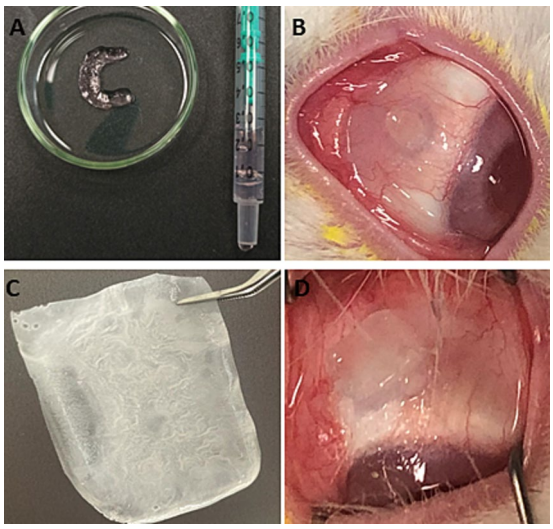

FIGURE 1
(A) Image of hydrogel A (ointment-like hydrogel) on a Petri dish. **(B)** Image of hydrogel A applied to the conjunctiva of a rabbit from group 3. **(C)** Image of hydrogel B (physically cross-linked hydrogel). **(D)** Image of rehydrated hydrogel B applied to the conjunctiva of a rabbit from group 4.

2.4 Release of AM proteins from hydrogel A and B

The release of AME proteins from the hydrogels was evaluated in a similar manner in both cases. Following the encapsulation of the lyophilized AM extract, 50 μL of hydrogel A and a fragment of hydrogel B, designed in a format suitable for application on the conjunctiva with dimensions of 0.5 × 0.5 × 0.1 cm, were placed in a release system developed by our group and previously reported (39).

Both hydrogels were exposed to the external environment while a buffering agent was introduced at the upper end, flowing uniformly over the surface of the material. Aliquots of this buffer containing the proteins released from the hydrogels were subsequently collected. The hydrogels gradually dissolved in the buffered solution, mimicking the action of tears.

Despite the stabilization of hydrogel B through physical interactions, the introduced liquid was able to dissolve the polymers comprising the matrix, ultimately leading to the complete dissolution of the hydrogel. The liquid used was an isotonic saline solution for ocular irrigation, known as Balanced Salt Solution (BSS; AJL Ophthalmic, Spain). Since the natural tear flow rate in the human eye is 2.2 μL per minute, this value was scaled up by a factor of 50–110 μL per minute to meet the experimental requirements. The total release of proteins was completed after 360 min, and samples were collected every 15 min to study the release kinetics. Protein quantification was performed indirectly using EZQ fluorescence with a BioTek Synergy Neo 2 multimode reader and GEO 5 3.1 software. Subsequently, the values were interpolated using a calibration curve in the range of 1–25 μg/mL. Finally, the data obtained were processed using GraphPad Prism software.

2.5 Animal studies

This study was carried out on male New Zealand White rabbits (n = 44, weight 2.5–2.7 kg), with all the animal procedures adhering to the guidelines set forth by the Association for Research in Vision and Ophthalmology (ARVO) regarding the Use of Animals in Ophthalmic and Vision Research. Approval for the experimental protocols was obtained from the Animal Experimentation Ethics Committee of the Basque Public Health System and the Institute for Health Research Biogipuzkoa (permit number: CEEA20/15), as well as the Provincial Council of Gipuzkoa (Cod. PRO-AE-SS-196), ensuring compliance with both European and national legislation.

An animal model of alkali corneal burn was established as described previously (40). Briefly, rabbits were sedated with a subcutaneous injection of Meloxicam (0.2 mg/kg: Boehringer Ingelheim, Spain) and an intramuscular injection of ketamine/xylazine (35/20 mg/kg: Halmein Pharmaceuticals, Germany/Carlier, Spain), followed by anaesthesia with Sevofluorane 3% (Abbvie, Spain) and topical anesthesia with 2–3 drops of Colircusi Anestésico Doble® (Alcon-Cusí, Spain). An alkali burn was induced in the right eye of each rabbit by placing an 8 mm strip of filter paper soaked in 1 M NaOH on the central cornea for 60 s under an

ophthalmic surgical microscope. Subsequently, the eyes were rinsed with 200 mL saline solution for 1 min, and eye drops containing tobramycin and dexamethasone phosphate (Alcon Cusi, Barcelona, Spain) were administered post-surgery (p.s.) to each animal. The rabbits were then randomly divided into four groups ($n = 11$ per group) and they received one of the following treatments: group 1 (no experimental treatment), post-surgical eye drops alone; group 2, Amniotic Membrane Transplantation (AMT); group 3, dynamic hydrogel (hydrogel A); and group 4, physically cross-linked ocular insert hydrogel (hydrogel B). Both hydrogels were loaded with the AME and the contralateral uninjured eye (native) was used as the control.

After inducing the corneal lesion, hydrogels A and B were placed in the conjunctival sac following different approaches. Hydrogel A was administered to rabbits in Group 3 via a syringe in gel format, spread over the entire corneal surface by blinking. Hydrogel B was pre-hydrated for 60 s in a Balanced Salt Solution (BSS) before it was placed in the upper conjunctival sac of Group 4 rabbits, applying gentle pressure to enhance gel adhesion. Hydrogels were administered every 12 h over 7 days by an experienced ophthalmologist. After inducing the corneal wound, the AM attached to the cornea as a monolayer in Group 2 (41) was removed on the 7th day of follow-up following administration of 2–3 drops of topical anesthesia.

2.6 Clinical examination

Corneal wound healing was monitored by capturing photographs (EOS 750D, Canon Inc., Japan) immediately post-surgery (day 0) and on days 7, 14, 21 and 28 p.s. The images were obtained under cobalt blue light post 0.1% fluorescein sodium staining and the area of the corneal epithelial lesion was quantified (mm^2) three times using Image J software (National Institutes of Health (NIH), Bethesda, MD, USA). Technical replicates were employed for the analysis of the de-epithelialized area, with three measurements performed for each biological replicate. The biological replicates consisted of nine specimens per group.

2.7 Histopathological examination

Two rabbits were selected randomly from each group and sacrificed with an overdose of anesthesia on day 2 post-alkali burn (acute healing), while the remaining animals were sacrificed on day 28 (late healing). The corneas were harvested, fixed in 4% paraformaldehyde, preserved in 30% sucrose, embedded in OCT to obtain cryostat sections (7 µm). The sections were stained with hematoxylin and eosin (H&E) or Masson trichrome and random fields of the injured area and the adjacent tissue were analyzed. Images were obtained under a light microscope (Nikon Eclipse 80i, Japan), and the epithelial and stromal thicknesses were measured at three random locations in each field using ImageJ software. The presence or absence of an endothelial layer and inflammatory cell density were recorded.

2.8 Statistical analysis

The data were analyzed using SPSS 22 software (IBM-SPSS, USA). In the analysis of the *in vivo* studies, and given the sample size and the non-normal distribution of the variables, non-parametric tests were used (Mann–Whitney U, Kruskal Wallis and Chi-squared). Variables with a normal distribution, such as the stromal and epithelial thickness, and their relationship with endothelial damage, were studied using parametric tests (ANOVA and Student T-test). Significance was set at $p < 0.05$.

3 Results

3.1 Proteomic characterization of the AM

The proteins in the AM tissue (group 2) and the AME introduced into the hydrogels (groups 3 and 4) were analyzed, identifying a total of 1,689 proteins. Of these, 1,059 were common to both the tissue and the extract, with 288 proteins (17%) identified exclusively in the AM tissue and 342 proteins (20%) specific to the AME (Figure 2A and Supplementary File S1 for the complete list of proteins in these formulations). The difference in composition may be attributed to the different protein extraction protocols used in this study. For protein extraction from the AM, a gentle homogenization protocol was employed, based on a non-aggressive approach designed to preserve the functionality and biological activity of the extracted proteins. In contrast, protein extraction from the AM tissue was performed using a Precellys device and a buffer containing 7 M urea, 2 M thiourea, and 4% CHAPS. This latter protocol was designed to obtain a broader spectrum of proteins, including those that are insoluble or membrane-associated.

A GO analysis was carried out to characterize the functional events in which the proteins identified in both the AME and the AM tissue are involved (Figure 2B). These processes can be mainly grouped as: (i) Cellular activity and wound healing consisting of cell adhesion, extracellular matrix remodeling and protein synthesis; (ii) Immune responses, combining the GO terms of innate immune responses, complement activation (classical pathway), complement activation and inflammatory responses; and (iii) Platelet aggregation, comprising the GO terms of blood coagulation, platelet activation and homotypic cell–cell adhesion.

3.2 AM protein release from the hydrogels

When evaluating the release kinetics of AM proteins from hydrogel A, it was observed that 34 ± 9% of the total protein content was rapidly released within the first 15 min (Figure 3A). Subsequently, the protein concentration in the collected BSS medium gradually decreased over time, eventually falling below the assay's detection threshold after 60 min. At this point, the cumulative protein release reached approximately 60%, corresponding to a release duration equivalent to 2 days when considering the natural tear flow rate in the human eye. These findings suggest that AM proteins are retained within hydrogel A via weak physical interactions, distinct from the dynamic bonds observed in hydrogel B, which influence the hydrogels' solubility in BSS during the experiment. The pronounced release of proteins during the first hour of the experiment (up to 30 ± 3 µg/mL, Figure 3B) is particularly significant for ocular regeneration. This initial burst release of AM proteins could potentially facilitate rapid activation of the healing process in the damaged area, while the

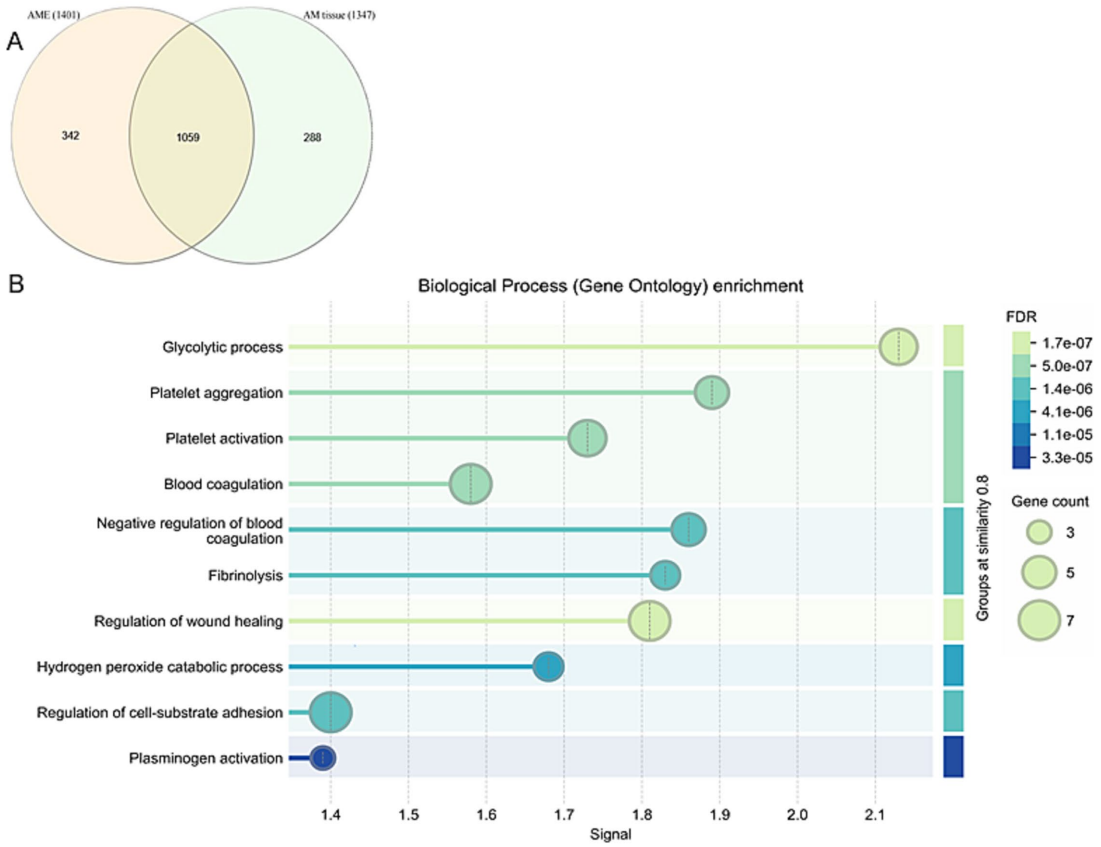

FIGURE 2
(A) Venn diagram representing exclusive and mutually inclusive proteins between AM proteins extract (AME) and AM tissue. **(B)** Gene Ontology (GO) analysis was performed to characterize the functional processes associated with the proteins identified in both the AME and AM tissues.

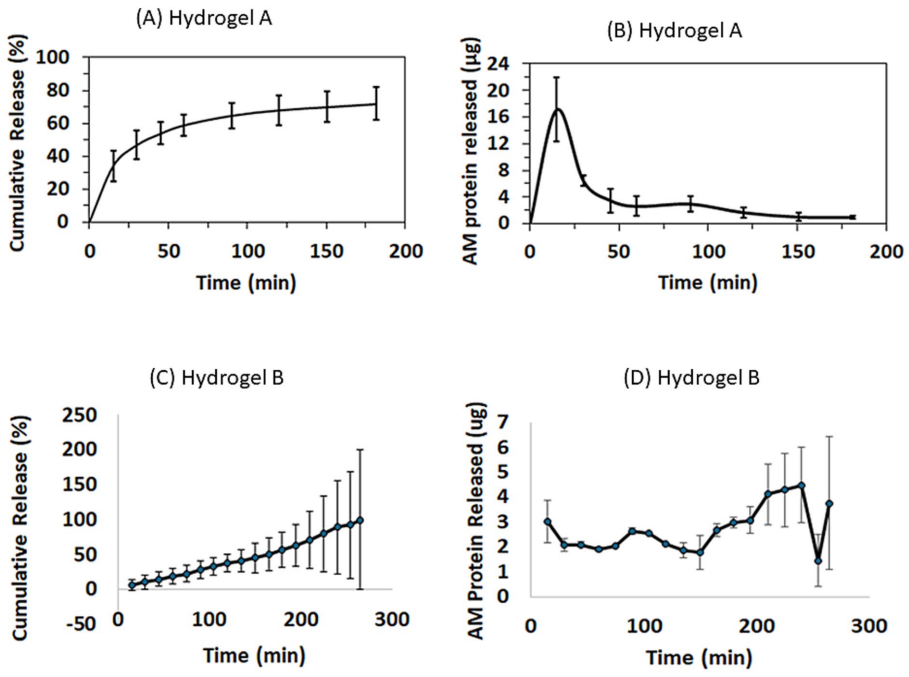

FIGURE 3
Release kinetics of AM proteins from Hydrogel A and Hydrogel B. **(A)** Cumulative release and **(B)** mass of AM protein released over time (µg) for Hydrogel A. **(C)** Cumulative release and **(D)** mass of AM protein released over time (µg) for Hydrogel B.

subsequent sustained release would help maintain this therapeutic activity over an extended period.

Hydrogel B gradually dissolved into the serum, releasing both the AM proteins and the polymers constituting the hydrogel. The total amount of released proteins was quantified every 15 min, showing that 50% of the total protein content was released after 165 min, 80% after 225 min, and 100% after 265 min (Figure 3C). The maximum protein release occurred at 241 min (Figure 3D). This sustained release highlights the material's ability to ensure a consistent flow of proteins into the animal's eye.

3.3 Clinical data

In this study, 44 rabbits were distributed evenly into four groups and a corneal lesion was induced in each one with 1 M NaOH as indicated in the Methods. Of these, eight rabbits were sacrificed on day 2 p.s. and 36 rabbits on day 28 p.s. to perform histological analyses (see section 3.3). While one of the four study groups did not receive any experimental treatment, Group 2 received AMT applied directly to the eye, whereas Groups 3 and 4 received the AME delivered through hydrogels. The ointment-like consistency of hydrogel A, combined with the mucoadhesive properties of HA-SH, facilitated its uniform spread across the cornea. By contrast, the physical crosslinking in hydrogel B conferred this matrix with remarkable stability and good mucoadhesion.

Following the induction of corneal wounds, Hydrogel A was applied to Group 3 animals every 12 h for 7 days in the upper conjunctival sac. The hydrogels were safely administered via syringe and demonstrated biocompatibility in the lower fornix. Daily general observations indicated that 6 h post-application, the hydrogel was no longer visible on the ocular surface, having completely degraded. After 12 h, no traces of the hydrogel were detected.

Similarly, after inducing corneal wounds, Hydrogel B was applied to Group 4 animals every 12 h for 7 days in the upper conjunctival sac, with gentle pressure applied to enhance gel adhesion. Observations revealed that the hydrogels were safely retained and showed biocompatibility in the upper fornix. Daily evaluations of the films demonstrated that, while the films exhibited mild wear 6 h post-application, they did not degrade or dissolve entirely. By the 12-h observation, no hydrogel remnants were detected.

In both cases, no signs of irritation, redness, or swelling of the eyes or ocular structures were observed in any animal as a result of hydrogel application. The animals were monitored and assessed over the 7-day application period to detect any potential signs of pathology.

The progression of epithelial defects was monitored for 28 days using fluorescein staining (Figure 4A) and a reduction in the epithelial lesion area (mm^2) was observed in all the treatment groups on days 7, 14, 21, and 28 p.s. relative to the day of intervention ($p < 0.005$, Wilcoxon test: Table 1). A high incidence of persistent epithelial defects and wound reopening was observed in 91.6% of corneas, probably reflecting the intensity of the alkaline burn and the fragility of the newly formed epithelial (42). There were statistically significant differences in the area of the epithelial defect between the groups on day 7 ($p = 0.014$, Kruskal-Wallis test), with significant differences between group 1 and group 4 ($p = 0.02$) and between group 2 and group 4 ($p = 0.006$, Mann–Whitney U test). However, there were no significant differences between the groups on days 14, 21 and 28 (Kruskal–Wallis test: Figures 4C–E). Hydrogel A facilitated the fastest healing, while eyes treated with hydrogel B exhibited delayed wound repair. Thus, the differences between the untreated eyes and those that received hydrogel B were only significant on day 7 p.s., with open wounds evident in all eyes (Figure 4B).

The proportion of completely healed corneas did not differ significantly between the untreated and treated eyes on the days studied (Figure 5). On day 14 p.s., the proportion of completely healed corneas was higher in group 3 (44.4%) and 4 (55.5%) than in the untreated eyes in group 1 (33.3%). The enhanced healing following these treatments, even after the treatment was discontinued on day 7 p.s., suggests that AM proteins may enhance the induction of wound closure in the early stages of healing.

3.4 Histological analysis

The histological analysis focused on the stromal, epithelial and endothelial layers, as well as assessing the presence of inflammatory cells during the early and late healing phases (days 2 and 28 p.s., respectively). No significant differences were observed in the stromal and epithelial thickness between groups (ANOVA test), despite the apparent increase in epithelial thickness in the eyes of group 2 animals on the days analyzed (Table 2). Central corneal sections exhibited a thicker stroma and thinner epithelium in wound sections relative to the native corneas (Figure 6A). Masson's trichrome staining highlighted severe alterations to the collagen staining that persisted from the early to the late healing phases (Figure 6B).

Abnormal epithelial regeneration was evident, with disrupted junctions between the epithelial layer and basement membrane observed (Figure 7). Fewer cells were present in the anterior stromal third on day 2 p.s. relative to day 28 p.s., with significant differences in the presence of inflammatory cells on day 28 p.s. between the eyes from group 2 animals relative to those from groups 1 and 3 ($p = 0.01$, Kruskal Wallis Test: Figure 8). Moreover, alterations to the endothelium were noted, with more extensive endothelial damage correlating with a significantly thinner epithelium ($p = 0.001$, Student T-test).

4 Discussion

Hydrogels represent a versatile platform in the realm of personalized and precision medicine, offering a range of functionalities. Moreover, the emergence of new biomaterials promises to overcome some of the limitations associated with existing therapeutic modalities. Hence, here we explore two distinct hydrogels as biocompatible matrices for the controlled release of AM proteins, with the aim of improving wound healing in response to severe, acute corneal lesions. Given that the nature of the hydrogel conditions the release of any of its components, two types of hydrogels were considered here: a state-of-the-art hydrogel based on dynamic bonds and another based on the physical binding of different biocompatible biopolymers. While the former is administered in the form of an ointment-like hydrogel, designed to ensure rapid release of any active ingredient, the latter is applied in the form of a film to ensure sustained release over time. In both of these cases, the active

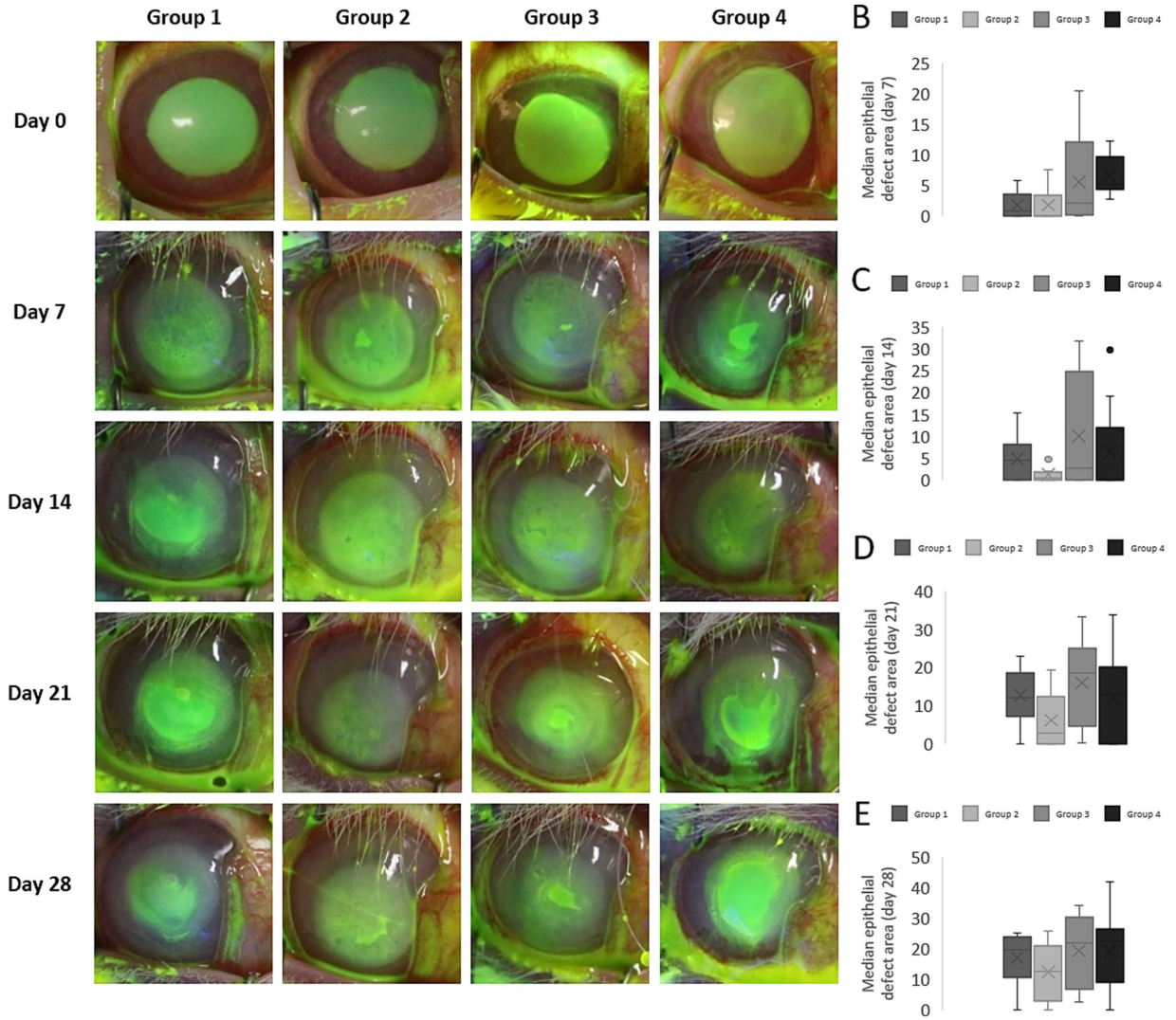

FIGURE 4
Evolution of the epithelial lesion in rabbit eyes. **(A)** The epithelial defect was monitored by fluorescein staining and a study of the lesion in each group showed significant wound healing on each day studied relative to the day of surgery. The wound area decreased until day 14 post-surgery (p.s.), after which reopening of the wounds was observed that possibly reflected the intensity of the alkaline burn and the fragility of the newly formed epithelium. **(B–E)** Median epithelial defect area (mm^2) on day 7 **(B)**, 14 **(C)**, 21 **(D)**, and 28 **(E)** p.s. The asterisks indicate significant differences relative to the control group ($p < 0.05$).

ingredient used here was a cocktail of proteins extracted from human AM tissue (AME).

The regenerative nature of proteins found in the AM has been studied widely (5, 43, 44) and as such, the protein profile of the AME obtained through AM sonication was analyzed to ensure that the majority of the proteins present in the AM were preserved in the AME. The proteomic analysis demonstrated that the protein composition of the AME was very similar to that of the AM tissue, sharing 62% of the proteins. The biological processes mediated by these proteins underscore their significant role in wound healing. These processes include (A) cell adhesion, (B) extracellular matrix (ECM) remodeling, (C) protein synthesis, (D) innate immune response, (E) plasminogen activation, (F) inflammatory responses, (G) blood coagulation, (H) platelet activation, and (I) homotypic cell–cell adhesion. Proteomic analyses have demonstrated that both the amniotic membrane (AM) as a tissue and its protein extracts preserve ECM proteins such as collagens, glycoproteins, proteoglycans, metalloproteinases, and growth factors, as previously described (45). These ECM proteins contribute to tensile strength, provide structural support, stabilize basal membrane components, and regulate fibrillary collagen growth.

Additionally, ECM glycoproteins—including fibrillin, fibrinogen, laminin, and vitronectin—were identified, along with growth factors such as transforming growth factor-beta (TGF-β) and epidermal growth factor (EGF), both of which are known to play pivotal roles in tissue regeneration and wound healing (46, 47). Proteins involved in coagulation pathways, platelet activation, and aggregation, which are directly linked to wound healing, were also identified. Pathways related to ATP synthesis, vascular endothelial growth factor (VEGF) signaling, the plasminogen activation cascade, glycolysis, and cytoskeletal regulation were associated with essential processes such as angiogenesis, collagen

TABLE 1 Median and Interquartile range (IQR) of the areas carrying epithelial defects (mm^2) in each group on the day of surgery and on days 7, 14, 21, and 28 post-surgery.

Group	Day 0	Day 7	Day 14	Day 21	Day 28
1	54.75 (50.21–60.69)	0.78* (0.00-3.44)	4.36* (0.00-8.03)	11.96* (7.18-18.45)	19.57* (10.52-23.75)
2	54.62 (51.91–60.14)	0.00* (0.00-3.32)	0.44* (0.00-1.63)	2.65* (0.00-12.23)	12.51* (2.63-20.81)
3	52.82 (49.62–58.41)	1.95* (0.16-12.05)	2.57* (0.00-24.77)	18.53* (4.45-25.10)	21.85* (6.70-30.32)
4	57.46 (56.50–62.12)	5.04* (4.27-9.66)	0.00* (0.00-11.93)	12.72* (0.00-20.06)	22.42* (8.89-26.43)

* Significant difference relative to day 0, p-value < 0.05.

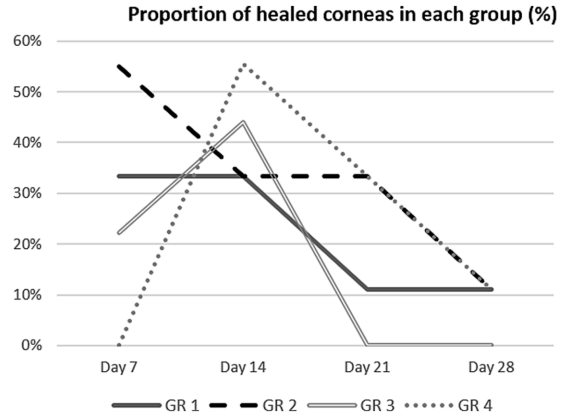

FIGURE 5
Proportion of fully healed corneas (percentage) in each group on days 7, 14, 21, and 28 post-surgery.

deposition, and epithelialization. Angiogenesis, the formation of new blood vessels from pre-existing ones, is vital for wound healing as it ensures the delivery of oxygen, nutrients, and growth factors to the injury site (48). The plasminogen activation pathway, specifically, is critical for breaking down blood clots and facilitating ECM remodeling, both of which are key to efficient wound repair. Controlled clot degradation prevents pathological scarring, while ECM remodeling supports cell migration, tissue restructuring, and regeneration (49).

The effectiveness of the two synthesized hydrogels was evaluated *in vivo* in a well-established model of an alkali corneal burn in albino rabbits. Various techniques exist to induce corneal lesions, each with its own advantages and challenges. For example, lesions induced by physical methods tend to exhibit rapid closure rates, making it difficult to discern significant differences between therapeutic interventions (50). Conversely, alkali burns with agents like NaOH produce more severe and persistent epithelial defects, mimicking clinical scenarios of severe corneal burns (51). Here, we opted to use an aggressive wound model involving the entire corneal layer, akin to scenarios warranting AMT in clinical practice (42). However, despite efforts to standardize the alkali burn technique (42), considerable heterogeneity persists in the literature regarding lesion size, NaOH concentration and the duration of exposure, complicating direct comparisons between studies (52–54).

The alkali burn model employed involved applying NaOH (1 M) for 60 s, which required approximately 3–7 days to achieve complete wound closure, enabling the effects of the hydrogels to be assessed over a 7-day period (40, 55). However, as the AMT was sutured onto the cornea, the initial measurements of fluorescein staining were taken from day 7 p.s. onward. In accordance with previous models, the initial closure phases were rapid in this model, making inter-group differences challenging to detect in the first week. Despite the aggressive nature of our model, no significant differences in epithelial defects were observed between the experimental groups on days 0, 14, 21, or 28 p.s., although subtle differences were noted between the control and hydrogel-treated corneas, as discussed below.

Corneas treated with AMT exhibited better epithelial defect outcomes relative to the untreated controls, even after AMT removal on day 7 p.s. Hence, AM proteins appear to exert a crucial influence on the early healing phases, possibly modulating wound closure pathways beyond the removal of the AMT (56, 57). Differences between the completely healed corneas on day 14 p.s. may reflect the proteins secreted in earlier phases, influenced by biomaterial presentation. The ointment-like formulation of hydrogel A facilitates contact but it may be associated with limited protein release when compared to the more solid formulations due to the more rapid clearing of the latter (58). Extended ointment application beyond day 7 p.s. might yield improved outcomes. Hydrogel B initially delayed epithelialization, possibly due to its mobile nature as it has been postulated that direct contact of the mobile hydrogel with the regenerating epithelium may have a negative effect on wound closure (55). However, subsequent improvements and stronger healing on days 14 and 21 p.s. suggest positive effects once these effects of friction have ceased.

The histological examination of epithelial thickness agreed well with the relative wound closure area. The aggressive nature of the model impeded epithelial regeneration and although AMT better restored epithelial thickness, there were only minimal differences with the other Groups (1, 3, and 4). Similarly, recent publications indicated that the full thickness of the epithelial layer could be recovered after chemical burns (51). There was little basal layer compaction with separation of the epithelial layer in some cases and this failure of the newly formed epithelium to bind to the basal layer could be related to the reopening of wounds *in vivo*. Histological studies to track the persistent epithelial defects indicated that reopening could occur after the healing associated with direct contact and in such cases, alterations were observed at the level of the epithelial layer and basal membrane. Indeed, intraepithelial pseudocysts have been described and displacement or duplication of Bowman's membrane in the epithelium of human corneas has been observed (59). Furthermore, fibrous material has been seen to accumulate between the basement membrane and the epithelium (60). Similarly, *in vivo* studies using the same burn model described the absence of a basement membrane between the epithelium and stroma, as well as an increase in the intercellular spaces between the regenerated epithelial cells (54). This could explain by the reopening of the wound in all the burned corneas, especially in those in which the ocular hydrogel insert was employed, the mobility of which could explain the size of the epithelial lesion on day 7 p.s. that closed after removal of the film.

TABLE 2 Stromal and epithelial thickness (μm, mean ± SD) in the central and lateral corneal sections on days 2 and 28 p.s. in each group, and in the native cornea.

Section	Day	Layer	Group 1	Group 2	Group 3	Group 4	NC
C	2	S	1,301 ± 261	1,032 ± 185	1,308 ± 155	1,024 ± 280	689 ± 96
C	2	E	0 ± 0	2.79 ± 3.95	0 ± 0	0 ± 0	17.08 ± 4.13
L	2	S	1,311 ± 257	935 ± 52	1,279 ± 84	1,288 ± 643	668 ± 117
L	2	E	1.87 ± 2.65	5.55 ± 5.04	2.33 ± 3.30	2.56 ± 3.63	18.98 ± 2.15
C	28	S	1,291 ± 115	1,280 ± 237	1,268 ± 179	1,125 ± 170	668 ± 79
C	28	E	6.14 ± 1.94	7.27 ± 5.90	5.85 ± 2.95	6.47 ± 4.89	16.58 ± 1.79
L	28	S	1,120 ± 293	1,391 ± 281	1,272 ± 255	1,371 ± 281	699 ± 133
L	28	E	8.92 ± 1.10	11.01 ± 2.79	8.42 ± 3.00	8.25 ± 3.28	17.35 ± 1.74

C, central section; L, lateral section; E, Epithelium; S, Stroma; NC, native cornea.

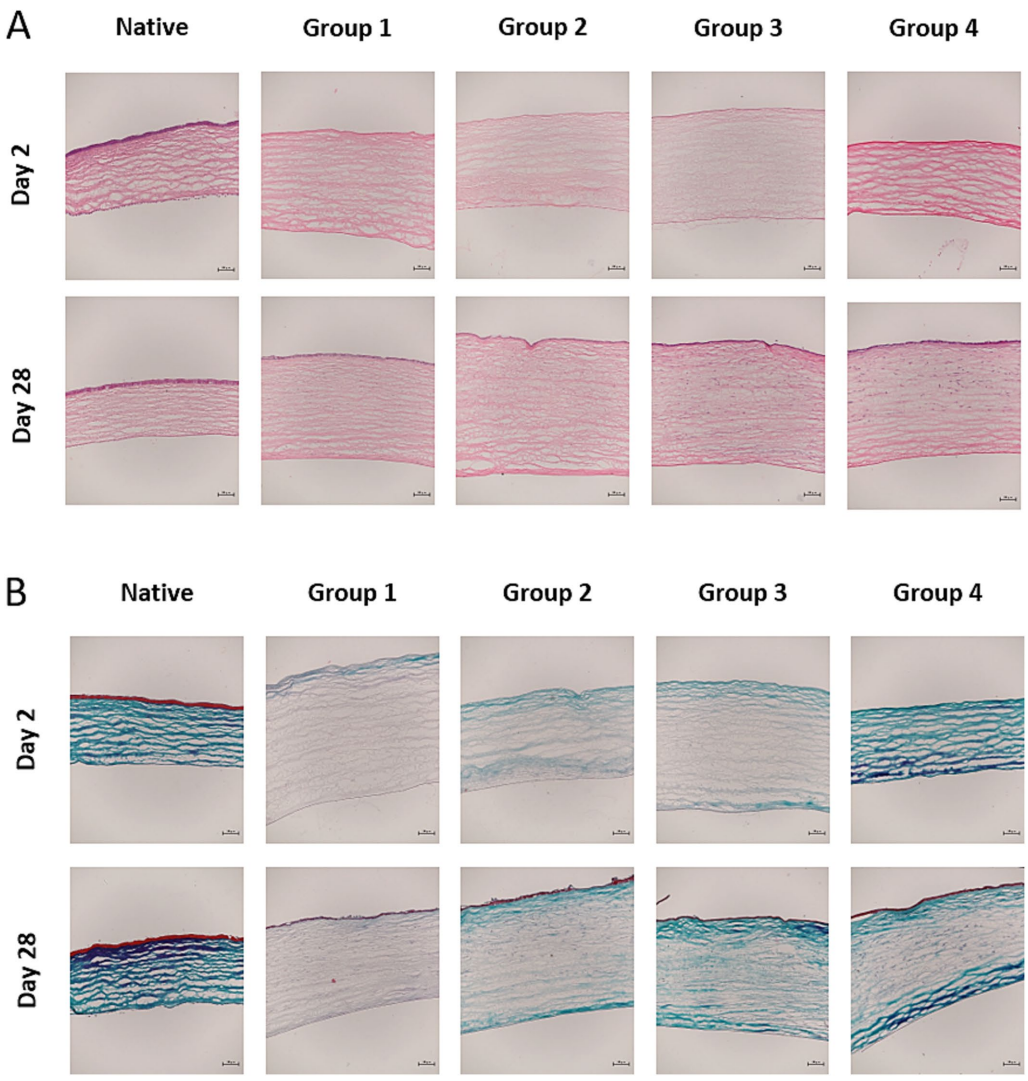

FIGURE 6
(A) Haematoxylin–eosin stained central sections on days 2 and 28 post-surgery (p.s.: 10x). In the early healing stage, the burned corneas exhibited stromal thickening, endothelial damage, a lack of epithelial regeneration, a keratocyte deficit in the corneal stroma and scant inflammatory cell infiltration. This together reflects the severity of the lesion provoked in the animal model. At a late healing stage (day 28 p.s.), stromal thickening persisted with a separation of collagen fibers in all the wounded corneas. There were no significant differences in the thickness of the layers analyzed between the groups, although the oedema in the central cornea was smaller in groups 2 and 4. **(B)** Masson trichrome stained central sections on days 2 and 28 p.s. (10x). Severe alterations to collagen staining were evident on day 2 p.s. that persisted to some extent on day 28 p.s. Scale bars 200 μm.

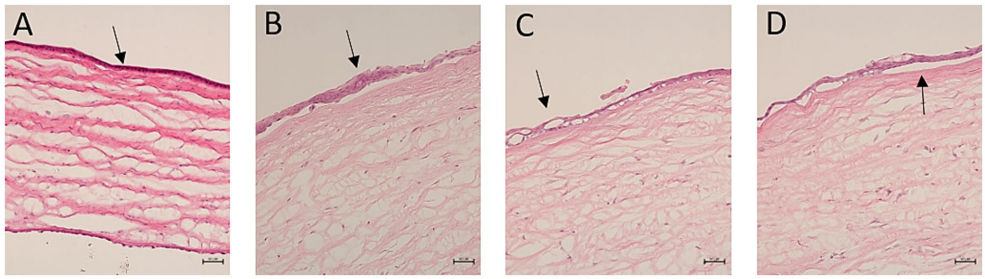

FIGURE 7
Hematoxylin–eosin stained corneal sections showing abnormal epithelial regeneration (20x). **(A)** The arrow indicates epithelial hypoplasia with monolayer cuboid cells; **(B)** the arrow indicates focal hyperplasia; **(C)** the arrow indicates a failure of the epithelial basal layer to compact; **(D)** the arrow indicates complete separation of the epithelial layer. Scale bars 100 μm.

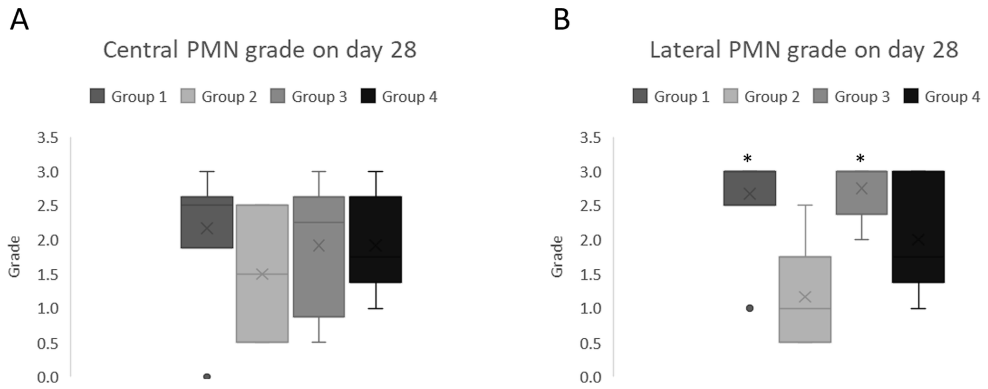

FIGURE 8
Median and Interquartile Range (IQR) of the inflammatory infiltration in the corneal sections on day 28 post-surgery. **(A)** Central sections; **(B)** lateral sections. The asterisks indicate significant differences relative to group 2 (AMT, $p < 0.05$: Kruskal Wallis test).

Consistent with previous studies, few cells were observed during the early phases of healing across most samples, particularly in the central regions. Notably, there was an absence of epithelial and endothelial layer formation, as well as a significant depletion of stromal cells in large areas of the stroma, although inflammatory cells were present. These findings align with prior reports indicating that the depth of alkali burns can extend to the endothelial layer, with damage to this layer observed in the same animal model (61). Similarly, other studies have demonstrated that immediately following alkali-induced damage, the majority of keratocytes are lost, becoming undetectable under light microscopy for up to 2 days post-injury (62). Furthermore, injuries caused by caustic agents such as NaOH are known to result in more severe tissue damage compared to physical agents. These injuries frequently serve as models for persistent epithelial defects, often characterized by recurrent wound reopening during follow-up periods (50, 51, 54). However, corneal cellularity recovered at all levels in the late healing phase, and although normal architecture was not restored, stromal thickening, inflammatory cell infiltration and an abnormal epithelium was achieved (51). Significant differences were evident in terms of inflammatory cell infiltration following AMT, possibly related to the known anti-inflammatory properties of this tissue (63). In this regard, we assume that the AM proteins delivered by hydrogel B (ocular insert hydrogel) will remain at the ocular surface for longer and hence, fewer inflammatory cells would be present than in the control eyes and following treatment with the hydrogel A ointment. Nevertheless, it must be borne in mind that the samples were obtained 21 days after the last contact of the proteins with the wound, which could have attenuated the effect of these proteins on corneal healing.

In conclusion, this study evaluated two promising hydrogels designed to gradually biodegrade and deliver sustained AM protein release to the corneal surface for over 7 days, with the aim of promoting corneal wound healing while minimizing irritation. The results indicate that these hydrogels can aid in the closure of caustic corneal wounds, producing more complete epithelialization and smaller lesions compared to untreated controls. Despite some limitations, such as insufficient mucoadhesion leading to de-epithelialization in the film-type hydrogel (hydrogel B), the study suggests that these hydrogels show potential as less invasive alternatives to AMT. They may offer a non-inferior option for promoting corneal wound healing, delivering similar benefits without requiring a more invasive surgical approach, thus lowering healthcare costs and simplifying patient management.

Data availability statement

The original contributions presented in the study are included in the article/Supplementary material. The mass spectrometry proteomics data have been deposited to the ProteomeXchange

Consortium https://proteomecentral.proteomexchange.org/ with identifier PXD055969.

Ethics statement

The animal studies were approved by Animal Experimentation Ethics Committee of the Basque Public Health System and the Institute for Health Research Biogipuzkoa (permit number: CEEA20/15), as well as the Provincial Council of Gipuzkoa (Cod. PRO-AE-SS-196). The studies were conducted in accordance with the local legislation and institutional requirements. Written informed consent was obtained from the owners for the participation of their animals in this study.

Author contributions

AB: Formal analysis, Investigation, Methodology, Writing – original draft, Writing – review & editing, Data curation. JM: Formal analysis, Investigation, Methodology, Writing – review & editing, Conceptualization, Funding acquisition, Supervision. MR: Formal analysis, Methodology, Data curation, Writing – original draft. JB: Methodology, Writing – original draft, Conceptualization, Investigation. MF: Investigation, Methodology, Writing – original draft, Data curation, Formal analysis. DE-U: Data curation, Formal analysis, Investigation, Methodology, Writing – original draft. AS: Data curation, Formal analysis, Investigation, Methodology, Writing – original draft. MC: Data curation, Formal analysis, Investigation, Methodology, Writing – original draft, Conceptualization, Funding acquisition, Writing – review & editing. IC: Data curation, Formal analysis, Investigation, Methodology, Writing – original draft. AD: Data curation, Formal analysis, Investigation, Methodology, Writing – original draft. JD: Formal analysis, Investigation, Methodology, Writing – original draft, Conceptualization, Funding acquisition. AnA: Formal analysis, Investigation, Methodology, Writing – original draft, Data curation. MA: Data curation, Formal analysis, Investigation, Methodology, Writing – original draft, Software. FE: Data curation, Formal analysis, Investigation, Methodology, Software, Writing – original draft, Conceptualization. EV: Formal analysis, Investigation, Methodology, Writing – original draft. ArA: Formal analysis, Investigation, Methodology, Writing – original draft, Conceptualization, Funding acquisition, Project administration, Supervision, Writing – review & editing.

Funding

The author(s) declare that financial support was received for the research, authorship, and/or publication of this article. This study was supported by the MINECO-Retos Fondos (RTC-2016-48231), the Gobierno Vasco (IT 1510 22), MINECO-Retos (PID2019-111139RB-I00), ELKARTEK (KK-2019-00086), FISS-21-RD21/0002/0041, Salud Gobierno Vasco (2021333047), the University of the Basque Country (projects COLLAB22/05 and GIU21/033).

Acknowledgments

The authors thank IKERBASQUE-Basque Foundation for Science and Proteomics Platform, CIC bioGUNE for their support in carrying out this project. The authors also wish to thank the UPV/EHU for the technical and human support provided by SGIker.

Conflict of interest

The authors declare that the research was conducted in the absence of any commercial or financial relationships that could be construed as a potential conflict of interest.

Publisher's note

All claims expressed in this article are solely those of the authors and do not necessarily represent those of their affiliated organizations, or those of the publisher, the editors and the reviewers. Any product that may be evaluated in this article, or claim that may be made by its manufacturer, is not guaranteed or endorsed by the publisher.

Supplementary material

The Supplementary material for this article can be found online at: https://www.frontiersin.org/articles/10.3389/fmed.2025.1498319/full#supplementary-material

References

1. Wagoner MD. Chemical injuries of the eye: current concepts in pathophysiology and therapy. *Surv Ophthalmol.* (1997) 41:275–313. doi: 10.1016/S0039-6257(96)00007-0

2. Bizrah M, Yusuf A, Ahmad S. An update on chemical eye burns. *Eye (Lond).* (2019) 33:1362–77. doi: 10.1038/s41433-019-0456-5

3. Mamede AC, Carvalho MJ, Abrantes AM, Laranjo M, Maia CJ, Botelho MF. Amniotic membrane: from structure and functions to clinical applications. *Cell Tissue Res.* (2012) 349:447–58. doi: 10.1007/s00441-012-1424-6

4. Dua HS, Gomes JA, King AJ, Maharajan VS. The amniotic membrane in ophthalmology. *Surv Ophthalmol.* (2004) 49:51–77. doi: 10.1016/j.survophthal.2003.10.004

5. Kim JC, Tseng SC. Transplantation of preserved human amniotic membrane for surface reconstruction in severely damaged rabbit corneas. *Cornea.* (1995) 14:473–84.

6. Tseng SC, Li DQ, Ma X. Suppression of transforming growth factor-beta isoforms, TGF-beta receptor type II, and myofibroblast differentiation in cultured human corneal and limbal fibroblasts by amniotic membrane matrix. *J Cell Physiol.* (1999) 179:325–35. doi: 10.1002/(SICI)1097-4652(199906)179:3<325::AID-JCP10>3.0.CO;2-X

7. Meller D, Pires RT, Mack RJ, Figueiredo F, Heiligenhaus A, Park WC, et al. Amniotic membrane transplantation for acute chemical or thermal burns. *Ophthalmology.* (2000) 107:980–9; discussion 90. doi: 10.1016/S0161-6420(00)00024-5

8. Kim JC, Tseng SC. The effects on inhibition of corneal neovascularization after human amniotic membrane transplantation in severely damaged rabbit corneas. *Korean J Ophthalmol.* (1995) 9:32–46. doi: 10.3341/kjo.1995.9.1.32

9. Tseng SC. Amniotic membrane transplantation for ocular surface reconstruction. *Biosci Rep.* (2001) 21:481–9. doi: 10.1023/A:1017995810755

10. Koizumi NJ, Inatomi TJ, Sotozono CJ, Fullwood NJ, Quantock AJ, Kinoshita S. Growth factor mRNA and protein in preserved human amniotic membrane. *Curr Eye Res.* (2000) 20:173–7. doi: 10.1076/0271-3683(200003)2031-9FT173

11. Keelan JA, Sato T, Mitchell MD. Interleukin (IL)-6 and IL-8 production by human amnion: regulation by cytokines, growth factors, glucocorticoids, phorbol esters, and bacterial lipopolysaccharide. *Biol Reprod.* (1997) 57:1438–44. doi: 10.1095/biolreprod57.6.1438

12. Bonci P, Bonci P, Lia A. Suspension made with amniotic membrane: clinical trial. *Eur J Ophthalmol*. (2005) 15:441–5. doi: 10.1177/112067210501500403

13. Liang L, Li W, Ling S, Sheha H, Qiu W, Li C, et al. Amniotic membrane extraction solution for ocular chemical burns. *Clin Experiment Ophthalmol*. (2009) 37:855–63. doi: 10.1111/j.1442-9071.2009.02159.x

14. Ana Boto-de-los-Bueis AD-H-Z, Garcia-Gomez I, Valiente BS-J, Garcia-Arranz M, Corral-Aragon A, Acera A. Time-dependent stability of growth factors and Endostatin in human amniotic membrane eye drops. Journal of. *Clin Exp Ophthalmol*. (2012) 3:3. doi: 10.4172/2155-9570.1000214

15. Hanafy AF, Abdalla AM, Guda TK, Gabr KE, Royall PG, Alqurshi A. Ocular anti-inflammatory activity of prednisolone acetate loaded chitosan-deoxycholate self-assembled nanoparticles. *Int J Nanomedicine*. (2019) 14:3679–89. doi: 10.2147/IJN.S195892

16. Lajunen T, Nurmi R, Kontturi L, Viitala L, Yliperttula M, Murtomaki L, et al. Light activated liposomes: functionality and prospects in ocular drug delivery. *J Control Release*. (2016) 244:157–66. doi: 10.1016/j.jconrel.2016.08.024

17. Kumar R, Sinha VR. Preparation and optimization of voriconazole microemulsion for ocular delivery. *Colloids Surf B Biointerfaces*. (2014) 117:82–8. doi: 10.1016/j.colsurfb.2014.02.007

18. Wang X, Wang S, Zhang Y. Advance of the application of nano-controlled release system in ophthalmic drug delivery. *Drug Deliv*. (2016) 23:2897–901. doi: 10.3109/10717544.2015.1116025

19. Mandal A, Bisht R, Rupenthal ID, Mitra AK. Polymeric micelles for ocular drug delivery: from structural frameworks to recent preclinical studies. *J Control Release*. (2017) 248:96–116. doi: 10.1016/j.jconrel.2017.01.012

20. Lin S, Ge C, Wang D, Xie Q, Wu B, Wang J, et al. Overcoming the anatomical and physiological barriers in topical eye surface medication using a peptide-decorated polymeric micelle. *ACS Appl Mater Interfaces*. (2019) 11:39603–12. doi: 10.1021/acsami.9b13851

21. Singh V, Bushetti SS, Raju SA, Ahmad R, Singh M, Ajmal M. Polymeric ocular hydrogels and ophthalmic inserts for controlled release of timolol maleate. *J Pharm Bioallied Sci*. (2011) 3:280–5. doi: 10.4103/0975-7406.80773

22. Lee SC, Kwon IK, Park K. Hydrogels for delivery of bioactive agents: a historical perspective. *Adv Drug Deliv Rev*. (2013) 65:17–20. doi: 10.1016/j.addr.2012.07.015

23. Zhang YS, Khademhosseini A. Advances in engineering hydrogels. *Science*. (2017) 356:6337. doi: 10.1126/science.aaf3627

24. VaKBK N. Eudragit a versatile polymer: a review. *Pharmacology*. (2011) 1:152–64.

25. Singh SN, Arora S, Singla Y. An overview of multifaceted significance of eudragit polymers in drug delivery systems. *Asian J Pharm Clin Res*. (2015) 8:1–6.

26. Calles JABJ, Vallés E, Allemandi D, Palma S. Polymers in ophthalmology. *Adv Polymers Med*. (2015):147–76. doi: 10.1007/978-3-319-12478-0_6

27. Jafariazar Z, Jamalinia N, Ghorbani-Bidkorbeh F, Mortazavi SA. Design and evaluation of ocular controlled delivery system for diclofenac sodium. *Iran J Pharm Res*. (2015) 14:23–31.

28. Kadajji Manjunatha MMK, Kulkarni G, Ismail M. Design and optimization of controlled release ocular inserts of Dorzolamide hydrochloride and Timolol maleate for treatment of Glaucoma. *Int J Res Pharmaceut Sci.* (2012) 3:2915–3922.

29. Franco P, De Marco I. Contact lenses as ophthalmic drug delivery systems: a review. *Polymers (Basel)*. (2021) 13:71102. doi: 10.3390/polym13071102

30. Griesser J, Hetenyi G, Bernkop-Schnurch A. Thiolated hyaluronic acid as versatile Mucoadhesive polymer: from the chemistry behind to product developments-what are the capabilities? *Polymers (Basel)*. (2018) 10:243. doi: 10.3390/polym10030243

31. Perera MM. Dynamic covalent bonds in self-healing, shape memory, and controllable stiffness hydrogels. *Polym Chem*. (2020) 11:1410–23. doi: 10.1039/C9PY01694E

32. Corfield APCS, Hicks SJ, Berry M, Ellingham R. Ocular mucins: purification, metabolism and functions. *Prog Retin Eye Res*. (1998) 16:627–56. doi: 10.1016/S1350-9462(96)00039-0

33. Wiśniewski JR, Zougman A, Nagaraj N, Mann M. Universal sample preparation method for proteome analysis. *Nat Methods*. (2009) 6:359–62. doi: 10.1038/nmeth.1322

34. Stefka Tyanova TT, Sinitcyn P, Carlson A, Hein MY, Geiger T, Mann M, et al. The Perseus computational platform for comprehensive analysis of (prote)omics data. *Nat Methods*. (2016) 13:731–40. doi: 10.1038/nmeth.3901

35. Zybailov BL, Florens L, Washburn MP. Quantitative shotgun proteomics using a protease with broad specificity and normalized spectral abundance factors. *Mol BioSyst*. (2007) 3:354–60. doi: 10.1039/b701483j

36. Yasset Perez-Riverol JB, Bandla C, García-Seisdedos D, Hewapathirana S, Kamatchinathan S, Kundu DJ, et al. Juan Antonio Vizcaíno the PRIDE database resources in 2022: a hub for mass spectrometry-based proteomics evidences. *Nucleic Acids Res*. (2022) 50:D543–52. doi: 10.1093/nar/gkab1038

37. Huang da W, Sherman BT, Lempicki RA. Systematic and integrative analysis of large gene lists using DAVID bioinformatics resources. *Nat Protoc*. (2009) 4:44–57. doi: 10.1038/nprot.2008.211

38. Fernandez MM CI, Santamaría A, Esporrín-Ubieto D, Calderón M. Viscoelastic behavior and bioadhesion of hydrogels to optimize ophthalmic drug delivery application. XVI Reunión del Grupo Especializado de Polímeros GEP 2022 y XVII Simposio Latinoamericano de Polímeros - SLAP 2022 (2022).

39. Esporrin-Ubieto D, Sonzogni AS, Fernandez M, Acera A, Matxinandiarena E, Cadavid-Vargas JF, et al. The role of Eudragit(R) as a component of hydrogel formulations for medical devices. *J Mater Chem B*. (2023) 11:9276–89. doi: 10.1039/D3TB01579C

40. Subasi S, Altintas O, Yardimoglu M, Yazir Y, Karaman S, Rencber SF, et al. Comparison of collagen cross-linking and amniotic membrane transplantation in an experimental alkali burn rabbit model. *Cornea*. (2017) 36:1106–15. doi: 10.1097/ICO.0000000000001276

41. Dallal MMS, Nikkhahi F, Imeni SM, Molaei S, Hosseini SK, Kalafi Z, et al. Amniotic membrane transplantation for persistent epithelial defects and ulceration due to *Pseudomonas keratitis* in a rabbit model. *J Ophthalmic Vis Res*. (2021) 16:552–7. doi: 10.18502/jovr.v16i4.9744

42. Villabona-Martinez V, Sampaio LP, Shiju TM, Wilson SE. Standardization of corneal alkali burn methodology in rabbits. *Exp Eye Res*. (2023) 230:109443. doi: 10.1016/j.exer.2023.109443

43. Kruse FE, Rohrschneider K, Volcker HE. Multilayer amniotic membrane transplantation for reconstruction of deep corneal ulcers. *Ophthalmology*. (1999) 106:1504–11. doi: 10.1016/S0161-6420(99)90444-X

44. Dudok DV, Nagdee I, Cheung K, Liu H, Vedovelli L, Ghinelli E, et al. Effects of amniotic membrane extract on primary human corneal epithelial and limbal cells. *Clin Experiment Ophthalmol*. (2015) 43:443–8. doi: 10.1111/ceo.12480

45. Ahmed K, Tauseef H, Ainuddin JA, Zafar M, Khan I, Salim A, et al. Assessment of the proteome profile of decellularized human amniotic membrane and its biocompatibility with umbilical cord-derived mesenchymal stem cells. *J Biomed Mater Res A*. (2024) 112:1041–56. doi: 10.1002/jbm.a.37685

46. Nunes QM, Li Y, Sun C, Kinnunen TK, Fernig DG. Fibroblast growth factors as tissue repair and regeneration therapeutics. *PeerJ*. (2016) 4:e1535. doi: 10.7717/peerj.1535

47. Maddaluno L, Urwyler C, Werner S. Fibroblast growth factors: key players in regeneration and tissue repair. *Development*. (2017) 144:4047–60. doi: 10.1242/dev.152587

48. Bao P, Kodra A, Tomic-Canic M, Golinko MS, Ehrlich HP, Brem H. The role of vascular endothelial growth factor in wound healing. *J Surg Res*. (2009) 153:347–58. doi: 10.1016/j.jss.2008.04.023

49. Kearney KJ, Ariens RAS, Macrae FL. The role of fibrin(ogen) in wound healing and infection control. *Semin Thromb Hemost*. (2022) 48:174–87. doi: 10.1055/s-0041-1732467

50. Ecenarro Jaime Echevarría M. Mecanismos celulares de la regeneración del defecto epitelial corneal tratado con suero derivado de plasma rico en factores de crecimiento (sPRGF) en solitario y combinado [doctoral tesis]. Bilbao: University of the Basque Country (UPV-EHU) (2018)

51. Griffith GL, Wirostko B, Lee HK, Cornell LE, McDaniel JS, Zamora DO, et al. Treatment of corneal chemical alkali burns with a crosslinked thiolated hyaluronic acid film. *Burns*. (2018) 44:1179–86. doi: 10.1016/j.burns.2018.01.016

52. Shahriari HA, Tokhmehchi F, Reza M, Hashemi NF. Comparison of the effect of amniotic membrane suspension and autologous serum on alkaline corneal epithelial wound healing in the rabbit model. *Cornea*. (2008) 27:1148–50. doi: 10.1097/ICO.0b013e318173138a

53. Gallego-Munoz P, Lorenzo-Martin E, Fernandez I, Herrero-Perez C, Martinez-Garcia MC. Nidogen-2: location and expression during corneal wound healing. *Exp Eye Res*. (2019) 178:1–9. doi: 10.1016/j.exer.2018.09.004

54. Li Y, Feng G, Yi Y, Lin J. The experimental investigation of epithelial healing in rabbit central corneal alkali wounds. *Yan Ke Xue Bao*. (1999) 15:74–7.

55. Zhang W, Nie L, Du L, Chen W, Wu Z, Jin Y. Topical treatment of corneal alkali burns with Glythymosin beta(4) solutions and in situ hydrogels via inhibiting corneal neovascularization and improving corneal epidermal recovery in experimental rabbits. *Burns*. (2017) 43:1742–7. doi: 10.1016/j.burns.2017.05.002

56. Imanishi J, Kamiyama K, Iguchi I, Kita M, Sotozono C, Kinoshita S. Growth factors: importance in wound healing and maintenance of transparency of the cornea. *Prog Retin Eye Res*. (2000) 19:113–29. doi: 10.1016/S1350-9462(99)00007-5

57. Kamil S, Mohan RR. Corneal stromal wound healing: major regulators and therapeutic targets. *Ocul Surf*. (2021) 19:290–306. doi: 10.1016/j.jtos.2020.10.006

58. Patel S, Mittal R, Sarantopoulos KD, Galor A. Neuropathic ocular surface pain: emerging drug targets and therapeutic implications. *Expert Opin Ther Targets*. (2022) 26:681–95. doi: 10.1080/14728222.2022.2122438

59. Lin SR, Aldave AJ, Chodosh J. Recurrent corneal erosion syndrome. *Br J Ophthalmol*. (2019) 103:1204–8. doi: 10.1136/bjophthalmol-2019-313835

60. Fogle JA, Kenyon KR, Stark WJ, Green WR. Defective epithelial adhesion in anterior corneal dystrophies. *Am J Ophthalmol*. (1975) 79:925–40. doi: 10.1016/0002-9394(75)90674-1

61. Kim EK, Kim HB, Chung YT, Kim IC. Endothelial F-actin changes in the alkali burned rabbit cornea. *Yonsei Med J*. (1994) 35:484–92. doi: 10.3349/ymj.1994.35.4.484

62. Chung JH, Kim HJ, Fagerholmb P, Cho BC. Effect of topically applied Na-hyaluronan on experimental corneal alkali wound healing. *Korean J Ophthalmol*. (1996) 10:68–75. doi: 10.3341/kjo.1996.10.2.68

63. Hao Y, Ma DH, Hwang DG, Kim WS, Zhang F. Identification of antiangiogenic and antiinflammatory proteins in human amniotic membrane. *Cornea*. (2000) 19:348–52. doi: 10.1097/00003226-200005000-00018

frontiers | Frontiers in Medicine

TYPE Original Research
PUBLISHED 19 February 2025
DOI 10.3389/fmed.2025.1547977

OPEN ACCESS

EDITED BY
Georgios D. Panos,
Aristotle University of Thessaloniki, Greece

REVIEWED BY
Mengxi Shen,
University of Miami Health System, United States
Kaicheng Wu,
Fudan University, China

*CORRESPONDENCE
Bin Gong
✉ gongbin_159@163.com

†These authors have contributed equally to this work and share first authorship

RECEIVED 19 December 2024
ACCEPTED 05 February 2025
PUBLISHED 19 February 2025

CITATION
Zhang C, Chen T, Jia R, Gong D, Liu Z, Wu C, Shu X, Han F and Gong B (2025) Intravitreal aflibercept for diabetic macular edema: structural and functional improvements. *Front. Med.* 12:1547977. doi: 10.3389/fmed.2025.1547977

Intravitreal aflibercept for diabetic macular edema: structural and functional improvements

Chuanhe Zhang[1,2†], Tianyu Chen[3†], Ru Jia[2], Di Gong[4], Zhigao Liu[5], Changlong Wu[2], Xiangwen Shu[2], Fangju Han[2] and Bin Gong[2*]

[1]The First Clinical Medical College, Jinan University, Guangzhou, Guangdong, China, [2]Department of Ophthalmology, Jinan Second People's Hospital, Jinan, Shandong, China, [3]Medical Affairs Department, Wuxi Second People's Hospital, Wuxi, Jiangsu, China, [4]Shenzhen Eye Hospital, Jinan University, Shenzhen Eye Institute, Shenzhen, Guangdong, China, [5]Department of Ophthalmology, Jinan Aier Eye Hospital, Jinan, Shandong, China

Introduction: The aim of this study was to evaluate the changes in macular structure and visual function of patients with diabetic macular edema (DME) after intravitreal aflibercept injection.

Methods: Twenty-five patients (43 eyes) diagnosed with DME were included in this study. All patients underwent aflibercept monthly for 3 months. The study's endpoints included the best corrected visual acuity (BCVA), central retinal thickness (CRT), fovea avascular zone (FAZ) area, vessel density of superficial retinal capillary plexus (SVD), vessel density of deep retinal capillary plexus (DVD), mean light sensitivity (MLS), 2° fixation rate (P1) and 4° fixation rate (P2).

Results: Before treatment and after the third treatment, the LogMAR BCVA was 0.69 ± 0.27 and 0.40 ± 0.18, the CRT was 471.10 ± 159.93 μm and 319.84 ± 113.51 μm, the MLS was 18.14 ± 3.97 dB and 21.68 ± 3.55 dB, P1 was 69 (47, 87)% and 88 (72, 92)%, and P2 was 90 (83, 97)% and 97 (93, 99)%, respectively. After treatment, CRT decreased, BVCA, MLS, and fixation stability improved (all $p < 0.001$). Post-treatment, FAZ area, SVD, and DVD showed no significant changes (all $P > 0.05$). MLS was negatively correlated with LogMAR BCVA and CRT, and positively correlated with P1 and P2.

Conclusion: In short term, aflibercept was effective in reducing CRT and improving BCVA, MLS, and fixation stability in DME patients.

KEYWORDS

diabetic macular edema, aflibercept, central retinal thickness, microperimetry, sensitivity

1 Introduction

Diabetic retinopathy (DR) is a common and unique microvascular complication of diabetes, while diabetic macular edema (DME) is one of the manifestations of DR, which mainly manifests as the thickening of the retina within the area of two-fold diameters of the optic disk at the central fovea of the macula, and is the major cause of central visual loss in DR patients (1). The pathogenesis of DME involves various factors and is associated with the disruption of the blood-retina barrier, which leads to the leakage of retinal blood vessels and liquid accumulation. In addition, vascular endothelial growth factors (VEGF) also have important roles in the pathogenesis of DME (2). Laser treatment is a conventional treatment for DME, which can

effectively reduce edema, but has limited effect on promoting the recovery of visual acuity in patients with vision impairment. Following the continuous advancements of the studies on DME, treatments of DME have also undergone drastic changes. Intravitreal administration of anti-VEGF agents is the preferred initial therapy for DME, with Aflibercept—a fusion protein targeting VEGF-A and Placental Growth Factor—notably enhancing retinal vessel permeability and mitigating macular edema (3–5). Previous studies mainly used optical coherence tomography angiography (OCTA) to examine the changes in macular structures; however, this approach has limited ability to evaluate visual function. Therefore, in the present study, we used microperimetry to evaluate the macular function, which can compensate for the limitations of OCTA examination, and we comprehensively evaluated the treatment effects on DME patients from the aspects of macular structures and function. The clinical significance of the treatment was also investigated in this study.

2 Methods

2.1 Study design and population

Patients diagnosed with DME in the Jinan Second People's Hospital between March 2021 and August 2021 were included in this prospective observational study. The inclusion criteria were as follows: (1) adults with Type 2 diabetes, presenting fasting blood glucose levels below 8.0 mmol/L and postprandial levels under 10.0 mmol/L; (2) blood pressure < 150/90 mmHg; (3) those confirmed with macular edema by fundus fluorescein angiography or optical coherence tomography (OCT), and with the central retinal thickness (CRT) of ≥250 μm; and (4) did not undergo ocular relevant treatments before the current treatment or did not receive treatment by intravitreal injection of drugs or pan-retinal photocoagulation within a half year before this treatment.

The exclusion criteria specified: (1) patients with prior eye traumas or other retinal conditions; (2) with severe cataracts that impair fundoscopic assessments; (3) with indications for vitreoretinal surgery, such as vitreous hemorrhage, epiretinal membrane, tractional detachment of retina; (4) subjects previously treated with intravitreal or periocular glucocorticoids; (5) patients with thromboembolic or coagulation disorders, those under anticoagulant therapy (aspirin excluded), or those with significant systemic illnesses; and (6) pregnant or lactating women.

The sample size was calculated using PASS software, with CRT reduction as the primary endpoint. Based on data from a previous study (6), parameters were set at a statistical power of 0.9, $\alpha = 0.05$ (two-tailed test), and a clinically meaningful difference of 73.8 μm. The required sample size was 13 eyes, while this study included 43 eyes, ensuring sufficient power for robust statistical analyses.

This research received approval from the Ethics Committee of Jinan Second People's Hospital (Approval No.: 20201203), adhering to the Declaration of Helsinki. This research was conducted according to established ethical guidelines.

2.2 Procedures

All patients underwent intravitreal injection of aflibercept (IVA) (once per month) continuously for 3 months. The examination was performed with OCT (CIRRUS HD-OCT, Carl Zeiss Meditec Inc., Dublin, CA, United States). Firstly, the OCT system was used for the scanning of the macular area to measure the CRT, after which the AngioPlex mode of OCTA was used for the 3 mm × 3 mm vertical and transverse cross scanning of the macular area, and the analysis program of the system was used for the layer classification of images. This process allowed for the division of the scans into the full-thickness retinal capillary plexus, superficial capillary plexus (SCP), deep capillary plexus (DCP), the foveal avascular zone (FAZ), and the choriocapillaris. To ensure reliability, all OCTA segmented images were carefully reviewed for the accuracy of the automatic segmentation of SCP and DCP. Any errors identified during this review process were manually corrected. The same doctor performed the OCTA examinations of all patients. The Image J software was used to measure the macular FAZ area of SCP, vessel density of superficial retinal capillary plexus (SVD), and vessel density of deep retinal capillary plexus (DVD). Specifically, the FAZ area was manually delineated using the Image J freehand selection tool, while SVD and DVD were quantified using thresholding and binarization techniques to isolate and calculate vessel density within the scanned regions (Figure 1). To ensure the highest level of accuracy, all OCTA images were independently reviewed and analyzed by two experienced ophthalmologists. Any discrepancies were resolved through discussion, and in cases where consensus could not be reached, a senior expert provided the final decision.

The MP-3 microperimetry (NIDEK, Japan) was used for the microperimetry, with the following parameters: the mode of MP1 Macula-10 deg. was selected. The 40 stimulation points were distributed as inner, medium, and outer concentric circles. The diameter of the inner cycle was 2°, and it consisted of 8 points; the diameter of the medium cycle was 6°, and it consisted of 16 points; the diameter of the outer cycle was 10°, and it consisted of 16 points. The background light was white with an illuminance of 31.4 asb. The fixation target utilized was a red cross, approximately 1° in size. The light sensitivity threshold varied between 0 and 34 dB. The mean light sensitivity (MLS) of the retina within the range of 10° (approximately 3 mm), as well as the 2° and 4° fixation rates, were measured. Fixation rates, defined as the proportion of fixation sites within a 2° or 4° diameter circle centered on the fovea to total fixation points (denoted as P1 and P2, respectively), were quantified. The examinations were performed in a dark room, and it was possible to perform a pupil dilation if the pupil was relatively small (<3.3 mm). The doctors helped patients to sit at the microperimetry and asked them to gaze at the fixation target. Next, the patients used split vision to feel the peripheral white stimulation points without tracking the points. Finally, patients were asked to press the response button when spotting any white points. Throughout the procedures, the patients were instructed to maintain fixation; the color photo of the fundus was automatically taken after the processes were completed and overlapped with the photos of microperimetry.

2.3 Outcomes

The patients' indicators, including intraocular pressure, best corrected visual acuity (BCVA), CRT, FAZ area, SVD, DVD, MLS, P1, P2, and other indicators, were collected before and 1 month after each

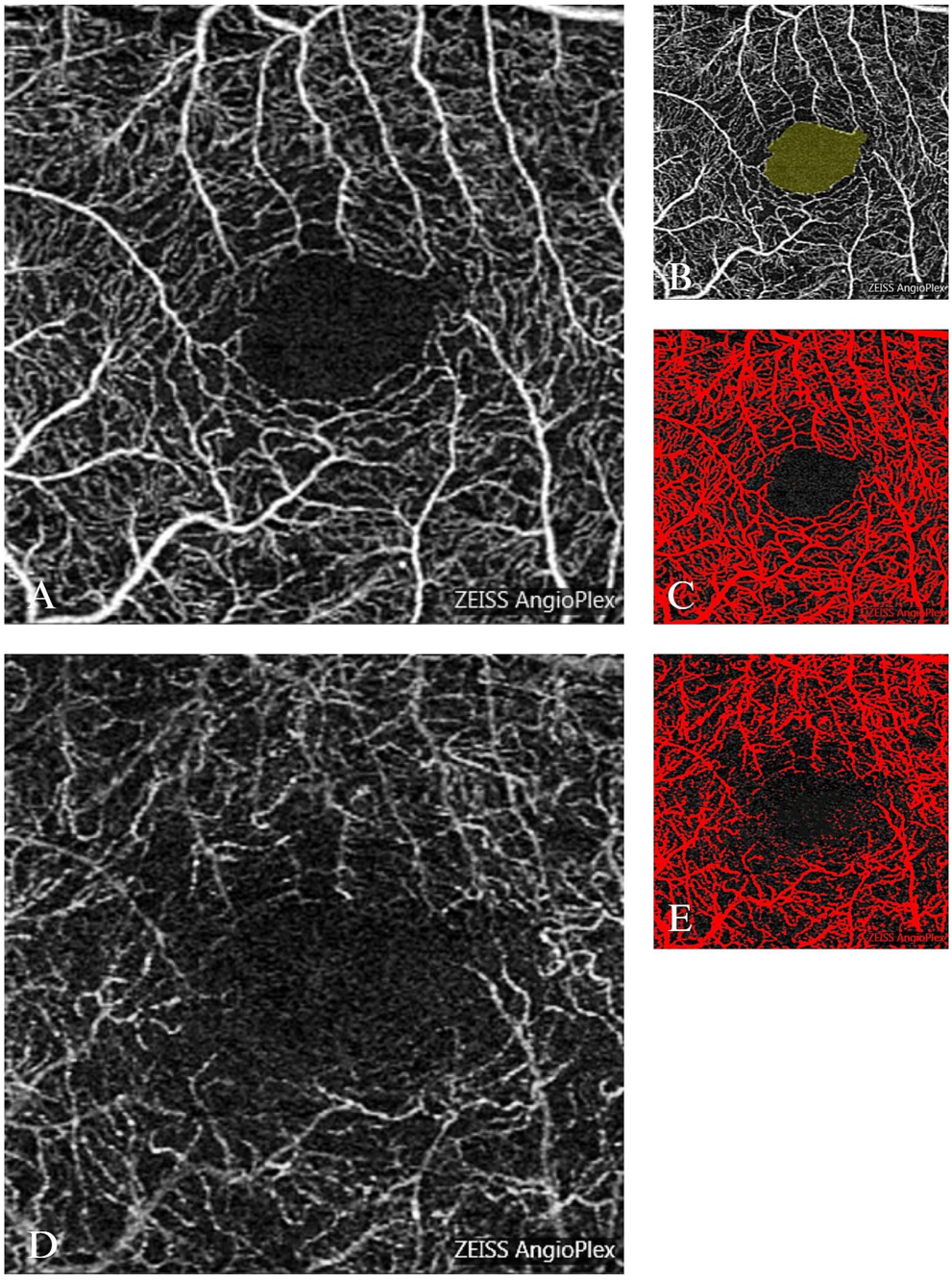

FIGURE 1
Optical coherence tomography angiography (OCTA) images and measurements of FAZ, SVD, and DVD. **(A)** OCTA image of the SCP. **(B)** FAZ outlined in yellow. **(C)** Superficial capillary outlined in red. **(D)** OCTA image of the DCP. **(E)** Deep capillary outlined in red.

treatment. BCVA was converted into a logarithm of the minimum angle of resolution (LogMAR) for analysis.

2.4 Statistical analysis

SPSS 26.0 software (Version 26.0) was used for all the statistical analyses in this study. The Shapiro–Wilk test was employed to assess the normality of the dataset. Normally distributed data were presented as mean ± standard deviation ($\overline{x} \pm s$), while non-normally distributed data were expressed as median and interquartile range. To account for intra-patient correlation between both eyes, generalized estimating equations (GEE) were applied to compare data across different time points before and after treatment, with multiple comparisons corrected using the Bonferroni method. Additionally, GEE was employed to assess correlations among various research indicators before and after each treatment session. GraphPad Prism 9.0 (GraphPad Software Inc.) software was used for figure plotting. Two side $p < 0.05$ was considered statistically significant.

3 Results

3.1 Baseline characteristics of patients

During the follow-up process, 3 samples had missing values, and the samples containing missing values were directly deleted. A total of 25 patients (43 eyes), including 22 eyes from 12 males and 21 eyes from 13 females, were enrolled in this study. The mean age of patients was 57.33 ± 10.30 years, and the duration of diabetes was 12.35 ± 5.47 years. The baseline characteristics of patients before treatment are shown in Table 1.

3.2 LogMAR BCVA and CRT changes after treatment

After three anti-VEGF treatments, the respective LogMAR BCVA of patients was 0.55 ± 0.26, 0.47 ± 0.19, and 0.40 ± 0.18, which was significantly lower than before the treatment (all $p < 0.001$), and the respective CRT was 370.30 ± 120.55 μm, 348.93 ± 115.72 μm, and 319.84 ± 113.51 μm, which was also significantly lower than before the treatment (all $p < 0.001$) (Table 2). The LogMAR BCVA and CRT were significantly different among different time points before and after treatment (*all* $p < 0.05$) (Table 2; Figures 2A,B; Supplementary Table 1).

TABLE 1 Baseline characteristics of patients.

Baseline characteristics	
Number of patients/eyes	25/43
Age (years) ($\bar{x} \pm s$; range)	57.33 ± 10.30(29–73)
Duration of diabetes (years) ($\bar{x} \pm s$; range)	12.35 ± 5.47(3–25)
Pretreatment LogMAR BCVA ($\bar{x} \pm s$; range)	0.69 ± 0.27(0.22–1.30)
Pretreatment CRT (μm) ($\bar{x} \pm s$; range)	471.10 ± 159.93(250–831)
Pretreatment FAZ area (mm^2) ($\bar{x} \pm s$; range)	0.37 ± 0.13(0.15–0.69)
Pretreatment SVD (%) ($\bar{x} \pm s$; range)	38.67 ± 4.55(29.09–52.96)
Pretreatment DVD (%) ($\bar{x} \pm s$; range)	40.96 ± 5.72(32.88–57.95)
Pretreatment MLS (dB) ($\bar{x} \pm s$; range)	18.14 ± 3.97(7.20–29.10)
Pretreatment P1 (%) M (P_{25}, P_{75})	69(47, 87)
Pretreatment P2 (%) M (P_{25}, P_{75})	90(83, 97)

3.3 FAZ area, SVD, and DVD changes after treatment

After three anti-VEGF treatments, the respective FAZ area was 0.38 ± 0.14 mm^2, 0.37 ± 0.14 mm^2, and 0.38 ± 0.13 mm^2, the respective SVD was (38.53 ± 4.38)%, (37.78 ± 4.09)%, and (38.29 ± 3.99)% and the respective DVD was (40.27 ± 5.18)%, (40.05 ± 4.99)%, and (40.34 ± 5.08)%. However, there was no statistically significant difference in FAZ area, SVD, and DVD at different time points before and after treatment ($p = 0.278$, $p = 0.149$, $p = 0.185$) (Table 2; Figures 2C–E; Supplementary Table 1).

3.4 MLS and P1/P2 changes after treatment

The respective MLS was 20.48 ± 3.96 dB, 21.04 ± 3.56 dB, and 21.68 ± 3.55 dB after three anti-VEGF treatments, which were all significantly increased compared with before the treatment (all $p < 0.001$). No significant change was observed between the first and second treatments ($p = 1.000$) or between the second and third treatments ($p = 0.081$), but a significant increase occurred after the third treatment compared to the first ($p = 0.007$) (Table 2; Figure 2F; Supplementary Table 1). Both P1 and P2 increased significantly after the treatment compared with before the treatment (*all* $p < 0.01$) (Table 2; Figures 2G,H; Supplementary Table 1). Pre- and post-treatment evaluations of DME patients utilized OCT, OCTA, and microperimetry, as depicted in Figure 3.

3.5 Correlation analysis of factors

GEE analysis revealed that, before treatment, LogMAR BCVA showed a positive correlated with CRT ($\beta = 241.173$, $p = 0.004$), and negative correlations with MLS ($\beta = -10.979$, $p < 0.001$), P1 ($\beta = -37.277$, $p < 0.001$), and P2 ($\beta = -27.196$, $p = 0.005$). It was insignificantly correlated with FAZ area, SVD, and DVD (all $P > 0.05$). CRT was negatively correlated with MLS ($\beta = -0.011$, $p < 0.001$) and P1 ($\beta = -0.070$, $p < 0.001$), and insignificantly correlated with FAZ

TABLE 2 Changes in LogMAR BCVA, CRT, FAZ area, SVD, DVD, and MLS in DME patients after anti-VEGF treatment.

Type	LogMAR BCVA	CRT (μm)	FAZ area (mm^2)	SVD (%)	DVD (%)	MLS (dB)	P1 (%)	P2 (%)
Before treatment	0.69 ± 0.27	471.10 ± 159.93	0.37 ± 0.13	38.67 ± 4.55	40.96 ± 5.72	18.14 ± 3.97	69(47,87)	90(83,97)
After the first treatment	0.55 ± 0.26***	370.30 ± 120.55***	0.38 ± 0.14	38.53 ± 4.38	40.27 ± 5.18	20.48 ± 3.96***	81(55,91)**	95(88,99)**
After the second treatment	0.47 ± 0.19***	348.93 ± 115.72***	0.37 ± 0.14	37.78 ± 4.09	40.05 ± 4.99	21.04 ± 3.56***	85(60,93)**	95(90,99)**
After the third treatment	0.40 ± 0.18***	319.84 ± 113.51***	0.38 ± 0.13	38.29 ± 3.99	40.34 ± 5.08	21.68 ± 3.55***	88(72,92)***	97(93,99)***
Wald χ^2	112.616	68.407	3.849	5.332	4.823	75.079	34.227	22.008
p-value	<0.001	<0.001	0.278	0.149	0.185	<0.001	<0.001	<0.001

p-values for the overall comparison of indicators among different time points before and after treatment; **$P < 0.01$, ***$P < 0.001$ (Bonferroni adjustment), comparison with the baseline level.

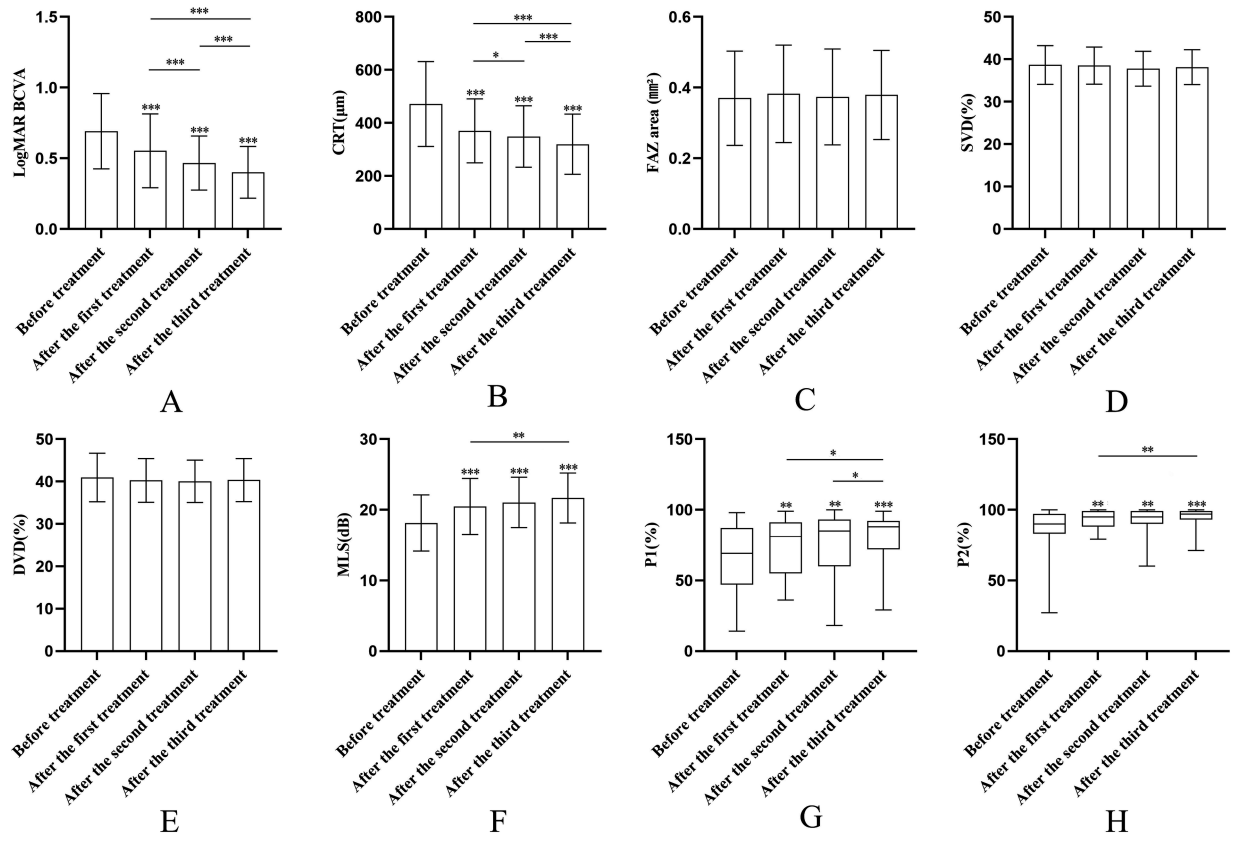

FIGURE 2
Changes of different indicators in DME patients after anti-VEGF treatment. **(A)** Changes in LogMAR BCVA following treatment. **(B)** Changes in CRT following treatment. **(C)** Changes in FAZ area following treatment. **(D)** Changes in SVD following treatment. **(E)** Changes in DVD following treatment. **(F)** Changes in MLS following treatment. **(G)** Changes in P1 following treatment. **(H)** Changes in P2 following treatment. *$p < 0.05$, **$p < 0.01$, ***$p < 0.001$ (Bonferroni adjustment).

area, SVD, DVD, and P2 (all $P > 0.05$). MLS was positively correlated with P1 ($\beta = 2.910$, $p < 0.001$) and P2 ($\beta = 1.711$, $p < 0.001$), negatively correlated with FAZ area ($\beta = -8.354$, $p = 0.009$), and insignificantly correlated with SVD and DVD (all $P > 0.05$) (Table 3).

After the third treatment, LogMAR BCVA was still positively correlated with CRT ($\beta = 246.882$, $p = 0.001$), and negatively correlated with MLS ($\beta = -14.355$, $p < 0.001$), P1 ($\beta = -33.419$, $p < 0.001$), and P2 ($\beta = -11.268$, $p = 0.020$), but had no significant correlation with FAZ area, SVD, and DVD (all $P > 0.05$). CRT was negatively correlated with MLS ($\beta = -0.012$, $p = 0.026$), and insignificantly correlated with FAZ, SVD, DVD, P1, and P2 (all $P > 0.05$). MLS was positively correlated with SVD ($\beta = 0.338$, $p < 0.001$), P1 ($\beta = 2.252$, $p = 0.002$), and P2 ($\beta = 0.858$, $p = 0.013$), and insignificantly correlated with FAZ area and DVD (all $P > 0.05$) (Table 3).

4 Discussion

The present study included DME patients who underwent treatment with IVA, finding that anti-VEGF treatment could effectively reduce the CRT, increase the retina's light sensitivity, and improve visual acuity. The findings on macular structures and function provided more valuable evidence for the safety and effectiveness of aflibercept for the treatment of DME.

The study demonstrated significant improvements in visual acuity and reductions in CRT post-treatment, aligning with findings by Qin et al. (7). The VISTA/VIVID-DME study showed that treating DME with anti-VEGF could significantly benefit BCVA and reduce CRT (8), which is in line with our results. These findings demonstrated that anti-VEGF treatment could significantly reduce the permeability of retinal vessels, reduce the exudation of liquids in blood vessels, improve the blood-retina barrier, and alleviate macular edema. In addition, the CRT of very few patients in this study was significantly reduced; however, the visual acuity did not significantly improve in this study after anti-VEGF treatment, which could be associated with the injuries of the retinal photoreceptor cell.

The FAZ is surrounded by the continuous retinal capillary plexus with no capillary structures. It is also a very important area for forming fine visual function, where the changes in morphology and density of surrounding capillaries could reflect the degree of macular ischemia, being closely associated with various retinal diseases, especially retinal vascular diseases (9). Occlusion of capillaries surrounding the macula could induce FAZ disruption and increase the area. Thus, the FAZ area in DR patients is larger than in healthy people, while the SVD and DVD are both reduced (10, 11). Indicators such as FAZ area, SVD, and DVD could visually reflect the retinal microcirculation and be used to further predict the progression of visual acuity and monitor the treatment responses (12). In this study, the FAZ area, SVD, and DVD in patients who underwent IVA

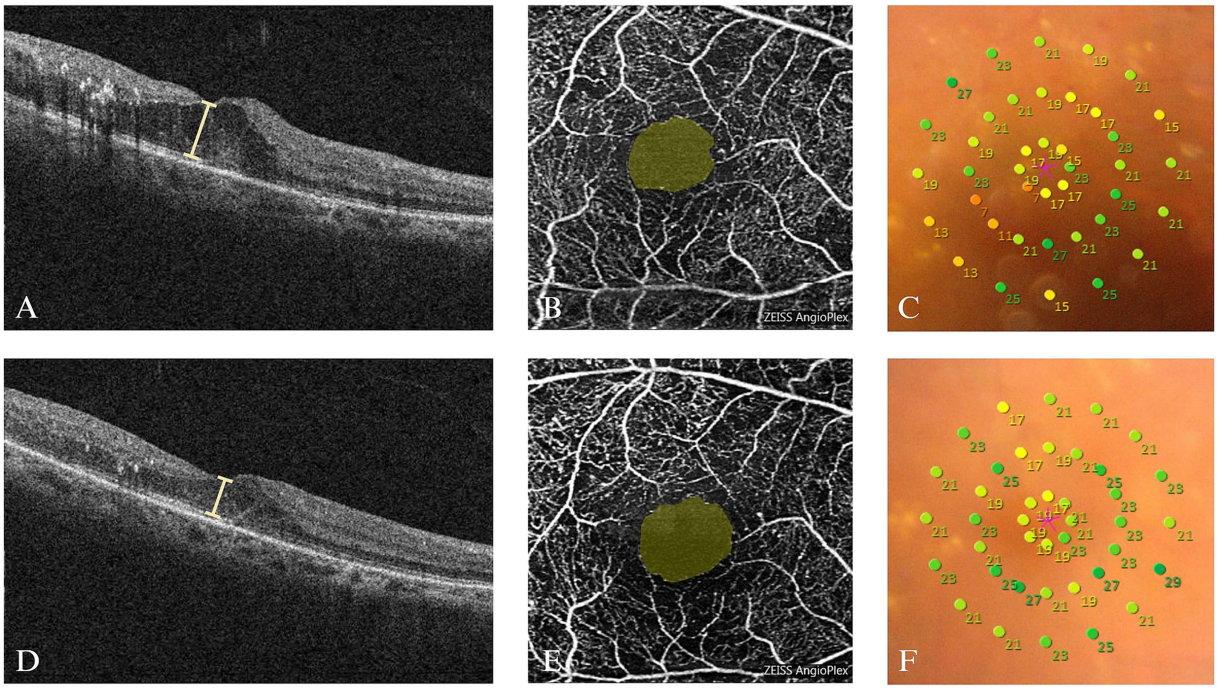

FIGURE 3
Examination findings of the right eye of a DME patient (female, 58 years old) before and after the third treatment. **(A)** The OCT image of the macula before treatment showing the cystoid macular edema; the CRT was 365 μm. **(B)** OCTA image before treatment showing the destruction of the arch ring and non-perfusion areas in the superficial capillary plexus. **(C)** A microperimetry image of the macular area in diameter of 10° before treatment showing the reduction of local retinal light sensitivity; the MLS was 19.3 dB. **(D)** Macular OCT image after treatment showing that macular edema was reduced compared to before; the CRT was 268 μm. **(E)** OCTA image after treatment showing that the superficial capillary plexus did not significantly change compared to before, and signal masking was found in some regions. **(F)** A microperimetry image of the macular area in diameter of 10° after treatment showing that the local retinal light sensitivity increased compared to before; the MLS was 21.7 dB.

treatment were not significantly different at different time points compared with before treatment. Similarly, Mirshahi et al. (13) found no substantial changes in FAZ areas or vascular density post-bevacizumab injections. Busch et al. (14) reported that after IVA for the treatment of DME (time points for observation were 3–25 months), the retinal microvascular density also did not change, which is consistent with our findings. We assumed that the blood glucose level in diabetes patients remains elevated, whose effects, along with the oppression from edema, could lead to irreversible injuries to the retinal vascular structures and could induce vascular obstruction, arch ring destruction, FAZ enlargement, and vascular density reduction. It was hypothesized that while anti-VEGF treatment may reduce fluid exudation, it does not effectively clear blocked blood vessels nor enhance macular blood perfusion. Nonetheless, this study documented enhanced regional blood perfusion in certain patients following anti-VEGF therapy. This improvement is likely linked to the rapid resolution of edema. When the macular edema was very severe, the exuded liquids could press the retinal blood vessels, thus masking the part of blood flow signals on OCTA; while after edema they disappeared, the masking effect reduced, and the signals reappeared again; however, the states of blood perfusion did not actually change. Under such circumstances, even the macular edema disappeared, and the visual benefits were generally limited. These findings suggest that using OCTA to examine the FAZ region and vascular density has important significance for early observation and early treatments of patients with DME.

There are still debates on the influence of anti-VEGF treatment on macular microcirculation in patients with diabetic macular edema. Mastropasqua et al. (15) found that within the 5 months' of follow-up of DME patients who underwent IVA, SVD and DVD were significantly increased. Hsieh et al. (16) used OCTA to examine the changes of biomarkers in DME patients treated with ranibizumab, finding that the vascular density close to the central fovea was increased compared to before the realizations of 3 treatments. Still, some studies suggested that anti-VEGF treatment could worsen retinal ischemia. For instance, in their retrospective study, Feucht et al. (17) treated patients with macular edema-induced non-proliferative diabetic retinopathy or branch retinal vein occlusion by intravitreal injection of bevacizumab, finding that the FAZ area increased after 6–8 weeks, which was indicative of the worsened retinal ischemia. Yet, the investigators speculated that such changes could be transient. As we could not evaluate the potential changes in retinal vascular density and FAZ in untreated eyes, it remains unclear whether IVA could prevent the progression of macular ischemia. Nonetheless, previous studies have demonstrated that IVA would at least not worsen the blood flow of the retina in most patients with DME. These findings suggested that the major cause of macular edema alleviation in the short-term treatment of DME by anti-VEGF could be the alleviation of retinal vascular exudation, while the retinal vascular occlusion did not significantly improve; nevertheless, the perfusion defect in macular vessels also did not worsen.

Currently, the visual functions of DME patients are generally evaluated by central visual acuity. However, the central visual acuity acquired by the visual acuity chart is not suitable for sophisticated quantitative evaluation of visual function (18–20). While morphological changes are generally used as indicators for treatments

TABLE 3 Correlation analysis of research indicators before and after each treatment using generalized estimating equations (GEE).

Research indicators		Before treatment		After the first treatment		After the second treatment		After the third treatment	
		β	*p*-value	*β*	*P*-value	*β*	*P*-value	*β*	*P*-value
LogMAR BCVA	CRT	241.173	0.004	153.950	0.093	94.363	0.184	246.882	0.001
	FAZ area	0.010	0.849	0.010	0.812	0.039	0.535	0.012	0.857
	SVD	−1.441	0.679	−3.035	0.156	−1.140	0.696	−3.926	0.124
	DVD	0.938	0.722	−0.587	0.790	−4.644	0.123	−2.112	0.511
	MLS	−10.979	<0.001	−10.364	<0.001	−10.953	<0.001	−14.355	<0.001
	P1	−37.277	<0.001	−10.290	0.356	−26.446	0.007	−33.419	<0.001
	P2	−27.196	0.005	−5.742	0.035	−14.422	0.005	−11.268	0.020
CRT	FAZ area	0.000	0.682	0.000	0.898	0.000	0.228	0.000	0.054
	SVD	−0.009	0.090	−0.003	0.427	−0.002	0.537	0.000	0.946
	DVD	−0.005	0.502	0.002	0.815	−0.002	0.723	−0.002	0.807
	MLS	−0.011	<0.001	−0.010	0.032	−0.009	0.162	−0.012	0.026
	P1	−0.070	<0.001	0.019	0.333	−0.024	0.266	−0.062	0.058
	P2	−0.043	0.065	−0.008	0.386	−0.026	0.163	−0.020	0.218
FAZ area	SVD	−0.439	0.919	−9.051	0.034	−0.435	0.925	1.436	0.805
	DVD	−8.759	0.099	−2.351	0.685	−0.247	0.961	2.764	0.624
	MLS	−8.354	0.009	−9.303	0.039	−2.817	0.469	−3.741	0.304
	P1	−49.465	0.057	−93.111	<0.001	1.999	0.966	−49.868	<0.001
	P2	−16.560	0.138	−27.199	<0.001	−9.622	0.320	−16.937	<0.001
SVD	DVD	0.750	<0.001	0.539	<0.001	0.451	0.006	0.453	0.019
	MLS	0.196	0.056	0.437	<0.001	0.305	0.010	0.338	<0.001
	P1	1.815	0.039	1.057	0.068	0.088	0.896	0.366	0.377
	P2	0.825	0.149	0.314	0.098	0.254	0.279	0.018	0.905
DVD	MLS	0.053	0.539	0.247	0.034	0.165	0.158	0.211	0.074
	P1	0.385	0.598	0.293	0.522	0.333	0.422	−0.080	0.868
	P2	0.216	0.641	0.038	0.849	0.172	0.432	−0.111	0.617
MLS	P1	2.910	<0.001	0.861	0.131	1.591	0.004	2.252	0.002
	P2	1.711	0.016	0.239	0.242	1.128	0.007	0.858	0.013
P1	P2	0.458	<0.001	0.247	<0.001	0.343	<0.001	0.341	<0.001

of DME, the change in visual function is the major concern of patients. MP-3 microperimetry could be used to automatically evaluate the retina's sensitivity in the macular area and quantify the visual function of the central fovea of the macula. Retinal sensitivity, as compared to central visual acuity, offers a more precise assessment of the nuances in macular visual function alterations. In addition, P1 and P2 could well reflect the stability of fixation of patients and reflect the quality of vision (21–23). Our results revealed that MLS, P1, and P2 increased significantly after treatment. In their study, Xu et al. (24) evaluated the retinal structures and visual function changes in DME patients 1 year after IVA, finding that the MLS at the central fovea was significantly improved, which was closely associated with the beneficial effects on BCVA. Ichio et al. (25) and Malagola et al. (26) treated DME patients with anti-VEGF (once per month) for 3 months and found that the MLS of the retina significantly increased compared with the baseline level. In addition, the thickness of the macular central fovea was significantly correlated with the MLS of the retina, which is in agreement with the findings of this study, demonstrating that intravitreal injection of anti-VEGF agents could significantly improve retinal sensitivity. However, several studies have demonstrated that the retinal sensitivity after anti-VEGF treatment showed no statistically significant change, which could be associated with the relatively high standard deviations and a limited number of eyes evaluated in the corresponding studies (27). Seidensticker et al. (28) found that the fixation stability of DME patients after intravitreal injection of ranibizumab significantly improved compared to before treatment, but the retinal sensitivity did not significantly change. The investigators speculated that the fixation stability could be used as an early indicator for evaluating the changes in visual function. These findings were not in agreement with the results of this study, which might be due to the difference in the length of disease duration of DME in the patients. Specifically, patients in Seidensticker's study mainly had long disease duration, and their anatomical structures of the retina were already significantly changed. Although CRT reduced and central visual

acuity improved, the retina surrounding the central fovea showed no significant functional improvement. An interesting observation in our study was that the changes in MLS between the first and second treatments, as well as between the second and third treatments, were not statistically significant. We believe this may be attributed to several factors. First, early structural recovery often precedes functional improvement. Functional recovery, such as changes in MLS, may take longer to manifest as it depends on the restoration of photoreceptor function, which may not progress linearly with structural changes. Second, subsequent treatments may require more time or cumulative effects to achieve further enhancements in retinal sensitivity. Additionally, inter-individual variability in baseline retinal damage, such as differences in photoreceptor integrity, may lead to varying responses among patients. Lastly, the observed changes during this interval might have been influenced by the sample size and variability, which could limit the statistical power to detect smaller but potentially meaningful improvements.

The findings of the present study demonstrated that MLS before and after treatment was associated with visual acuity but also with CRT, which was in agreement with the results of a study by Vujosevic et al. (29). Previous studies have demonstrated that the macular central fovea thickness measured by OCT is significantly associated with BCVA (30, 31), which is consistent with our results. Several researchers divided the macular area into 9 regions, after which they explored the association between microperimetry and OCTA findings. Their findings showed that the retinal sensitivity of central fovea on the temporal side was moderately associated with vascular density, while the associations in the other 8 regions were not statistically significant (32). In this study, MLS of the retina in the 10° was measured, and the findings showed that MLS correlated with SVD and DVD only after treatment. In contrast, before treatment, LogMAR BCVA showed a negative correlation with both P1 and P2, whereas MLS exhibited a positive correlation with these parameters. However, these correlations changed after treatment, which we believe may be attributed to several factors. One possible explanation is that anti-VEGF therapy, such as aflibercept, primarily reduces macular edema and improves CRT in the short term, resulting in rapid improvements in BCVA and MLS. In contrast, fixation stability (P1 and P2) may recover more gradually, as it relies on more complex interactions between retinal structure and function. Another contributing factor could be individual differences, such as the severity of macular edema or the extent of retinal damage, which might influence how patients respond to treatment. These variations could have contributed to the observed changes in correlation patterns. While extending the follow-up period would undoubtedly provide deeper insights, our current findings emphasize the short-term effectiveness of aflibercept in improving retinal structure and function. We will aim to incorporate longer follow-up durations in future studies to further clarify these changes in retinal structure and function. Moreover, we propose retinal sensitivity and fixation stability as valuable metrics for assessing DME treatment efficacy.

The present study has some limitations. The study's sample size was relatively small, so future studies with larger sample sizes are needed to further verify and confirm the reported findings. The follow-up time of this study was relatively short. The retinal sensitivity and vascular density in this study were calculated as the mean values of the measured macular regions, while the visual function and blood flow changes in some small regions might be neglected. In the current study, we used the latest generation of MP-3 microperimetry. The differences in parameters and internal programs of different devices could also influence the findings.

5 Conclusion

In conclusion, treating DME patients with aflibercept within a short time led to reduced retinal thickness, increased retinal sensitivity, and improved visual acuity. Furthermore, improvements in visual function are associated with changes in retinal structure, and retinal sensitivity and fixation stability could be used as reliable supplementary functional parameters for evaluating the processes of DME treatment. Yet, more studies are needed to further investigate the influence of anti-VEGF treatment on retinal microcirculation and the correlation between macular structures and visual function.

Data availability statement

The original contributions presented in the study are included in the article/Supplementary material, further inquiries can be directed to the corresponding author.

Ethics statement

The studies involving humans were approved by Jinan Second People's Hospital (Approval no.: 20201203). The studies were conducted in accordance with the local legislation and institutional requirements. The participants provided their written informed consent to participate in this study.

Author contributions

CZ: Conceptualization, Formal analysis, Writing – original draft. TC: Data curation, Methodology, Writing – original draft. RJ: Data curation, Resources, Writing – original draft. DG: Methodology, Writing – review & editing. ZL: Investigation, Validation, Writing – review & editing. CW: Visualization, Writing – review & editing. XS: Supervision, Writing – review & editing. FH: Resources, Writing – review & editing. BG: Conceptualization, Data curation, Writing – review & editing.

Funding

The author(s) declare that no financial support was received for the research, authorship, and/or publication of this article.

Conflict of interest

The authors declare that the research was conducted in the absence of any commercial or financial relationships that could be construed as a potential conflict of interest.

Generative AI statement

The authors declare that no Gen AI was used in the creation of this manuscript.

Publisher's note

All claims expressed in this article are solely those of the authors and do not necessarily represent those of their affiliated organizations, or those of the publisher, the editors and the reviewers. Any product that may be evaluated in this article, or claim that may be made by its manufacturer, is not guaranteed or endorsed by the publisher.

Supplementary material

The Supplementary material for this article can be found online at: https://www.frontiersin.org/articles/10.3389/fmed.2025.1547977/full#supplementary-material

References

1. Lechner J, O'Leary OE, Stitt AW. The pathology associated with diabetic retinopathy. *Vis Res*. (2017) 139:7–14. doi: 10.1016/j.visres.2017.04.003

2. Zhang J, Zhang J, Zhang C, Zhang J, Gu L, Luo D, et al. Diabetic macular edema: current understanding, molecular mechanisms and therapeutic implications. *Cells*. (2022) 11:3362. doi: 10.3390/cells11213362

3. Jhaveri CD, Glassman AR, Ferris FL 3rd, Liu D, Maguire MG, Allen JB, et al. Aflibercept monotherapy or bevacizumab first for diabetic macular edema. *N Engl J Med*. (2022) 387:692–703. doi: 10.1056/NEJMoa2204225

4. Cai S, Yang Q, Li X, Zhang Y. The efficacy and safety of aflibercept and conbercept in diabetic macular edema. *Drug Des Devel Ther*. (2018) 12:3471–83. doi: 10.2147/DDDT.S177192

5. Schmidt-Erfurth U, Garcia-Arumi J, Bandello F, Berg K, Chakravarthy U, Gerendas BS, et al. Guidelines for the Management of Diabetic Macular Edema by the European Society of Retina Specialists (EURETINA). *Ophthalmologica*. (2017) 237:185–222. doi: 10.1159/000458539

6. Campos A, Campos EJ, do Carmo A, Caramelo F, Martins J, Sousa JP, et al. Evaluation of markers of outcome in real-world treatment of diabetic macular edema. *Eye vis*. (2018) 5:27. doi: 10.1186/s40662-018-0119-9

7. Qin S, Zhang C, Qin H, Xie H, Luo D, Qiu Q, et al. Hyperreflective foci and subretinal fluid are potential imaging biomarkers to evaluate anti-VEGF effect in diabetic macular edema. *Front Physiol*. (2021) 12:791442. doi: 10.3389/fphys.2021.791442

8. Brown DM, Schmidt-Erfurth U, Do DV, Holz FG, Boyer DS, Midena E, et al. Intravitreal Aflibercept for diabetic macular edema: 100-week results from the VISTA and VIVID studies. *Ophthalmology*. (2015) 122:2044–52. doi: 10.1016/j.ophtha.2015.06.017

9. Laotaweerungsawat S, Psaras C, Haq Z, Liu X, Stewart JM. Racial and ethnic differences in foveal avascular zone in diabetic and non-diabetic eyes revealed by optical coherence tomography angiography. *PLoS One*. (2021) 16:e0258848. doi: 10.1371/journal.pone.0258848

10. Samara WA, Shahlaee A, Adam MK, Khan MA, Chiang A, Maguire JI, et al. Quantification of diabetic macular ischemia using optical coherence tomography angiography and its relationship with visual acuity. *Ophthalmology*. (2017) 124:235–44. doi: 10.1016/j.ophtha.2016.10.008

11. Al-Sheikh M, Akil H, Pfau M, Sadda SR. Swept-source OCT angiography imaging of the foveal avascular zone and macular capillary network density in diabetic retinopathy. *Invest Ophthalmol Vis Sci*. (2016) 57:3907–13. doi: 10.1167/iovs.16-19570

12. AttaAllah HR, Mohamed AAM, Ali MA. Macular vessels density in diabetic retinopathy: quantitative assessment using optical coherence tomography angiography. *Int Ophthalmol*. (2019) 39:1845–59. doi: 10.1007/s10792-018-1013-0

13. Mirshahi R, Falavarjani KG, Molaei S, Habibi A, Anvari P, Khorasani MA, et al. Macular microvascular changes after intravitreal bevacizumab injection in diabetic macular edema. *Can J Ophthalmol*. (2021) 56:57–65. doi: 10.1016/j.jcjo.2020.07.004

14. Busch C, Wakabayashi T, Sato T, Fukushima Y, Hara C, Shiraki N, et al. Retinal microvasculature and visual acuity after intravitreal Aflibercept in diabetic macular edema: an optical coherence tomography angiography study. *Sci Rep*. (2019) 9:1561. doi: 10.1038/s41598-018-38248-1

15. Mastropasqua R, D'Aloisio R, Di Nicola M, Di Martino G, Lamolinara A, Di Antonio L, et al. Relationship between aqueous humor cytokine level changes and retinal vascular changes after intravitreal aflibercept for diabetic macular edema. *Sci Rep*. (2018) 8:16548. doi: 10.1038/s41598-018-35036-9

16. Hsieh YT, Alam MN, Le D, Hsiao CC, Yang CH, Chao DL, et al. OCT angiography biomarkers for predicting visual outcomes after Ranibizumab treatment for diabetic macular edema. *Ophthalmol Retina*. (2019) 3:826–34. doi: 10.1016/j.oret.2019.04.027

17. Feucht N, Schönbach EM, Lanzl I, Kotliar K, Lohmann CP, Maier M. Changes in the foveal microstructure after intravitreal bevacizumab application in patients with retinal vascular disease. *Clin Ophthalmol*. (2013) 7:173–8. doi: 10.2147/OPTH.S37544

18. Gulyesil FF, Inan S, Gobeka HH, Sabaner MC, Alizada A. Retinal ultrastructural, electrophysiological, and microvascular morphological outcomes in diabetic macular edema treated with intravitreal bevacizumab. *Ir J Med Sci*. (2022) 192:149–59. doi: 10.1007/s11845-022-02979-y

19. Santos AR, Raimundo M, Alves D, Lopes M, Pestana S, Figueira J, et al. Microperimetry and mfERG as functional measurements in diabetic macular oedema undergoing intravitreal ranibizumab treatment. *Eye*. (2021) 35:1384–92. doi: 10.1038/s41433-020-1054-2

20. Kalinowska A, Nowomiejska K, Brzozowska A, Maciejewski R, Rejdak R. Metamorphopsia score and central visual field outcomes in diabetic cystoid macular edema. *Biomed Res Int*. (2018) 2018:1–10. doi: 10.1155/2018/4954532

21. Qian T, Xu X, Liu X, Yen M, Zhou H, Mao M, et al. Efficacy of MP-3 microperimeter biofeedback fixation training for low vision rehabilitation in patients with maculopathy. *BMC Ophthalmol*. (2022) 22:197. doi: 10.1186/s12886-022-02419-6

22. Fujino R, Asaoka R, Aoki S, Sugiura A, Kusakabe M, Asano-Shimizu K, et al. The usefulness of the retinal sensitivity measurement with a microperimetry for predicting the visual prognosis of branch retinal vein occlusion with macular edema. *Graefes Arch Clin Exp Ophthalmol*. (2020) 258:1949–58. doi: 10.1007/s00417-020-04759-9

23. Molina-Martín A, Pérez-Cambrodí RJ, Piñero DP. Current clinical application of Microperimetry: a review. *Semin Ophthalmol*. (2018) 33:620–8. doi: 10.1080/08820538.2017.1375125

24. Xu Y, Qu Y, Suo Y, Gao J, Chen X, Liu K, et al. Correlation of retinal layer changes with vision gain in diabetic macular edema during conbercept treatment. *BMC Ophthalmol*. (2019) 19:123. doi: 10.1186/s12886-019-1131-0

25. Ichio A, Sugimoto M, Matsubara H, Mochida D, Kato K, Kondo M. Effects of intravitreal Aflibercept on retinal function and improvement of macular edema associated with diabetic retinopathy. *Transl Vis Sci Technol*. (2020) 9:2. doi: 10.1167/tvst.9.11.2

26. Malagola R, Spinucci G, Cofone C, Pattavina L. Prospective microperimetry and OCT evaluation of efficacy of repeated intravitreal bevacizumab injections for persistent clinically significant diabetic macular edema. *Int Ophthalmol*. (2013) 33:261–7. doi: 10.1007/s10792-012-9685-3

27. Vujosevic S, Berton M, Bini S, Casciano M, Cavarzeran F, Midena E. Hyperreflective retinal spots and visual function after anti-vascular endothelial growth factor treatment in center-involving diabetic macular edema. *Retina*. (2016) 36:1298–308. doi: 10.1097/IAE.0000000000000912

28. Seidensticker F, Reznicek L, Cserhati S, Liegl RG, Langer J, Wolf A, et al. Improvement of fixation in diabetic macular oedema patients under intravitreal ranibizumab treatment. *Klin Monatsbl Augenheilkd*. (2013) 230:524–9. doi: 10.1055/s-0032-1327930

29. Vujosevic S, Midena E, Pilotto E, Radin PP, Chiesa L, Cavarzeran F. Diabetic macular edema: correlation between microperimetry and optical coherence tomography findings. *Invest Ophthalmol Vis Sci*. (2006) 47:3044–51. doi: 10.1167/iovs.05-1141

30. Yozgat Z, Dogan M, Sabaner MC, Gobeka HH, Yazgan AS. Impacts of intravitreal anti-VEGF therapy on retinal anatomy and neurophysiology in diabetic macular edema. *Int Ophthalmol*. (2021) 41:1783–98. doi: 10.1007/s10792-021-01737-w

31. Ou WC, Brown DM, Payne JF, Wykoff CC. Relationship between visual acuity and retinal thickness during anti-vascular endothelial growth factor therapy for retinal diseases. *Am J Ophthalmol*. (2017) 180:8–17. doi: 10.1016/j.ajo.2017.05.014

32. Alonso-Plasencia M, Abreu-González R, Gómez-Culebras MA. Structure-function correlation using OCT angiography and Microperimetry in diabetic retinopathy. *Clin Ophthalmol*. (2019) 13:2181–8. doi: 10.2147/OPTH.S220877

frontiers | Frontiers in Ophthalmology

TYPE Methods
PUBLISHED 13 March 2025
DOI 10.3389/fopht.2025.1547363

OPEN ACCESS

EDITED BY
Georgios D. Panos,
Aristotle University of Thessaloniki, Greece

REVIEWED BY
Wen Wen,
Fudan University, China
Senmao Li,
University of Cologne, Germany
Hongfei Ye,
Xinhua Hospital Affiliated to Shanghai Jiaotong University School of Medicine, China
Yingxiang Huang,
Capital Medical University, China

*CORRESPONDENCE
Zhongcui Sun
zhongcui.sun@aliyun.com

†These authors have contributed equally to this work

RECEIVED 18 December 2024
ACCEPTED 25 February 2025
PUBLISHED 13 March 2025

CITATION
Gu R, Guo Y, Zong Y, Jiang R and Sun Z (2025) Levitation of posteriorly dislocated intraocular lens: I.V. catheter connected to the vitreotome aspiration.
Front. Ophthalmol. 5:1547363.
doi: 10.3389/fopht.2025.1547363

Levitation of posteriorly dislocated intraocular lens: I.V. catheter connected to the vitreotome aspiration

Ruiping Gu[1,2,3†], Yue Guo[1,2,3†], Yuan Zong[1,2,3], Rui Jiang[1,2,3] and Zhongcui Sun[1,2,3*]

[1]Department of Ophthalmology, Eye and ENT Hospital of Fudan University, Shanghai, China, [2]Key Laboratory of Myopia and Related Eye Diseases, National Health Commission (NHC), Shanghai, China, [3]Key Laboratory of Myopia and Related Eye Diseases, Chinese Academy of Medical Sciences, Shanghai, China

Background: To introduce a new, simple, and affordable technique that uses a 22G intravenous (I.V.) catheter connected to the vitreotome aspiration to lift the intraocular lens (IOLs) off the retina.

Methods: This retrospective, non-comparative, single surgeon, interventional, consecutive case series examined 4 patients (4 eyes) who underwent the surgical procedure from March 12 and October 22, 2023. Reliability, reproducibility, and intraoperative and postoperative complications of the technique were analyzed.

Results: Four patients presenting with posteriorly dislocated IOLs were included. After a complete 23G vitrectomy under wide-angle viewing system or high magnification contact lens, the 22G I.V. catheter was connected to the vitreotome aspiration and active aspiration was applied. When the IOLs were lifted towards the posterior chamber by continuous vacuum aspiration, they were be safely grasped using intraocular forceps and reposited with scleral fixation suturing or removed through a limbal incision. None of the IOLs fell during active aspiration.

Conclusion: Connection of I.V. catheter with vitreotome aspiration to lift the IOLs off the retina was a new, simple, safe, and affordable technique.

KEYWORDS

posteriorly dislocated intraocular lens, I.V. catheter, vitreotome aspiration, vitrectomy 23-gauge, intraocular forceps

Background

Dislocation of a posterior chamber intraocular lens IOL into the vitreous cavity is an uncommon but significant complication (1, 2). Various methods have been described to manage the dislocated IOL (3, 4). One critical step is lifting the IOL off the retina into the posterior chamber. Traditional techniques involve grasping the haptic and lift the IOL off

the retina using vitreous forceps (5). However, directly grasping the IOL with forceps can easily cause inadvertent retinal damage since the IOL frequently rests on the retinal surface or even in front of the macula. Perfluorocarbon liquid (PFCL) was used to safely float the IOL off the retina and into the position behind the pupil (5). Nevertheless, during the injection of PFCL, the IOL may float across the surface of the PFCL bubble and cause retinal damage. Santos and Roig-Melo and Agarwal et al. described the successful use of sleeve- and sleeveless extrusion cannula to levitate dislocated IOLs (6, 7).

In this study, we introduce a new, simple, and affordable technique that uses 22G (22-gauge) I.V. catheter connected to the vitreotome aspiration to lift the IOL off the retina.

Methods

This study was a retrospective noncomparative series of consecutive cases done at the Eye and Ear, Nose, and Throat (EENT) Hospital of Fudan University (Shanghai, China) between March 12 and October 22, 2023. The protocols and informed consent forms were approved by the institutional review board of the EENT hospital of Fudan University. Clinical records of patients with posteriorly dislocated IOLs were reviewed. All surgeries were performed by one surgeon (Zhongcui Sun). Informed consents were taken from all the patients. Subjects with less than 6 months of postoperative follow up were excluded.

All the participants underwent preoperative and postoperative ophthalmological examinations, including the best-corrected visual acuity (BCVA) test, dilated indirect slit-lamp biomicroscope examination, intraocular pressure (IOP) test using a non-contact tonometer (Nidek NT400, Nidek Co., Ltd., Aichi, Japan), corneal endothelial cell density count using a non-contact specular microscope (Topcon America Corporation, Paramus, NJ, USA), and axial length (AL) measurement using IOLMaster 700 (version 3.01; Carl Zeiss Meditec, Jena, Germany). Intraoperative conditions were recorded, including types of dislocated IOLs, fall of IOL during removement, or any other intraoperative complications. Postoperative examination focused on BCVA, IOP, and anterior and posterior segment findings, with particular attention to identifying any postoperative complications.

Surgery techniques

After a standard three-port pars plane complete vitrectomy, a 22G I.V. catheter was connected to the vitreotome aspiration and the vacuum was set to 300 mm Hg, with the cutting function turned off (Figures 1A, B). One of the trocar-cannulas (supertemporal or supranasal) was pulled out and the 22G catheter was directly inserted through the scleral tunnel (Figure 1C). Active aspiration was applied only when catheter tip was placed very close to the anterior surface of the IOL optical surface (Figure 1D). Vacuum was adjusted by the foot switch and titrated according to the ability to

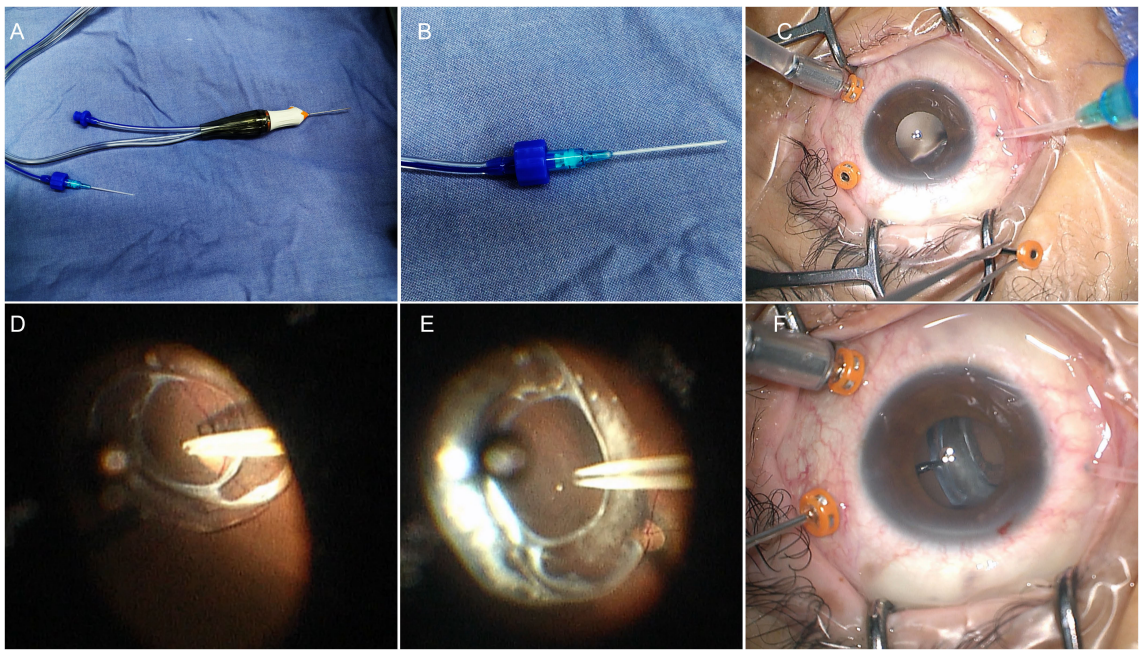

FIGURE 1
The 22-Gauge I.V. catheter connected to the vitreotome aspiration to lift the IOL off the retina. **(A)** The I.V. catheter connected to the vitreotome aspiration system. **(B)** Magnification of the connection. **(C)** Insert the catheter through the scleral tunnel directly. **(D)** The catheter tip was placed on the center of the anterior surface of the IOL optic. **(E)** Aspirate the IOL from the posterior retina. **(F)** Grasped the IOLs with the forceps in anterior segment.

TABLE 1 Demographics of eyes with 22G (22-gauge) I.V. catheter connected to the vitreotome aspiration levitation of dislocated posterior chamber IOL (vision in logMAR).

Patients	Age/ sex	Past medical history in IOL dislocated eye	Axial length (mm)	BCVA Preoperative (logMAR)	IOP Preoperative (mmHg)	Type of IOL levitated	IOL repositioning or IOL exchange	BCVA postoperative (logMAR)	IOP postoperative (mmHg)
1	58/F	In 2001, underwent scleral buckling surgery for RRD in the right eye. In 2005, experienced retinal re-detachment in the right eye, and underwent vitrectomy+ phacoemulsification and IOL implantation+ pneumatic retinopexy	22.86	1.30	14	3-piece foldable	Repositioning with sutureless intrascleral fixation	1	17.6mmHg
2	70/M	In 1983, underwent scleral buckling surgery for RRD in left eye In 2001, underwent phacoemulsification and IOL implantation in the left eye. In 2006, underwent vitrectomy with silicon oil tamponade and remove for retinal re-detachment.	26.95	0.70	15	Plate haptic	IOL exchange with sutured scleral fixation	0.7	18mmHg
3	60/F	In 2008, underwent phacoemulsification and IOL implantation in the left eye	25.41	0.22	16	1-piece foldable	Repositioning with sutured scleral fixation	0.22	20mmHg
4	70/M	In 2023, underwent vitrectomy+ phacoemulsification and IOL implantation for BRVO induced vitreous hemorrhage	23.1	0.52	15	1-piece foldable	Repositioning with sutured scleral fixation	0.1	14mmHg

BCVA, best corrected visual acuity; F, female; IOL, intraocular lens; IOP, intraocular pressure; M, male; RRD, rhegmatogenous retinal detachment; BRVO, branch retinal vein occlusion.

10.3389/fopht.2025.1547363

lift the IOL (Figure 1E). The IOL was then lifted towards the posterior chamber by continuous vacuum aspiration, grasped by intraocular forceps (Figure 1F) and reposited with scleral fixation suturing or removed through a limbal incision. The surgical video was submitted as Supplementary Material (Supplementary Video S1).

Results

The study included four eyes of four patients (two males and two females; mean age 64.5 ± 6.40 years; range 58-70 years). All patients had a history of one or more times of ocular surgeries and denied any history of ocular trauma. Patients' characteristics were summarized in Table 1. The average AL was 24.58 ± 1.95 mm, preoperative mean IOP was 15 ± 0.82 mmHg, and preoperative mean BCVA was 0.69 ± 0.46 (log MAR). Among the four dislocated IOLs, one was a plate-haptic IOL, two were one-piece foldable IOLs, and one was a three-piece foldable IOL. IOL exchange with sutured scleral fixation of a new IOL was performed in the patient with a plate-haptic IOL. Repositioning with scleral fixation suturing of the primary IOL was performed in the other three patients. A circular mark may appear on the surface of the foldable IOL during suction and soon disappeared, and the IOL returned to transparency (Figure 2). None of the IOLs fell during active aspiration. No intraoperative complication was observed during 6-month follow-up. The IOLs remained well-positioned in all four patients. The mean BCVA was 0.50 ± 0.42 (log MAR), and the mean IOP was 17.4 ± 2.50 mmHg.

Discussion

Dislocation of a posterior chamber intraocular lens (IOL) into the vitreous cavity is an uncommon but serious complication (1, 2). Numerous techniques for managing posteriorly dislocated IOLs have been described (3, 4). Intraocular forceps are often used to manipulate dislocated IOLs and are typically the standard treatment in vitreoretinal surgery (5). However, IOLs can be slippery and difficult to grasp, especially plate haptic IOLs. Accidental iatrogenic retinal damage during lifting an IOL from the retinal surface are not uncommon with this approach.

PFCL is used to protect the posterior retina from damage and to facilitate the anterior dislocation of luxated IOLs (8, 9). High density of PFCL allows for levitating the IOL into the pupillary plane. Low viscosity of PFCL facilitates easy aspiration and injection in a 23-gauge vitrectomy system. However, possible retained PFCL causes ocular toxicity, including uncontrolled intraocular pressure (IOP), corneal epithelial toxicity, and decreased retinal sensitivity.

Santos, Roig-Melo, and Agarwal et al. (6, 7) described the successful use of sleeve and sleeveless extrusion cannulas connected to the vitrectome vacuum to elevate dislocated IOLs. The vacuum created by the extrusion cannula is strong enough to hold the optic surface of an IOL. No pressure is exerted on the IOL while trying to create suction, and no passive suction flow to move the IOL is attempted. This prevents any uncontrolled movement of the IOL that could be detrimental to the retina. The linear control of the foot pedal allows for precise regulation of the vacuum during IOL levitation. Thus, lifting the IOL with vacuum aspiration appears to be safer than intraocular forceps and avoids the need for PFCL.

The extrusion cannula is primarily used for internal drainage of subretinal fluid in eyes with rhegmatogenous retinal detachments and for removing hemorrhage, gas, or silicone oil in the subretinal space (10). However, not all eye centers are supplied with the costly extrusion cannula, and not all extrusion cannulas can be connected to vitrectomy vacuum aspiration system. We introduce an easy, simple, and affordable technique that uses a 22G intravenous I.V. catheter connected to the vitreotome aspiration system. The 22G I.V. catheter, a common hospital supply, is easily accessible and inexpensive. The catheter is disposable and prevents iatrogenic infection. The catheter can connect to the vitreotome aspiration perfectly. Additionally, the 22G I.V. catheter can smoothly pass through a 23G scleral tunnel without further enlargement. If the

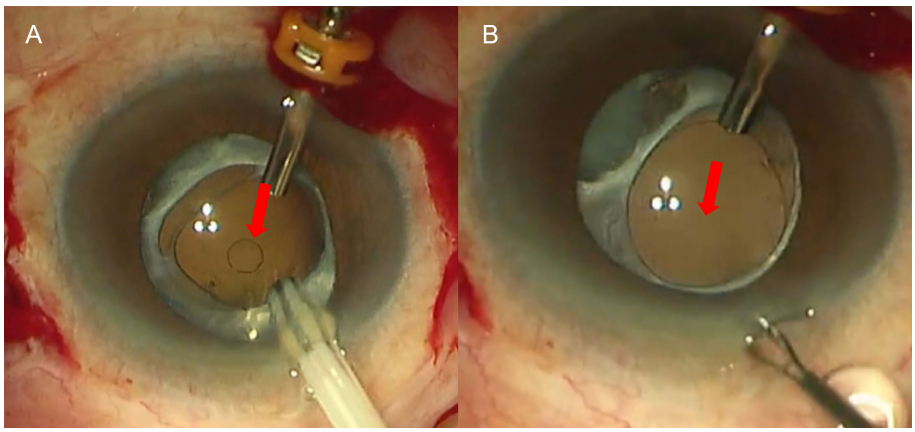

FIGURE 2
A circular mark on the surface of an IOL during suction and subsequent transparency restoration. **(A)** A circular mark appeared on the surface of the foldable IOL during suction; **(B)** it disappeared a few seconds later. Red arrow indicates the location of the circular mark.

catheter is inserted through a corneal limbal incision, the incision is small and self-sealing. The length of I.V. catheter is 31mm, long enough to reach the IOL above the posterior retina, regardless of the entrances through a limbal incision or a scleral incision. This technique was reproducible in all the cases and was effective for dislocation of any type of IOL especially the plate haptic IOLs which are difficult to grasp using intraocular forceps. In case of a foldable IOL, a circular mark will be left on the surface of the IOL during suction. The mark will soon disappear and the IOLs will return transparency. Although this surgical technique was controllable, the surgeon had to ensure that suction pressure was maintained throughout the entire suction process. This was especially crucial when grasping the IOL haptic with the left hand—any interruption in suction pressure could have caused the IOL to dislocate again, posing a risk of iatrogenic retinal injury. Additionally, since the core principle of this technique relied on suction pressure, a thorough vitrectomy had to be performed beforehand. If any vitreous was inadvertently aspirated during suction, it could have led to retinal tears or even retinal dialysis. Therefore, a comprehensive peripheral retinal examination needed to be conducted before concluding the surgery.

In conclusion, a 22G I.V. catheter connected to vitrectome aspiration can be an easy and affordable method for removal of dislocated IOLs.

Data availability statement

The original contributions presented in the study are included in the article/Supplementary Material. Further inquiries can be directed to the corresponding author.

Ethics statement

The studies involving humans were approved by the institutional review board of the EENT Hospital of Fudan University. The studies were conducted in accordance with the local legislation and institutional requirements. The participants provided their written informed consent to participate in this study. Written informed consent was obtained from the individual(s) for the publication of any potentially identifiable images or data included in this article.

Author contributions

RG: Writing – original draft, Writing – review & editing. YG: Writing – original draft, Writing – review & editing. YZ: Writing – original draft, Writing – review & editing. RJ: Writing – original draft, Writing – review & editing. ZS: Funding acquisition, Supervision, Validation, Visualization, Writing – original draft, Writing – review & editing.

Funding

The author(s) declare that no financial support was received for the research and/or publication of this article.

Conflict of interest

The authors declare that the research was conducted in the absence of any commercial or financial relationships that could be construed as a potential conflict of interest.

The reviewer WW declared a shared affiliation with the author(s) to the handling editor at the time of review.

Generative AI statement

The author(s) declare that no Generative AI was used in the creation of this manuscript.

Publisher's note

Supplementary material

The Supplementary Material for this article can be found online at: https://www.frontiersin.org/articles/10.3389/fopht.2025.1547363/full#supplementary-material

References

1. Ascaso FJ, Huerva V, Grzybowski A. Epidemiology, etiology, and prevention of late IOL-capsular bag complex dislocation: review of the literature. *J Ophthalmol.* (2015) 2015:805706. doi: 10.1155/2015/805706

2. Davis D, Brubaker J, Espandar L, Stringham J, Crandall A, Werner L, et al. Late in-the-bag spontaneous intraocular lens dislocation: evaluation of 86 consecutive cases. *Ophthalmology*. (2009) 116:664–70. doi: 10.1016/j.ophtha.2008.11.018

3. Yang CS, Chao YJ. Long-term outcome of combined vitrectomy and transscleral suture fixation of posterior chamber intraocular lenses in the management of posteriorly dislocated lenses. *J Chin Med Assoc.* (2016) 79:450–5. doi: 10.1016/j.jcma.2016.01.016

4. Sella S, Rubowitz A, Sheen-Ophir S, Ferencz JR, Assia EI, Ton Y. Pars plana vitrectomy for posteriorly dislocated intraocular lenses: risk factors and surgical approach. *Int Ophthalmol.* (2021) 41:221–9. doi: 10.1007/s10792-020-01570-7

5. Mello MJ, Scott IU, Smiddy WE, Flynn HW, Feuer W. Surgical management and outcomes of dislocated intraocular lenses. *Ophthalmology*. (2000) 107:62–7. doi: 10.1016/S0161-6420(99)00017-2

6. Santos A, Roig-Melo EA. Management of posteriorly dislocated introcular lens: a new technique. *Ophthalmic Surg Lasers*. (2001) 32:260–2. doi: 10.3928/1542-8877-20010501-18

7. Agarwal A, Narang P, Agarwal A, Kumar DA. Sleeveless-extrusion cannula for levitation of dislocated intraocular lens. *Brit J Ophthalmol*. (2014) 98:910–4. doi: 10.1136/bjophthalmol-2013-304700

8. Lewis H, Sanchez G. The use of perfluorocarbon liquids in the repositioning of posteriorly dislocated intraocular lenses. *Ophthalmology*. (1993) 100:1055–9. doi: 10.1016/S0161-6420(13)31541-3

9. Lee SJ, Kim IG, Park JM. Management of posteriorly dislocated crystalline lens with perfluorocarbon liquid and fibrin glue-assisted scleral-fixated intraocular lens implantation. *J Cataract Refr Surg*. (2013) 39:334–8. doi: 10.1016/j.jcrs.2013.01.022

10. Flynn HW, Lee WG, Parel JM. Design features and surgical use of a cannulated extrusion needle. *Graef Arch Clin Exp*. (1989) 227:304–8. doi: 10.1007/BF02169401

frontiers | Frontiers in Medicine

TYPE Original Research
PUBLISHED 19 March 2025
DOI 10.3389/fmed.2025.1557611

OPEN ACCESS

EDITED BY
Georgios D. Panos,
Aristotle University of Thessaloniki, Greece

REVIEWED BY
Lidawani Lambuk,
Universiti Sains Malaysia, Malaysia
Satish Rojekar,
Icahn School of Medicine at Mount Sinai, United States
Viliana Gugleva,
Medical University of Varna, Bulgaria
Velichka Andonova,
Medical University of Varna, Bulgaria
Binapani Mahaling,
Harvard Medical School, United States

*CORRESPONDENCE
Élodie Boisselier
✉ Elodie.Boisselier@fmed.ulaval.ca

RECEIVED 08 January 2025
ACCEPTED 03 March 2025
PUBLISHED 19 March 2025

CITATION
Raîche-Marcoux G, Méthot S, Tchatchouang A, Bettoli C, Maranda C, Loiseau A, Proulx S, Rochette PJ, Genin E and Boisselier É (2025) Localization of fluorescent gold nanoparticles throughout the eye after topical administration.
Front. Med. 12:1557611.
doi: 10.3389/fmed.2025.1557611

Localization of fluorescent gold nanoparticles throughout the eye after topical administration

Gabrielle Raîche-Marcoux[1], Sébastien Méthot[1], Ange Tchatchouang[1], Camille Bettoli[2], Cloé Maranda[1], Alexis Loiseau[1], Stéphanie Proulx[1], Patrick J. Rochette[1], Emilie Genin[2] and Élodie Boisselier[1]*

[1]CHU de Québec Research Center-Université Laval and Department of Ophthalmology and Otolaryngology-Head and Neck Surgery, Faculty of Medicine, Université Laval, Quebec City, QC, Canada, [2]Université de Bordeaux, CNRS, Bordeaux INP, ISM, UMR 5255, Talence, France

The human eye is a highly intricate sensory organ. When a condition requiring treatment occurs, eyedrops, which represent 90% of all ophthalmic treatments, are most frequently used. However, eyedrops are associated with low bioavailability, with less than 0.02% of therapeutic molecules reaching the anterior chamber. Thus, new delivery systems are required to ensure sufficient drug concentration over time at the target site. Gold nanoparticles are a promising avenue for drug delivery; however, they can be difficult to track in biological systems. Fluorescent gold nanoparticles, which have the same ultrastability and biocompatibility as their nonfluorescent counterpart, could act as an effective imaging tool to study their localization throughout the eye after administration. Thus, this study (1) synthesized and characterized fluorescent gold nanoparticles, (2) validated similar properties between nonfluorescent and fluorescent gold nanoparticles, and (3) determined their localization in the eye after topical application on *ex vivo* rabbit eyes. The fluorescent gold nanoparticles were synthesized, characterized, and identified in the cornea, iris, lens, and posterior segment of rabbit eyeballs, demonstrating tremendous potential for future drug delivery research.

KEYWORDS

gold nanoparticles, click chemistry, fluorescence imaging, ophthalmology, biodistribution

1 Introduction

The eye is one of the most complex and sophisticated sensory organs, and the anatomical structure and physiology of the eye are specifically adapted to allow the passage of light (1). Anatomically, the eye is divided into the anterior and posterior segments, which make up one-third and two-thirds of its total dimension, respectively (2).

The anterior segment encompasses the lacrimal apparatus, cornea, conjunctiva, anterior and posterior chambers, iris, ciliary bodies, lens, and aqueous humor (3). In addition, the anterior segment is very exposed to the environment; thus, it is prone to injuries. The corneal tissue features a complex anatomy that provides significant resistance against the entry of foreign substances and microbes, thereby safeguarding vision (4). Blinking, baseline and reflex tearing, and drainage mechanisms help eliminate harmful microbes, foreign particles, and substances, including drug molecules, from the surface of the eye quickly (5–8). The highly dynamic tear film, which has a renewal rate of 1–3 μL/min for an overall volume of 3–6 μL for a typical human eye, adds an additional layer of protection (9). In addition, the unique structure of the corneal tear film, with its lipid, aqueous, and

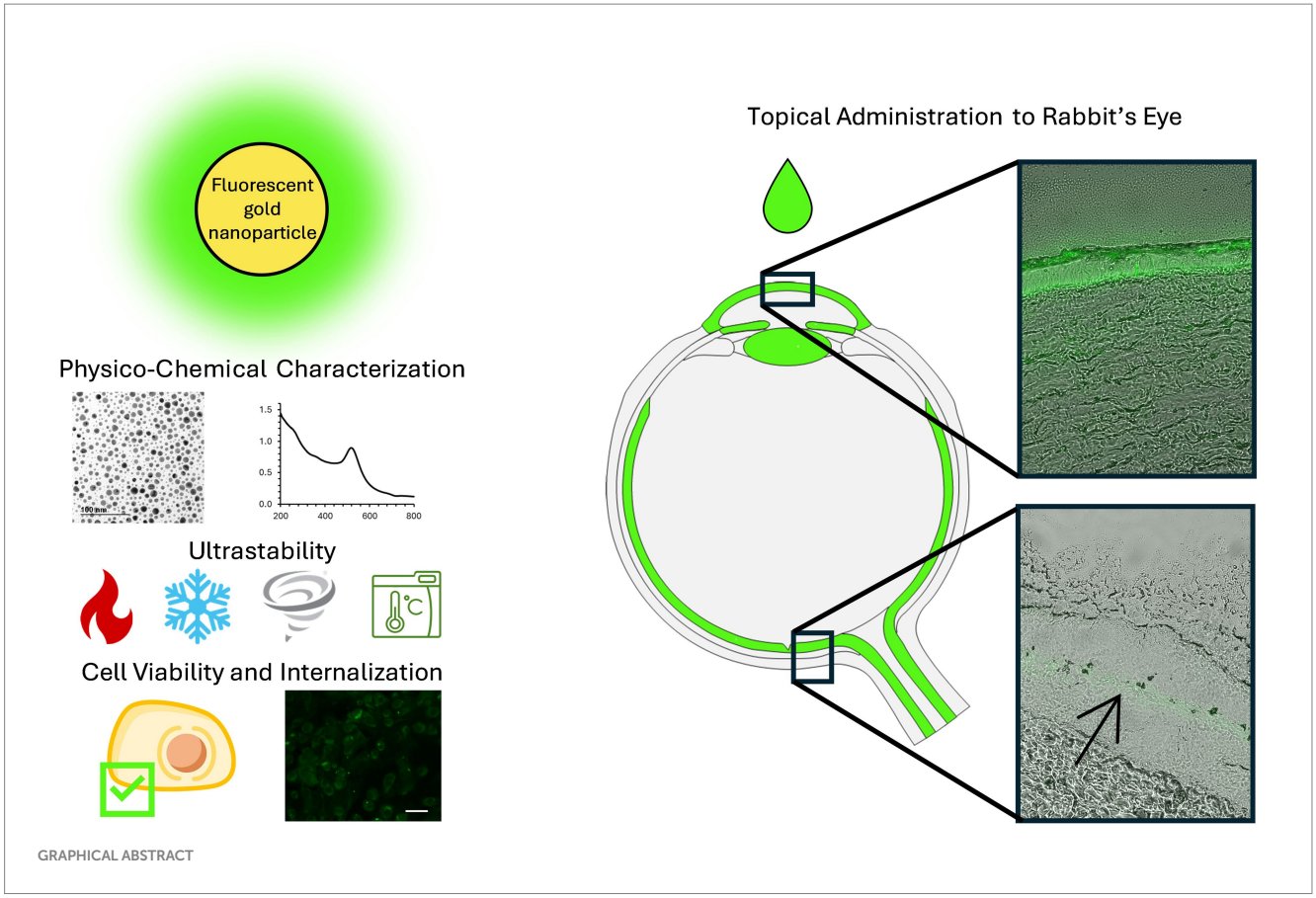

mucoid layers, impedes the rapid absorption of drug molecules by the corneal epithelial cells (10). Thus, considerable efforts have been directed toward enhancing the permeability and retention time of therapeutic substances on the ocular surface (11). Furthermore, creating drug formulations that require less frequent application will greatly improve patient compliance and overall quality of life (12).

The posterior segment, which includes the sclera, choroid, Bruch's membrane, retina, vitreous humor, and the optic nerve, is vascularized and not easily accessible for noninvasive therapies (13–15). Procedures to control neovascularization in the posterior segment of the eye include laser photocoagulation (16) and photodynamic therapy (17), and, prior to the development of antivascular endothelial growth factor (VEGF) therapy, these methods were the standard treatments to prevent further choroidal neovascularization (18, 19). Despite their success, these treatments have limited effects on overall vision, with reports of choroidal neovascularization recurrences and vision loss (20, 21). In addition, these treatments are not suitable for all patients due to varying individual conditions and disease progressions (22). Intravitreal injections of anti-VEGF agents, e.g., ranibizumab (23), bevacizumab (24), and aflibercept (25), are effective in terms of reversing retinal neovascularization. Intravitreal injections increase local drug concentrations in the vitreous chamber; however, they can be painful and require frequent clinic visits and administration by specialists (26). Complications from repeated intravitreal injections can include retinal detachment, hemorrhaging, retinal toxicity, corneal abrasion, temporary elevation of intraocular pressure, and endophthalmitis (27).

Ocular drug administration is crucial for treating common eye diseases, e.g., glaucoma (28), macular degeneration (29), diabetic retinopathy (30), infections (e.g., conjunctivitis, keratitis, and endophthalmitis) (31), and autoimmune disorders (e.g., Sjögren syndrome and uveitis) (32). Each route of ocular administration (topical, intracameral, intravitreal, or periocular) has its advantages and disadvantages. Indeed, intracameral injections bypass pre-corneal barriers, providing high bioavailability for various classes of active molecules. However, potential complications include the toxic effects of active molecules on corneal endothelial cells and toxic anterior segment syndrome (33). Periocular injections (retrobulbar, peribulbar, sub-Tenon, and subconjunctival) are considered less invasive and associated with fewer potential side effects compared to intravitreal injections. However, scleral barriers to the choroid, combined with elimination through blood and lymphatic flow in the subconjunctival space, lead to lower bioavailability in the retina (34). Eyedrops are the most widely used administration pathway, representing 90% of all ophthalmic treatments (35). Eyedrops are noninvasive and can be self-administered, thereby eliminating further doctor visits, which reduces healthcare system congestion. Eyedrops are applied directly to the desired tissue, and systemic administration of therapeutic agents targeting the eye requires high concentrations, which could lead to toxicity (36). The primary disadvantages of eyedrops are the low bioavailability and patient compliance, which reduces the activity of the active molecule (37). Thus, new ocular delivery systems must be developed to ensure that drugs reach the target site in sufficient concentrations over the prescribed period to achieve the desired therapeutic effect.

Drug delivery systems that utilize nanomaterials can play a pivotal role in targeting ocular tissues for treatment. Using such delivery systems offers several advantages, e.g., promoting drug absorption by enhancing their passage through barrier tissues, controlling their release through local administration, and targeting drug action on specific tissues (38, 39). In recent reviews on nanotechnology-based drug delivery systems in ophthalmology, works on biodistribution of micelles, liposomes, dendrimers, nanosuspensions, nanoemulsions and polymerics nanoparticles are mentioned but studies on gold nanoparticles (AuNPs) are often completely omitted (40–48). Among the reviews citing studies on AuNPs in ophthalmology (34, 49–58), the AuNPs are injected intravenously (59–61), intravitreally (62–65), in the subretinal space (66), administered orally (67), used solely *in vitro* (68–72), used on retinal explants (73), loaded onto contact lenses (74–76) or not used for drug-carrying purposes (77–80).

Mucoadhesion, which is the ability to adhere to mucosal tissues, is a leading strategy for topical administration of nanocarriers on the ocular surface (81), and a recent study demonstrated that AuNPs have mucoadhesive properties; thus, AuNPs are promising candidates for drug delivery systems in ophthalmology (82). In addition to their mucoadhesive properties, AuNPs have unique optical characteristics, e.g., surface plasmon resonance (83) that are beneficial for various biomedical applications (84–89). The polyethylene glycol (PEG) modified AuNPs (AuNPs-PEG_{2000}) developed in our laboratory are ultrastable (90) and mucoadhesive; thus, they are highly relevant candidates for drug delivery in ophthalmology (91).

To optimize the potential of these patented AuNPs-PEG_{2000} (CA3043775) as drug delivery systems, experiments were conducted to better understand their drug loading and drug release properties (92). The next step was an investigation into their behavior and distribution in the eye after topical application. However, they are currently difficult to track with currently available technologies without damaging the biological tissues; thus, we sought to modify them to emit fluorescence without impacting their other properties. This would allow the new fluorescent AuNPs-PEG_{2000}-Nap to act as an imaging tool in place of the nonfluorescent AuNPs-PEG_{2000}. Therefore, the goal of this study was to (1) synthesize and characterize the fluorescent AuNPs-PEG_{2000}-Nap, (2) validate similar properties between the nonfluorescent and fluorescent AuNPs-PEG_{2000} and AuNPs-PEG_{2000}-Nap, and (3) determine their localization in the eye after topical application using *ex vivo* rabbit eyes. The results of this study are expected to facilitate better understanding of the behavior of the AuNPs-PEG_{2000} in physiological conditions and their potential as drug delivery systems in ophthalmology.

2 Materials and methods

2.1 Materials

Gold chloride trihydrate ($HAuCl_4 \bullet 3H_2O$), sodium borohydride ($NaBH_4$), chlorohydric acid (HCl), nitric acid (HNO_3), sodium chloride (NaCl), potassium chloride (KCl), sodium phosphate dibasic (Na_2HPO_4), potassium phosphate monobasic (KH_2PO_4), basic fuchsine (pararosaniline hydrochloride), sodium metabisulfite, isopropanol, and acetonitrile were all purchased from VWR International (Ville Mont-Royal, QC, Canada). Anhydrous copper(II) sulfate ($CuSO_4$), ascorbic acid, 4-bromo-1,8-naphthalimide anhydride, 2-methoxyethylamine, sodium azide, absolute ethanol, petroleum ether, and ethyl acetate were purchased from Sigma-Aldrich (St. Louis, MO, United States). Polyethylene glycol methyl ether thiol with a molecular weight of 2000 g/ mol (referred to as HS-PEG_{2000}) was purchased from Laysan Bio (Arab, AL, United States). Polyethylene glycol alkyne thiol (referred to as HS-PEG_{2000}-ALK) was purchased from Biopharma PEG (Watertown, MA, United States). All glassware used to synthesize the AuNPs was washed thoroughly with aqua regia (3:1 HCl:HNO_3) and rinsed with nanopure water prior to experimentation. Mucins from the bovine submaxillary gland were purchased from Cedarlane Laboratories (Burlington, ON, Canada). 3-(4,5-dimethylthiazol-2-yl)-5-(3-carboxymethoxyphenyl)-2-(4-sulfophenyl)-2H-tetrazolium (MTS) was obtained from Promega (Madison, WI, United States). Research-grade human eyes were provided by the "Ocular tissue for vision research" infrastructure of the Vision Sciences Research Network, in collaboration with our local eye bank (Banque d'Yeux du Center Universitaire d'Ophtalmologie, Québec, QC, Canada) and Héma-Québec (Québec, QC, Canada) with next of kin consent. This study followed the Declaration of Helsinki and was approved by the CHU de Québec-Université Laval ethics committee (DR-002-955). Eight healthy corneas (age 55–66 years; median 61.5; SD ± 4.6) were used for the characterization of the fluorescence emission, and three (aged 44, 52, and 71 years) were used for hCEC cell isolation and culture, as reported previously (93, 94). Irradiated human fibroblasts (iHFL) were isolated from the foreskin of a 10-day-old donor (95, 96). The OCT compound was obtained from Sakura Finetek (Torrance, CA, United States). Albino rabbit heads ($N = 6$) were obtained from the Rolland Pouliot & Fils slaughterhouse (Saint-Henri-de-Lévis, QC, Canada).

2.2 Synthesis and characterization of 4-azido-N-(2-methoxyethyl)-1,8-naphthalimide

Here, 2-methoxyethylamine (2.59 mL, 29.9 mmol, 2.07 eq) was added to a solution of 4-bromo-1,8-naphthalimide anhydride (4 g, 14.4 mmol, 1 eq) in 50 mL of absolute ethanol. The mixture was refluxed overnight under stirring and then cooled to 0°C by immersing the flask in an ice bath. The solid was collected by filtration to obtain the key intermediate 4-bromo-N-(2-methoxyethyl)-1,8-naphthalimide (4,67 g, 97% yield).

^{1}H NMR (300 MHz, $CDCl_3$) δ: 8.66 (d, J = 7.3 Hz, 1H, ArH), 8.55 (d, J = 9.0 Hz, 1H, ArH), 8.41 (d, J = 7.8 Hz, 1H, ArH), 8.03 (d, J = 7.8 Hz, 1H, ArH), 7.84 (t, J = 7.6 Hz, 1H, ArH), 4.43 (t, J = 5.8 Hz, 2H, CH_2), 3.73 (t, J = 5.8 Hz, 2H, CH_2), 3.37 (s, 3H, CH_3).

Then, NaN_3 (775 mg, 11.9 mmol, 1.5 eq) was slowly added to a solution of the key intermediate (3 g, 7.95 mmol, 1 eq) in 114 mL of dimethylformamide. The mixture was heated at 70°C under stirring for 2 h. The solvent was removed under reduced pressure. The residue was purified by chromatography on silica gel (petroleum ether/ethyl acetate: gradient from 8:2 to 5:5). 4-azido-N-(2-methoxyethyl)-1,8-naphthalimide was obtained as a pale yellow solid (2.11 g, 84% yield).

^{1}H NMR (300 MHz, $CDCl_3$) δ: 8.65 (d, J = 7.3 Hz, 1H, ArH), 8.59 (d, J = 7.9 Hz, 1H, ArH), 8.44 (d, J = 8.5 Hz, 1H, ArH), 7.74 (t, J = 7.9 Hz, 1H, ArH), 7.47 (d, J = 7.9 Hz, 1H, ArH), 4.44 (t, J = 5.9 Hz, 2H, CH_2), 3.73 (t, J = 5.9 Hz, 2H, CH_2), 3.38 (s, 3H, CH_3).

The results of the NMR analysis are in agreement with the published values for 4-bromo-N-(2-methoxyethyl)-1,8-naphthalimide and 4-azido-N-(2-methoxyethyl)-1,8-naphthalimide (97). They were recorded using a spectrometer Avance 300 MHz (Bruker). The obtained ^{1}H NMR spectra are provided as Supplementary Material (Supplementary Figures 1, 2).

2.3 Synthesis of HS-PEG$_{2000}$-nap

In a 25-mL Erlenmeyer flask, 0.02 g of HS-PEG$_{2000}$-ALK (0.005 mmol) was dissolved in 15 mL of acetonitrile. The 4-azido-N-(2-methoxyethyl)-1,8-naphthalimide, 0.0148 g (0.050 mmol) was added to the mixture. Copper sulfate (0.00160 g; 0.005 mmol) and ascorbic acid (0.00176 g; 0.005 mmol) were then added to the Erlenmeyer flask. The mixture was kept at 22°C and shaken using an orbital shaker at 250 rpm overnight in darkness.

2.4 Synthesis of AuNPs-PEG$_{2000}$-nap 1%

Stirring at 400 rpm, 250 µL of an aqueous solution of 0.1 g/mL of gold chloride trihydrate (0.06 mmol) was added to 15 mL of a 1:1 acetonitrile:isopropanol mix. 0.0099 g of a HS-PEG$_{2000}$ and 750 µL of HS-PEG$_{2000}$-Nap solution obtained previously were added to 30 mL of isopropanol prior to addition to the gold solution. The resulting solution was mixed for 1 h at 400 rpm. While increasing the mixing speed to 700 rpm, a fresh solution of 0.028 g of NaBH4 (0.74 mmol) in 10 mL of ice-cold water was added dropwise to the gold solution using a peristaltic pump (1 mL/min). The mixture was then stirred at 400 rpm for 3 h to allow the nanoparticles to grow and stabilize in the dark. The solution was evaporated using a rotary evaporator under reduced pressure. Then, 10 mL of water was added to resuspend the nanoparticles. The purification of the nanoparticles performed by dialysis (molecular weight cutoff: 16,000 g/mol) for 7 days, changing the dialysate at least four times per day. After 7 days, the AuNPs-PEG$_{2000}$-Nap 1% were transferred to a polycarbonate centrifuge tube (#355631) and centrifuged with a 70 Ti rotor using the Optima L-90 K Ultracentrifuge from Beckman Coulter Inc. (Indianapolis, IN, United States) at 220,000 g for 18 h. Then, the supernatant was removed and replaced with ultrapure water. The AuNPs-PEG$_{2000}$-Nap 1% were resuspended and moved back to a new dialysis bag with the same molecular weight cutoff for seven supplementary days (dialysates changed four times per day). The AuNPs-PEG$_{2000}$-Nap 1% were then centrifugated again, and the supernatant was changed with ultrapure water. To determine the concentration of the AuNPs in the resultant solution, a known volume of the solution was freeze-dried and weighed ($n = 3$).

2.5 Synthesis of AuNPs-PEG$_{2000}$-nap 100%

To obtain AuNPs-PEG$_{2000}$-Nap 100%, 250 µL of an aqueous solution of 0.1 g/mL of gold chloride trihydrate (0.06 mmol) was added to 7.5 mL of the previously synthesized HS-PEG$_{2000}$-Nap and 7.5 mL of isopropanol. All the following steps remain the same as those for the AuNPs-PEG$_{2000}$-Nap 1%.

2.6 Characterization of AuNPs-PEG$_{2000}$-nap

2.6.1 UV–visible spectroscopy

Here, a quartz cuvette (pathlength: 1 mm × 10 mm) from Hellma (#104.002-QS) was used (Markham, ON, Canada). The UV–visible spectra were collected from 200 to 800 nm using a Cary Eclipse 50 Bio UV–vis spectrophotometer from Varian (Winnipeg, MB, Canada).

2.6.2 First derivative of plasmon band spectra

The UV–visible spectra were normalized using the intensity of the peak of the plasmon band of AuNPs-PEG$_{2000}$-Nap 1% ($\lambda = 517.5$ nm) and AuNPs-PEG$_{2000}$-Nap 100% ($\lambda = 519.0$ nm). Then, the data between 430 nm and 630 nm were derived for AuNPs-PEG$_{2000}$-Nap 1% and AuNPs-PEG$_{2000}$-Nap 100%. Here, the inflection point of the derivative was used to determine the position of the plasmon band peak (98–100).

2.6.3 Fluorescence spectroscopy

The fluorescence spectra of the AuNPs-PEG$_{2000}$-Nap 1 and 100% samples were obtained using a Fluorolog-3 instrument (Horiba). A 5 × 5 mm light path quartz cuvette from Hellma Analytics was used (#111.057-QS). The excitation wavelength exhibited optimal results at 420 nm; thus, the scans for emission were recorded from 490 to 600 nm.

2.6.4 Transmission electron microscopy

Copper grids covered with a vaporized carbon film were purchased from Ted Pella (California, United States). AuNPs-PEG$_{2000}$-Nap 1 and 100% were diluted to a concentration of approximately 0.01 mg/mL, and a 5-µL droplet was deposited on each grid and left to dry overnight. Image acquisition was performed using a JEM 1230 from JEOL Ltd. (Tokyo, Japan). Here, the voltage was set to 80 kV, and a 50,000× zoom factor was used. To characterize the size of the gold core, at least 3,000 AuNPs-PEG$_{2000}$-Nap 1% and AuNPs-PEG$_{2000}$-Nap 100% were counted and analyzed for each sample using the ImageJ software.

2.6.5 Dynamic light scattering

DLS measurements were performed using the NanoBrook Omni particle analyzer from Brookhaven Instruments Corporation (Holtsville, NY, United States). Each AuNPs-PEG$_{2000}$-Nap was diluted to a concentration of 0.033 mg/ mL in PBS (1X). Prior to analysis, the samples were filtered through a 0.2-µm pore size filter. The apparatus was set to an angle of 173° at 25°C. After an equilibrium time of 2 min, 10 measurements of 120 s were performed for each sample. BI-SCP disposable plastic cuvettes from Brookhaven Instruments Corporation (Holtsville, NY, United States) were used for the analysis. The treatment of the size distribution was performed using the CONTIN algorithm.

2.6.6 Elemental analysis

Elemental analysis was performed using an ICP-OES, which requires the oxidation of gold prior to analysis. Here, AuNPs-PEG$_{2000}$-Nap 1 and 100% were diluted to a 1:9.5 aqua regia to water ratio and a final AuNP concentration of 0.20 mg/mL. Blank standards containing 5% aqua regia were also analyzed to confirm the absence of contamination specific to the method. The sample preparation was performed in 15-mL tubes from Sarstedt (#62.554.100) (Montreal, QC, Canada). The tubes were heated to 90°C, with care being taken to avoid boiling. The tube caps were left on the tubes and closed by a quarter of a turn. The apparatus used in the experiments was the ICP-OES-5110 (Agilent) in radial mode (Mississauga, ON, Canada).

The calibration methods of the yttrium internal standard and standard addition were performed to prevent matrix effects. Acquisition was achieved at 242.8 nm and 181.9 nm for gold and sulfur quantification, respectively.

2.6.7 Molecular weight approximation

The molecular weight (MW) of the AuNPs was determined approximatively following a previously published method (101). Briefly, while assuming monodisperse spherical AuNPs, the volume (V) of the gold core can be estimated as follows.

$$V = \frac{4\pi \times \left(\text{radius in } \mathring{A} \right)^3}{3}$$

The number of gold atoms found in the metallic core, n(Au), can be estimated as follows.

$$n(Au) = \frac{V \text{ in } \mathring{A}^3}{17\ \mathring{A}^3}$$

With the MW of the Au and S, the number of thiol groups n(S) on the surface can be estimated as follows.

$$\frac{n(Au) \times MW(Au)}{\%\text{Au atoms}} = \frac{n(S) \times MW(S)}{\%\text{S atoms}}$$

Finally, the MW of AuNPs-Nap 1 and 100% can be estimated using the following equation.

$$MW(\text{AuNPs} - \text{PEG}_{2000} - \text{Nap}\,1\%) = \left[n(Au) \times MW(Au) \right] + 0.01\left[n(S) \times \left(MW(\text{PEG} - \text{Nap}) \right) \right] + 0.99\left[n(S) \times MW(\text{PEG}) \right]$$

$$MW(\text{AuNPs} - \text{PEG}_{2000} - \text{Nap}\,100\%) = \left[n(Au) \times MW(Au) \right] + 0.01\left[n(S) \times \left(MW(\text{PEG} - \text{Nap}) \right) \right]$$

2.6.8 Graft density approximation

The graft density ρ_g was determined using the calculated number of ligands n(S) used in the approximation of the MW. The surface of the metallic core A, assuming monodisperse spherical nanoparticles, can be calculated as follows.

$$A = 4\pi \times \left(\text{radius in nm} \right)^2$$

Thus, the graft density can be evaluated as follows.

$$\rho_g = \frac{n(S)}{A}$$

2.7 Biolocalization in human corneas

The human corneas were rinsed with PBS to remove the storing liquid and placed on a small support (epithelium side up). A punched out 6-mm diameter rubber stencil was centered on the cornea to ensure that the deposited drop remained on the cornea and did not flow over and to the side after application. A drop (50 µL, 1 mg/mL) of AuNPs-PEG_{2000}, AuNPs-PEG_{2000}-Nap 1%, and AuNPs-PEG_{2000}-Nap 100% were placed on top of the corneas. Then, the corneas were placed in the dark for 2 h before being prepared for tissue imaging.

2.8 Ultrastability assays

The protocol used to qualify the ultrastability properties strictly followed the previously established protocol (90).

2.9 Quantification of mucoadhesion

The protocol used to quantify the adsorbed mucins on the surface of the AuNPs strictly followed a previously published PAS coloration protocol (101).

2.10 MTS assays

MTS viability assay was performed according to the manufacturer's instructions (Promega, Madison, WI). Briefly, hCECs (1×10^4) in corneal epithelium medium [Dulbecco–Vogt modification of Eagle's medium (Gibco, Waltham, MA, United States) with Ham's F12 (3:1) (Life Technologies, Carlsbad, CA, United States), supplemented with 5% FetalClone II serum (HyClone, Logan, UT, United States), 5 µg/mL insulin (SAFC Bioscience, Lenexa, KS, United States), 0.4 µg/mL hydrocortisone (Teva, Toronto, ON, Canada), 10 ng/ mL epidermal growth factor (R&D Systems, Oakville, ON, Canada), 10^{-10} mol/ L cholera toxin (Sigma-Aldrich, St. Louis, MO, USA), 100 µg/mL Penicillin (Fresenius Kabi, Homburg, Germany), and 25 µg/mL Gentamycin (Galenova, Saint-Hyacinthe, QC, Canada)] and incubated at 37°C for 4 h prior to the addition of AuNPs (AuNPs-PEG_{2000} and AuNPs-PEG_{2000}-Nap 1%, at concentrations of 0, 0.001, 0.1, 0.25, 0.50, 0.75 and 1.00 µM). After 18 h, MTS (2 mg/mL) was added to each well, and the plates were incubated at 37°C for 1 h. Then, the optical density (OD) was measured using a microplate reader (Biorad Model 550, Mississauga, ON, Canada) at a wavelength of 490 nm. OD of the blank solution (AuNPs, no cells) was subtracted, and results presented relative to the control (0 µM AuNPs, which represents 100% viability). Experiments were performed using 3 different cell populations, in triplicate.

2.11 Internalization assays

hCECs (0.3×10^6 cells) were plated directly in six-well plates (9.6 cm^2) in the corneal epithelium medium described above. Before the cells reached confluence, AuNPs-PEG_{2000} and AuNPs-PEG_{2000}-Nap 1% (500 µL, 1 mg/mL, diluted with PBS) were added. After a waiting time of 30 min, the cells were rinsed with PBS before

image acquisition was performed using an Axio Imager Z2 Upright Microscope (Carl Zeiss, North York, ON, Canada).

2.12 Biolocalization with rabbit eyes

The rabbit eyeballs were removed from the skull and placed on a small support (cornea side up). A 20-mm diameter rubber gasket well was centered on the cornea to ensure that the deposited drop remained on the cornea and did not flow onto the globe after application. A drop (50 µL, 1 mg/mL) of AuNPs-PEG_{2000}-Nap 1% was placed in the middle of the stencil. Here, two waiting times were tested, i.e., 2 h [to maximize the interactions mucins-AuNPs, as previously demonstrated (101)] and 3 min (n = 3 eyes per condition). For the 2-h waiting time, the eyeballs were placed in the dark before the drop was applied. After 2 h, the globes were prepared for imaging. For the 3-min waiting time, which mimics the renewal rate of the tear film (9), the eyeballs were washed thoroughly with PBS to ensure that no AuNPs-PEG_{2000}-Nap 1% remained on the ocular surface. The eyeballs were then placed in the dark for 2 h for comparison with the first waiting time before tissue preparation for imaging. The controls (n = 3 eyes) received a drop of PBS and were placed in the dark for 2 h prior to tissue preparation.

2.13 Tissue preparation for imaging

The dissections were performed to separate the corneas, irises, lenses, and posterior segment of the eyes, and to avoid all cross-contamination. The centers of all corneas were cut using a 6-mm biopsy punch before being placed (endothelium down) in an OCT compound from Sakura Finetek (Torrance, CA, United States). The cut samples were then stored at 80°C at least overnight before making cuts using a cryostat microtome (Leica, Concord, Canada). The irises were placed flat with the posterior epithelium down in the OCT compound, and the lens was placed with the epithelium side up. A portion of the posterior segment was removed using a 10-mm biopsy punch to facilitate manipulation. The punched sample was put in the OCT compound. All samples were stored at 80°C at least overnight before making microtome cryostat cuts. Prior to being placed on microscope slides, the samples of the corneas (human and rabbit), iris, and posterior segments were sliced (thickness: 8 µm), and the lens samples were prepared with a thickness of 16 µm. Upon microscopic examination, samples without AuNPs were used to determine the exposure time that prevented the background signal and endogenous fluorescence in the sample.

3 Results and discussion

The development of effective delivery systems relies heavily on optimizing formulation and process parameters and thoroughly characterizing the physicochemical and biological properties of nanocarriers. In ocular drug delivery, key factors to assess include particle size and distribution, surface charges, encapsulation efficiency, drug loading capacity, drug release profiles, uptake mechanisms, stability, and safety or toxicity (102). Additionally, the delivery system must meet specific ocular requirements such as sterility, osmolality, pH, surface tension, and viscosity to ensure compatibility and efficacy. Important properties, like particle size and polydispersity index, are critical for the physical stability of nanocarriers. For ocular formulations, particles larger than 10 µm are generally unsuitable (103). Smaller, monodisperse particles are preferred for their enhanced stability, biodistribution (104), and reduced risks of instability issues like sedimentation during storage (105). Their small size facilitates faster penetration into the tear film's mucin layer, reduces irritation, and enhances uptake by corneal epithelial cells (106). While smaller nanoparticles show greater absorption into the aqueous humor, they are cleared more quickly from tear fluid (107). The shape and surface morphology of nanoparticles also influence their biodistribution, cellular uptake, and toxicity. Spherical nanoparticles are generally more effective in enhancing drug performance compared to other shapes like cubes or rods (108). Surface modifications are also important factors for biodistribution: different polymeric nanoparticles, and even different polymeric shells will have different biodistribution profiles in the anterior and posterior segment (109, 110).

To investigate the localization of nonfluorescent AuNPs after eyedrop application, a strategy was required to determine their trajectory accurately. As previously synthesized, the gold core combined into the PEGylated ligands created a furtive drug delivery system (111, 112); thus, the goal was to minimally modify the AuNPs-PEG2000, that are small, spherical, stable and biocompatible, to generate an imaging tool that would be visible in microscopy and replicate the nonfluorescent AuNPs-PEG2000 behavior. Here, fluorescence microscopy was selected for its sensitivity (113), its compatibility with animal and human tissues (114), and the minimal modification required to the AuNPs-PEG2000 to make them fluorescent (115, 116). Once the characteristics of the AuNPs-PEG2000 and fluorescent AuNPs-PEG2000-Nap were determined to be equivalent, internalization assays were conducted prior to performing biolocalization experiments.

3.1 Synthesis and physicochemical characterization of fluorescent AuNPs

3.1.1 Synthesis of fluorescent AuNPs-PEG_{2000}-nap

To obtain AuNPs-PEG_{2000}-Nap, the first step involved synthesizing the fluorescent ligand (HS-PEG_{2000}-Nap; Scheme 1). Here, a heterobifunctional PEGylated ligand (HS-PEG_{2000}-ALK), with an alkyne functional group on one end (dedicated to the click reaction) and a thiol group (-SH) on the other, was employed to covalently bond the naphthalimide (Nap) fluorophore and coordinate with the Au atoms of the core (through the thiol group). The click reaction (117) was performed with stoichiometric equivalents of reagents, and the azido-naphthalimide equivalent was 10 times the molar equivalent of the ligand. The advantage of this molecule lies in its difference in fluorescence emission before and after the click reaction (118). In fact, prior to the click reaction, the azido-naphthalimide was very weakly fluorescent, whereas it became a strong fluorophore after the formation of the triazole heterocycle.

Here, the synthesis process was a modified version of the Brust–Schiffrin synthesis (119) based on specific experimental conditions leading to small ultrastable AuNPs (90). Two types of AuNPs-PEG_{2000}-Nap were obtained with this synthesis, i.e., AuNPs-PEG_{2000}-Nap 1% and AuNPs-PEG_{2000}-Nap 100%, where 1 and 100% of the ligands used for the synthesis were the HS-PEG_{2000}-Nap,

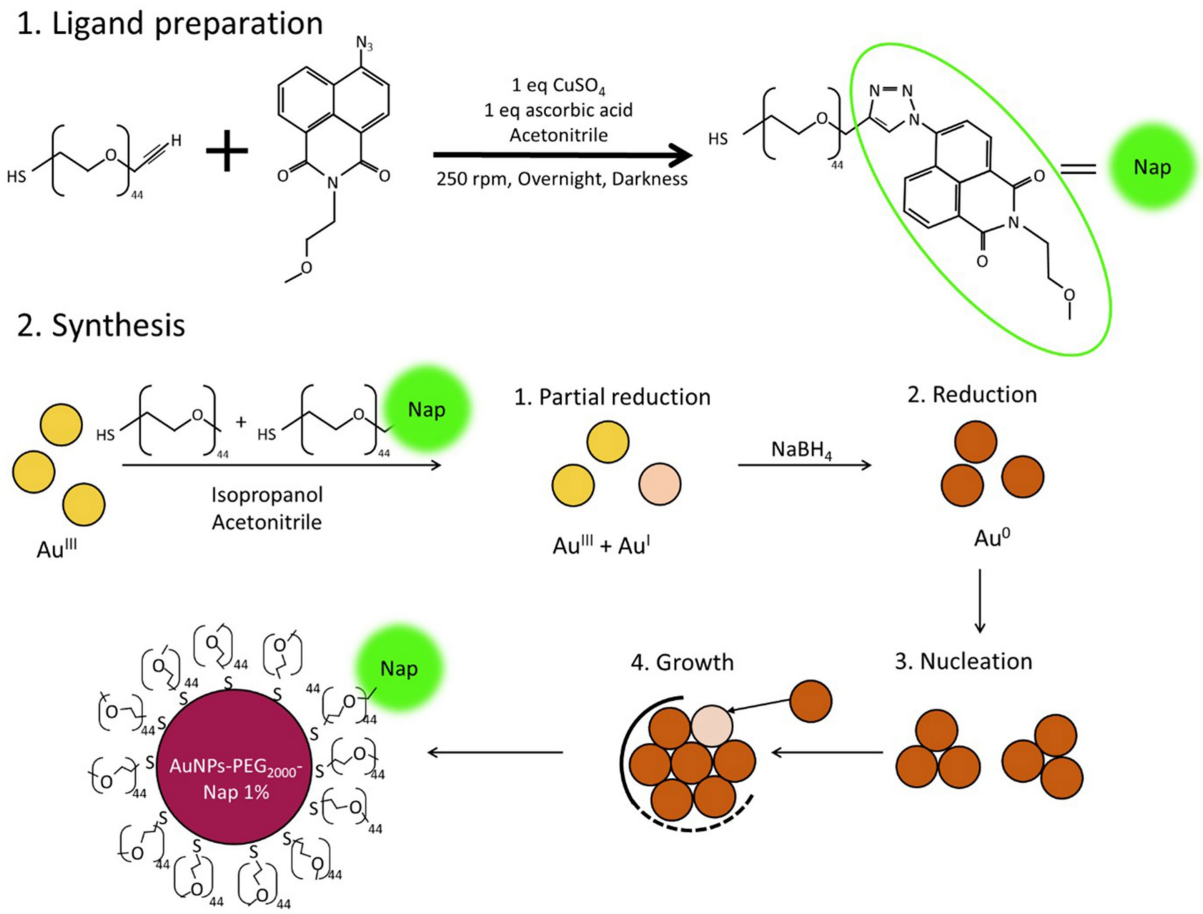

SCHEME 1
AuNPs-Nap synthesis. The proportion between the HS-PEG_{2000}-Nap and HS-PEG_{2000} varies from 1 to 100%. For the experimental details, refer to the description in the Materials and Methods.

respectively. For the AuNPs-PEG_{2000}-Nap 1%, the remaining 99% of the ligands were monofunctional HS-PEG_{2000} (90). Once the fluorescent HS-PEG_{2000}-Nap was obtained, it was added in different proportions in the synthesis of the AuNPs. Mixing the PEGylated ligands with chloroauric aid ($HAuCl_4$) caused a partial reduction of the Au atoms. Note that the success of this synthesis is dependent on the balance between the crystal growth and the ligand capping speeds, i.e., if the crystal growth outpaces the ligand capping speed, the particles will not stabilize properly and will precipitate. In addition, acetonitrile in the reaction mixture slows the crystal growth because its nitrogen atoms partially stabilize the Au core growth. Furthermore, $NaBH_4$ exhibits lower reducing strength in acetonitrile compared to water, which further slows the crystal growth. This slower growth allows for better capping and results in more stable AuNPs (120).

Prior to characterization, the synthesis was purified via dialysis and precipitation by ultracentrifugation to further change the dialysate (refer to the Materials and Methods).

3.1.2 Physicochemical characterization of AuNPs-PEG_{2000}-nap 1 and 100%

The UV–visible spectra showed that the surface plasmon resonance absorbance peaks for AuNPs-PEG_{2000}-Nap 1% and AuNPs-PEG_{2000}-Nap 100% are centered at 517.5 nm and 519.0 nm, respectively (Table 1). In addition, the elemental analysis via ICP-OES revealed varying weight percentages of gold and sulfur in the AuNPs. Here, AuNPs-PEG_{2000}-Nap 1% contained 48.5% gold and 0.41% sulfur, and AuNPs-PEG_{2000}-Nap 100% contained 62.5% gold and 0.67% sulfur (Table 1). The TEM observations showed that the gold core diameters were 6.0 ± 3.0 nm and 4.8 ± 2.4 nm for the AuNPs-PEG_{2000}-Nap 1% and AuNPs-PEG_{2000}-Nap 100%, respectively (Table 1). Based on the metallic core diameters and elemental compositions, the molecular weights were calculated to be 2,002, 334 g/mol for AuNPs-PEG_{2000}-Nap 1% and 1,185,970 g/mol for AuNPs-PEG_{2000}-Nap 100% (Table 1). DLS measurements showed hydrodynamic diameters of 29 ± 1 nm for AuNPs-PEG_{2000}-Nap 1% and 34.0 ± 0.6 nm for AuNPs-PEG_{2000}-Nap 100% (Table 1). In addition, the graft density for AuNPs-PEG_{2000}-Nap 1% was 3.05 ligands per nm^2 of gold core, and that for the AuNPs-PEG_{2000}-Nap 100% was 3.10 ligands per nm^2 of gold core (Table 1).

The core diameter and number of ligands were the highest for AuNPs-PEG_{2000}-Nap 1%, and the percentage of sulfur atoms was the lowest, which can be attributed to the varying behavior of the AuNPs based on their molecular weights, especially during the stabilization of the gold core. In water, PEG alone can adopt Gaussian coil or flat plate configurations (121), and it stabilizes molecules or proteins with

10.3389/fmed.2025.1557611

TABLE 1 Characterization of AuNPs-PEG$_{2000}$-Nap 1% and AuNPs-PEG$_{2000}$-Nap 100%.

	AuNPs-PEG$_{2000}$-Nap 1%	AuNPs-PEG$_{2000}$-Nap 100%
Position of plasmon band peak (nm)[a]	517.5	519.0
% Au atoms[b]	48.5	62.5
% S atoms[b]	0.41	0.67
Core diameter (nm)[c]	6.0 ± 3.0	4.8 ± 2.4
Hydrodynamic diameter (nm)[d]	29 ± 1	34.0 ± 0.6
Number of ligands[e]	345	224
Molecular weight (g/mol)[f]	2,002,334	1,185,970
Graft density (number of ligand/nm^2)[f]	3.05	3.10

[a]The position of the plasmon band peak was obtained using ultraviolet (UV)-visible spectroscopy.
[b]% Au and S atoms were determined by elemental analysis using inductively coupled plasma optical emission spectroscopy (ICP-OES).
[c]The core diameters were determined by transmission electron microscopy (TEM).
[d]The hydrodynamic diameters were determined by dynamic light scattering (DLS).
[e]The number of ligands was calculated per AuNPs-PEG$_{2000}$-Nap.
[f]The molecular weights and graft density were calculated theoretically. Experimental and calculation details are described in the Materials and Methods Section.

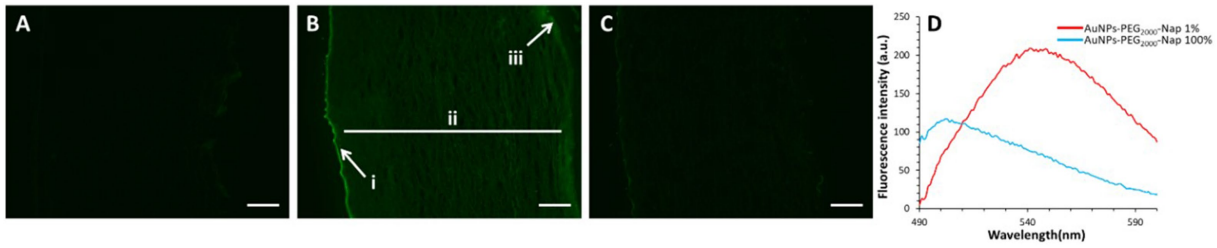

FIGURE 1
Characterization of the fluorescence emission of AuNPs-PEG2000 and AuNPs-PEG2000-Nap using *ex vivo* human corneas and fluorescence spectroscopy. **(A)** AuNPs-PEG2000 were deposited on a research-grade human cornea to be used as a control. **(B)** AuNPs-PEG2000-Nap 1% were placed on a human cornea, where i is the Bowman's layer, ii is the stroma, and iii is the Descemet's membrane. **(C)** AuNPs-PEG2000-Nap 100% were placed on a human cornea. **(D)** The fluorescence emission spectra of AuNPs-PEG2000-Nap 1 and 100%. Scale bar: 5 μm.

wrapped or expanded configurations (122). During AuNPs-PEG$_{2000}$-Nap growth (refer to Scheme 1), the utilization of these two types of PEG (HS-PEG$_{2000}$-Nap and HS-PEG$_{2000}$) in different proportions can lead to different behaviors, resulting in the core diameters ranging from 6. 0 ± 3.0 nm to 4.8 ± 2.4 nm, which are still quite similar on the nanometer scale. It is likely that HS-PEG$_{2000}$-Nap experiences more steric hindrance, thereby reducing the thiol group's ability to reach the gold core. This steric hindrance may also enhance stabilization, producing smaller cores than expected. Consequently, the smaller gold core of AuNPs-PEG$_{2000}$-Nap 100% leads to a smaller number of stabilizing ligands around the nanoparticles, thereby making AuNPs-PEG$_{2000}$-Nap 1% have the largest gold core diameter and number of ligands. With the largest core diameter, AuNPs-PEG$_{2000}$-Nap 1% contained 6,652 gold atoms, which is significantly more than the AuNPs-PEG$_{2000}$-Nap 100%, which had 3,406 gold atoms. However, for AuNPs-PEG$_{2000}$-Nap 1%, this only represents 0.41% by mass despite having 345 sulfur atoms. The graft density showed very similar numbers of ligands per nm^2 of gold core surface for both AuNPs-PEG$_{2000}$-Nap 1 and 100%, i.e., 3.05 and 3.10 ligands/nm^2, respectively.

Continuing the physical characterization of AuNPs-PEG$_{2000}$-Nap 1 and 100%, the fluorescence emission of the nanoparticles was tested with *ex vivo* human corneas (Figure 1) to identify the best AuNPs-PEG$_{2000}$-Nap for colocalization experiments. A drop (50 μL, 1 mg/mL) of AuNPs-PEG$_{2000}$ (Figure 1A), AuNPs-PEG$_{2000}$-Nap 1% (Figure 1B), and AuNPs-PEG$_{2000}$-Nap 100% (Figure 1C) was deposited on the top of the human corneas and incubated at room temperature for 2 h before being prepared for image acquisition (Materials and Methods). The fluorescence emission spectra of AuNPs-PEG$_{2000}$-Nap 1% and AuNPs-PEG$_{2000}$-Nap 100% (Figure 1D) were also obtained in water. The AuNPs-PEG$_{2000}$-Nap 1% ($\lambda_{max,\ emission}$ = 544 nm) had the highest fluorescence emission intensity and was the most visible in the cornea. In fact, AuNPs-PEG$_{2000}$-Nap 1% could be found in the Bowman's layer, throughout the entire stroma and the Descemet's membrane, with a stronger affinity with the Bowman's layer. For AuNPs-PEG$_{2000}$-Nap 100% ($\lambda_{max,\ emission}$ = 503 nm), the fluorescence was less discernible in the cornea than with AuNPs-PEG$_{2000}$-Nap 1%. The difference in the fluorescence emission spectra could hypothetically come from the difference in the steric hindrance between AuNPs-PEG$_{2000}$-Nap 1% and AuNPs-PEG$_{2000}$-Nap 100% (123). The presence of Nap groups on all 224 PEGylated ligands of AuNPs-PEG$_{2000}$-Nap 100% could cause steric hindrance, thereby not permitting the Nap group free rotations and reducing the extent of the intramolecular charge transfer, which could explain the blue shift observed in the fluorescence spectra (Figure 1D) (124, 125). The difference in the emission intensities is likely due to aggregation-caused quenching. For the AuNPs-PEG$_{2000}$-Nap 100%, the aromatic Nap fluorophores are closer and can give rise to intermolecular

interactions, e.g., π-π stacking, which commonly results in reduced fluorescence (126). Between the two fluorescent AuNPs-PEG_{2000}-Nap 1 and 100%, the AuNPs-PEG_{2000}-Nap 1% appear to present better fluorescent properties for further physiological experiments. The AuNPs-PEG_{2000}-Nap could potentially benefit from fine-tuning experiments to investigate the number of Nap groups required to realize optimal fluorescence while modifying the other AuNP properties minimally.

3.2 Biological properties of AuNPs-PEG2000-nap

With the goal of using AuNPs-PEG2000 as ocular drug delivery systems, these nanoobjects must exhibit several critical biological properties, e.g., ultrastability under conditions mimicking formulation steps and the physiological environment, mucoadhesion, and biocompatibility. The following three sections describe the biological properties of the AuNPs and their behavior in the presence of human corneal epithelial cells (hCEC).

3.2.1 Ultrastability

Frequently, the weak colloidal stability of AuNPs excludes their utilization in specific fields (127). For example, instability in physiological buffering salts restricts the utilization of many types of nanoparticles for biomedical applications [e.g., drug delivery (128), gene therapy (129), biosensing (130), and imaging (131)] because blood is a rich and highly ionic media (132). In addition, for nanoparticles, the loss of colloidal stability can result in precipitation, reshaping, corrosion, and, most importantly, the loss of key physicochemical properties like delivery, optoelectronic, biocompatibility, biodegradability, magnetic, or catalytic abilities (133). Thus, it is crucial to preserve the original size, shape, structure, composition, and aggregation state of the nanoparticles in biological environments for the required duration to achieve the intended use (134). This preservation is essential for maintaining the functionality of nanoparticles and preventing undesired effects (135). Given that nonfluorescent AuNPs-PEG_{2000} can withstand harsh conditions (90), e.g., several cycles of freeze-drying, heating, ultracentrifugation, and autoclave sterilization, the goal was to verify that the fluorescent AuNPs-PEG_{2000}-Nap 1 and 100% would support the same conditions. In this study, their colloidal stability was assessed using different methodologies, including UV–visible spectroscopy, DLS, and TEM (Table 2).

An interesting characteristic of AuNPs is the ability of the conduction electrons of the gold atoms to oscillate coherently when irradiated by the oscillating electric field of light. The localized surface plasmon resonance (LSPR) effect causes an absorbance band in the electromagnetic spectrum, typically in the visible light range. The absorption peak can be altered by variations in different factors, e.g., the particle size and shape, coating, the distance between particles, pH, temperature, the number and types of the ligands linked to the gold core, and the surrounding physicochemical environment (136, 137). Here, the plasmonic band shift, which was measured accurately with the first derivative, was used to determine the colloidal stability of AuNPs-PEG_{2000}-Nap 1 and 100% to different treatments (Supplementary Figure 3) (98). The colloidal stability results for AuNPs-PEG_{2000}-Nap 1 and 100% are shown in Table 2.

The UV–visible spectra were obtained with 0.050 mg/mL of AuNPs-PEG_{2000}-Nap 1 and 100% before and after three cycles of 24-h freeze-drying, three periods of 12-h heating at 65°C, and three precipitations by ultracentrifugation, and sterilization using an autoclave (Table 2). Tables 2A,B show the colloidal stability results for AuNPs-PEG_{2000}-Nap 1% and AuNPs-PEG_{2000}-Nap 100%, respectively. As can be seen, the UV–visible spectrum for each AuNP-PEG_{2000}-Nap observed after treatment, represented by the full red lines, is nearly the same as the initial spectrum, represented by the full black lines. The LSPR position of AuNPs-PEG_{2000}-Nap 1% before and after all treatments, which was determined by calculating the derivative of the spectra, remained at 517.5 nm (Supplementary Figure 1). For AuNPs-PEG_{2000}-Nap 100%, the derivative of the plasmon bands exhibited a slight shift, translating into a disturbance of the gold core. Specifically, only the sterilization caused a 0.75 nm shift of the plasmon band peak of AuNPs-PEG_{2000}-Nap 1%, and it caused a 2.00 nm shift for AuNPs-PEG_{2000}-Nap 100% (Supplementary Figure 4).

AuNPs-PEG_{2000}-Nap 1% were able to sustain the ultrastability testing as very small variations in the UV–visible spectra, the TEM images, and the hydrodynamic diameters can be observed. AuNPs-PEG_{2000}-Nap 100% also exhibited little variation in the physicochemical parameters after freeze-drying, centrifugation, sterilization, and heating. In addition, the plasmon bands observed in the UV–visible spectroscopy remained similar with no variations in the observed plasmon band peak position. However, a slight increase in the intensity of the entire spectrum of AuNPs-PEG_{2000}-Nap 1% was observed after sterilization and heating, which is likely due to the evaporation of a small part of the total volume. For AuNPs-PEG_{2000}-Nap 100%, a slight reduction in the global intensity was observed after centrifugation, which suggests that some of the AuNPs-PEG_{2000}-Nap 100% could aggregate during this step. The mean core of the diameter of AuNPs-PEG_{2000}-Nap 1 and 100%, extracted from TEM images using the ImageJ software, did not vary significantly after each treatment (Table 2). The DLS experiments yielded quite similar results after all treatments and showed no signs of aggregation for AuNPs-PEG_{2000}-Nap 1%. However, the same cannot be said for AuNPs-PEG_{2000}-Nap 100%. Here, the hydrodynamic diameter varied significantly depending on the treatment, especially after freeze-drying (from 34.0 ± 0.6 nm to 332 ± 74 nm, as shown in Table 2B). The increased number of Nap groups appeared to alter the colloidal stability, thereby leading to a likely agglomeration in the solution. Note that a detectable level of fluorescence was maintained after all treatments for both AuNPs (Supplementary Figure 5).

To the best of our knowledge, the ultrastable AuNPs-PEG_{2000}-Nap 1% are the first reported fluorescent AuNPs that can sustain autoclave sterilization without major changes in their UV–visible spectra and both the core and hydrodynamic diameters, as previously showcased with their nonfluorescent counterpart (90). As mentioned previously, colloidal stability is essential to preserve the functionality of AuNPs-PEG_{2000} and AuNPs-PEG_{2000}-Nap, especially if AuNPs-PEG_{2000} are used as a drug delivery system for topically applied treatments (102). The results of the physical characterization suggest that AuNPs-PEG_{2000}-Nap 1% could be a promising candidate as an imaging tool for AuNPs-PEG_{2000}. Combined with the ultrastability assay, the previous fluorescence experiments (Figure 1) have both shown that AuNPs-PEG_{2000}-Nap 1% is the most suitable fluorescent probe for imaging purposes while offering the same

TABLE 2 Ultrastability characterization of (A) AuNPs-PEG$_{2000}$-Nap 1% and (B) AuNPs-PEG$_{2000}$-Nap 100% before treatment and after three cycles of 24-h freeze-drying, sterilization by an autoclave, three precipitations by ultracentrifugation, and three periods of 12-h heating at 65°C.

A	Before	Freeze-drying	Sterilization	Centrifugation	Heat
UV–visible	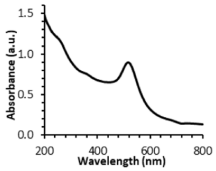	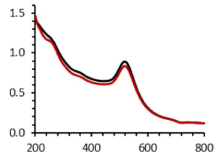	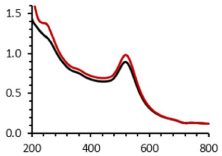	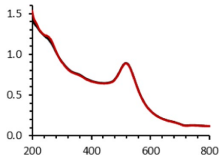	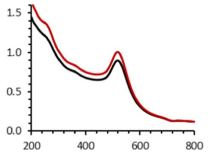
TEM (diameter)	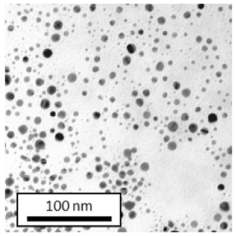 (6.0 ± 3.0) nm	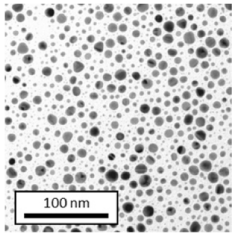 (6.4 ± 2.4) nm	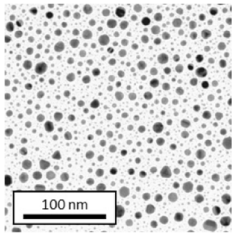 (8.2 ± 3.0) nm	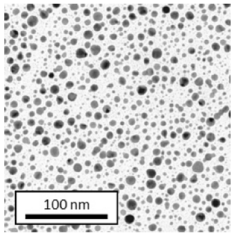 (5.4 ± 3.0) nm	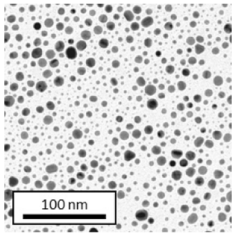 (6.2 ± 2.8) nm
DLS (diameter)	(29.0 ± 1.0) nm	(28.6 ± 0.6) nm	(27.8 ± 0.4) nm	(26.8 ± 0.8) nm	(28.0 ± 0.6) nm
B	Before	Freeze-drying	Sterilization	Centrifugation	Heat
UV–visible	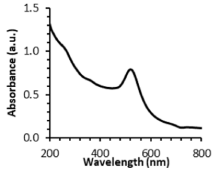	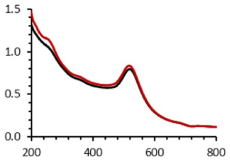	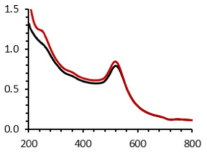	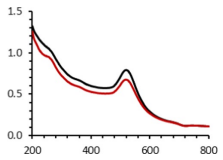	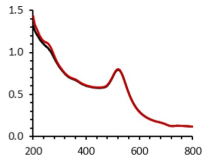
TEM (diameter)	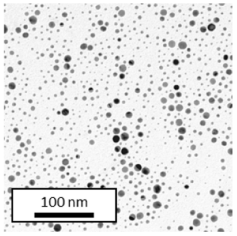 (4.8 ± 2.4) nm	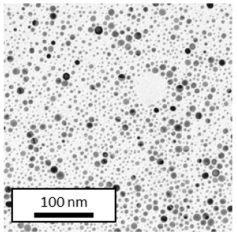 (4.0 ± 2.6) nm	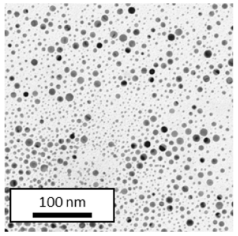 (4.8 ± 2.6) nm	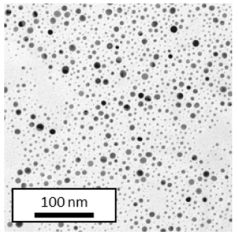 (4.2 ± 2.4) nm	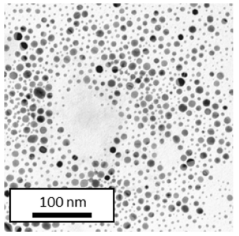 (4.6 ± 2.4) nm
DLS (diameter)	(34.0 ± 0.6) nm	(332 ± 74) nm	(37.4 ± 1.6) nm	(42.2 ± 1.6) nm	(39.4 ± 1.8) nm

The UV–visible spectra of the AuNPs-PEG2000-Nap before and after the different treatments are represented by the solid black and solid red lines, respectively. The core diameters and hydrodynamic diameters were obtained from the TEM images and DLS, respectively. The experimental details are given in the Materials and Methods.

10.3389/fmed.2025.1557611

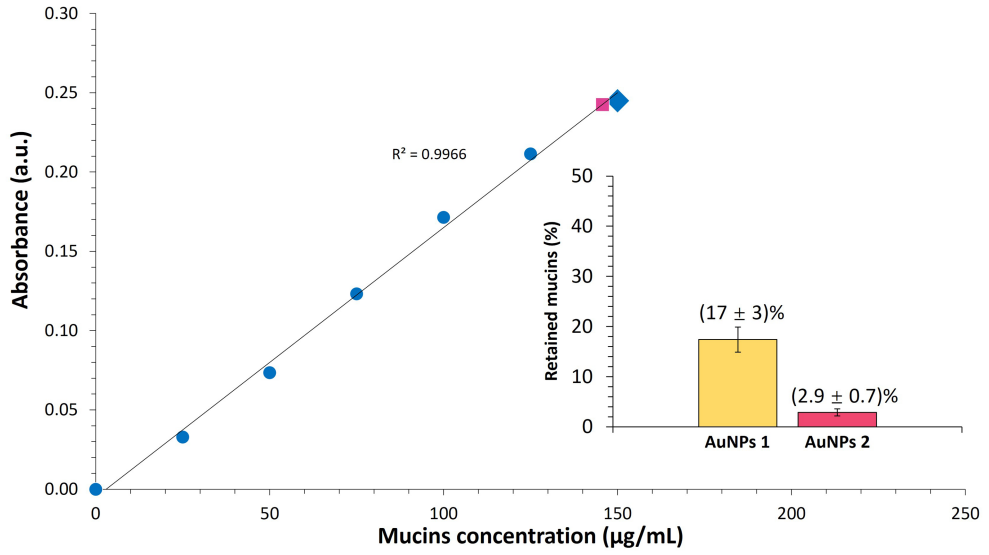

FIGURE 2
Quantitative analysis of mucins adsorbed on AuNPs. The calibration curve of the mucins is represented by the blue circles. The yellow triangle represents the absorbance coming from the concentration of mucins still free after the mix between the AuNPs (1 mg/mL) with an initial mucin concentration of 150 µg/mL (large blue diamond), and the pink square represents mucins still free after contact with AuNPs-PEG_{2000}-Nap 1% (1 mg/mL). Insert: Histogram of the percentage of adsorbed mucins on AuNPs-PEG_{2000} (AuNPs 1) and AuNPs-PEG_{2000}-Nap 1% (AuNPs 2). The data are reported as the mean ± standard deviation (n = 3).

properties as the nonfluorescent AuNPs-PEG_{2000} (90). Thus, we focus on AuNPs-PEG_{2000}-Nap 1% in all subsequent experiments.

3.2.2 Mucoadhesion

Various techniques have been developed to study mucoadhesion in order to quantify and characterize how different materials interact with mucins (81, 138, 139). Mucins are glycoproteins found in the airways, gastrointestinal tract, genitourinary tract, nasal cavity, mouth, throat, and ocular surface (140). As the bottom layer of the tear film, the mucoid layer on the ocular surface is responsible for the maintenance of the lacrimal fluid, lubrication to facilitate blinking, ensuring a smooth surface for vision, and protection by trapping and removing pathogens and debris (141). Mucoadhesive drug delivery systems can increase their residence time in the precorneal film, which could broaden the drug release window and potentially reduce the required number of eyedrop applications (142).

A protocol adapted for AuNPs mucoadhesion involves the periodic acid/Schiff's reagent (PAS) coloration method (143). This method analyzes the mucin content and mucoadhesion by oxidizing saccharide hydroxyl groups and reacting them with decolored fuchsin, resulting in a color change that is detectable by UV–visible spectroscopy (144). A protocol has been perfected and optimized for its combination with AuNPs, in consideration of their high visible light absorbance (108).

The nonfluorescent AuNPs-PEG_{2000} could adsorb 11 ± 4% of the 150 µg of mucins they were incubated with, and the AuNPs-PEG_{2000}-Nap 1% were able to retain 2.9 ± 0.7% of the same initial amount of mucins (Figure 2). AuNPs can exhibit mucoadhesive properties due to their ability to bind to mucins through two main mechanisms, i.e., (1) the formation of S-S bonds with the thiol groups at the metallic core and (2) the direct interaction of the cysteine groups with the gold core via Au-S bonds. The presence of some peripheral Nap groups on AuNPs-PEG_{2000}-Nap 1% could account for the observed differences compared with conventional AuNPs-PEG_{2000}. When mucins attempt to interact near the core, the steric hindrance from the Nap groups may prevent the access of many proteins. In addition, the very high graft density (3.05 ligands/nm^2) of PEGylated ligands on AuNPs-PEG_{2000}-Nap 1% could contribute to the high motility in mucus (145). In fact, the AuNPs-PEG_{2000} and AuNPs-PEG_{2000}-Nap 1% exhibited low percentages of adsorbed mucins; however, their high draft density could increase the diffusion into the mucous layer. This could potentially increase the residence time of the drug delivery systems, which would increase the local concentrations of therapeutic molecules near the corneal epithelial cells.

3.2.3 Cytotoxicity

In a previous paper, MTS viability assays with different types of AuNPs, including AuNPs-PEG_{2000}, were performed at low AuNP concentrations (from 0.0005 to 0.406 µM) (90), and showed a high cell viability for all concentrations tested. Herein, a MTS viability assay was conducted to determine if the addition of the Nap group to the AuNPs-PEG_{2000} could impact cell viability. We also increased the range of AuNP concentrations to evaluate the highest concentration that could affect cell viability. Results for each AuNP concentration and type (Figure 3) show a similar viability between the AuNPs-PEG_{2000} and the AuNPs-PEG_{2000}-Nap 1% for all the concentrations tested, meaning that fluorescent molecules covalently bonded to PEG do not impact biological response differently that the non-fluorescent ones (only descriptive statistics were used). Furthermore, results show that concentrations between 0,0001 and 0,75 µM AuNPs had a cell viability similar to the control (no AuNPs), and only a 9 ± 14 and a 22 ± 28% cell death was observed for the highest concentration of AuNPs (1 µM) for, respectively the AuNPs-PEG_{2000} and the AuNPs-PEG_{2000}-Nap 1%. These results indicate that AuNPs-PEG_{2000}-Nap 1%

are adequate for fluorescent biolocalization studies and biodistribution experiments.

3.2.4 Cell internalization

Finally, prior to performing *ex vivo* localization experiments, AuNPs-PEG_{2000} and AuNPs-PEG_{2000}-Nap 1% were placed into wells of hCECs for 30 min to gather data on possible AuNPs internalization into the cells. After incubation for 30 min, the wells were rinsed with a phosphate-buffered saline (PBS) wash and then observed under an epifluorescence microscope using the fluorescein isothiocyanate (FITC) filters. The results indicate that some hCECs exhibit a small degree of autofluorescence in the same wavelength range as the AuNPs-PEG_{2000}-Nap 1% emission (Figure 4A). However, the distinction between this background fluorescence and the emitted fluorescence coming from AuNPs-PEG_{2000}-Nap 1% observed in Figure 4 is obvious because the cells are clearly visible in Figure 4B compared with Figure 4A. In addition, this assay confirmed that AuNPs-PEG_{2000}-Nap 1% are internalized into hCECs because fluorescence can be observed in the cytoplasm and is absent in the nucleus. If the AuNPs-PEG_{2000}-Nap 1% had covered the surface of the cell without penetrating the cells, the fluorescence would have been uniform, and a distinction between the cytoplasm and nucleus would not be observable.

Thus, the AuNPs-PEG_{2000}-Nap 1% emit strong fluorescence with minimal change to the original nonfluorescent AuNPs-PEG_{2000} by simply adding a fluorescent probe to 1% of their attached PEGylated ligands (approximately 3–4 Nap groups per gold core). In addition, they exhibit the same ultrastability properties as the AuNPs-PEG_{2000}, i.e., they can sustain rigorous conditions without significantly impacting the plasmon band position, the colloidal stability measured by DLS, and the gold core diameter measured using TEM images. Furthermore, compared to the AuNPs-PEG_{2000}, addition of the PEG_{2000}-Nap 1% did not reduce cell viability, as shown by the results of the MTS assay (Figure 3). Combined, these similarities demonstrate that AuNPs-PEG2000-Nap 1% can be utilized as a substitute for AuNPs-PEG2000 to study their biodistribution and biolocalization.

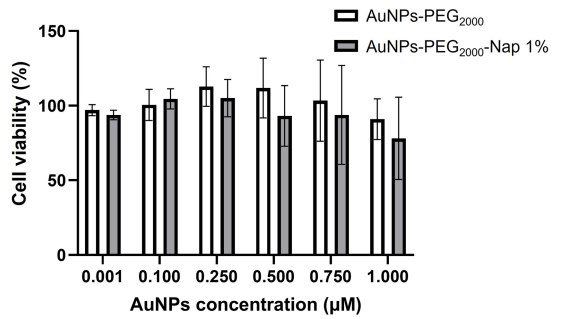

FIGURE 3
Effect AuNPs-PEG_{2000} and AuNPs-PEG_{2000}-Nap 1% on cell viability. The hCECs were cultured as monolayers (10,000 cells per well, three wells per condition, repeated using three different populations) and exposed to increasing doses of AuNPs-PEG_{2000} and AuNPs-PEG_{2000}-Nap 1% for 18 h. Cell viability was assessed using an MTS assay. Results are presented as mean ± standard deviation.

3.3 Biolocalization study using AuNPs-PEG_{2000}-nap 1%

A significant challenge in clinical translation lies in the lack of animal models that accurately replicate the human ocular system's anatomy and physiology. Rodents are commonly used for safety and efficacy evaluations due to their cost-effectiveness and ease of handling. However, the extrapolation of pharmacodynamic responses from rodents to humans can be unreliable due to significantly different anatomy (146). Compared to rodents, rabbits exhibit greater anatomical and physiological similarities to humans, particularly regarding eye size, vitreous humor volume, and internal structure, providing a comparable pathway for topically administered compounds (147). Nevertheless, key differences remain, such as the higher viscosity of rabbit aqueous humor, larger anterior chambers, and greater blinking frequency, which must be carefully considered (148). In this study, *ex vivo* rabbit eyeballs were used, thereby eliminating significant factors impacting biodistribution and elimination of topically applied nanoparticles, such as tear film dynamics, blinking and systemic circulation (149, 150). Whole eyeballs from slaughterhouse rabbits were used in the biolocalization experiments. Here, a drop (50 μL, 1 mg/mL) of AuNPs-PEG_{2000}-Nap 1% diluted in PBS was placed on the cornea for each eyeball. The application time was either 3 min to replicate the renewal

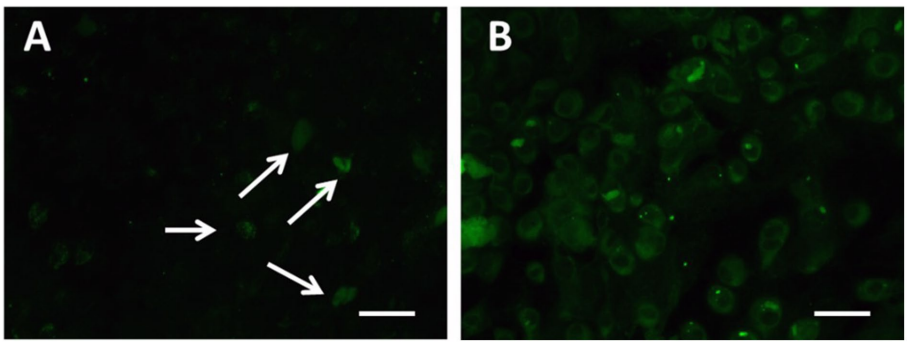

FIGURE 4
Fluorescence assay of internalized of **(A)** control AuNPs-PEG_{2000} and **(B)** AuNPs-PEG_{2000}-Nap 1% (green) by cultured hCECs with FITC filters. The arrows point to hCECs slightly showing autofluorescence. Scale bars: 10 μm.

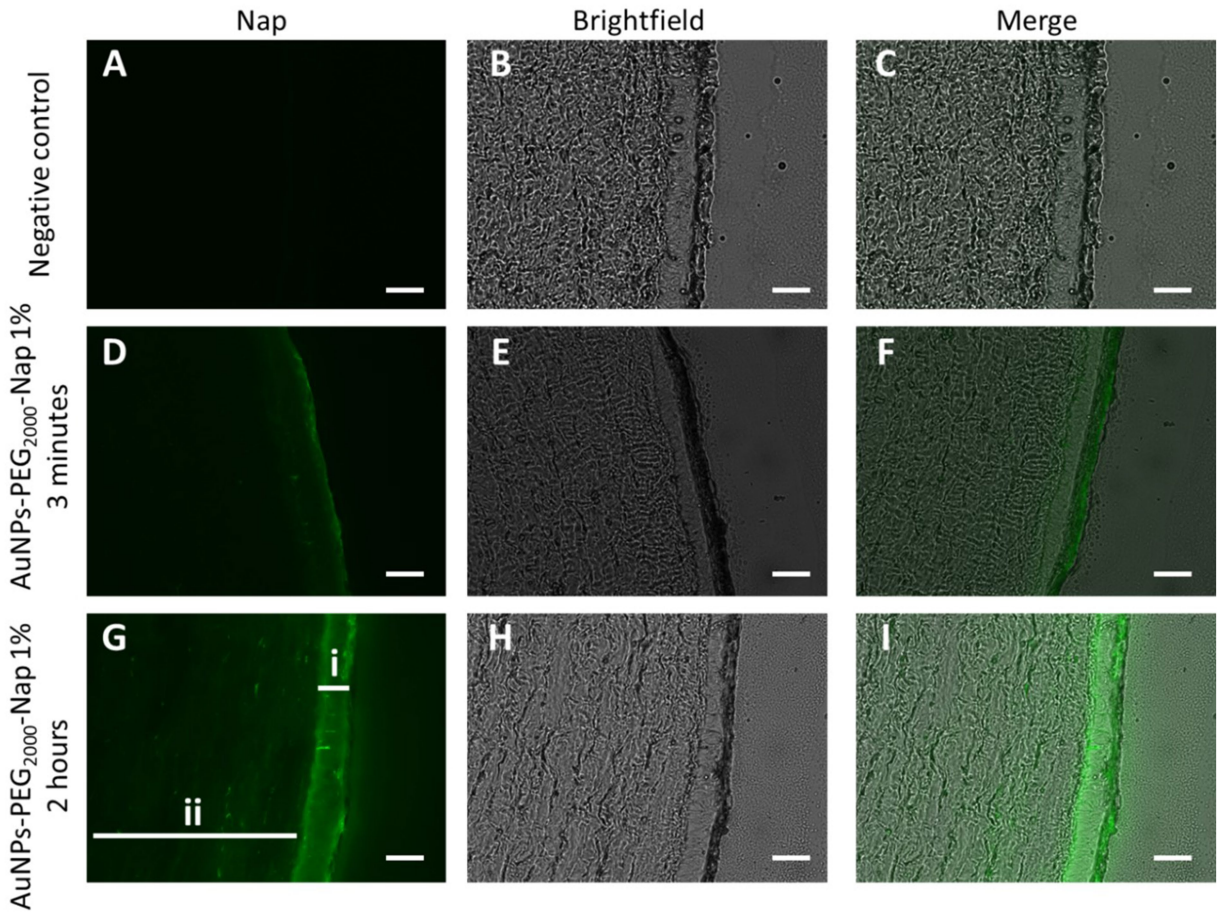

FIGURE 5
Localization of AuNPs-PEG_{2000}-Nap 1% (green) in rabbit cornea cross-sections observed under a fluorescence microscope using the FITC filter (first column), brightfield (middle column), and merge of the two (third column). Images of the cornea **(A)**, **(B)**, and **(C)** after 2-h PBS application; **(D)**, **(E)**, and **(F)** 3-min application of AuNPs-PEG_{2000}-Nap 1% followed by a 2-h wait; and **(G)**, **(H)**, and **(I)** 2-h application of AuNPs-PEG_{2000}-Nap 1%, where i is the multistratified epithelium, and ii is the stroma. Scale bars: 50 μm.

rate of the tear film (9) or 2 h to increase the interaction probability with the tear film and their diffusion. In addition, the corneas, irises, lenses and posterior segments were dissected carefully to avoid contamination between the different ocular tissues and then embedded in an optimum cutting temperature (OCT) compound and cut at the cryostat. No fixation steps were carried out before microscopy in order to avoid any physicochemical modification of the eye tissues that could impact the localization of AuNPs-PEG_{2000}-Nap 1%. Therefore, this method provides a more direct way to observe the biodistribution of gold nanoparticles in the different structures of the eye (151).

3.3.1 Cornea

The human cornea comprises three cellular layers (i.e., the epithelium, stroma, and endothelium) and two acellular layers that separate them (i.e., Bowman's layer and Descemet's membrane) (152).

AuNPs-PEG_{2000}-Nap 1% were found in the cornea for both application times (Figure 5). Note that more AuNPs-PEG_{2000}-Nap 1% were found in the corneal epithelium after 2 h, as the epithelial layer was more defined, clearly observable, and brighter, as shown in Figure 5G. The 3-min application was sufficient for AuNPs-PEG_{2000}-Nap 1% to adhere to the ocular surface because fluorescence can be observed in the corneal epithelium (Figure 5D) even after the vigorous PBS wash. Fluorescent AuNPs-PEG_{2000}-Nap 1% were also found in the stroma for both application times, which means that the AuNPs-PEG_{2000}-Nap 1% were not confined to the direct application site or the corneal epithelium, benefiting motility by their high graft density. In addition, there appeared to be an affinity between AuNPs-PEG_{2000}-Nap 1% and the corneal epithelium because the brightness levels between the epithelial layer and the stroma present a clear intensity difference, especially after 2 h.

The AuNPs-PEG_{2000}-Nap 1% are not the first AuNPs to be topically applied and found in the corneal epithelium and stroma (77, 79, 80) but they are the only PEGylated AuNPs synthesized from a one-pot synthesis.

3.3.2 Iris

The iris plays a crucial role in visual function by regulating the amount of light entering the eye and reaching the retina (153). The iris also participates in the circulation of aqueous humor, thereby helping to regulate the intraocular pressure (154).

Fluorescence can be faintly observed in the Nap images (Figure 6) without any clear preference for an iris structure. For the image obtained after the 3-min application, the lumen of a blood vessel was visible, in addition to the outermost periphery of the

10.3389/fmed.2025.1557611

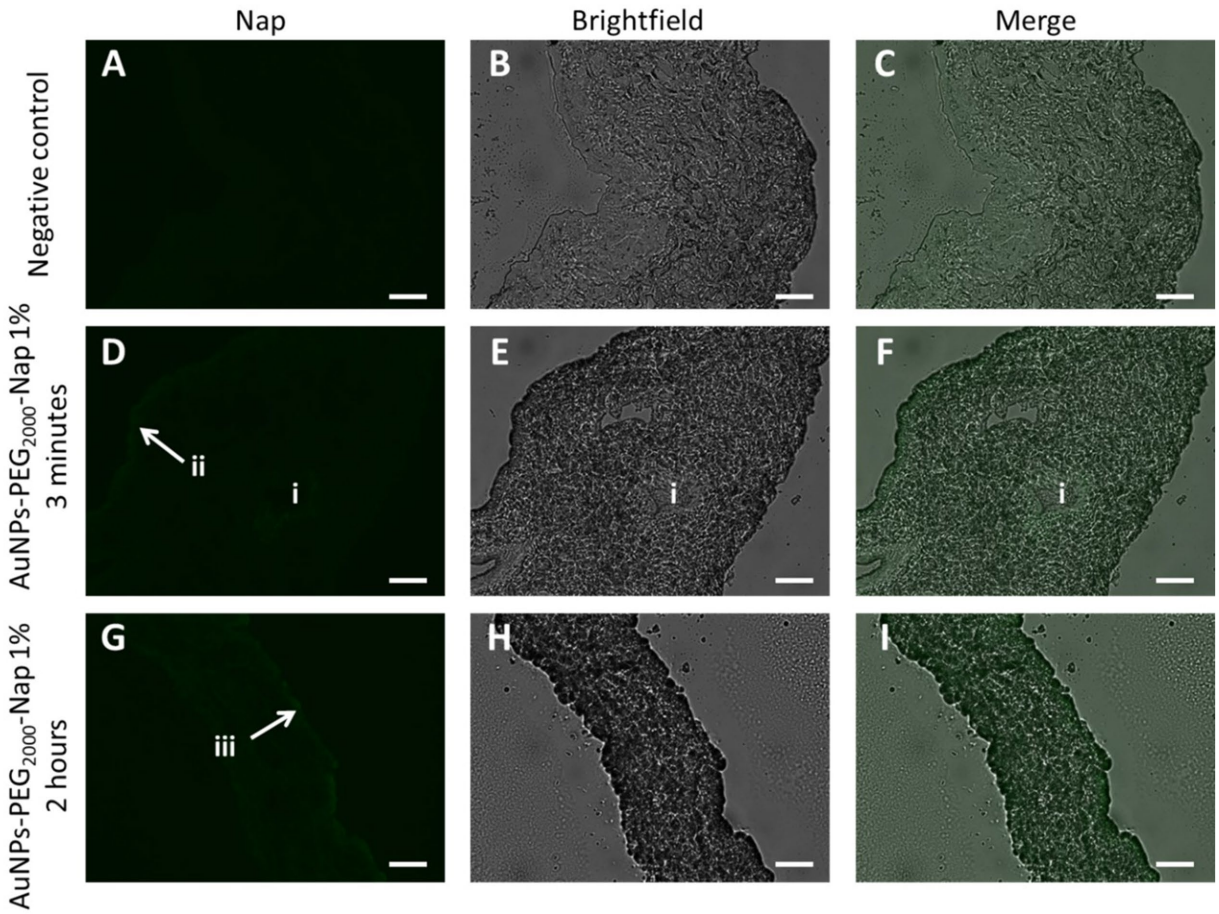

FIGURE 6
Localization of AuNPs-PEG_{2000}-Nap 1% (green) in rabbit iris cross-sections observed under a fluorescence microscope using the FITC filter (first column), brightfield (middle column), and the merge of the two (third column). Images of the iris **(A)**, **(B)**, and **(C)** after 2-h PBS application; **(D)**, **(E)**, and **(F)** 3-min application of AuNPs-PEG_{2000}-Nap 1% followed by a 2-h wait; and **(G)**, **(H)**, and **(I)** 2-h application of AuNPs-PEG_{2000}-Nap 1%, where i represents the lumen of a blood vessel, ii represents a peripheral region where AuNPs-PEG_{2000}-Nap 1% can be seen, and iii shows AuNPs-PEG_{2000}-Nap 1% accumulation in the outermost structure of the iris. Scale bars: 50 μm.

structure (Figure 6D), and AuNPs-PEG_{2000}-Nap 1% can be observed in the extremity of the iris for the 2-h application (Figure 6G).

Note that the experiments were conducted using eyes from albino rabbits, which possess no pigment; thus, the iris pigment epithelium and the pigmented anterior surface were difficult to identify. However, AuNPs-PEG_{2000}-Nap 1% had a strong affinity with the corneal epithelium (Figure 5); thus, we can expect to find AuNPs in similar cell types in other tissues, e.g., the epithelium of the iris. Nevertheless, it is important to underline that it is impossible to discern with certitude the exact iris structure in which the AuNPs-PEG_{2000}-Nap 1% were found, only that they were found in the iris after only a 3-min application.

3.3.3 Lens

The lens, which is an elastic and transparent biconvex structure located in the posterior chamber, comprises four parts, i.e., the lens capsule, epithelial cells, lens fibers, and zonules (155).

As shown in Figure 7, AuNPs-PEG_{2000}-Nap 1% were observed in the anterior part of the lens after the 3-min application. In fact, the fluorescent probe accumulated slightly in the epithelial cell monolayer of the lens (Figure 7C). Note that the epithelium of the lens is only located on its anterior part. In the images of the posterior part of the lens (Figures 7G,L), no AuNPs-PEG_{2000}-Nap 1% can be observed. Knowing this, the possibility of the AuNPs-PEG_{2000}-Nap 1% being in the lens capsule rather than the lens epithelium is excluded because fluorescence would be visible on the posterior part of the lens. The same tendencies were observed for the 2-h application.

To conclude on the distribution of the AuNPs in the anterior segment of the eye, the AuNPs-Nap 1% were readily observed in the corneal epithelium, the iris, potentially in its pigment epithelium, and in the lens epithelium. The fluorescent probe successfully crossed the anterior part of the rabbits' eyeballs; however, most of the fluorescence was observed in the cornea.

3.3.4 Posterior segment

In these experiments, the sampled posterior segment comprised the retina, choroid, and sclera. The retina, which is located in the posterior part of the eye, is a transparent, light-sensitive tissue composed of multiple cellular layers (156). The retina includes the light-transducing neural retina and the retinal pigment epithelium (RPE) (157). The neural retina is a layered structure comprising six major types of neurons organized into three nuclear layers containing

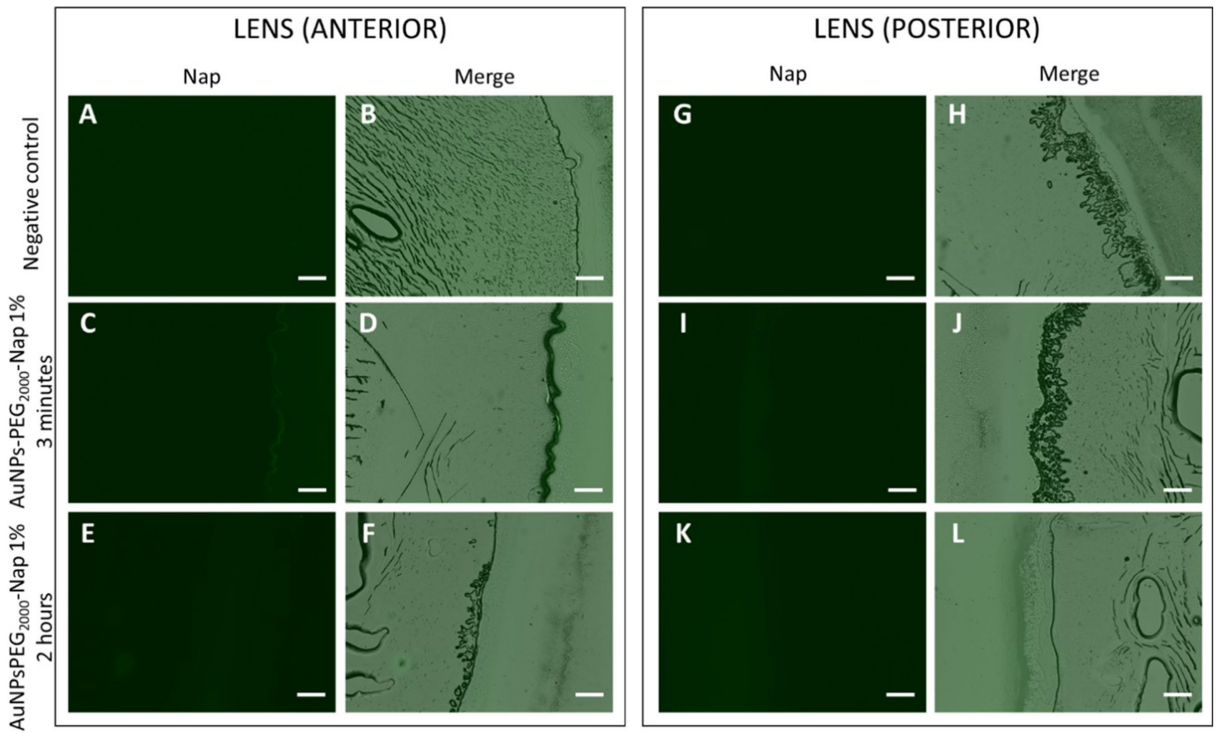

FIGURE 7
Localization of AuNPs-PEG_{2000}-Nap 1% (green) in the rabbit lens cross-sections observed under a fluorescence microscope using the FITC filter (first column) and the merge of the brightfield and FITC filter (second column) divided in two parts, where the anterior segment is closest to the cornea, and the posterior segment is closest to the back of the eye. Images of the anterior part of the lens **(A)** and **(B)** after 2-h PBS application; **(C)** and **(D)** 3-min application of AuNPs-PEG_{2000}-Nap 1% followed by a 2-h wait; and **(E)** and **(F)** 2-h application of AuNPs-PEG_{2000}-Nap 1%; **(G)** and **(H)** images of the posterior part of the lens after 2-h PBS application; **(I)** and **(J)** 3-min application of AuNPs-PEG_{2000}-Nap 1% followed by a 2-h wait, and **(K)** and **(L)** 2-h application of AuNPs-PEG_{2000}-Nap 1%. Scale bar: 50 μm.

neuronal cell bodies (or somas) and two plexiform layers where synapses occur (158).

Experimentally, a sample of the back of the eyeball was taken using a 10-mm diameter biopsy punch to facilitate manipulations. Here, the three-layering tissues, i.e., the retina, choroid, and sclera, were kept together. The AuNPs-PEG_{2000}-Nap 1% were found in the posterior segment of the eye, as shown in Figure 8. For both application times, the AuNPs-PEG_{2000}-Nap 1% were organized in a thin line in a specific structure of the retina; however, due to the lack of melanin pigment in albino rabbits, it is difficult to distinguish exactly where the choroid ends and the retina begins, thereby making it difficult to precisely identify the tissue sublayers where the AuNPs-PEG_{2000}-Nap 1% are found. However, we did not expect to find them there because the AuNPs-PEG_{2000}-Nap 1% had to go through the vitreous humor to migrate from the lens to the retina. The vitreous humor is a viscoelastic extracellular matrix hydrogel with a water content between 98 and 99.7% (159). The findings of this study demonstrate that the AuNPs-PEG_{2000}-Nap 1% does not need to be injected via an intravitreous pathway to be found in the retina.

The AuNPs-PEG_{2000}-Nap 1% are not the only AuNPs that were found in the retina after topical application (160). However, this phenomenon was previously demonstrated only in a mouse model, whose eye volume is approximately one hundred times smaller than that of a rabbit. Furthermore, *in vivo* biodistribution experiments benefit from having two possible routes for topically applied nanocarriers: the corneal and the non-corneal routes. Evidence also suggests that the non-corneal route is beneficial in bringing more nanocarriers into the posterior segment of the eye (104, 161–164). However, according to the design of our *ex vivo* experiments, it is impossible for the AuNPs-PEG_{2000}-Nap 1% to take a route other than the corneal route. Thus, future *in vivo* experiments will be able to highlight the duality of corneal and non-corneal routes in addition to validating which route is preferable for PEGylated AuNPs.

Following the previous observations made in the anterior segment, where AuNPs-PEG_{2000}-Nap 1% were frequently found in the corneal epithelium, observed in the iris, and successfully located and retained in the monolayer of the lens epithelium, it is possible that AuNPs-PEG_{2000}-Nap 1% may be also found in the RPE. This structure is a monolayer of pigmented cells forming part of the blood-retina barrier (165), which is heavily involved in the transport of ions, water, and metabolic waste from the subretinal space to the blood (166, 167), as well as the transport of nutrients from the blood to the photoreceptors (168, 169). In addition, RPE cells perform specialized phagocytosis, which is crucial in terms of maintaining the health of photoreceptors by digesting their aged outer segments. This process prevents photo-oxidative damage to photoreceptors (170). RPE cells do not divide; thus, they must process the ingested material efficiently to avoid toxic buildup in their lysosomes, which can lead to retinal disorders (171). This could be the reason why the AuNPs-PEG_{2000}-Nap 1% were concentrated in this region of the posterior segment. This creates an extremely dynamic environment where AuNPs-PEG_{2000}-Nap 1% could potentially be found, fitting the

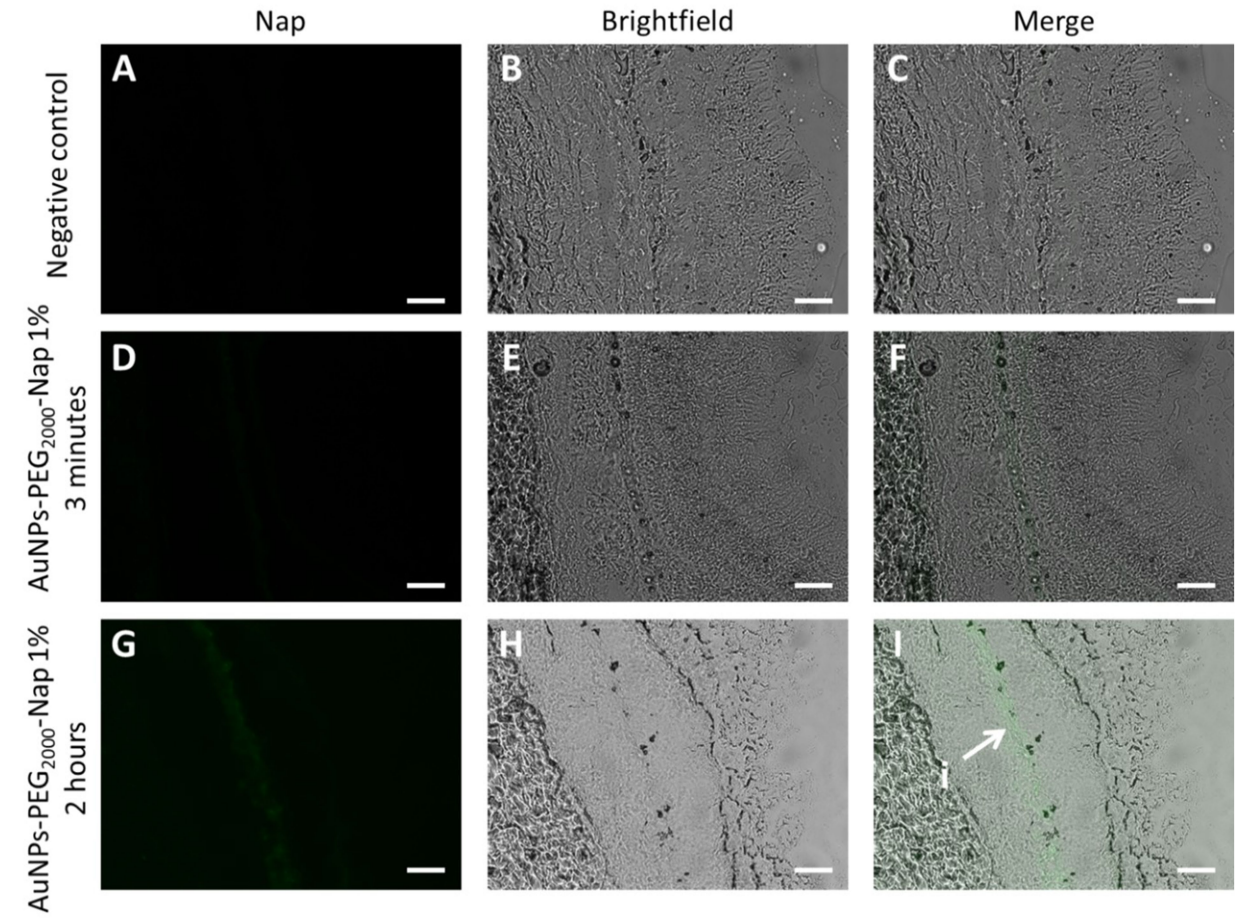

FIGURE 8
Localization of AuNPs-PEG_{2000}-Nap 1% (green) in rabbit posterior segment cross-sections observed under a fluorescence microscope using the FITC filter (first column), brightfield (middle column), and merge of the two (third column). Images of the posterior segment after **(A)**, **(B)**, and **(C)** 2-h PBS application; **(D)**, **(E)**, and **(F)** 3-min application of AuNPs-PEG_{2000}-Nap 1% followed by a 2-h wait; and **(G)**, **(H)**, and **(I)** 2-h application of AuNPs-PEG_{2000}-Nap 1%, where i AuNPs-PEG_{2000}-Nap 1% form a thin line. Scale bars: 50 μm.

description of tissues where they were observed in this study. However, further studies are required to investigate and confirm possibility.

4 Conclusion

In conclusion, AuNPs-PEG_{2000}-Nap 1% were synthesized and exhibited similar properties as their nonfluorescent counterpart (AuNPs-PEG_{2000}), e.g., ultrastability, low mucoadhesion, and low cytotoxicity, and they were internalized by the cells. When applied topically to *ex vivo* rabbit eyeballs, they demonstrated a strong affinity with the cornea, specifically the corneal epithelium. In addition, they were found in the iris, the lens epithelium, and the posterior segment of the eye. These results represent a tremendous opportunity for research on the potential of AuNPs as drug delivery systems.

The nanoparticle synthesis protocol developed in this study has the potential to be adapted for the creation of various types of AuNPs tailored to various applications and different target sites. This adaptability could be particularly beneficial for research focusing on the controlled release of active molecules in the cornea. By functionalizing the polymeric corona, it may be possible to increase mucoadhesion, thereby improving the delivery and retention of therapeutic agents (101).

Previously, nonfluorescent AuNPs-PEG_{2000} have demonstrated significant potential as drug carriers, particularly for delivering anti-inflammatory molecules (92). Building upon this foundation, future studies could investigate the encapsulation and release of active compounds designed to treat pathologies affecting the posterior segment of the eye. Such research could yield valuable insights and results, given that AuNPs can reach the back of the eye, thereby offering a promising delivery mechanism for drugs targeting this challenging area.

In this context, AuNPs have emerged as particularly promising candidates. For example, they have considerably potential for the targeted delivery of therapeutic molecules to the cornea, and they can reach the posterior segment of the eye. This dual functionality makes them an exciting prospect for future research, with the potential to advance the field of ocular drug delivery significantly. Thus, the continued investigation of their properties and applications could lead to new and more effective treatments for a range of eye conditions, benefiting patients with both anterior and posterior segment diseases.

Data availability statement

The original contributions presented in the study are included in the article/Supplementary material, further inquiries can be directed to the corresponding author.

Ethics statement

Animal ethical approval was not required for the study involving animals in accordance with the local legislation and institutional requirements because albino rabbit heads were obtained from the Rolland Pouliot & Fils slaughterhouse (Saint-Henri-deLévis, QC, Canada). This study adhered to the ethical principles outlined in the Declaration of Helsinki and was approved by the CHU de Québec–Université Laval Ethics Committee (protocol number DR-002-955). The research-grade human eyes used in this study were provided by the "Ocular Tissue for Vision Research" infrastructure of the Vision Sciences Research Network, in collaboration with the Banque d'Yeux du Centre Universitaire d'Ophtalmologie (Québec, QC, Canada) and Héma-Québec (Québec, QC, Canada). The tissue acquisition process involved next-of-kin consent.

Author contributions

GR-M: Conceptualization, Formal analysis, Methodology, Writing – original draft, Writing – review & editing. SM: Formal analysis, Methodology, Writing – review & editing. AT: Formal analysis, Methodology, Writing – review & editing. CB: Methodology, Writing – review & editing. CM: Methodology, Writing – review & editing. AL: Methodology, Writing – review & editing. SP: Funding acquisition, Resources, Supervision, Writing – review & editing. PR: Formal analysis, Resources, Supervision, Writing – review & editing. EG: Conceptualization, Formal analysis, Funding acquisition, Resources, Supervision, Writing – review & editing. EB: Conceptualization, Formal analysis, Funding acquisition, Project administration, Resources, Supervision, Writing – review & editing.

Funding

The author(s) declare that financial support was received for the research and/or publication of this article. This work was funded by the Canadian Institutes of Health Research (CIHR), the Natural Sciences and Engineering Research Council of Canada, the Fondation du CHU de Québec, The Vision Health Research Network (VHRN), and the Fonds de Recherche du Québec-Nature et Technologie (FRQ-NT, Samuel de Champlain Grant in association with the Conseil Franco-Québécois de Coopération Universitaire (CFQCU)). Infrastructures were supported by grants from the Canadian Funds for Innovation.

Acknowledgments

GRM acknowledges scholarships from Fonds de Recherche du Québec-Santé (FRQS), la Fondation du CHU de Québec-Desjardins, la Fondation des maladies de l'œil, and the VHRN. CM acknowledges scholarships from the Fondation des maladies de l'œil, the VHRN, and the Faculty of Medicine of Université Laval. AL acknowledges scholarship from CIHR. SP and PJR are Senior Research Scholars from the Fonds de Recherche du Québec-Santé (FRQ-S), and members of the Laboratoire d'Organogénèse Expérimentale (LOEX), and VHRN scientific networks. EB is a Junior 2 Research Scholar from the Fonds de Recherche du Québec-Santé (FRQ-S), and a member of the Center de recherche sur les matériaux avancés (CERMA), Regroupement québécois de recherche sur la fonction, l'ingénierie et les applications des protéines (PROTEO), Centre québécois sur les matériaux fonctionnels (CQMF), and VHRN scientific networks.

Conflict of interest

The authors declare that the research was conducted in the absence of any commercial or financial relationships that could be construed as a potential conflict of interest.

Generative AI statement

The authors declare that no Gen AI was used in the creation of this manuscript.

Publisher's note

All claims expressed in this article are solely those of the authors and do not necessarily represent those of their affiliated organizations, or those of the publisher, the editors and the reviewers. Any product that may be evaluated in this article, or claim that may be made by its manufacturer, is not guaranteed or endorsed by the publisher.

Supplementary material

The Supplementary material for this article can be found online at: https://www.frontiersin.org/articles/10.3389/fmed.2025.1557611/full#supplementary-material

References

1. Land MF. The human eye: structure and function. *Nat Med.* (1999) 5:1229. doi: 10.1038/15713

2. Baujat B, Krastinova D, Bach CA, Coquille F, Chabolle F. Orbital morphology in exophthalmos and Exorbitism. *Plast Reconstr Surg.* (2006) 117:542–50. doi: 10.1097/01.prs.0000200773.00268.56

3. Gupta A, Kafetzis KN, Tagalakis AD, Yu-Wai-Man C. RNA therapeutics in ophthalmology - translation to clinical trials. *Exp Eye Res.* (2021) 205:108482. doi: 10.1016/j.exer.2021.108482

4. Bucolo C, Drago F, Salomone S. Ocular drug delivery: a clue from nanotechnology. *Front Pharmacol.* (2012) 3:3. doi: 10.3389/fphar.2012.00188

5. Braun RJ, King-Smith PE, Begley CG, Li L, Gewecke NR. Dynamics and function of the tear film in relation to the blink cycle. *Prog Retin Eye Res*. (2015) 45:132–64. doi: 10.1016/j.preteyeres.2014.11.001

6. Herbaut A, Liang H, Denoyer A, Baudouin C, Labbé A. Tear film analysis and evaluation of optical quality: a review of the literature. *J Fr Ophtalmol*. (2019) 42:e21:–e35. doi: 10.1016/j.jfo.2018.12.001

7. McCulley JP, Shine WE. Meibomian gland function and the tear lipid layer. *Ocul Surf*. (2003) 1:97–106. doi: 10.1016/S1542-0124(12)70138-6

8. Portal C, Gouyer V, Gottrand F, Desseyn J-L. Ocular mucins in dry eye disease. *Exp Eye Res*. (2019) 186:107724. doi: 10.1016/j.exer.2019.107724

9. Dartt DA, Willcox MDP. Complexity of the tear film: importance in homeostasis and dysfunction during disease. *Exp Eye Res*. (2013) 117:1–3. doi: 10.1016/j.exer.2013.10.008

10. Bron AJ, Tiffany JM, Gouveia SM, Yokoi N, Voon LW. Functional aspects of the tear film lipid layer. *Exp Eye Res*. (2004) 78:347–60. doi: 10.1016/j.exer.2003.09.019

11. Castro-Balado A, Mondelo-García C, Zarra-Ferro I, Fernández-Ferreiro A. New ophthalmic drug delivery systems. Farmacia Hospitalaria: Organo Oficial de Expresion Cientifica de la Sociedad Espanola de. *Farm Hosp*. (2020) 44:149. doi: 10.7399/fh.11388

12. Mehuys E, Delaey C, Christiaens T, Van Bortel L, Van Tongelen I, Remon J-P, et al. Eye drop technique and patient-reported problems in a real-world population of eye drop users. *Eye*. (2020) 34:1392–8. doi: 10.1038/s41433-019-0665-y

13. Nayak K, Misra M. A review on recent drug delivery systems for posterior segment of eye. *Biomed Pharmacother*. (2018) 107:1564–82. doi: 10.1016/j.biopha.2018.08.138

14. Cabrera FJ, Wang DC, Reddy K, Acharya G, Shin CS. Challenges and opportunities for drug delivery to the posterior of the eye. *Drug Discov Today*. (2019) 24:1679–84. doi: 10.1016/j.drudis.2019.05.035

15. Ranta V-P, Mannermaa E, Lummepuro K, Subrizi A, Laukkanen A, Antopolsky M, et al. Barrier analysis of periocular drug delivery to the posterior segment. *J Control Release*. (2010) 148:42–8. doi: 10.1016/j.jconrel.2010.08.028

16. Nozaki M, Ando R, Kimura T, Kato F, Yasukawa T. The role of laser photocoagulation in treating diabetic macular edema in the era of intravitreal drug administration: a descriptive review. *Medicina*. (2023) 59:1319. doi: 10.3390/medicina59071319

17. Raizada K, Naik M. Photodynamic therapy for the eye. Treasure Island (FL): StatPearls Publishing (2023).

18. Campochiaro PA, Akhlaq A. Sustained suppression of VEGF for treatment of retinal/choroidal vascular diseases. *Prog Retin Eye Res*. (2021) 83:100921. doi: 10.1016/j.preteyeres.2020.100921

19. Seah I, Zhao X, Lin Q, Liu Z, Su SZZ, Yuen YS, et al. Use of biomaterials for sustained delivery of anti-VEGF to treat retinal diseases. *Eye*. (2020) 34:1341–56. doi: 10.1038/s41433-020-0770-y

20. Borrelli E, Grosso D, Barresi C, Lari G, Sacconi R, Senni C, et al. Long-term visual outcomes and morphologic biomarkers of vision loss in eyes with diabetic macular edema treated with anti-VEGF therapy. *Am J Ophthalmol*. (2022) 235:80–9. doi: 10.1016/j.ajo.2021.09.002

21. Tan Y, Fukutomi A, Sun MT, Durkin S, Gilhotra J, Chan WO. Anti-VEGF crunch syndrome in proliferative diabetic retinopathy: a review. *Surv Ophthalmol*. (2021) 66:926–32. doi: 10.1016/j.survophthal.2021.03.001

22. Foss A, Rotsos T, Empeslidis T, Chong V. Development of macular atrophy in patients with wet age-related macular degeneration receiving anti-VEGF treatment. *Ophthalmologica Journal International d'Ophtalmol Int J Ophthalmol Zeitschrift Fur Augenheilkunde*. (2022) 245:204–17. doi: 10.1159/000520171

23. Chatziralli I. Ranibizumab for the treatment of diabetic retinopathy. *Expert Opin Biol Ther*. (2021) 21:991–7. doi: 10.1080/14712598.2021.1928629

24. Bahar I, Kaiserman I, McAllum P, Rootman D, Slomovic A. Subconjunctival Bevacizumab Injection for Corneal Neovascularization. *Cornea*. (2008) 27:142–7. doi: 10.1097/ICO.0b013e318159019f

25. Ohr M, Kaiser PK. Intravitreal aflibercept injection for neovascular (wet) age-related macular degeneration. *Expert Opin Pharmacother*. (2012) 13:585–91. doi: 10.1517/14656566.2012.658368

26. Hussain RM, Hariprasad SM, Ciulla TA. Ophthalmic surgery, lasers and imaging. *Retina*. (2017) 48:780–4. doi: 10.3928/23258160-20170928-01

27. Ghasemi Falavarjani K, Nguyen QD. Adverse events and complications associated with intravitreal injection of anti-VEGF agents: a review of literature. *Eye*. (2013) 27:787–94. doi: 10.1038/eye.2013.107

28. Conlon R, Saheb H, Ahmed IIK. Canadian journal of ophthalmology. *J Canadien d'Ophtalmologie*. (2017) 52:114–24. doi: 10.1016/j.jcjo.2016.07.013

29. Mitchell P, Liew G, Gopinath B, Wong TY. Age-related macular degeneration. *Lancet*. (2018) 392:1147–59. doi: 10.1016/S0140-6736(18)31550-2

30. Mansour SE, Browning DJ, Wong K, Flynn HW Jr, Bhavsar AR. The evolving treatment of diabetic retinopathy. *Clin Ophthalmol*. (2020) 14:653–78. doi: 10.2147/OPTH.S236637

31. Sharma S. Diagnosis of infectious diseases of the eye. *Eye*. (2012) 26:177–84. doi: 10.1038/eye.2011.275

32. de Andrade FA, Fiorot SHS, Benchimol EI, Provenzano J, Martins VJ, Levy RA. The autoimmune diseases of the eyes. *Autoimmun Rev*. (2016) 15:258–71. doi: 10.1016/j.autrev.2015.12.001

33. Gautam M, Gupta R, Singh P, Verma V, Verma S, Mittal P, et al. Intracameral drug delivery: a review of agents, indications, and outcomes. *J Ocul Pharmacol Ther*. (2023) 39:102–16. doi: 10.1089/jop.2022.0144

34. Kim HM, Woo SJ. Ocular drug delivery to the retina: current innovations and future perspectives. *Pharmaceutics*. (2021) 13:13. doi: 10.3390/pharmaceutics13010108

35. Yavuz B, Pehlivan SB, Unlü N. Dendrimeric systems and their applications in ocular drug delivery. *TheScientificWorldJOURNAL*. (2013) 2013:732340. doi: 10.1155/2013/732340

36. Jünemann AGM, Chorągiewicz T, Ozimek M, Grieb P, Rejdak R. Drug bioavailability from topically applied ocular drops. Does drop size matter? *Ophthalmology J*. (2016) 1:29–35. doi: 10.5603/OJ.2016.0005

37. Gaudana R, Ananthula HK, Parenky A, Mitra AK. Ocular drug delivery. *AAPS J*. (2010) 12:348–60. doi: 10.1208/s12248-010-9183-3

38. Honda M, Asai T, Oku N, Araki Y, Tanaka M, Ebihara N. Liposomes and nanotechnology in drug development: focus on ocular targets. *Int J Nanomedicine*. (2013) 8:495. doi: 10.2147/IJN.S30725

39. Yasukawa T, Ogura Y, Tabata Y, Kimura H, Wiedemann P, Honda Y. Drug delivery systems for vitreoretinal diseases. *Prog Retin Eye Res*. (2004) 23:253–81. doi: 10.1016/j.preteyeres.2004.02.003

40. Ranch K, Chawnani D, Jani H, Acharya D, Patel CA, Jacob S, et al. An update on the latest strategies in retinal drug delivery. *Expert Opin Drug Deliv*. (2024) 21:695–712. doi: 10.1080/17425247.2024.2358886

41. Wang R, Gao Y, Liu A, Zhai G. A review of nanocarrier-mediated drug delivery systems for posterior segment eye disease: challenges analysis and recent advances. *J Drug Target*. (2021) 29:687–702. doi: 10.1080/1061186X.2021.1878366

42. Meza-Rios A, Navarro-Partida J, Armendariz-Borunda J, Santos A. Therapies based on nanoparticles for eye drug delivery. *Ophthalmol Therapy*. (2020) 9:1–14. doi: 10.1007/s40123-020-00257-7

43. Jumelle C, Gholizadeh S, Annabi N, Dana R. Advances and limitations of drug delivery systems formulated as eye drops. *J Control Release*. (2020) 321:1–22. doi: 10.1016/j.jconrel.2020.01.057

44. Bonilla L, Espina M, Severino P, Cano A, Ettcheto M, Camins A, et al. Lipid nanoparticles for the posterior eye segment. *Pharmaceutics*. (2022) 14:90. doi: 10.3390/pharmaceutics14010090

45. Baig MS, Karade SK, Ahmad A, Khan MA, Haque A, Webster TJ, et al. Lipid-based nanoparticles: innovations in ocular drug delivery. *Front Mol Biosci*. (2024) 11:11. doi: 10.3389/fmolb.2024.1421959

46. Tsung T-H, Tsai Y-C, Lee H-P, Chen Y-H, Lu D-W. Biodegradable polymer-based drug-delivery Systems for Ocular Diseases. *Int J Mol Sci*. (2023) 24:12976. doi: 10.3390/ijms241612976

47. Biswas A, Choudhury AD, Bisen AC, Agrawal S, Sanap SN, Verma SK, et al. Trends in formulation approaches for sustained drug delivery to the posterior segment of the eye. *AAPS PharmSciTech*. (2023) 24:217. doi: 10.1208/s12249-023-02673-x

48. Bhandari M, Nguyen S, Yazdani M, Utheim TP, Hagesaether E. The therapeutic benefits of Nanoencapsulation in drug delivery to the anterior segment of the eye: a systematic review. *Front Pharmacol*. (2022) 13:13. doi: 10.3389/fphar.2022.903519

49. Vaneev A, Tikhomirova V, Chesnokova N, Popova E, Beznos O, Kost O, et al. Nanotechnology for topical drug delivery to the anterior segment of the eye. *Int J Mol Sci*. (2021) 22:12368. doi: 10.3390/ijms222212368

50. Li Q, Weng J, Wong SN, Thomas Lee WY, Chow SF. Nanoparticulate drug delivery to the retina. *Mol Pharm*. (2021) 18:506–21. doi: 10.1021/acs.molpharmaceut.0c00224

51. Shafiq M, Rafique M, Cui Y, Pan L, Do C-W, Ho EA. An insight on ophthalmic drug delivery systems: focus on polymeric biomaterials-based carriers. *J Control Release*. (2023) 362:446–67. doi: 10.1016/j.jconrel.2023.08.041

52. Akhter MH, Ahmad I, Alshahrani MY, Al-Harbi AI, Khalilullah H, Afzal O, et al. Drug delivery challenges and current Progress in Nanocarrier-based ocular therapeutic system. *Gels*. (2022) 8:82. doi: 10.3390/gels8020082

53. Zhang T, Jin X, Zhang N, Jiao X, Ma Y, Liu R, et al. Targeted drug delivery vehicles mediated by nanocarriers and aptamers for posterior eye disease therapeutics: barriers, recent advances and potential opportunities. *Nanotechnology*. (2022) 33:162001. doi: 10.1088/1361-6528/ac46d5

54. Mobaraki M, Soltani M, Zare Harofte S, Zoudani EL, Daliri R, Aghamirsalim M, et al. Biodegradable nanoparticle for cornea drug delivery: focus review. *Pharmaceutics*. (2020) 12:1232. doi: 10.3390/pharmaceutics12121232

55. Yang Y, Lockwood A. Topical ocular drug delivery systems: innovations for an unmet need. *Exp Eye Res*. (2022) 218:109006. doi: 10.1016/j.exer.2022.109006

56. Tawfik M, Chen F, Goldberg JL, Sabel BA. Nanomedicine and drug delivery to the retina: current status and implications for gene therapy. *Naunyn Schmiedeberg's Arch Pharmacol*. (2022) 395:1477–507. doi: 10.1007/s00210-022-02287-3

57. Khiev D, Mohamed ZA, Vichare R, Paulson R, Bhatia S, Mohapatra S, et al. Emerging Nano-formulations and nanomedicines applications for ocular drug delivery. *Nano*. (2021) 11:173. doi: 10.3390/nano11010173

58. Chaudhari P, Lewis SA, Ghate V. Nanotechnology-based non-invasive strategies in ocular therapeutics: approaches, limitations to clinical translation, and safety concerns. *Contact Lens and Anterior Eye*. (2025):102367. doi: 10.1016/j.clae.2025.102367

59. Kim JH, Kim JH, Kim K-W, Kim MH, Yu YS. Intravenously administered gold nanoparticles pass through the blood–retinal barrier depending on the particle size, and induce no retinal toxicity. *Nanotechnology*. (2009) 20:505101. doi: 10.1088/0957-4484/20/50/505101

60. Singh R, Batoki JC, Ali M, Bonilha VL, Anand-Apte B. Nanomedicine: nanotechnology. *Biol Med*. (2020) 28:102205. doi: 10.1016/j.nano.2020.102205

61. Sun Y-N, Wang C-D, Zhang X-M, Ren L, Tian X-H. Shape dependence of gold nanoparticles onIn VivoAcute toxicological effects and biodistribution. *J Nanosci Nanotechnol*. (2011) 11:1210–6. doi: 10.1166/jnn.2011.3094

62. Kim JH, Kim MH, Jo DH, Yu YS, Lee TG, Kim JH. The inhibition of retinal neovascularization by gold nanoparticles via suppression of VEGFR-2 activation. *Biomaterials*. (1865) 32:1865–71. doi: 10.1016/j.biomaterials.2010.11.030

63. Bakri SJ, Pulido JS, Mukherjee P, Marler RJ, Mukhopadhyay D. Absence of histologic retinal toxicity of intravitreal NANOGOLD in a rabbit model. *Retina*. (2008) 28:147–9. doi: 10.1097/IAE.0b013e3180dc9360

64. Luo L-J, Jian H-J, Harroun SG, Lai J-Y, Unnikrishnan B, Huang C-C. Targeting nanocomposites with anti-oxidative/inflammatory/angiogenic activities for synergistically alleviating macular degeneration. *Appl Mater Today*. (2021) 24:101156. doi: 10.1016/j.apmt.2021.101156

65. Jo DH, Kim JH, Son JG, Piao Y, Lee TG, Kim JH. Inhibitory activity of gold and silica nanospheres to vascular endothelial growth factor (VEGF)-mediated angiogenesis is determined by their sizes. *Nano Res*. (2014) 7:844–52. doi: 10.1007/s12274-014-0445-8

66. Hayashi A, Naseri A, Pennesi ME, de Juan E. Subretinal delivery of immunoglobulin G with gold nanoparticles in the rabbit eye. *Jpn J Ophthalmol*. (2009) 53:249–56. doi: 10.1007/s10384-009-0655-x

67. Dong Y, Wan G, Yan P, Qian C, Li F, Peng G. Fabrication of resveratrol coated gold nanoparticles and investigation of their effect on diabetic retinopathy in streptozotocin induced diabetic rats. *J Photochem Photobiol B Biol*. (2019) 195:51–7. doi: 10.1016/j.jphotobiol.2019.04.012

68. Karthikeyan B, Kalishwaralal K, Sheikpranbabu S, Deepak V, Haribalaganesh R, Gurunathan S. Gold nanoparticles downregulate VEGF-and IL-1β-induced cell proliferation through Src kinase in retinal pigment epithelial cells. *Exp Eye Res*. (2010) 91:769–78. doi: 10.1016/j.exer.2010.09.003

69. Karakoçak BB, Raliya R, Davis JT, Chavalmane S, Wang W-N, Ravi N, et al. Biocompatibility of gold nanoparticles in retinal pigment epithelial cell line. *Toxicol in Vitro*. (2016) 37:61–9. doi: 10.1016/j.tiv.2016.08.013

70. Wang Y, Xia R, Hu H, Peng T. Biosynthesis, characterization and cytotoxicity of gold nanoparticles and their loading with N-acetylcarnosine for cataract treatment. *J Photochem Photobiol B Biol*. (2018) 187:180–3. doi: 10.1016/j.jphotobiol.2018.08.014

71. Mitra M, Kandalam M, Rangasamy J, Shankar B, Maheswari UK, Swaminathan S, et al. Molecular vision (2013) 19:1029.

72. Trigueros S, Domènech EB, Toulis V, Marfany G. In vitro gene delivery in retinal pigment epithelium cells by plasmid DNA-wrapped gold nanoparticles. *Gen Dent*. (2019) 10:289. doi: 10.3390/genes10040289

73. Apaolaza PS, Busch M, Asin-Prieto E, Peynshaert K, Rathod R, Remaut K, et al. Hyaluronic acid coating of gold nanoparticles for intraocular drug delivery: evaluation of the surface properties and effect on their distribution. *Exp Eye Res*. (2020) 198:108151. doi: 10.1016/j.exer.2020.108151

74. Maulvi FA, Patil RJ, Desai AR, Shukla MR, Vaidya RJ, Ranch KM, et al. Effect of gold nanoparticles on timolol uptake and its release kinetics from contact lenses: in vitro and in vivo evaluation. *Acta Biomater*. (2019) 86:350–62. doi: 10.1016/j.actbio.2019.01.004

75. Li Q, Ma C, Ma Y, Ma Y, Mao Y, Meng Z. Journal of biomaterials science. *Polymer Edition*. (2021) 32:1618–34. doi: 10.1080/09205063.2021.1927656

76. Guo Q, Jia L, Qinggeletu R, Zhang XY. In vitro and in vivo evaluation of ketotifen-gold nanoparticles laden contact lens for controlled drug delivery to manage conjunctivitis. *J Drug Delivery Sci Technol*. (2021) 64:102538. doi: 10.1016/j.jddst.2021.102538

77. Salem HF, Ahmed SM, Omar MM. Liposomal flucytosine capped with gold nanoparticle formulations for improved ocular delivery. *Drug Des Devel Ther*. (2016) 10:277. doi: 10.2147/DDDT.S91730

78. Pereira DV, Petronilho F, Pereira HRSB, Vuolo F, Mina F, Possato JC, et al. Effects of gold nanoparticles on endotoxin-induced uveitis in rats. *Invest Ophthalmol Vis Sci*. (2012) 53:8036. doi: 10.1167/iovs.12-10743

79. Sharma A, Tandon A, Tovey JCK, Gupta R, Robertson JD, Fortune JA, et al. Nanomedicine: nanotechnology. *Biol Med*. (2011) 7:505–13. doi: 10.1016/j.nano.2011.01.006

80. Tandon A, Sharma A, Rodier JT, Klibanov AM, Rieger FG, Mohan RR. BMP7 gene transfer via gold nanoparticles into stroma inhibits corneal fibrosis in vivo. *PLoS One*. (2013) 8:e66434. doi: 10.1371/journal.pone.0066434

81. Neves J d, Bahia MF, Amiji MM, Sarmento B. Mucoadhesive nanomedicines: characterization and modulation of mucoadhesion at the nanoscale. *Expert Opin Drug Deliv*. (2011) 8:1085–104. doi: 10.1517/17425247.2011.586334

82. Hock N, Racaniello GF, Aspinall S, Denora N, Khutoryanskiy VV, Bernkop-Schnürch A. Thiolated nanoparticles for biomedical applications: mimicking the workhorses of our body. *Advan Sci*. (2022) 9:e2102451. doi: 10.1002/advs.202102451

83. Yeh Y-C, Creran B, Rotello VM. Gold nanoparticles: preparation, properties, and applications in bionanotechnology. *Nanoscale*. (1871) 4:1871–80. doi: 10.1039/C1NR11188D

84. Alex S, Tiwari A. Functionalized gold nanoparticles: synthesis, properties and applications—a review. *J Nanosci Nanotechnol*. (1869) 15:1869–94. doi: 10.1166/jnn.2015.9718

85. Bansal SA, Kumar V, Karimi J, Singh AP, Kumar S. Role of gold nanoparticles in advanced biomedical applications. *Nanoscale Advan*. (2020) 2:3764–87. doi: 10.1039/D0NA00472C

86. Cabuzu D, Cirja A, Puiu R, Grumezescu AM. Biomedical applications of gold nanoparticles. *Curr Top Med Chem*. (2015) 15:1605–13. doi: 10.2174/1568026615666150414144750

87. Cordeiro M, Ferreira Carlos FF, Pedrosa P, Lopez A, Baptista PV. Gold nanoparticles for diagnostics: advances towards points of care. *Diagnostics*. (2016) 6:6. doi: 10.3390/diagnostics6040043

88. Kong F-Y, Zhang J-W, Li R-F, Wang Z-X, Wang W-J, Wang W. Unique roles of gold nanoparticles in drug delivery, targeting and imaging applications. *Molecules*. (2017) 22:22. doi: 10.3390/molecules22091445

89. Marangoni VS, Cancino-Bernardi J, Zucolotto V. Synthesis, Physico-chemical properties, and biomedical applications of gold Nanorods—a review. *J Biomed Nanotechnol*. (2016) 12:1136–58. doi: 10.1166/jbn.2016.2218

90. Masse F, Desjardins P, Ouellette M, Couture C, Omar MM, Pernet V, et al. Synthesis of Ultrastable gold nanoparticles as a new drug delivery system. *Molecules*. (2019) 24:24. doi: 10.3390/molecules24162929

91. Masse F, Ouellette M, Lamoureux G, Boisselier E. Gold nanoparticles in ophthalmology. *Med Res Rev*. (2019) 39:302–27. doi: 10.1002/med.21509

92. Raiche-Marcoux G, Loiseau A, Maranda C, Poliquin A, Boisselier E. Parametric drug release optimization of anti-inflammatory drugs by gold nanoparticles for topically applied ocular therapy. *Int J Mol Sci*. (2022) 23:23. doi: 10.3390/ijms232416191

93. Gaudreault M, Carrier P, Larouche K, Leclerc S, Giasson M, Germain L, et al. Influence of Sp1/Sp3 expression on corneal epithelial cells proliferation and differentiation properties in reconstructed tissues. *Investig Ophthalmol Vis Sci*. (2003) 44:1447. doi: 10.1167/iovs.02-0707

94. Germain L, Auger FA, Grandbois E, Guignard R, Giasson M, Boisjoly H, et al. Pathobiology: journal of immunopathology. *Mol Cell Biol*. (1999) 67:140–7. doi: 10.1159/000028064

95. Bisson F, Rochefort E, Lavoie A, Larouche D, Zaniolo K, Simard-Bisson C, et al. Irradiated human dermal fibroblasts are as efficient as mouse fibroblasts as a feeder layer to improve human epidermal cell culture lifespan. *Int J Mol Sci*. (2013) 14:4684–704. doi: 10.3390/ijms14034684

96. Le-Bel G, Giasson CJ, Deschambeault A, Carrier P, Germain L, Guérin SL. The presence of a feeder layer improves human corneal endothelial cell proliferation by altering the expression of the transcription factors Sp1 and NFI. *Exp Eye Res*. (2018) 176:161–73. doi: 10.1016/j.exer.2018.07.009

97. Montoya LA, Pluth MD. Selective turn-on fluorescent probes for imaging hydrogen sulfide in living cells. *Chem Commun*. (2012) 48:4767–9. doi: 10.1039/c2cc30730h

98. Loiseau A, Zhang L, Hu D, Salmain M, Mazouzi Y, Flack R, et al. Core–Shell gold/silver nanoparticles for localized surface Plasmon resonance-based naked-eye toxin biosensing. *ACS Appl Mater Interfaces*. (2019) 11:46462–71. doi: 10.1021/acsami.9b14980

99. Chen P, Liedberg B. Curvature of the localized surface Plasmon resonance peak. *Anal Chem*. (2014) 86:7399–405. doi: 10.1021/ac500883x

100. Chen P, Tran NT, Wen X, Xiong Q, Liedberg B. Inflection point of the localized surface Plasmon resonance peak: a general method to improve the sensitivity. *ACS Sensors*. (2017) 2:235–42. doi: 10.1021/acssensors.6b00633

101. Ouellette M, Masse F, Lefebvre-Demers M, Maestracci Q, Grenier P, Millar R, et al. Insights into gold nanoparticles as a mucoadhesive system. *Sci Rep*. (2018) 8:14357. doi: 10.1038/s41598-018-32699-2

102. Onugwu AL, Nwagwu CS, Onugwu OS, Echezona AC, Agbo CP, Ihim SA, et al. Nanotechnology based drug delivery systems for the treatment of anterior segment eye diseases. *J Control Release*. (2023) 354:465–88. doi: 10.1016/j.jconrel.2023.01.018

103. Zimmer A, Kreuter J. Microspheres and nanoparticles used in ocular delivery systems. *Adv Drug Deliv Rev*. (1995) 16:61–73. doi: 10.1016/0169-409X(95)00017-2

104. Hironaka K, Inokuchi Y, Tozuka Y, Shimazawa M, Hara H, Takeuchi H. Design and evaluation of a liposomal delivery system targeting the posterior segment of the eye. *J Control Release*. (2009) 136:247–53. doi: 10.1016/j.jconrel.2009.02.020

105. Alvarez-Trabado J, Diebold Y, Sanchez A. Designing lipid nanoparticles for topical ocular drug delivery. *Int J Pharm*. (2017) 532:204–17. doi: 10.1016/j.ijpharm.2017.09.017

106. Lai SK, Wang Y-Y, Hanes J. Mucus-penetrating nanoparticles for drug and gene delivery to mucosal tissues. *Adv Drug Deliv Rev*. (2009) 61:158–71. doi: 10.1016/j.addr.2008.11.002

107. Toropainen E, Fraser-Miller SJ, Novakovic D, Del Amo EM, Vellonen K-S, Ruponen M, et al. Biopharmaceutics of topical ophthalmic suspensions: importance of viscosity and particle size in ocular absorption of indomethacin. *Pharmaceutics*. (2021) 13:452. doi: 10.3390/pharmaceutics13040452

108. Jo DH, Kim JH, Lee TG, Kim JH. Nanomedicine: Nanotechnology. *Biol Med*. (2015) 11:1603–11. doi: 10.1016/j.nano.2015.04.015

109. Mahaling B, Katti DS. Understanding the influence of surface properties of nanoparticles and penetration enhancers for improving bioavailability in eye tissues in vivo. *Int J Pharm*. (2016) 501:1–9. doi: 10.1016/j.ijpharm.2016.01.053

110. Mahaling B, Katti DS. Nanomedicine: Nanotechnology. *Biol Med*. (2016) 12:2149–60. doi: 10.1016/j.nano.2016.05.017

111. Reznickova A, Slavikova N, Kolska Z, Kolarova K, Belinova T, Hubalek Kalbacova M, et al. PEGylated gold nanoparticles: stability, cytotoxicity and antibacterial activity. *Colloids Surf A Physicochem Eng Asp*. (2019) 560:26–34. doi: 10.1016/j.colsurfa.2018.09.083

112. Henson JC, Brickell A, Kim J-W, Jensen H, Mehta JL, Jensen M. PEGylated gold nanoparticle toxicity in cardiomyocytes: assessment of size, concentration, and time dependency. *IEEE Trans Nanobiosci*. (2022) 21:387–94. doi: 10.1109/TNB.2022.3154438

113. Sasaki A. Recent advances in the standardization of fluorescence microscopy for quantitative image analysis. *Biophys Rev*. (2022) 14:33–9. doi: 10.1007/s12551-021-00871-0

114. Hickey SM, Ung B, Bader C, Brooks R, Lazniewska J, Johnson IRD, et al. Fluorescence microscopy—an outline of hardware, biological handling, and fluorophore considerations. *Cells*. (2022) 11:35. doi: 10.3390/cells11010035

115. Fan J, Cheng Y, Sun M. Functionalized gold nanoparticles: synthesis, properties and biomedical applications. *Chem Rec*. (2020) 20:1474–504. doi: 10.1002/tcr.202000087

116. Chatterjee S, Lou X-Y, Liang F, Yang Y-W. Surface-functionalized gold and silver nanoparticles for colorimetric and fluorescent sensing of metal ions and biomolecules. *Coord Chem Rev*. (2022) 459:214461. doi: 10.1016/j.ccr.2022.214461

117. Boisselier E, Salmon L, Ruiz J, Astruc D. How to very efficiently functionalize gold nanoparticles by "click" chemistry. *Chem Commun*. (2008):5788. doi: 10.1039/b812249k

118. Le Droumaguet C, Wang C, Wang Q. Fluorogenic click reaction. *Chem Soc Rev*. (2010) 39:1233–9. doi: 10.1039/B901975H

119. Perala SRK, Kumar S. On the mechanism of metal nanoparticle synthesis in the Brust–Schiffrin method. *Langmuir: ACS J Surfaces and Colloids*. (2013) 29:9863–73. doi: 10.1021/la401604q

120. Lu Y, Chen W In: DMP Mingos, editor. Gold clusters, colloids and nanoparticles I. Berlin: Springer International Publishing (2014). 117.

121. Rubinson KA, Krueger S. Poly(ethylene glycol)s 2000–8000 in water may be planar: a small-angle neutron scattering (SANS) structure study. *Polymer*. (2009) 50:4852–8. doi: 10.1016/j.polymer.2009.08.023

122. Pai SS, Hammouda B, Hong K, Pozzo DC, Przybycien TM, Tilton RD. The conformation of the poly(ethylene glycol) chain in mono-PEGylated lysozyme and mono-PEGylated human growth hormone. *Bioconjug Chem*. (2011) 22:2317–23. doi: 10.1021/bc2003583

123. Liu D, Li P-Y, Wang S-J, Gong B, Lu T, Li G-Y. Spectrochimica Acta. *Part A, Molecular and Biomolecular Spectroscopy*. (2022) 271:120872. doi: 10.1016/j.saa.2022.120872

124. Stewart DJ, Dalton MJ, Long SL, Kannan R, Yu Z, Cooper TM, et al. Steric hindrance inhibits excited-state relaxation and lowers the extent of intramolecular charge transfer in two-photon absorbing dyes. *Physical Chem Chem Physics: PCCP*. (2016) 18:5587–96. doi: 10.1039/C5CP07716H

125. Lyu Y, Becerril LM, Vanzan M, Corni S, Cattelan M, Granozzi G, et al. The interaction of amines with gold nanoparticles. *Adv Mater*. (2024) 36:2211624. doi: 10.1002/adma.202211624

126. Qi J, Hu X, Dong X, Lu Y, Lu H, Zhao W, et al. Towards more accurate bioimaging of drug nanocarriers: turning aggregation-caused quenching into a useful tool. *Adv Drug Deliv Rev*. (2019) 143:206–25. doi: 10.1016/j.addr.2019.05.009

127. Phan HT, Haes AJ. What does nanoparticle stability mean? *J Phys Chem C*. (2019) 123:16495–507. doi: 10.1021/acs.jpcc.9b00913

128. Amina SJ, Guo B. A review on the synthesis and functionalization of gold nanoparticles as a drug delivery vehicle. *Int J Nanomedicine*. (2020) 15:9823–57. doi: 10.2147/IJN.S279094

129. Pissuwan D, Niidome T, Cortie MB. The forthcoming applications of gold nanoparticles in drug and gene delivery systems. *J Control Release*. (2011) 149:65–71. doi: 10.1016/j.jconrel.2009.12.006

130. Chen PC, Mwakwari SC, Oyelere AK. Nanotechnology. *Sci Applic*. (2008) 1:45–66. doi: 10.2147/NSA.S3707

131. Wu Y, Ali MRK, Chen K, Fang N, El-Sayed MA. Gold nanoparticles in biological optical imaging. *Nano Today*. (2019) 24:120–40. doi: 10.1016/j.nantod.2018.12.006

132. Sun M, Liu F, Zhu Y, Wang W, Hu J, Liu J, et al. Salt-induced aggregation of gold nanoparticles for photoacoustic imaging and photothermal therapy of cancer. *Nanoscale*. (2016) 8:4452–7. doi: 10.1039/C6NR00056H

133. Zhang M, Shao S, Yue H, Wang X, Zhang W, Chen F, et al. High stability au NPs: from design to application in nanomedicine. *Int J Nanomedicine*. (2021) 16:6067–94. doi: 10.2147/IJN.S322900

134. Kyriakides TR, Raj A, Tseng TH, Xiao H, Nguyen R, Mohammed FS, et al. Biocompatibility of nanomaterials and their immunological properties. *Biomed Mater*. (2021) 16:042005. doi: 10.1088/1748-605X/abe5fa

135. Martínez R., Navarro Poupard M. F., Álvarez A., Soprano E., Migliavacca M. in Nanoparticles for biomedical applications (Eds.: E. J. Chung, L. Leon and C. Rinaldi), Elsevier, Ch. 2, London, (2020), pp. 5.

136. Xavier J, Vincent S, Meder F, Vollmer F. Advances in optoplasmonic sensors – combining optical nano/microcavities and photonic crystals with plasmonic nanostructures and nanoparticles. *Nano*. (2018) 7:1–38. doi: 10.1515/nanoph-2017-0064

137. Arcas AS, Jaramillo L, Costa NS, Allil RCSB, Werneck MM. Localized surface plasmon resonance-based biosensor on gold nanoparticles for Taenia solium detection. *Appl Opt*. (2021) 60:8137. doi: 10.1364/AO.432990

138. Bansil R, Turner BS. Mucin structure, aggregation, physiological functions and biomedical applications. *Curr Opin Colloid Interface Sci*. (2006) 11:164–70. doi: 10.1016/j.cocis.2005.11.001

139. Mackie AR, Goycoolea FM, Menchicchi B, Caramella CM, Saporito F, Lee S, et al. Innovative methods and applications in Mucoadhesion research. *Macromol Biosci*. (2017) 17:1600534. doi: 10.1002/mabi.201600534

140. Corfield AP. Biochimica et Biophysica Acta (BBA). *General Subjects*. (2015) 1850:236–52. doi: 10.1016/j.bbagen.2014.05.003

141. Hori Y. Secreted mucins on the ocular surface. *Investig Ophthalmol Vis Sci*. (2018) 59:DES151. doi: 10.1167/iovs.17-23623

142. Ludwig A. The use of mucoadhesive polymers in ocular drug delivery. *Adv Drug Deliv Rev*. (2005) 57:1595–639. doi: 10.1016/j.addr.2005.07.005

143. Mantle M, Allen A. A colorimetric assay for glycoproteins based on the periodic acid/Schiff stain. *Biochem Soc Trans*. (1978) 6:607–9. doi: 10.1042/bst0060607

144. Robins JH, Abrams GD, Pincock JA. The structure of Schiff reagent aldehyde adducts and the mechanism of the Schiff reaction as determined by nuclear magnetic resonance spectroscopy. *Can J Chem*. (1980) 58:339–47. doi: 10.1139/v80-055

145. Guo Y, Ma Y, Chen X, Li M, Ma X, Cheng G, et al. Mucus penetration of surface-engineered nanoparticles in various pH microenvironments. *ACS Nano*. (2023) 17:2813–28. doi: 10.1021/acsnano.2c11147

146. Rodrigues GA, Lutz D, Shen J, Yuan X, Shen H, Cunningham J, et al. Topical drug delivery to the posterior segment of the eye: addressing the challenge of preclinical to clinical translation. *Pharm Res*. (2018) 35:245. doi: 10.1007/s11095-018-2519-x

147. Loiseau A, Raîche-Marcoux G, Maranda C, Bertrand N, Boisselier E. Animal models in eye research: focus on corneal pathologies. *Int J Mol Sci*. (2023) 24:16661. doi: 10.3390/ijms242316661

148. Shen J, Durairaj C, Lin T, Liu Y, Burke J. Ocular pharmacokinetics of Intravitreally administered Brimonidine and dexamethasone in animal models with and without blood–retinal barrier breakdown. *Invest Ophthalmol Vis Sci*. (2014) 55:1056. doi: 10.1167/iovs.13-13650

149. Hung KH, Yeh LK. Ex Vivo and In Vivo Animal Models for mechanical and chemical injuries of corneal epithelium. *J Vis Exp*. (2022) 182: e63217. doi: 10.3791/63217

150. Mascolini MV, Toniolo I, Carniel EL, Fontanella CG. Ex vivo, in vivo and in silico studies of corneal biomechanics: a systematic review. *Physical Eng Sci Med*. (2024) 47:403–41. doi: 10.1007/s13246-024-01403-2

151. Stradleigh TW, Ishida AT. Fixation strategies for retinal immunohistochemistry. *Prog Retin Eye Res*. (2015) 48:181–202. doi: 10.1016/j.preteyeres.2015.04.001

152. Espana EM, Birk DE. Composition, structure and function of the corneal stroma. *Exp Eye Res*. (2020) 198:108137. doi: 10.1016/j.exer.2020.108137

153. Yang H, Yu PK, Cringle SJ, Sun X, Yu D-Y. Iridal vasculature and the vital roles of the iris. *J Nat Sci*. (2015) 1:157.

154. Stauss HM, Rarick KR, Leick KM, Burkle JW, Rotella DL, Anderson MG. American journal of physiology. *Regulatory, Integrative Comparative Physiol*. (2011) 300:R1333–43. doi: 10.1152/ajpregu.00561.2010

155. Bloemendal H, de Jong W, Jaenicke R, Lubsen NH, Slingsby C, Tardieu A. Ageing and vision: structure, stability and function of lens crystallins. *Prog Biophys Mol Biol*. (2004) 86:407–85. doi: 10.1016/j.pbiomolbio.2003.11.012

156. Hendrickson A. Development of retinal layers in prenatal human retina. *Am J Ophthalmol*. (2016) 161:29–35.e1. doi: 10.1016/j.ajo.2015.09.023

157. Rajendran Nair DS, Seiler MJ, Patel KH, Thomas V, Martinez Camarillo JC, Humayun MS, et al. Tissue engineering strategies for retina regeneration. *Appl Sci*. (2021) 11:2154. doi: 10.3390/app11052154

158. Masland RH. The fundamental plan of the retina. *Nat Neurosci*. (2001) 4:877–86. doi: 10.1038/nn0901-877

159. Le Goff MM, Bishop PN. Adult vitreous structure and postnatal changes. *Eye*. (2008) 22:1214–22. doi: 10.1038/eye.2008.21

160. Laradji A, Karakocak BB, Kolesnikov AV, Kefalov VJ, Ravi N. Hyaluronic acid-based gold nanoparticles for the topical delivery of therapeutics to the retina and the retinal pigment epithelium. *Polymers*. (2021) 13:3324. doi: 10.3390/polym13193324

161. Puglia C, Santonocito D, Romeo G, Intagliata S, Romano GL, Strettoi E, et al. Lipid nanoparticles traverse non-corneal path to reach the posterior eye segment: in vivo evidence. *Molecules*. (2021) 26:4673. doi: 10.3390/molecules26154673

162. Qi Q, Wei Y, Zhang X, Guan J, Mao S. Challenges and strategies for ocular posterior diseases therapy via non-invasive advanced drug delivery. *J Control Release*. (2023) 361:191–211. doi: 10.1016/j.jconrel.2023.07.055

163. Hughes PM, Olejnik O, Chang-Lin JE, Wilson CG. Topical and systemic drug delivery to the posterior segments. *Adv Drug Deliv Rev*. (2010) 57:2010–32. doi: 10.1016/j.addr.2005.09.004

164. Gu Y, Xu C, Wang Y, Zhou X, Fang L, Cao F. Multifunctional nanocomposites based on liposomes and layered double hydroxides conjugated with Glycylsarcosine for efficient topical drug delivery to the posterior segment of the eye. *Mol Pharm*. (2019) 16:2845–57. doi: 10.1021/acs.molpharmaceut.8b01136

165. Bok D. The retinal pigment epithelium: a versatile partner in vision. *J Cell Sci*. (1993) 1993:189–95. doi: 10.1242/jcs.1993.Supplement_17.27

166. Boulton M, Dayhaw-Barker P. The role of the retinal pigment epithelium: topographical variation and ageing changes. *Eye*. (2001) 15:384–9. doi: 10.1038/eye.2001.141

167. Hamann S. International review of cytology, vol. 215. United States: Academic Press (2002). 395 p. Available at: https://www.biblio.com/book/international-review-cytology-vol-215-survey/d/1548311742

168. Besch D, Jägle H, Scholl HPN, Seeliger MW, Zrenner E. Inherited multifocal RPE-diseases: mechanisms for local dysfunction in global retinoid cycle gene defects. *Vis Res*. (2003) 43:3095–108. doi: 10.1016/j.visres.2003.09.020

169. Strauss O. The retinal pigment epithelium in visual function. *Physiol Rev*. (2005) 85:845–81. doi: 10.1152/physrev.00021.2004

170. Valiente-Soriano FJ, Salinas-Navarro M, Di Pierdomenico J, García-Ayuso D, Lucas-Ruiz F, Pinilla I, et al. Tracing the retina to analyze the integrity and phagocytic capacity of the retinal pigment epithelium. *Sci Rep*. (2020) 10:7273. doi: 10.1038/s41598-020-64131-z

171. Kwon W, Freeman SA. Phagocytosis by the retinal pigment epithelium: recognition, resolution, recycling. *Front Immunol*. (2020) 11:11. doi: 10.3389/fimmu.2020.604205

frontiers | Frontiers in Medicine

TYPE Original Research
PUBLISHED 25 March 2025
DOI 10.3389/fmed.2025.1569767

OPEN ACCESS

EDITED BY
Georgios D. Panos,
Aristotle University of Thessaloniki, Greece

REVIEWED BY
Songtao Yuan,
Nanjing Medical University, China
Bhim Bahadur Rai,
Australian National University, Australia

*CORRESPONDENCE
Juan Li
✉ lijuan0915@126.com
Ziqing Gao
✉ gaozq70@163.com

†These authors have contributed equally to this work

RECEIVED 01 February 2025
ACCEPTED 13 March 2025
PUBLISHED 25 March 2025

CITATION
Li N, Dong J, Wang J, Ren X, Guo J, Li J and Gao Z (2025) Treatment of traumatic subluxation of the crystalline lens with custom-made capsular hook.
Front. Med. 12:1569767.
doi: 10.3389/fmed.2025.1569767

Treatment of traumatic subluxation of the crystalline lens with custom-made capsular hook

Ning Li[1†], Jie Dong[2†], Jianfeng Wang[1], Xiaohui Ren[1], Juanjuan Guo[1], Juan Li[1*] and Ziqing Gao[1*]

[1]Department of Ophthalmology, The First Affiliated Hospital of Bengbu Medical University, Bengbu, China, [2]Department of Ophthalmology, Shenyang Fourth People's Hospital, Shenyang, China

Objective: Traumatic rupture of the lens zonules, leading to lens dislocation, is common in clinical practice and often requires surgical treatment. We aim to study capsular hooks, formed from 5-0 or 6-0 polypropylene sutures by heat shaping, to fix the capsular bag and reshape the lens zonular.

Methods: A retrospective analysis was conducted on 16 patients (16 eyes) with traumatic subluxation of the crystalline lens who visited our department. Capsular hooks were fabricated using 5-0 or 6-0 polypropylene sutures, shape by heat, to fix the anterior capsular opening. The sutures passed out of the eye, punctured the sclera and traversed it parallel to the limbus for 2–3 mm, exiting through the conjunctiva to form a suture tunnel parallel to the limbus, securing the suture and preventing loosening. Changes in best-corrected visual acuity (BCVA) after surgery, intraocular lens centration, and surgical complications were assessed.

Results: Post-operative follow-up was 6–30 months, with an average of 10 ± 5.9 months. The BCVA improved from a pre-operative median of 2.15 (1.67) logMAR to a postoperative median of 0.25 (0.38) logMAR (paired sample Wilcoxon signed-rank test, $Z = 3.516$, $p < 0.001$). Postoperatively, the intraocular lenses were well-centered, the capsular bags were securely fixed, and no capsular hooks dislodgement occurred. One patient experienced combined vitreous hemorrhage during surgery. Another patient (case 2) developed rhegmatogenous retinal detachment 2 years post-surgery. After pars plana vitrectomy, the retina was reattached, and the final visual acuity remained stable.

Conclusion: Long-term follow-up data suggest that using custom-made capsular hooks offers a reliable solution for maintaining long-term stability of the capsular bag in patients with traumatic crystalline lens subluxation. This technique maintains the centering of the IOL postoperatively, showing effectiveness and safety, and it holds potential for broader clinical application.

KEYWORDS

zonules, lens dislocation, traumatic cataract, capsular hook, capsular tension ring

1 Introduction

The zonules of the lens are crucial for maintaining its normal position (1). Congenital or acquired factors can damage the zonules, resulting in lens dislocation, a condition characterized by abnormal lens positioning (2). Crystalline lens dislocation is a frequently encountered ophthalmological condition. Zonular defects are commonly seen in congenital conditions, such as Marfan syndrome (3–5), spherophakia (6), and homocystinuria (2, 7). Traumatic

rupture of the crystalline lens zonules, leading to lens dislocation, is also common in clinical practice and often requires surgical treatment (8, 9).

Clinically, lens dislocation is often classified into mild (<4 clock hours), moderate (4–8 clock hours), and severe (>8 clock hours) based on the extent of zonular rupture (10). For mild subluxation of the lens, the combination of a standard capsular tension ring (CTR) and intraocular lens (IOL) implantation in the capsular bag can effectively solve the problem of centering the IOL (11). However, for moderate and severe subluxation of the lens, surgical challenges increase. Some patients may not be candidates for IOL implantation in a single procedure, often requiring staged lens extraction followed by suspended IOL implantation (12, 13).

With advancements in surgical techniques and evolving treatment approaches, we have abandoned the traditional surgical method in the treatment of traumatic subluxation of the crystalline lens. Instead, we should try our best to preserve the patient's capsular bag and reshape the lens zonular. In the absence of commercial capsular fixation devices, and for the purpose of solving the long-term fixation problem of the capsular bag, we used custom-made capsular hooks, formed from 5-0 or 6-0 polypropylene sutures by heat shaping, to fix the capsular bag. This approach has been applied to 16 patients with traumatic crystalline lens subluxation, yielding favorable outcomes. This technique can also be used for congenital subluxation of the lens and lens dislocation caused by other zonular lesions.

2 Materials and methods

2.1 Patient eligibility

In this study, a retrospective analysis was conducted on 16 patients (16 eyes) with traumatic crystalline lens subluxation who were treated at the Department of Ophthalmology, The First Affiliated Hospital of Bengbu Medical University from April 2021 to August 2024. Eligible patients had a history of ocular trauma and were diagnosed with lens subluxation through slit-lamp microscope examination after pupil dilation. Exclusion criteria included congenital lens subluxation, active infectious ocular conditions, and sever vitreoretional complications, such as retinal detachment, subreinal hemorrhage, etc. Before the operation, the patients were fully informed about the surgical procedure and signed the informed consent forms. All procedures were conducted following the principles of the 1964 Declaration of Helsinki and its subsequent amendments. Approved by the Hospital Ethics Committee (2022033), this study introduced a new surgical technology. Patients were followed up at 6–30 months postoperatively, with an average of 10 ± 5.9 months.

2.2 Surgical technique

The custom-made capsular hook is formed by heat shaping of 5-0 or 6-0 polypropylene sutures (Ethicon, Somerville, New Jersey, United States) into a hook shape. This suture is approved for use in ophthalmic surgeries. The manufacturing method of the custom-made capsular hook is the same as that of Jin et al. (14). The suture is heat-shaped into an acute angle (<15°) by a cautery device, and the head end of the hook is about 1 mm long. All surgeries were performed by the same experienced doctor (NL). Retrobulbar block anesthesia was administered using 2% lidocaine. In cases where vitreous herniation into the anterior chamber was noted, either a limbal or pars plana approach was employed to remove the incarcerated vitreous, thereby preventing intraoperative vitreous disturbance. The 25G vitrectomy system (Constellation Vision, Alcon Laboratories Inc., Fort Worth, Texas, United States) was used. A 3 o'clock clear corneal side incision was made, and sodium hyaluronate gel (HYMIOS, Bloomage Biotechnology Co., Ltd., Shandong, China) was injected into the anterior chamber. The main incision was a 2.8 mm clear corneal incision, positioned to avoid the area with the most severe lens dislocation. The anterior capsule was punctured with a 25G needle, and continuous circular capsulorhexis was completed, with the opening measuring 5 mm. Capsular hooks (CapsuleCare, Madhu Instruments Pvt. Ltd., New Deli, India) were inserted to prevent further extension of the zonular rupture, with 2–4 hooks placed depending on the extent of the rupture. Adequate hydrodissection was performed to facilitate nuclear rotation and reduce intraoperative zonular injury. Phacoemulsification (Centurion, Alcon Laboratories Inc., Fort Worth, Texas, United States) was carried out with an energy of 60%, a negative pressure of 450 mmHg, a bottle height of 80 cmH_2O, and a flow rate of 40 cc/min. The lens cortex was aspirated with a negative pressure of 500 mmHg, a bottle height of 75 cmH_2O, and a flow rate of 35 cc/min. Before removing the phacoemulsification needle and aspiration needle from the anterior chamber, sodium hyaluronate gel was injected from the side incision to maintain the stability of the anterior chamber and prevent further extension of the lens zonular rupture. A injectable CTR (ACPi-11, Bausch & Lomb, Rochester, NY, United States) was implanted into the capsular bag, along with a foldable IOL. The capsular hooks were removed. A 6-0 or 5-0 polypropylene suture with a long needle entered the anterior chamber via a clear corneal incision, passed through the back of the iris and the front of the capsular bag, and penetrated the sclera 2 mm behind the limbus at the area with the most severe lens dislocation. The needle, held by a needle holder, punctured the sclera and traversed it parallel to the limbus for 2–3 mm, exiting through the conjunctiva to form a suture tunnel parallel to the limbus, securing the suture and preventing loosening. While tightening the suture, a 25G retinal forceps (MR-G114T-4, Suzhou Mingren, Suzhou, China) clamped the hook and introduced it into the anterior chamber. The tail of the hook was inserted into the capsulorhexis opening, and the retinal forceps were released. The tension of the suture outside the eye was adjusted to ensure that the hook exerted a pulling force on the anterior capsular opening. One hook can fix the zonular rupture of less than 6 clock hours, two hooks can fix the zonular rupture of approximately 8 clock hours, and for some patients with zonular rupture exceeding 8 clock hours, three hooks can be made for fixation. After adjusting the tension of the hook, the exposed suture was cut off and pushed into the scleral tunnel. The sodium hyaluronate gel in the anterior chamber and capsular bag was aspirated to deepen the anterior chamber and close the incision. For patients who underwent total vitrectomy, the capsular hook fixation was performed after the vitrectomy. The surgical process of the 6-0 polypropylene suture custom-made hook is shown in Figure 1. The surgical process of the 5-0 polypropylene suture custom-made hook is shown in Figure 2.

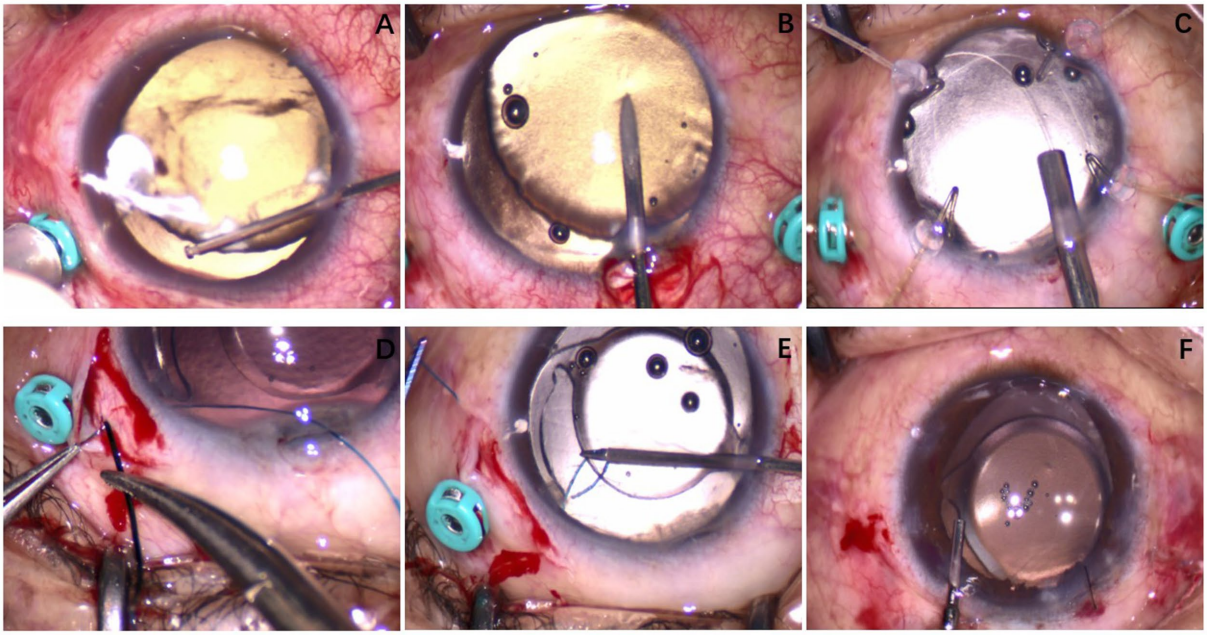

FIGURE 1
Case 4: A custom-made capsular hook was made using a 6-0 polypropylene suture. **(A)** The patient had zonular dehiscence approximately at the 9 o'clock position, secondary glaucoma, and corneal edema during the operation; anterior chamber vitreous herniation was visible. An anterior chamber vitrectomy was performed. **(B)** The anterior capsule was punctured with a 25G needle. **(C)** After phacoemulsification cataract extraction, a CTR was implanted into the capsular bag. **(D)** The 6-0 polypropylene suture was passed through the sclera. **(E)** The custom-made capsular hook was used to fix the capsulorhexis opening of the lens. **(F)** At the end of the operation, the intraocular lens was centrally positioned.

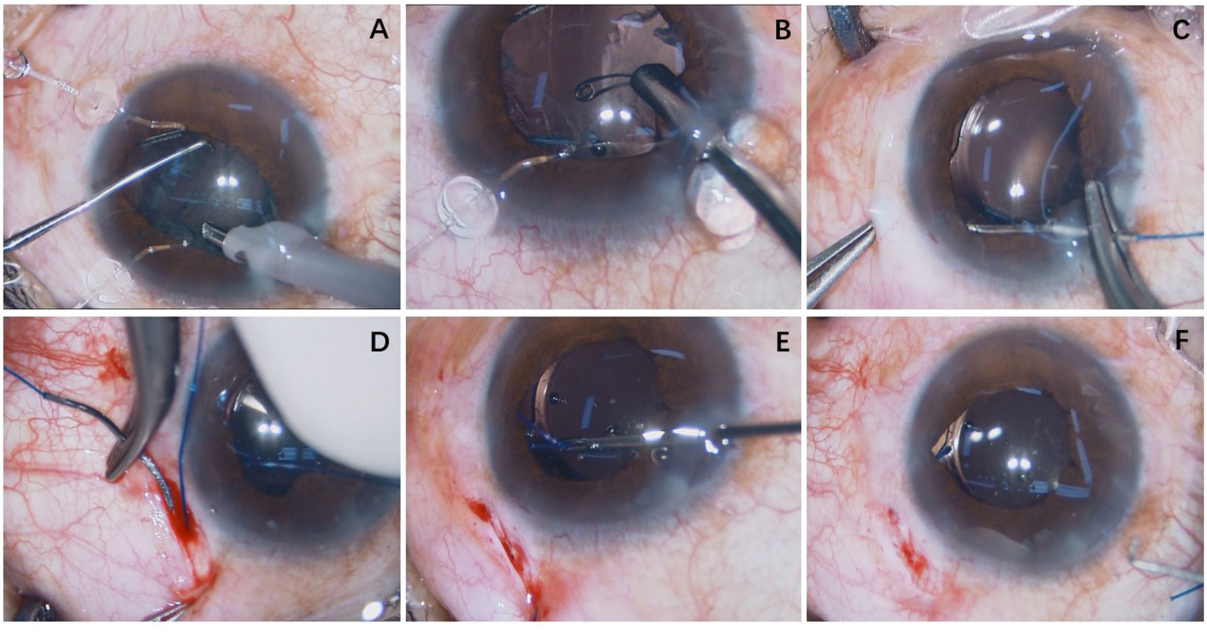

FIGURE 2
Case 16: A custom-made capsular hook was made using a 5-0 polypropylene suture. **(A)** Phacoemulsification cataract extraction was completed using two capsular hooks. **(B)** The capsular tension ring was implanted into the capsular bag before the irrigation/aspiration step. **(C)** A 5-0 polypropylene suture needle was advanced through the anterior chamber through a clear corneal incision, passing posterior to the iris and anterior to the capsular bag and exiting the eye 2 mm posterior to the limbus. **(D)** The polypropylene suture was passed through the sclera. **(E)** The custom-made capsular hook was used to fix the capsulorhexis opening of the lens. **(F)** At the end of the operation, the intraocular lens was centrally positioned.

2.3 Ophthalmic examinations

All examinations were conducted by the same experienced ophthalmologist (NL). Pre-operative examination items included slit-lamp microscopy, ultrasound biomicroscopy (UBM-840, Quantel Medical, Clermont-Ferrand, France), B-mode ultrasound, and ophthalmic biometry (IOLMaster 700, Carl Zeiss Meditec AG, Jena, Germany). Intraocular pressure was measured by a non-contact tonometer (NT-530, Nidek Co., Ltd., Gamagori, Japan). Best-corrected visual acuity (BCVA) values, measured by an experienced optometrist, were converted to logMAR. Follow-up visits were conducted at 1, 3, 6, and 12 months after the operation. These visits included evaluating the centration of the intraocular lens, position of the hook, and exposure of sutures under the slit-lamp biomicroscope, as well as optometry, intraocular pressure measurement, and fundus examination. The BCVA at the final follow-up was meticulously recorded and will be employed for in-depth statistical analysis. Post-operative complications were also recorded.

2.4 Statistical analysis

The BCVA data of patients before and after surgery were meticulously collated. Since the analysis focuses solely on the single variable of visual acuity, multiple corrections are not required. Both groups' datasets are complete, with no missing values, allowing for a complete case analysis. To assess normality, the Shapiro–Wilk test was performed on the data.

To assess the normality of the preoperative and postoperative differences, the Shapiro–Wilk test was performed. A p-value greater than 0.05 indicated that the differences followed a normal distribution. Additionally, a histogram of the normality test was incorporated to further evaluate whether the data conformed to a normal distribution. If the normal probability plot exhibited a bell-shaped curve (higher in the middle and lower at both ends), it suggested that the data followed a normal distribution. Conversely, a deviation from this pattern implied non-normality.

For variables that followed a normal distribution, data were summarized as mean ± standard deviation (SD). In contrast, for variables that did not conform to a normal distribution, data were reported as median and interquartile range (IQR) to better represent the central tendency and variability of the dataset.

For normally distributed differences, a paired sample t-test was conducted for statistical analysis, Cohen's d was reported to quantify the effect size. However, if the Shapiro–Wilk test yielded a significant result ($p < 0.05$), indicating that the differences deviated from a normal distribution, a paired sample Wilcoxon signed-rank test was applied instead, with the Hodges–Lehmann median difference reported as a measure of effect size. To assess the uncertainty of the Hodges–Lehmann median difference, bootstrapping was performed using the boot package in R version 4.2.2 (The R Foundation, Vienna, Austria). The original difference data were resampled 1,000 times, and the 95% confidence interval for the Hodges–Lehmann median difference was computed.

A p-value less than 0.05 was considered statistically significant. Statistical analyses were conducted using SPSS version 25.0 (IBM Corp., Armonk, NY, United States) and R version 4.2.2 (The R Foundation, Vienna, Austria).

3 Results

This technique was applied to 16 patients (16 eyes) (Table 1). Seven patients (cases 1, 2, 3, 4, 6, 10, and 16) received capsular hooks made of 5-0 polypropylene sutures, whereas the remaining patients had capsular hooks made of 6-0 polypropylene sutures. Seven patients (cases 1, 2, 4, 9, 11, 13, and 15) had secondary glaucoma before surgery, with intraocular pressure normalizing post-treatment. Ten patients (cases 4, 5, 6, 7, 9, 10, 11, 12, 13, and 15) had vitreous herniation in the anterior chamber preoperatively and underwent anterior vitrectomy via the limbal or pars plana approach. One patient (case 8) had vitreous hemorrhage before surgery and underwent total vitrectomy through the pars plana approach. Ten patients received one hook, five patients with zonular rupture of more than 6 clock hours received two hooks, and one patient (case 13) with 10 clock hours of zonular dehiscence received three hooks. One patient (case 10) had puncture site bleeding during the second needle fixation. Due to the large amount of bleeding, blood dispersed into the vitreous cavity requiring total vitrectomy through the pars plana approach during the operation. No other intraoperative complications occurred. Post-operative follow-up was 6–30 months, with an average of 10 ± 5.9 months.

The Shapiro–Wilk normality test indicated that the differences in BCVA did not follow a normal distribution ($W = 0.855$, $p = 0.016$). This finding was further supported by the histogram, which suggested a skewed distribution (Figure 3). Consequently, a paired sample Wilcoxon signed-rank test was performed, revealing a significant improvement in BCVA from a preoperative median of 2.15 (1.67) logMAR to a postoperative median of 0.25 (0.38) logMAR ($Z = 3.519$, $p < 0.001$). The Hodges–Lehmann median difference was −1.75 (95% CI: −2.10 to −1.40), suggesting that the median postoperative BCVA was 1.75 logMAR units lower than preoperative values. After surgery, all patients maintained well-centered IOLs, with no complications such as dislocation of the IOL-capsular bag complex, hook loosening, suture exposure (Figure 4), vitreous hemorrhage, or cystoid macular edema. One patient (case 2) had rhegmatogenous retinal detachment 2 years after surgery. After pars plana vitrectomy, the retina was reattached, and the final visual acuity remained stable.

4 Discussion

Lens subluxation is a common clinical condition. In China, traditional surgical approaches for lens dislocation, particularly in cases of moderate to severe subluxation, often involve removing the dislocated lens and performing one-stage or two-stage suspension of the IOL. These approaches, however, do not preserve the lens zonules and may lead to vitreous disturbance during the procedure. The probability of post-operative vitreoretinal complications such as vitreous hemorrhage and retinal detachment is high. Furthermore, these procedures can cause considerable surgical trauma, resulting in poor visual prognosis and adverse physical, psychological, and economic effects for the patient.

However, advancements in technology, surgical methods, material innovation, and conceptual developments have led to a paradigm shift in the management of moderate and severe subluxation. Current approaches emphasize the preservation of the capsular bag and restoration of the lens zonules whenever feasible. Surgical success

TABLE 1 Demographic and clinical data of eyes with subluxated lens.

Case	Sex	Age	Eye	Zonular defect (clock hours)	BCVA (logMAR)		IOP (mmHg)		Follow-up (months)	Management	Hooks used for fixation	Complications		
					Preoperative	Postoperative	Preoperative	Postoperative				Preoperative	Intraoperative	Postoperative
1	F	66	L	8	0.7	0.2	36	15	12	Phaco + CTR + capsular hook + goniosynechialysis	2	SG	None	None
2	M	56	R	6	2.1	0.5	42	18	30	Phaco + CTR + capsular hook + goniosynechialysis	1	SG	None	RRD
3	M	71	L	5	2.4	0.3	15	14	8	Phaco + CTR + capsular hook	1	None	None	None
4	M	49	L	9	2.3	0.2	Over	19	6	Phaco + CTR + capsular hook + two-point pars plana vitrectomy	2	SG, vitreous herniation	none	none
5	M	54	R	5	0.8	0.1	13	14	10	Phaco + CTR + capsular hook + two-point pars plana vitrectomy	1	Vitreous herniation	None	None
6	F	70	R	8	0.7	0.1	18	16	12	Phaco + CTR + capsular hook + one-point pars plana vitrectomy	2	Vitreous herniation	None	None
7	M	68	L	6	2.4	0.5	16	17	6	Phaco + CTR + capsular hook + limbal vitrectomy	1	Vitreous herniation	None	None
8	M	39	R	6	2.5	0.5	15	16	10	Phaco + CTR + capsular hook + pars plana vitrectomy	1	VH	None	None
9	M	53	L	5	3.0	0.8	Over	19	8	Phaco + CTR + capsular hook + limbal vitrectomy	1	SG, vitreous herniation	None	None
10	M	74	L	7	0.6	0.4	14	15	6	Phaco + CTR + capsular hook + pars plana vitrectomy	2	Vitreous herniation	VH	None
11	F	76	R	7	2.5	0.2	32	15	12	Phaco + CTR + capsular hook + one-point vitrectomy	2	Vitreous herniation	None	None

(Continued)

10.3389/fmed.2025.1569767

10.3389/fmed.2025.1569767

TABLE 1 (Continued)

Case	Sex	Age	Eye	Zonular defect (clock hours)	BCVA (logMAR)		IOP (mmHg)		Follow-up (months)	Management	Hooks used for fixation	Complications		
					Preoperative	Postoperative	Preoperative	Postoperative				Preoperative	Intraoperative	Postoperative
12	M	37	R	5	1.1	0	13	15	6	Phaco + CTR + capsular hook	1	Vitreous herniation	None	None
13	M	69	L	10	1.7	0.3	45	17	10	Phaco + CTR + capsular hook + limbal vitrectomy	3	SG, vitreous herniation	None	None
14	F	74	R	5	2.4	0.3	38	14	12	Phaco + CTR + capsular hook + goniosynechialysis	1	SG	None	None
15	F	61	R	6	0.4	0	11	15	6	Phaco + CTR + capsular hook + two-point pours plana vitrectomy	1	SG, vitreous herniation	None	None
16	M	55	L	7	2.2	0.1	18	17	6	Phaco + CTR + capsular hook	1	None	None	None

F, female; M, male; BCVA, best-corrected visual acuity; IOP, intraocular pressure; SG, secondary glaucoma; VH, vitreous hemorrhage; RRD, rhegmatogenous retinal detachment.

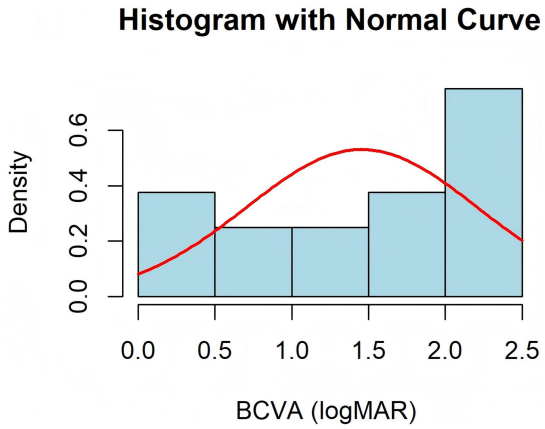

FIGURE 3
Histogram plot of BCVA.

relies on the use of long-term capsular fixation devices during and after the operation. Common intraoperative capsular stabilization devices include iris and capsular hooks. Due to their structural advantages and optimal angles, capsular hooks offer superior intraoperative support in stabilizing the capsule and preventing the extension of zonular rupture. Consequently, they are widely used in lens dislocation surgery. Proper post-operative capsular fixation is the key to maintaining long-term capsular stability and centering the IOL.

Various approaches for managing lens dislocation have been employed domestically and internationally. In 1998, Professor Robert Cionni's team reported the treatment of four patients with lens subluxation using the MCTR, achieving favorable outcomes (15). Many studies have also reported that the treatment of subluxation of the lens using the MCTR has good post-operative results (16–18). Doctors represented by Professor Ike Ahmed in Canada choose the capsular tension segment (CTS) for long-term capsular fixation (19, 20). An Israeli doctor, Assia, used the capsular anchor for capsular fixation. He first conducted experiments on rabbit eyes, with a good fixation effect (21). Subsequently, Professor Yokrat Ton reported the application of the capsular anchor in patients with subluxation of the lens and dislocation of the IOL-capsular bag complex. The long-term capsular fixation effect was good, and the IOL was centered (22). Japanese scholars, Asano et al. (23), reported the use of a capsular hook made of 5-0 polypropylene sutures for capsular fixation, with patients followed up for 2 years. The position of the IOL was good, and the capsular bag complex remained stable for a long time. This method evolved from the early self-made capsular hook of 5-0 polypropylene sutures by this team and was improved to achieve good results (24). Polish doctors, Krix-Jachym et al. (25), reported that the use of iris hooks for long-term capsular fixation also achieved good results. Professor Karadag et al. (26) also reported applying this surgical method.

Professor Jiang Yongxiang was an early adopter of the MCTR for lens dislocation treatment in China, achieving excellent results. It was also the best treatment method. However, MCTR is currently out of stock in China, preventing many patients from benefiting from this successful treatment option. Professor Haiying Jin reported the use of polypropylene sutures to make iris hooks in 2018 (27). In 2019, he reported the use of 5-0 polypropylene sutures, heat-shaped into

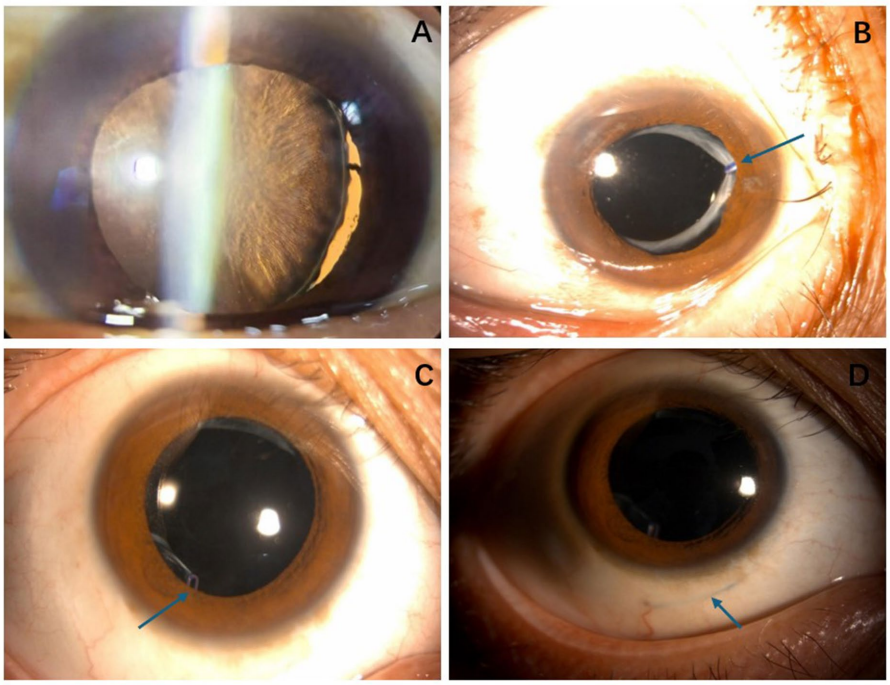

FIGURE 4
(A) Case 16: Lens zonule rupture occurred at approximately the 6 o'clock position after trauma. **(B)** Case 16: Six months after surgery, the intraocular lens was properly centered, and the capsular tension ring remained securely fixed (arrow). **(C)** Case 12: One year after the operation, the intraocular lens remained centered, and the tension ring could be seen at the lower anterior capsular opening (arrow). **(D)** Case 12: One year after the surgery, the 6-0 polypropylene sutures were located within the scleral lamellae, with no signs of loosening or exposure (arrow).

capsular hooks, to stabilize the dislocated intraocular lens-capsular bag complex. Later, he applied this technique to 10 patients with lens dislocation and achieved good results (28). Later, this method was quickly adopted throughout China. In the absence of commercial capsular fixation devices such as MCTR, CTS, and capsular anchors, it effectively solved the long-term fixation problem of the capsular bag. Moreover, this approach does not entail any extra financial strain on patients, ensuring that the treatment remains cost-accessible and alleviating potential economic concerns during the medical process. Professor Jiang Yongxiang's team also reported the treatment of 148 eyes of patients with Marfan syndrome using CTR combined with implantable capsular hooks. Compared with the MCTR, the CTR-CH procedure was a feasible, safe, and efficient approach for managing EL in patients with MFS (29).

According to the safety and effectiveness data provided above, our team adopted a surgical approach for traumatic crystalline lens subluxation, achieving favorable outcomes. This approach involves phacoemulsification cataract extraction, using capsular hooks, CTR, and IOL implantation in the capsular bag combined with anterior capsular fixation with custom-made capsular hooks. However, most studies primarily examine congenital lens dislocation, particularly in conditions like Marfan and Marchesani syndromes, with limited focus on the surgical management of traumatic lens dislocation. Blunt ocular trauma is a major cause of traumatic subluxation of the lens. Due to external forces, the rupture or relaxation of the lens zonules occurs, resulting in an abnormal lens position. This condition can also result in cataract formation and visual impairment. Traumatic lens dislocation is distinct from other subluxation types in that it may involve injuries other than zonular injuries, such as angle recession, iris root rupture, traumatic mydriasis, hyphema, and vitreous hemorrhage. Zonular rupture can cause damage to the ciliary epithelium and ora serrata, potentially resulting in vitreous hemorrhage and retinal detachment. Trauma-induced vitreous anterior membrane injury can lead to vitreous incarceration in the anterior chamber and forward movement of the lens-iris diaphragm due to lens dislocation. The consequent angle closure and angle recession can cause secondary glaucoma. Elevated pre-operative intraocular pressure and corneal edema may occur in some patients as a result of vitreous contact with the corneal endothelium. Surgical intervention is necessary to address these complications. Unlike other lens dislocation surgeries, the removal of incarcerated vitreous from the anterior chamber is required to facilitate the procedure and prevent interference during the procedure. In some cases, anterior vitreous removal and indentation may be necessary to examine the ora serrata and ciliary epithelium for possible lacerations. For patients with vitreous hemorrhage, vitrectomy is often required in one stage, which brings more challenges to our surgery.

Of the 16 patients in our study, seven had secondary glaucoma. All patients had elevated intraocular pressure preoperatively, and conservative treatments showed minimal effect. Corneal edema was pronounced, which hindered surgical visibility. Thus, we used a 25-gauge vitrectomy system for illumination, which enabled us to perform continuous circular capsulorhexis and resolve the issue of the absent red reflex. The support and elevation provided by the light guide fiber also helped prevent lens sinking, limiting further lens dislocation. Anterior vitrectomy was performed in cases 4, 9, 11, and 13. Cases 1, 2, and 15 underwent goniosynechialysis under gonioscopy. The above surgical operations effectively resolved pupil block and

separated adherent or narrow angles, thus addressing the glaucoma. The post-operative intraocular pressure remained stable for a long time, confirming the success of our approach to secondary glaucoma. Cases 5, 6, 7, and 15 had vitreous incarceration in the anterior chamber. However, the vitreous incarceration and lens dislocation did not cause pupil block, angle stenosis, or adhesions, so intraocular pressure remained stable. Anterior vitrectomy was performed in these cases to resolve the vitreous incarceration. Intraoperative indentation did not reveal any lacerations in the ciliary epithelium or ora serrata. Case 8, which had a large amount of pre-operative vitreous hemorrhage, underwent combined anterior and posterior segment surgery. This approach addressed the lens dislocation and managed the associated vitreoretinal conditions, leading to a favorable outcome.

In case 10, vitreous hemorrhage occurred when the second needle of the 5-0 suture punctured the tissue. This was likely due to the suture needle damaging blood vessels in the pars plana of the ciliary body. Although we avoided puncturing at the 3 and 9 o'clock positions, vitreous hemorrhage still occurred. This indicates that vitreous hemorrhage is a common complication during suture needle puncture, but the incidence is not high. Due to timely vitrectomy, the visual prognosis was not considerably impacted by the hemorrhage. Case 2 developed retinal detachment 2 years post-surgery. We did not perform anterior vitrectomy or check the ora serrata during the operation, with the pre-operative ultrasound biomicroscopy (UBM) and B-ultrasound showing abnormalities in the ciliary epithelium and ora serrata. Thus, we concluded a tractional horseshoe-shaped hole caused by post-operative vitreous detachment contributed to the retinal detachment. Intraoperative exploration confirmed this, revealing no vitreous proliferation or traction at the suture site. After vitrectomy, the retina was reattached and visual acuity remained stable. This underscores the potential risk of retinal detachment following surgery, which necessitates thorough pre-operative discussions with patients. Case 9 had an iris root rupture, which was successfully repaired using the modified sewing machine method in a single-stage procedure, resulting in good post-operative iris morphology. Case 12 was a patient with high myopia. Pre-operative UBM showed zonular laxity, but the lens position remained centered without significant deviation. During surgery, a CTR and foldable IOL were implanted in the capsular bag. When the viscoelastic agent was aspirated, a zonular rupture occurred at approximately the 6 o'clock position. This was likely due to the zonular disease associated with high myopia, liquefied vitreous, and elevated intraoperative perfusion pressure. To address the rupture, a 6-0 polypropylene suture was used to secure the anterior capsular opening at the 6 o'clock position. After the operation, the IOL was centered, with a well-fixed capsular bag. This case illustrates that self-made capsular hooks can be an effective solution for centering the IOL in the presence of zonular rupture caused by intraoperative injury.

Through the surgical management of 16 patients with traumatic lens subluxation, we have identified several key principles. First, detailed preoperative evaluations, such as anterior segment photography, intraocular pressure measurement, ocular B-ultrasound, and UBM examination (30), are extremely necessary. Intraoperatively, careful vitreous management, especially when dealing with incarcerated vitreous in the anterior chamber or vitreoretinal complications such as vitreous hemorrhage, is crucial. The main incision should avoid the area with the most severe lens dislocation. Good continuous circular capsulorhexis is a crucial step in preserving the capsular bag. Due to the lack of zonular traction and poor capsular tension, a 25 g needle can be used to puncture the anterior capsule and create a flap. To prevent capsule tearing or complications with hook placement during or after the operation, the size of the capsulorhexis opening should not be too large, which could result in poor fixation. Preventing further zonular injury during the procedure requires maintaining anterior chamber stability. Before making the main incision, sodium hyaluronate gel should be injected to maintain the stability of the anterior chamber. According to the range of lens dislocation of the patient, an appropriate number of capsular stabilization devices should be selected, with the capsular hook being highly recommended. Adequate hydrodissection is important to reduce resistance during nuclear rotation, which helps prevent the worsening of zonular rupture. Perfusion pressure should be reduced during the operation, and sodium hyaluronate gel should be injected into the anterior chamber before withdrawing the phacoemulsification and aspiration needles. When performing CTR implantation, if zonular support is insufficient, the CTR should be placed in the capsular bag before cortex aspiration. However, if the zonular support is acceptable, the CTR can be implanted after cortex aspiration. The maximum support of CTR should be directed toward the area with the most severe dislocation. This facilitates the effective expansion of the capsular bag and ensures full outward expansion of the equatorial portion. Therefore, CTR implantation is an essential material for the long-term stability of the IOL-capsular bag complex. When selecting an IOL, foldable lenses should be prioritized for easier positioning, and one-piece non-plate IOLs are particularly recommended. After implanting the IOL, the capsular hook can be removed. 5-0 and 6-0 polypropylene sutures can be heat-shaped into hook shapes, with no difference in the long-term fixation effect of the capsular bag. The hook should be formed at an acute angle, with the head retaining a minimum length of 1 mm to prevent loosening after the procedure. Once the suture exits the eye, it should pass through the sclera before the hook is implanted. The 6-0 polypropylene suture, being thinner and having a sharper needle, is recommended for creating the capsular hook, especially when considering the difficulty of passing through the sclera. For patients who need intraoperative indentation or vitrectomy, it is crucial to secure the hook after properly managing the vitreous to prevent the loosening of the hook from the capsular opening. If loosening occurs, the hook can be repositioned by performing indentation of the pars plana under microscopic guidance. In the case of iris root rupture, repair should be attempted during the procedure. Some patients in the 16-patient cohort experienced mydriasis, with the largest dilation reaching 6 mm. Pupiloplasty was not performed during the operation, and photophobia was not detected after the operation. Therefore, for patients with traumatic mydriasis with photophobia, pupiloplasty can be completed in the second stage. Regular post-operative follow-up and rational drug use are also important.

However, our study also has certain limitations. The cohort size was relatively modest, which may not comprehensively represent the full spectrum of clinical scenarios. Moreover, the follow-up duration for a subset of patients was inadequate. This shortcoming restricts our ability to draw definitive conclusions regarding the long-term stability and fixation effectiveness of the capsular bag, which undoubtedly necessitates extended and more in - depth observation. Another notable limitation lies in the singularity of the surgical approach we utilized. In the realm of capsular bag fixation, there exist several

well-established techniques, such as the MCTR and CTS. Regrettably, we did not perform a side-by-side comparison between our method and these alternative procedures. Such a comparative analysis would have been invaluable in discerning the relative advantages and disadvantages of each approach, thereby providing more robust evidence-based guidance for clinical practice.

5 Conclusion

According to long-term follow-up data, heat-shaped 5-0 or 6-0 polypropylene sutures can be used in patients with traumatic crystalline lens subluxation to fix the anterior capsular opening with custom-made capsular hooks, thereby achieving long-term stability of the capsular bag. This technique maintains the centering of the IOL postoperatively, showing effectiveness and safety. Moreover, this approach does not entail any extra financial strain on patients, and it holds potential for broad clinical applications.

Data availability statement

The datasets presented in this study can be found in online repositories. The names of the repository/repositories and accession number(s) can be found in the article/supplementary material.

Ethics statement

The studies involving humans were approved by the First Affiliated Hospital of Bengbu Medical University. The studies were conducted in accordance with the local legislation and institutional requirements. The participants provided their written informed consent to participate in this study. Written informed consent was obtained from the individual(s) for the publication of any potentially identifiable images or data included in this article.

Author contributions

NL: Conceptualization, Data curation, Formal analysis, Funding acquisition, Methodology, Project administration, Writing – original draft, Writing – review & editing. JD: Conceptualization, Data curation, Investigation, Methodology, Project administration, Writing – review & editing. JFW: Conceptualization, Data curation, Writing – review & editing. XHR: Conceptualization, Data curation, Writing – review & editing. JJG: Writing – review & editing. JL: Investigation, Methodology, Writing – review & editing. ZQG: Formal analysis, Methodology, Writing – review & editing.

Funding

The author(s) declare that financial support was received for the research and/or publication of this article. This work was supported by Anhui Provincial Department of Science and Technology, Anhui Province Clinical Medical Research Transformation Project (202427b10020008); Department of Education of Anhui Province, Key Project of Scientific Research Project (Natural Science) of Higher Education institutions of Anhui Province (2022AH051419); and New Technology New Project of the First Affiliated Hospital of Bengbu Medical College (2022033).

Conflict of interest

The authors declare that the research was conducted in the absence of any commercial or financial relationships that could be construed as a potential conflict of interest.

Generative AI statement

The authors declare that no Gen AI was used in the creation of this manuscript.

Publisher's note

References

1. Bassnett S. Zinn's zonule. *Prog Retin Eye Res*. (2021) 82:100902. doi: 10.1016/j.preteyeres.2020.100902

2. Chee SP, Ti SE, Chan SW. Management of the subluxated crystalline lens: a review. *Clin Exp Ophthalmol*. (2021) 49:1091–101. doi: 10.1111/ceo.13975

3. Jin G, Zou M, Li L, Liu Z, Young C, Qi H, et al. Corneal biomechanics and their association with severity of lens dislocation in Marfan syndrome. *Int Ophthalmol*. (2024) 44:148. doi: 10.1007/s10792-024-03079-9

4. Rasul A, Roos L, Groth K, Riise P, Bach-Holm D, Kessel L. Epidemiology of ectopia lentis and outcomes after surgery in a Danish population. *J Cataract Refract Surg*. (2022) 48:1394–402. doi: 10.1097/j.jcrs.0000000000001008

5. Kjeldsen S, Andersen N, Groth K, Larsen D, Hjortdal J, Berglund A, et al. Ocular morbidity in Marfan syndrome: a nationwide epidemiological study. *Br J Ophthalmol*. (2023) 107:1051–5. doi: 10.1136/bjophthalmol-2021-320871

6. Jin GM, Fan M, Cao QZ, Lin JX, Zhang YC, Lin JQ, et al. Trends and characteristics of congenital ectopia lentis in China. *Int J Ophthalmol*. (2018) 11:1545–9. doi: 10.18240/ijo.2018.09.19

7. Mohamed AS, Al Anzi T, Alhashem A, Alrukban H, Al Harbi F, Mohamed S. Clinical, biochemical and molecular characteristics of classic homocystinuria in Saudi Arabia and the impact of newborn screening on prevention of the complications: a tertiary center experience. *JIMD Rep*. (2024) 66:e12454. doi: 10.1002/jmd2.12454

8. Wang J, Liu Q, Lou H. Clinical analysis of surgical treatment of lens dislocation. *Int Eye Sci*. (2020) 5:3.

9. Glickman A, Szczucki B, Kalivoda EJ, Furiato A, Cabrera G. Bedside ocular ultrasound diagnosis of a traumatic lens dislocation. *Cureus*. (2021) 13:e14666. doi: 10.7759/cureus.14666

10. Liu Y, Chen T, Jiang Y. Correlation of posterior segment lesions with anterior segment biometric parameters and FBN1 genotype in patients with Marfan

syndrome. *Chin J Ophthalmol*. (2024) 60:601–10. doi: 10.3760/cma.j.cn112142-20230829-00065

11. Shen T, Ping X. Diagnosis and treatment strategies for subluxation of the lens. *Chin J Ophthalmol*. (2021) 57:5. doi: 10.3760/cma.j.cn112142-20201015-00686

12. Wang A, Fan Q, Jiang Y, Lu Y. Primary scleral-fixated posterior chamber intraocular lenses in patients with congenital lens subluxation. *BMC Ophthalmol*. (2021) 21:411. doi: 10.1186/s12886-021-02182-0

13. Fiorentzis M, Viestenz A, Heichel J, Seitz B, Hammer T, Viestenz A. Methods of fixation of intraocular lenses according to the anatomical structures in trauma eyes. *Clin Anat*. (2018) 31:6–15. doi: 10.1002/ca.22898

14. Jin H, Ou Z, Zhang Q. Intrascleral fixation of implantable polypropylene capsular hook (s): a new sutureless technique to reposition dislocated intraocular lens-capsular bag complex. *Retina*. (2019) 39:S44–9. doi: 10.1097/IAE.0000000000001915

15. Cionni RJ, Osher RH. Management of profound zonular dialysis or weakness with a new endocapsular ring designed for scleral fixation. *J Cataract Refract Surg*. (1998) 24:1299–306. doi: 10.1016/s0886-3350(98)80218-6

16. Vasavada AR, Praveen MR, Vasavada VA, Yeh R-Y, Srivastava S, Koul A, et al. Cionni ring and in-the-bag intraocular lens implantation for subluxated lenses: a prospective case series. *Am J Ophthalmol*. (2012) 153:1144–53.e1. doi: 10.1016/j.ajo.2011.11.012

17. Cai L, Han X, Jiang Y, Qiu X, Qian D, Lu Y, et al. Three-year outcomes of Cionni-modified capsular tension ring implantation in children under 8 years old with ectopia lentis. *Am J Ophthalmol*. (2021) 224:74–83. doi: 10.1016/j.ajo.2020.11.011

18. Chen T, Deng M, Zhang M, Chen J, Chen Z, Jiang Y. Visual outcomes of lens subluxation surgery with Cionni modified capsular tension rings in Marfan syndrome. *Sci Rep*. (2021) 11:2994. doi: 10.1038/s41598-021-82586-6

19. Toygar O, Snyder ME, Riemann CD. Dangling lens phacoemulsification: a novel technique for near complete zonular dehiscence. *J Refract Surg*. (2015) 31:835–8. doi: 10.3928/1081597x-20151111-10

20. Canabrava S, Rodrigues G, Halabi NN, Rezende AC, Cardoso M. 18-month results of double-flanged 5-0 polypropylene suture transscleral bag fixation in subluxated cataracts. *Arq Bras Oftalmol*. (2023) 86:113–20. doi: 10.5935/0004-2749.20230022

21. Ton Y, Michaeli A, Assia EI. Repositioning and scleral fixation of the subluxated lens capsule using an intraocular anchoring device in experimental models. *J Cataract Refract Surg*. (2007) 33:692–6. doi: 10.1016/j.jcrs.2006.12.022

22. Ton Y, Naftali M, Gortzak RL, Assia EI. Management of subluxated capsular bag-fixated intraocular lenses using a capsular anchor. *J Cataract Refract Surg*. (2016) 42:653–8. doi: 10.1016/j.jcrs.2016.04.002

23. Asano Y, Yaguchi S, Nishimura E, Soda M, Kozawa T. Modified capsule expander implantation to reposition and fixate the capsular bag in eyes with subluxated cataractous lenses and phacodonesis: intermediate-term results. *J Cataract Refract Surg*. (2015) 41:598–606. doi: 10.1016/j.jcrs.2014.06.031

24. Yaguchi S, Yaguchi S, Asano Y, Kozawa T, Miyawaki T, Negishi K, et al. Repositioning and scleral fixation of subluxated lenses using a T-shaped capsule stabilization hook. *J Cataract Refract Surg*. (2011) 37:1386–93. doi: 10.1016/j.jcrs.2011.06.015

25. Krix-Jachym KM, Błagun N, Kicińska AK, Dyda W, Rękas MT. Sutureless technique for repositioning and scleral fixation of the capsular bag-intraocular lens complex with permanent use of iris retractors. *J Cataract Refract Surg*. (2022) 48:118–24. doi: 10.1097/j.jcrs.0000000000000838

26. Karadag R, Sari U, Gunes B. Intra-scleral fixation of the iris hooks for trans-scleral capsular bag fixation in patient with zonular dialysis. *Int Ophthalmol*. (2018) 38:1765–8. doi: 10.1007/s10792-017-0623-2

27. Ou Z, Zhao P, Zhang Q, Jin H. Flexible polypropylene iris retractors made by cautery thermoplasticity: an instant intraoperative solution for small pupil vitrectomy. *Retina*. (2018) 38:2272–4. doi: 10.1097/IAE.0000000000002247

28. Ou Z, Zhao P, Zhang Q. Intrascleral fixation of implantable polypropylene capsular hook (s): a sutureless technique to fixate the capsular bag for intraocular lens implantation in subluxated lenses. *Retina*. (2019) 39:S33–8. doi: 10.1097/IAE.0000000000002425

29. Chen Z, Jia W, Chen T. Safety and efficacy of capsular tension ring and capsular hook implantation for managing ectopia lentis in Marfan syndrome: real-world study. *J Cataract Refract Surg*. (2024) 50:698–706. doi: 10.1097/j.jcrs.0000000000001434

30. Jia W-N, Wang Q-Y, Niu L-L, Chen Z-X, Jiang Y-X. Morphometric assessment of the ciliary body in patients with Marfan syndrome and ectopia lentis: a quantitative study using ultrasound biomicroscopy. *Am J Ophthalmol*. (2023) 251:24–31. doi: 10.1016/j.ajo.2023.03.003

frontiers | Frontiers in Medicine

TYPE Original Research
PUBLISHED 03 April 2025
DOI 10.3389/fmed.2025.1555620

OPEN ACCESS

EDITED BY
Horace Massa,
Hôpitaux Universitaires de Genève (HUG), Switzerland

REVIEWED BY
Ritika Mukhija,
Sussex Eye Hospital, United Kingdom
Martin Kronschläger,
Hanusch Hospital, Austria

*CORRESPONDENCE
Marcus Ang
✉ marcus.ang@snec.com.sg

RECEIVED 05 January 2025
ACCEPTED 20 March 2025
PUBLISHED 03 April 2025

CITATION
Cheong EZK, Ng Yin Ling C, Wong QY, Chua CSQ, Htoon HM and Ang M (2025) Clinical outcomes of DMEK comparing endothelium-out injector and endothelium-in pull-through techniques in Asian eyes. *Front. Med.* 12:1555620. doi: 10.3389/fmed.2025.1555620

Clinical outcomes of DMEK comparing endothelium-out injector and endothelium-in pull-through techniques in Asian eyes

Ezekiel Ze Ken Cheong[1], Clarissa Ng Yin Ling[2], Qiu Ying Wong[2,3], Chloe Si Qi Chua[2,3], Hla Myint Htoon[1,3] and Marcus Ang[1,2,3]*

[1]Ophthalmology and Visual Sciences Academic Clinical Program, Duke-NUS Medical School, Singapore, Singapore, [2]Singapore National Eye Centre, Singapore, Singapore, [3]Singapore Eye Research Institute, Singapore, Singapore

This is a prospective interventional study of 180 consecutive Descemet membrane endothelial keratoplasty (DMEK) cases, comparing injector (endothelium-out) and pull-through (endothelium-in) surgical techniques in Asian eyes. The main outcome measures were 5-year graft survival and intraoperative and postoperative complications. In our study, a pull-through technique for DMEK was employed more frequently in PBK (66.2%) than in FECD (10.7%) eyes ($p < 0.001$). Overall 5-year graft survival was 90% (98% in FECD and 64% in PBK eyes; $p < 0.001$). We observed higher rates of intraoperative donor graft tears (6.5% vs. 0.8%; $p = 0.049$) and persistent postoperative corneal edema (19.4% vs. 6.8%; $p = 0.022$) in pull-through DMEK than injector DMEK. However, multivariable analysis suggested that surgical technique was not a significant factor associated with graft survival, that is, PBK as the surgical indication was the main factor associated with graft failure (hazard ratio = 12.5; $p < 0.01$) and postoperative complications (odds ratio = 4.41; $p < 0.01$), regardless of surgical technique used. In our Asian study cohort, both injector (endothelium-out) and pull-through (endothelium-in) surgical techniques for DMEK had comparable clinical outcomes, when adjusted for confounders.

KEYWORDS

Descemet membrane endothelial keratoplasty (DMEK), clinical outcomes, graft survival, surgical techniques, pull-through, endothelium-in

Introduction

Descemet membrane endothelial keratoplasty (DMEK) is gaining popularity (1) as a treatment for diseased or damaged Descemet membranes and corneal endothelium (2). Compared to Descemet stripping automated endothelial keratoplasty (DSAEK), DMEK has the potential for faster visual recovery (3) and lower complication and rejection rates (4), despite being technically more challenging (5). Despite these advantages, complication and failure rates remain higher for advanced pseudophakic bullous keratopathy (PBK), compared with eyes with Fuchs endothelial cell dystrophy (FECD) (6, 7). As such, DMEK techniques have been continually refined for efficiency and effectiveness (8), especially for PBK patients with poorer prognoses.

Recently, DMEK donor insertion with the endothelium folded inward ("endothelium-in") and "pulled-through" into the anterior chamber has been described

(Figure 1) (9–11). This has some advantages over the traditional injector technique as DMEK donors naturally scroll up with the endothelial layer facing outward ("endothelium-out") (12, 13). Ensuring the graft adopts the correct orientation ("endothelium-down") after unscrolling requires surgical dexterity and maneuvers, which can possibly result in intraoperative endothelial cell loss, especially for surgeons with less experience (14, 15). Pull-through techniques have been reported to have quicker unfolding and positioning times than injector techniques (16, 17). This may lead to reduced surgical manipulation (18) and less endothelial cell exposure to shearing forces (19). Pull-through techniques may thus provide surgical predictability and control for challenging eyes such as those with a previous vitrectomy, fixated intraocular lens (IOL), or iris abnormalities (20).

Current studies for pull-through DMEK report reduced intraoperative endothelial cell losses (11, 21), with similar clinical outcomes to injector techniques (19, 22). However, there is currently a lack of direct comparative studies assessing clinical outcomes between pull-through and injector DMEK techniques, especially in the Asian context where surgical indications and challenges might differ (23, 24). Thus, we present here our report on the outcomes of consecutive DMEKs completed with both injector and pull-through techniques in our local population of Asian eyes—with a focus on graft survival and intraoperative and postoperative complications.

Methods

Study design and participants

We conducted a prospective interventional study of 180 consecutive DMEK surgeries completed by a single cornea specialist (MA) at a tertiary ophthalmology center—Singapore National Eye Centre—from July 2016 to September 2023. All DMEKs in that timeframe completed by the cornea surgeon for the indications of FECD and PBK were included. DMEK as a regraft for failed previous keratoplasties was excluded to reduce confounding ocular comorbidities. Our study was conducted as part of the Singapore Corneal Transplant Registry, which monitors clinical data and outcomes of corneal transplants in Singapore (25), with ethics approval from the local institutional review board (CIRB Ref 2011/577/A) and in accordance with the Declaration of Helsinki. Written informed consent was obtained from all subjects. All cases were at various stages of follow-up. Basic demographic data, clinical outcomes, best-corrected visual acuity (BCVA), ECD, and DMEK donor graft details were compiled from electronic health records.

Abbreviations: BCVA, best-corrected visual acuity; CIs, confidence intervals; ECD, endothelial cell density; ECL, endothelial cell loss; DMEK, Descemet membrane endothelial keratoplasty; DSAEK, Descemet stripping automated endothelial keratoplasty; FECD, Fuchs endothelial cell dystrophy; HR, hazard ratio; IOL, intraocular lens; IOP, intraocular pressure; logMAR, logarithm of the minimum angle of resolution; PBK, pseudophakic bullous keratopathy.

Surgical procedure

All donor tissues were obtained from the Singapore Eye Bank and underwent stringent monitoring and quality assurance. For the intraoperative procedure, techniques previously described were used (10, 26, 27). All grafts were prepared intraoperatively by the surgeon and were not preloaded. Essentially, the donor cornea was prepared by the surgeon using the SCUBA technique (28). This was followed by donor graft trephination according to size. In this series, the employment of an injector or pull-through technique was based on the surgeon's choice. In general, pull-through DMEK was chosen for eyes with greater surgical challenges such as PBK eyes with poor anterior chamber visualization. For the standard injector technique, the stained DMEK graft was inserted using a glass injector (Geuder AG, Germany) while in the natural endothelium-out scroll conformation and unfolded into the endothelium-down orientation using air and a balanced salt solution in a shallow anterior chamber as previously described (26, 29). For the pull-through technique, the DMEK graft was tri-folded after staining, pulled into the EndoGlide cartridge (CORONET DMEK EndoGlide; Network Medical Products, United Kingdom), and pulled through into the anterior chamber in the endothelium-down orientation (Figure 1); 20% sulfur hexafluoride gas was injected to achieve 80% fill to tamponade the graft. All wounds, if required, were closed with a single 10/0 nylon suture.

Postoperative management

As previously described (27), all patients remained in a face-up posture for at least 2 h and had IOP routinely assessed and managed with topical treatment before discharge. All patients received standard postoperative topical antibiotics (levofloxacin 0.5%; Santen, Japan) and topical corticosteroid regime (prednisolone acetate; Allergan, United States) following a standard tapering dose as previously described (30). Patients generally had follow-up visits at 1 day, 1 week, 1 month, 3 months, and 6 months postoperatively, after which they were continually followed up every 6 months. Given that pull-through DMEK is a relatively newer technique than the more established and traditional injector technique, most of the pull-through cases did not yet have visits beyond the 24-month mark. At each follow-up visit, they were examined by slit-lamp biomicroscopy, and BCVA was measured using the Snellen chart and subsequently converted to logarithm of the minimum angle of resolution (logMAR) units for statistical analysis (31). ECD measurements were obtained via non-contact specular microscopy (CellChek 20; Konan Medical Corp, Japan) by certified ophthalmic technicians as previously described (32). ECD measurements were obtained from the built-in automatic endothelial cell segmentation software, using the center method to measure cell area. ECD measurement was not part of routine testing at every follow-up and was only ordered for patients requiring closer monitoring or non-improving vision.

Clinical outcomes

Intraoperative complications recorded were as previously defined (27): DMEK donor graft tears, decentered graft placements,

10.3389/fmed.2025.1555620

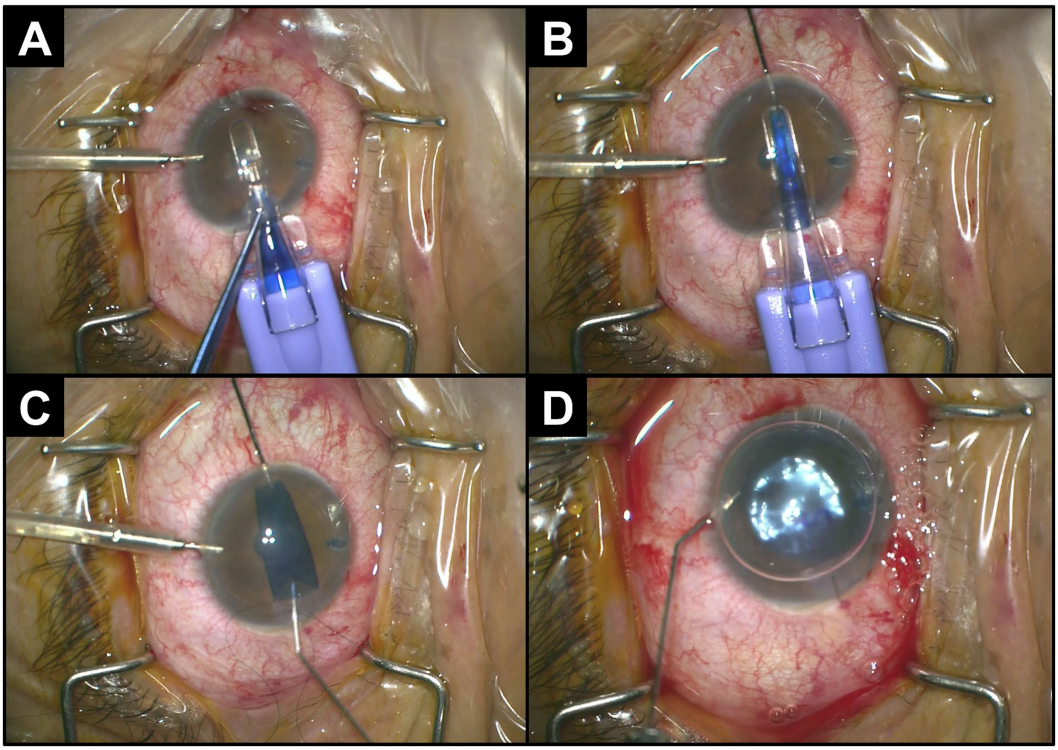

FIGURE 1
Intraoperative procedure for pull-through DMEK. **(A)** Insertion of the cartridge into the anterior chamber through a clear cornea incision. **(B)** Grasping and pulling-through of graft with forceps. **(C)** Natural unfolding of the graft with endothelium-down. **(D)** Injection of gas to tamponade the donor graft to the recipient cornea.

development of any bleeding (hyphema), high vitreous pressure, and aqueous misdirection defined as a flat anterior chamber with high intraocular pressure (IOP) in the presence of a patent peripheral iridectomy. Postoperative complications recorded include the following: cystoid macular edema, persistent cornea edema or haze (without detachment or rejection), early signs of graft rejection (keratic precipitates, stromal infiltrates, and Khodadoust lines), partial and complete detachments (lack of adherence of <30% and ≥30%, respectively, of the graft surface area) (30), need for rebubbling, retinal detachment, and new-onset glaucoma or ocular hypertension. Graft failure was defined as persistent, irreversible loss of corneal clarity irrespective of visual acuity, from any cause (33). Surviving grafts were defined as clear and functional grafts without an outcome of graft failure.

Statistical analyses

SPSS 26.0 (SPSS; IBM Corp, United States) and GraphPad Prism (Prism; GraphPad, United States) were used for all statistical analyses in this study. Descriptive statistics included mean ± standard deviation for continuous variables, whereas categorical variables included frequency distribution and percentages in parentheses. All between-group comparisons of continuous parameters were performed using independent *t*-tests (paired for applicable comparisons). All between-group comparisons of categorical parameters were performed using Fisher's exact or chi-square tests. Graft survival was analyzed using Kaplan–Meier plots, log-rank tests, and Cox regression analysis. Multivariable analysis models were built using potentially confounding independent variables that were found to be significantly different in the descriptive characteristics of the cohort. Cox regression analysis of graft survival was reported as hazard ratio (HR), logistic regression analyses of intraoperative and postoperative complications were reported as odds ratio (OR), and linear regression of endothelial cell loss (ECL) was reported as beta coefficient. Upper and lower 95% confidence intervals (CIs) were labeled in graphs and as a range for HR, OR, and beta. Tests were all two-sided if applicable, with statistical significance set at a p-value of <0.05. Statistical significance was indicated with a single asterisk for $p < 0.05$, a double asterisk for $p < 0.01$, and a triple asterisk for $p < 0.001$. ECD and BCVA were analyzed for up to 24 months post-DMEK. ECL was defined as the percentage loss of ECD compared to the preoperative donor ECD.

Results

We analyzed 180 eyes of 160 subjects who underwent DMEK at a mean age of 69.5 ± 10.1 years (Table 1). In total, 65.6% of eyes underwent injector DMEK ($n = 118$), and 34.4% of eyes underwent pull-through DMEK ($n = 62$); 31.4% ($n = 37$) of the injector-DMEK cases and 62.9% ($n = 39$) of the pull-through DMEK cases were male ($p < 0.001$); 57.2% of surgical indications were FECD ($n = 103$) and

TABLE 1 Descriptive characteristics of 180 DMEK recipient eyes and donor DMEK grafts.

Characteristics	All eyes n = 180	Insertion technique		P
		Injector	Pull-through	
		n = 118	n = 62	
Recipient characteristics				
Age at DMEK	69.5 ± 10.1	69.9 ± 9.1	68.8 ± 11.8	0.493
Ethnicity				
Chinese	155 (86.1)	105 (89.0)	50 (80.6)	0.472
Indian	6 (3.3)	3 (2.5)	3 (4.8)	
Malay	6 (3.3)	3 (2.5)	3 (4.8)	
Others	13 (7.2)	7 (5.9)	6 (9.7)	
Sex				
Male	76 (42.2)	37 (31.4)	39 (62.9)	<0.001***
Female	104 (57.8)	81 (68.6)	23 (37.1)	
Glaucoma pre-DMEK				
Glaucomatous	45 (25.0)	19 (16.1)	26 (41.9)	<0.001***
Non-glaucomatous	135 (75.0)	99 (83.9)	36 (58.1)	
Indication for DMEK				
FECD	103 (57.2)	92 (78.0)	11 (17.7)	<0.001***
PBK	77 (42.8)	26 (22.0)	51 (82.3)	
Donor characteristics				
Age*	62.4 ± 7.5	62.0 ± 7.4	63.9 ± 7.7	0.397
Sex*				
Male	111 (64.2)	74 (64.9)	37 (62.7)	0.297
Female	62 (35.8)	30 (35.1)	22 (37.3)	
ECD	2,833 ± 223	2,838 ± 211	2,825 ± 246	0.709
CV†	34.1 ± 3.7	34.7 ± 3.8	33.1 ± 3.4	<0.01**
HEX†	57.4 ± 6.9	56.3 ± 7.0	59.4 ± 6.3	<0.01**

FECD, Fuchs endothelial cell dystrophy; PBK, pseudophakic bullous keratopathy; BCVA, best-corrected visual acuity; CV, coefficient of variation; HEX, hexagonality.
*Donor age and gender data: 114 injector, 59 pull-through, 173 total.
†Donor CV and HEX data: 111 injector, 61 pull-through, 172 total.

42.8% were PBK (n = 77). Pull-through DMEK was mostly employed for surgically challenging eyes; 82.3% (n = 51) were PBK eyes, whereas only 22.0% (n = 26) of injector DMEKs were PBK eyes ($p < 0.001$). Pull-through DMEK was also associated with a greater rate of prior glaucoma before surgery ($p < 0.001$).

Clinical outcomes of injector vs. pull-through techniques

The clinical outcomes of both injector and pull-through techniques, in terms of complications and final graft outcomes, are compared in Table 2. We observed a higher rate of intraoperative donor graft tear (6.5% vs. 0.8%; $p = 0.049$) and postoperative corneal edema (19.4% vs. 6.8%; $p = 0.022$) in pull-through DMEK than injector DMEK. We also noted early signs of immune graft rejection in 4.4% (n = 8) of eyes; however, all were single episodes that fully resolved with increased topical steroids, and all grafts recovered clarity and remained clear. Of the 16 eyes (8.9%) with partial or complete graft detachment, eight required rebubbling to reattach the graft (4.4% of overall rebubbling rate). All rebubbling procedures were successful. The choice of surgical technique, injector or pull-through, was not found to be associated with different outcomes of graft survival ($p = 0.192$). Subgroup analysis within the two DMEK indications of FECD (Supplementary Table 1) and PBK (Supplementary Table 2) was also used to compare the clinical outcomes of the two techniques. There was no significant difference detected between the injector and pull-through techniques in both the FECD and PBK subgroups. Within the PBK cases, pull-through DMEK did not show significantly greater rates of intraoperative graft tears (7.8% vs. 0%; $p = 0.294$) or postoperative cornea edema (23.5% vs. 15.4%; $p = 0.556$).

DMEK graft survival

The 5-year overall cumulative graft survival (Figure 2) was 90% (95% CIs = [86–94%]), significantly greater for the FECD group than the PBK group (98% vs. 64%; log-rank $p < 0.001$). Survival curves for the two different techniques (injector vs. pull-through) were significantly different (log-rank $p = 0.017$). However, comparing

TABLE 2 Comparison of visual outcomes, intraoperative, postoperative complications, and final graft outcomes between injector and pull-through surgical techniques.

Outcomes	All eyes *n* = 180	Insertion technique		*P*
		Injector	Pull-through	
		n = 118	*n* = 62	
Intraoperative complications				
Any complication	21 (11.7)	10 (8.5)	11 (17.7)	0.087
Donor graft tear	5 (2.8)	1 (0.8)	4 (6.5)	0.049*
Aqueous misdirection	3 (1.7)	2 (1.7)	1 (1.6)	1.00
Hyphema	8 (4.4)	5 (4.2)	3 (4.8)	1.00
High vitreous pressure	2 (1.1)	1 (0.8)	1 (1.6)	1.00
Decentered graft	5 (2.8)	2 (1.7)	3 (4.8)	0.341
Postoperative complications				
Any complication	48 (26.7)	26 (22.0)	22 (35.5)	0.075
Cystoid macula edema	7 (3.9)	6 (5.1)	1 (1.6)	0.425
Early rejection signs	8 (4.4)	5 (4.2)	3 (4.8)	1.00
Partial detachment	13 (7.2)	9 (7.6)	4 (6.5)	1.00
Complete detachment	3 (1.7)	1 (0.8)	2 (3.2)	0.273
Rebubbling required	8 (4.4)	5 (4.2)	3 (4.8)	1.00
Corneal haze/edema	20 (11.1)	8 (6.8)	12 (19.4)	0.022*
Ocular hypertension	9 (5.0)	5 (4.2)	4 (6.5)	0.497
Retinal detachment	2 (1.1)	1 (0.8)	1 (1.6)	1.00
Final graft outcome				
Clear and surviving	169 (93.8)	113 (95.8)	56 (90.3)	0.192
Graft failure	11 (6.1)	5 (4.2)	6 (9.7)	
Visual outcomes (logMAR)				
Pre-DMEK BCVA	0.96 ± 0.61	0.76 ± 0.45	1.35 ± 0.67	<0.001***
Post-DMEK BCVA*	0.30 ± 0.37	0.24 ± 0.31	0.41 ± 0.43	<0.01**
Post-DMEK BCVA ≥6/12	132 (73.3)	94 (79.7)	38 (61.3)	0.013*
% improvement in BCVA	66.4 ± 35.3	66.0 ± 37.8	67.2 ± 30.2	0.828

logMAR, logarithm of the minimum angle of resolution; BCVA, best-corrected visual acuity. *Postop BCVA defined as the best BCVA score within 24 months postoperatively.

within the FECD and PBK groups, there were no significant differences in the survival curves between the pull-through and injector techniques (log-rank $p = 0.624$ and 0.258, respectively). Cox regression analysis (Table 3) suggested that the pull-through technique was associated with graft failure in the univariable analysis (HR = 10.5; 95% CIs = [2.42–55.9]; $p < 0.01$). However, after adjusting for age, sex, prior glaucoma, and surgical indication in the multivariable analysis, the association was no longer statistically significant (HR = 2.64; 95% CIs = [0.526–16.3]; $p = 0.256$). However, PBK remained significantly associated with graft failure (HR = 12.5; 95% CIs = [2.11–101]; $p < 0.01$) when compared to FECD.

Multivariable analysis of intraoperative and postoperative complications

We observed that the pull-through technique was associated with higher rates of intraoperative donor graft tear and postoperative corneal edema (Table 2). However, given that there were many possible confounders as shown in Table 1, a multivariable analysis was conducted. We observed that the pull-through technique, after adjusting for age, sex, prior glaucoma, and DMEK indication, was not associated with increased incidence of any intraoperative (OR = 1.38; 95% CIs = [0.436–4.38]; $p = 0.581$) or postoperative complications (OR = 0.93; 95% CIs = [0.384–2.19]; $p = 0.871$). Specifically, it was not significantly associated with intraoperative graft tear (OR = 5.18; 95% CIs = [0.425–136]; $p = 0.232$) nor persistent postoperative corneal edema (OR = 1.51; 95% CIs = [0.467–5.15]; $p = 0.494$). However, we found that PBK remained significantly associated with postoperative corneal edema (OR = 7.69; 95% CIs = [1.83–40.7]; $p < 0.01$) and other postoperative complications (OR = 4.41; 95% CIs = [1.78–11.3]; $p < 0.01$), unlike FECD.

Postoperative endothelial cell density and loss

The mean donor ECD was 2,833 ± 223 cells/mm^2. Figure 3 shows the ECD at various timepoints post-DMEK for the different surgical indications and techniques utilized. Mean ECD was not significantly

different between injector and pull-through DMEK within the first 3 months (2,039 vs. 2,016 cells/mm^2; $p = 0.875$) or within 6 to 12 months (1,941 vs. 1,848 cells/mm^2; $p = 0.311$). Significant differences were detected from 18 to 24 months when comparing between FECD and PBK (1,692 vs. 1,342 cells/mm^2; $p = 0.020$) and between injector and pull-through techniques (1,637 vs. 1,246 cells/mm^2; $p = 0.038$). However, there were no differences when comparing the ECL between injector and pull-through at all timepoints: 1 to 3 months (28.5% vs. 30.4%; $p = 0.709$), 6 to 12 months (30.3% vs. 36.1%; $p = 0.166$), and 18 to 24 months (54.2% vs. 42.8%; $p = 0.083$). The multivariable analysis did not find any variable that was associated with significantly different ECLs at all three timepoints.

Visual outcomes

Preoperative and postoperative BCVA are described in Table 2. Eyes undergoing pull-through DMEK had poorer BCVA preoperatively (logMAR 1.35 vs. 0.76; $p < 0.001$) and postoperatively (logMAR 0.41 vs. 0.24; $p < 0.01$) but did not have any significant different percentage improvement in BCVA post-DMEK compared to injector DMEK (67.2% vs. 66.0%; $p = 0.828$). Overall, 79.7% ($n = 94$) of injector-DMEKs and 61.3% ($n = 38$) of pull-through DMEKs achieved a postoperative BCVA of 6/12 or better ($p = 0.013$). Longitudinally, FECD eyes had better visual outcomes than PBK: preoperatively (logMAR 0.68 vs. 1.33; $p < 0.001$), 1 to 3 months post-DMEK (logMAR 0.32 vs. 0.43; $p = 0.047$), 6 to 12 months post-DMEK (logMAR 0.25 vs. 0.43; $p < 0.01$), and 18 to 24 months post-DMEK (logMAR 0.25 vs. 0.61; $p < 0.001$).

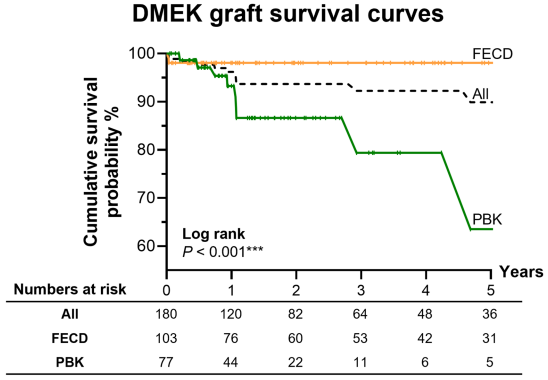

FIGURE 2
Kaplan–Meier curve of cumulative graft survival probability. DMEK graft survival curves over 5 years, comparing FECD and PBK. Overall 5-year survival was 90% (95% CIs = [86–94%]). The numbers at risk at each year across 5 years are indicated in the table below each graph. Survival curves were significantly different when comparing indications (log-rank $p < 0.001$) of FECD and PBK.

Discussion

In our prospective study of consecutive DMEK cases performed in Asian eyes with 57.2% FECD, the overall 5-year graft survival was 90% (98% in FECD, 64% in PBK), which is similar to the findings of Price et al. (34), who showed 93% in FECD eyes, and Birbal et al. (35), who showed 90% in a cohort of 89.2% FECD eyes. In our cases, PBK was significantly associated with graft failure (HR = 12.5; $p < 0.01$) and incidence of postoperative complications (OR = 4.41; $p < 0.01$). The pull-through donor insertion technique had comparable graft survival compared to the injector insertion technique when adjusted for the indication of PBK, agreeing with the recent systematic review of Ong et al. (11) and the findings of Price et al. (19).

We did observe an overall higher rate of intraoperative graft tears in pull-through DMEK (6.5% vs. 0.8%; $p = 0.049$). There is overall a risk of small peripheral tears due to the pulling-through of the graft with forceps (9), as opposed to the injector technique which does not involve grasping during the graft insertion phase of DMEK. We, however, did not note any tears or significant difficulties during the loading and preparation of the grafts in either method. There was a higher rate of persistent postoperative corneal edema in our pull-through cases (19.4% vs. 6.8%; $p = 0.022$). However, our multivariable analysis adjusted for confounders, suggesting that PBK is the main contributing factor (OR = 7.69; $p < 0.01$), rather than the pull-through technique (OR = 1.51; $p = 0.494$). We did not observe any difference in rebubbling rate for pull-through vs. injector techniques (4.8% vs. 4.2%; $p > 0.99$), which agrees with the findings of other comparative studies (11, 19, 36).

TABLE 3 Cox regression of DMEK graft survival using multiple variables.

Variables	A: Univariable		B: Multivariable	
	Hazard ratio (95% CIs)	*P*	Hazard ratio (95% CIs)	*P*
Age at DMEK	0.978 (0.915–1.04)	0.491	0.961 (0.899–1.03)	0.236
Male sex	2.34 (0.698–8.19)	0.164	0.877 (0.208–3.63)	0.854
Prior glaucoma	1.57 (0.340–5.58)	0.509	0.752 (0.154–2.96)	0.696
DMEK indication of PBK (vs. FECD)	13.5 (3.29–91.1)	<0.01**	12.5 (2.11–101)	<0.01**
Pull-through technique (vs. injector)	10.5 (2.42–55.9)	<0.01**	2.64 (0.526–16.3)	0.256

PBK, pseudophakic bullous keratopathy; FECD, Fuchs endothelial cell dystrophy.

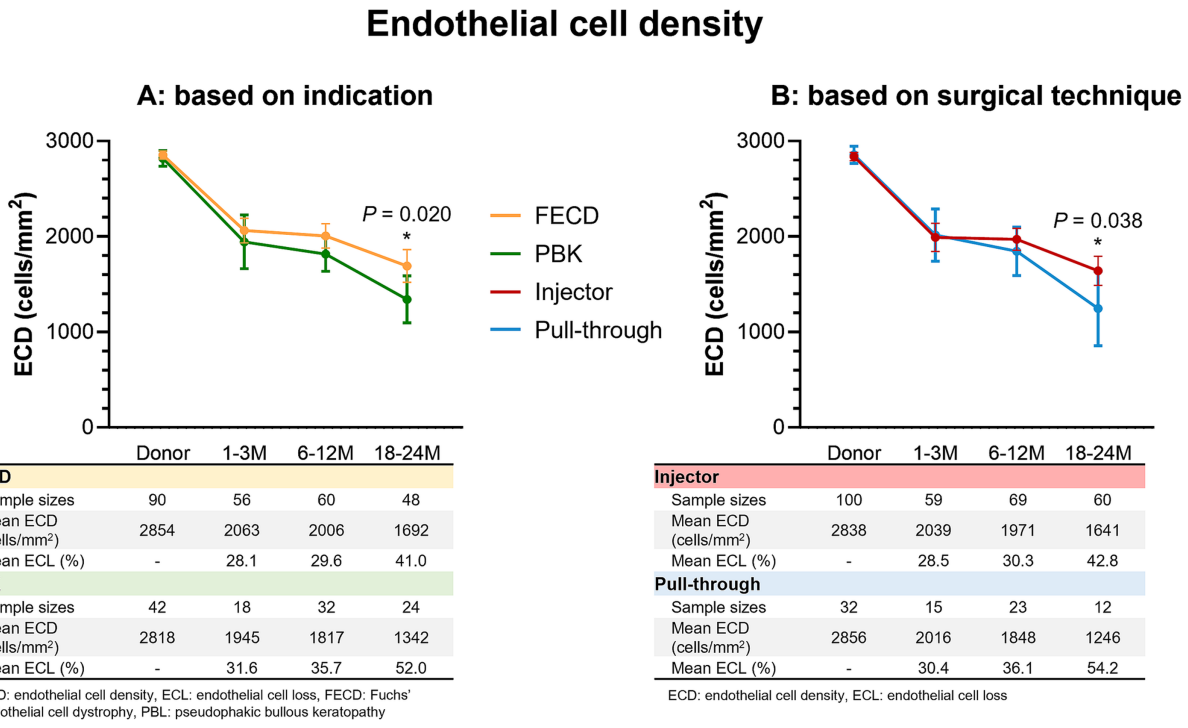

	Donor	1-3M	6-12M	18-24M
FECD				
Sample sizes	90	56	60	48
Mean ECD (cells/mm²)	2854	2063	2006	1692
Mean ECL (%)	-	28.1	29.6	41.0
PBK				
Sample sizes	42	18	32	24
Mean ECD (cells/mm²)	2818	1945	1817	1342
Mean ECL (%)	-	31.6	35.7	52.0

ECD: endothelial cell density, ECL: endothelial cell loss, FECD: Fuchs' endothelial cell dystrophy, PBL: pseudophakic bullous keratopathy

	Donor	1-3M	6-12M	18-24M
Injector				
Sample sizes	100	59	69	60
Mean ECD (cells/mm²)	2838	2039	1971	1641
Mean ECL (%)	-	28.5	30.3	42.8
Pull-through				
Sample sizes	32	15	23	12
Mean ECD (cells/mm²)	2856	2016	1848	1246
Mean ECL (%)	-	30.4	36.1	54.2

ECD: endothelial cell density, ECL: endothelial cell loss

FIGURE 3
Post-DMEK endothelial cell density and loss. Post-DMEK endothelial cell density (ECD) and endothelial cell loss (ECL) at 1–3 months, 6–12 months, and 18–24 months post-DMEK, comparing **(A)** FECD (yellow) and PBK (green) DMEK indications and **(B)** injector (red) and pull-through (blue) surgical techniques. 95% of CIs are indicated as vertical error bars at each timepoint. ECD was significantly different at 18–24 months post-DMEK for comparisons between surgical indications (p = 0.020) and surgical techniques (p = 0.038).

We found no significant difference in ECL between the injector and pull-through DMEK in the postoperative period up to 24 months. The multivariable analysis did not highlight pull-through as a significant variable for increased ECL. The 6- to 12-month post-DMEK ECL in our pull-through cases was 30.3%, compared to another study showing a pooled ECL of 28.1% at 6 months and 29.6% at 12 months (11). In terms of visual outcomes, we found that eyes with FECD had better 2-year postoperative BCVA than PBK eyes, at all timepoints, which is consistent with previous reports(37, 38). Nonetheless, we found that the percentage improvement in BCVA after surgery was similar when comparing both surgical indications and surgical techniques. Overall, our findings suggest that PBK was the most important independent factor for graft failure, postoperative complications, and poorer visual outcomes, all of which are consistent with the current literature (6, 8).

The potential advantages of the pull-through technique include the minimization of endothelial contact with the insertion device (22) and quicker graft unfolding and positioning times due to the spontaneous unfurling into its natural endothelium-out configuration (39). The pull-through technique could also be useful in younger donor grafts, given their tendency to form tighter scrolls than older donors (40, 41). In addition, the pull-through insertion method results in better control of the donor graft (18), whereas the graft is left free-floating in the anterior chamber in the injection method (42). This element of graft handling is especially crucial in eyes with difficult visualization and shallow anterior chambers (43), which are more common in Asian eyes due to darker irises and narrower palpebral fissures with smaller, deeper-set eyes (23). In addition, pulling-through also circumvents reliance on normal anterior segment structures such as an intact iris diaphragm (44), increasing its utility for eyes with aniridia or iridocorneal syndrome (45). Potential concerns of holding the graft with forceps in pull-through DMEK are peripheral graft tears and endothelial cell damage with intraoperative ECL. Forceps-free endothelium-in injection of the DMEK graft has been described (46), which may help reduce the graft tears or ECL, but this removes the benefit of bimanual graft control afforded by the pull-through technique. In addition, the endothelial cell area potentially damaged by each forceps bite is relatively minimal and confined to only one distal end of the graft periphery (9). A novel infusion forceps for pull-through DMEK has been developed, which can grasp the donor tissue and additionally control anterior chamber depth at the same time (47), highlighting the continual innovation for DMEK techniques and devices.

Key strengths of our study are that we prospectively analyzed consecutive DMEK outcomes which minimizes selection bias and represents real-world results of the two surgical techniques. We also reported a relatively large sample size and analyzed a broad range of clinical outcomes such as graft survival, complications, ECL, and visual outcomes. One limitation of our study is that pull-through DMEK was more likely to be chosen for surgically challenging eyes (PBK, prior glaucoma, etc.), with a likely poorer prognosis. However, we mitigated this by adjusting for confounders in our multivariable analyses and reported no significant difference in outcomes between pull-through and injector DMEK, when performed by an experienced cornea surgeon. Furthermore, it would not have been feasible to randomize surgical techniques in our patient population. Nonetheless, more comprehensive

multicenter studies and/or randomized controlled trials are required to conclusively compare injector and pull-through techniques (11), especially given the relative novelty of pull-through DMEK.

We recognize that DMEK indications, surgical complexity, and clinical practice in the global population might differ from our experience but, nonetheless, we strived to contribute to the growing body of knowledge for pull-through DMEKs and to provide valuable insight into DMEK techniques and outcomes in our local Asian population. In our experience, pull-through DMEK for complex eyes has been a valuable technique, with the controlled intraoperative graft unfolding helping alleviate potential hurdles such as an abnormal anterior segment anatomy or fixated IOLs. We demonstrated that pulling-through could be a good choice for PBK patients, especially those who might have poor corneal clarity for intraoperative visualization, given the similar clinical outcomes in pull-through and injector DMEKs for PBK. This prospective DMEK study had varying follow-up periods and sample sizes; nonetheless, our routine and serial follow-up compared favorably with other DMEK studies (37, 38). Finally, we would have ideally also measured and compared graft preparation, unfolding, and total operation times to be able to report a comprehensive comparison of the surgical techniques.

To conclude, our comparative study on consecutive DMEK suggests that the pull-through technique could have comparable clinical outcomes with traditional donor injector techniques, despite being employed for the most challenging cases. This was demonstrated in multivariate analyses with adjustment for confounders such as prior glaucoma and PBK as a surgical indication. Given the challenges of DMEK graft insertion and positioning for some eyes, pull-through DMEK may be a useful technique that offers better graft control.

Data availability statement

The original contributions presented in the study are included in the article/Supplementary material, further inquiries can be directed to the corresponding author.

Ethics statement

The studies involving humans were approved by SingHealth Institutional Review Board. The studies were conducted in accordance with the local legislation and institutional requirements. The participants provided their written informed consent to participate in this study.

Author contributions

EC: Data curation, Formal analysis, Investigation, Methodology, Project administration, Software, Validation, Visualization, Writing – original draft, Writing – review & editing. CN: Formal analysis, Methodology, Project administration, Supervision, Validation, Visualization, Writing – original draft, Writing – review & editing. QW: Conceptualization, Data curation, Formal analysis, Funding acquisition, Investigation, Methodology, Project administration, Resources, Supervision, Validation, Writing – original draft, Writing – review & editing. CC: Conceptualization, Data curation, Formal analysis, Funding acquisition, Investigation, Methodology, Project administration, Resources, Supervision, Validation, Writing – original draft, Writing – review & editing. HH: Methodology, Software, Validation, Visualization, Writing – original draft, Writing – review & editing. MA: Conceptualization, Data curation, Formal analysis, Funding acquisition, Investigation, Methodology, Project administration, Resources, Supervision, Validation, Visualization, Writing – original draft, Writing – review & editing.

Funding

The author(s) declare that no financial support was received for the research and/or publication of this article.

Conflict of interest

The authors declare that the research was conducted in the absence of any commercial or financial relationships that could be construed as a potential conflict of interest.

Generative AI statement

The author(s) declare that no Gen AI was used in the creation of this manuscript.

Publisher's note

Supplementary material

The Supplementary material for this article can be found online at: https://www.frontiersin.org/articles/10.3389/fmed.2025.1555620/full#supplementary-material

References

1. Moura-Coelho N, Papa-Vettorazzi R, Reyes A, Cunha JP, Guell JL. Ultrathin DSAEK versus DMEK – review of systematic reviews. *Eur J Ophthalmol.* (2023) 34:913–23. doi: 10.1177/11206721231214605

2. Melles GR, Ong TS, Ververs B, van der Wees J. Descemet membrane endothelial keratoplasty (DMEK). *Cornea.* (2006) 26:199–206. doi: 10.1097/01.ico.0000248385.16896.34

3. Price FW, Price MO. Evolution of endothelial keratoplasty. *Cornea.* (2013) 32:S28–32. doi: 10.1097/ICO.0b013e3182a0a307

4. Santander-García D, Dapena I, Baydoun L, Melles GRJ. DMEK complications: current treatment and recommendations. *Expert Rev Ophthalmol.* (2018) 13:33–46. doi: 10.1080/17469899.2018.1429917

5. Green M, Wilkins MR. Comparison of early surgical experience and visual outcomes of DSAEK and DMEK. *Cornea*. (2015) 34:1341–4. doi: 10.1097/ICO.0000000000000590

6. Fajardo-Sanchez J, de Benito-Llopis L. Clinical outcomes of Descemet membrane endothelial Keratoplasty in Pseudophakic eyes compared with triple-DMEK at 1-year follow-up. *Cornea*. (2021) 40:420–4. doi: 10.1097/ICO.0000000000002636

7. Brockmann T, Brockmann C, Maier AKB, Schroeter J, Bertelmann E, Torun N. Primary Descemet's membrane endothelial Keratoplasty for Fuchs endothelial dystrophy versus bullous keratopathy: histopathology and clinical results. *Curr Eye Res*. (2018) 43:1221–7. doi: 10.1080/02713683.2018.1490773

8. Zwingelberg SB, Büscher F, Schrittenlocher S, Rokohl AC, Loreck N, Wawer-Matos P, et al. Long-term outcome of Descemet membrane endothelial Keratoplasty in eyes with Fuchs endothelial corneal dystrophy versus Pseudophakic bullous keratopathy. *Cornea*. (2022) 41:304–9. doi: 10.1097/ICO.0000000000002737

9. Busin M, Leon P, Scorcia V, Ponzin D. Contact Lens-assisted pull-through technique for delivery of tri-folded (endothelium in) DMEK grafts minimizes surgical time and cell loss. *Ophthalmology*. (2016) 123:476–83. doi: 10.1016/j.ophtha.2015.10.050

10. Ang M, Mehta JS, Newman SD, Han SB, Chai J, Tan D. Descemet membrane endothelial Keratoplasty: preliminary results of a donor insertion pull-through technique using a donor mat device. *Am J Ophthalmol*. (2016) 171:27–34. doi: 10.1016/j.ajo.2016.08.023

11. Ong HS, Htoon HM, Ang M, Mehta JS. "Endothelium-out" and "endothelium-in" Descemet membrane endothelial Keratoplasty (DMEK) graft insertion techniques: a systematic review with Meta-analysis. *Front Med*. (2022) 9:868533. doi: 10.3389/fmed.2022.868533

12. Yu AC, Myerscough J, Spena R, Fusco F, Socea S, Furiosi L, et al. Three-year outcomes of tri-folded endothelium-in Descemet membrane endothelial Keratoplasty with pull-through technique. *Am J Ophthalmol*. (2020) 219:121–31. doi: 10.1016/j.ajo.2020.07.004

13. Dua HS, Freitas R, Sadek Y, Ting DSJ, Nubile M, Mohammed I, et al. An approach to reduce Descemet's membrane scrolling: relevance to Descemet's membrane endothelial keratoplasty (DMEK). *Indian J Ophthalmol*. (2023) 71:3178–85. doi: 10.4103/IJO.IJO_1531_23

14. Debellemaniere G, Guilbert E, Courtin R, Panthier C, Sabatier P, Gatinel D, et al. Impact of surgical learning curve in Descemet membrane endothelial Keratoplasty on visual acuity gain. *Cornea*. (2017) 36:1–6. doi: 10.1097/ICO.0000000000001066

15. Deng SX, Lee WB, Hammersmith KM, Kuo AN, Li JY, Shen JF, et al. Descemet membrane endothelial Keratoplasty: safety and outcomes: a report by the American Academy of ophthalmology. *Ophthalmology*. (2018) 125:295–310. doi: 10.1016/j.ophtha.2017.08.015

16. Parekh M, Baruzzo M, Favaro E, Borroni D, Ferrari S, Ponzin D, et al. Standardizing Descemet membrane endothelial Keratoplasty graft preparation method in the eye Bank-experience of 527 Descemet membrane endothelial Keratoplasty tissues. *Cornea*. (2017) 36:1458–66. doi: 10.1097/ICO.0000000000001349

17. Parekh M, Ruzza A, Ferrari S, Ahmad S, Kaye S, Ponzin D, et al. Endothelium-in versus endothelium-out for Descemet membrane endothelial keratoplasty graft preparation and implantation. *Acta Ophthalmol*. (2017) 95:194–8. doi: 10.1111/aos.13162

18. Viola P, Neri E, Testa V, Parekh M, Cian R, Grassetto A, et al. Clinical outcomes of preloaded Descemet membrane endothelial Keratoplasty with endothelium inward: a 24-month comparative analysis between Fuchs endothelial corneal dystrophy and bullous keratopathy. *Cornea*. (2023) 42:1133–9. doi: 10.1097/ICO.0000000000003138

19. Price MO, Lisek M, Kelley M, Feng MT, Price FW. Endothelium-in versus endothelium-out insertion with Descemet membrane endothelial Keratoplasty. *Cornea*. (2018) 37:1098–101. doi: 10.1097/ICO.0000000000001650

20. Ting D. S. J., Ang M. In modern Keratoplasty: surgical techniques and indications, 415–429, Cham: Springer, (2023)

21. Chong EW, Bandeira F, Finn P, Mehta JS, Chan E. Evaluation of Total donor endothelial viability after endothelium-inward versus endothelium-outward loading and insertion in Descemet membrane endothelial Keratoplasty. *Cornea*. (2020) 39:104–9. doi: 10.1097/ICO.0000000000002014

22. Parekh M, Romano V, Hassanin K, Testa V, Wongvisavavit R, Ferrari S, et al. Delivering endothelial Keratoplasty grafts: modern day transplant devices. *Curr Eye Res*. (2022) 47:493–504. doi: 10.1080/02713683.2021.2016852

23. Hayashi T, Oyakawa I, Kato N. Techniques for learning Descemet membrane endothelial Keratoplasty for eyes of Asian patients with shallow anterior chamber. *Cornea*. (2017) 36:390–3. doi: 10.1097/ICO.0000000000001093

24. Shimizu T, Hayashi T, Yuda K, Takahashi H, Oyakawa I, Yamazaki K, et al. Short axial length and Iris damage are associated with Iris posterior Synechiae after Descemet membrane endothelial Keratoplasty in Asian eyes. *Cornea*. (2018) 37:1355–9. doi: 10.1097/ICO.0000000000001698

25. Tan D, Ang M, Arundhati A, Khor WB. Development of selective lamellar Keratoplasty within an Asian corneal transplant program: the Singapore corneal transplant study (an American ophthalmological society thesis). *Trans Am Ophthalmol Soc*. (2015) 113:T10.

26. Ang M, Wilkins MR, Mehta JS, Tan D. Descemet membrane endothelial keratoplasty. *Br J Ophthalmol*. (2016) 100:15–21. doi: 10.1136/bjophthalmol-2015-306837

27. Ang M, Ting DSJ, Kumar A, May KO, Htoon HM, Mehta JS. Descemet membrane endothelial Keratoplasty in Asian eyes: intraoperative and postoperative complications. *Cornea*. (2020) 39:940–5. doi: 10.1097/ICO.0000000000002302

28. Price MO, Giebel AW, Fairchild KM, Price FW. Descemet's membrane endothelial keratoplasty: prospective multicenter study of visual and refractive outcomes and endothelial survival. *Ophthalmology*. (2009) 116:2361–8. doi: 10.1016/j.ophtha.2009.07.010

29. Groeneveld-van Beek EA, Lie JT, van der Wees J, Bruinsma M, Melles GR. Standardized 'no-touch' donor tissue preparation for DALK and DMEK: harvesting undamaged anterior and posterior transplants from the same donor cornea. *Acta Ophthalmol*. (2013) 91:145–50. doi: 10.1111/j.1755-3768.2012.02462.x

30. Woo JH, Ang M, Htoon HM, Tan D. Descemet membrane endothelial Keratoplasty versus Descemet stripping automated endothelial Keratoplasty and penetrating Keratoplasty. *Am J Ophthalmol*. (2019) 207:288–303. doi: 10.1016/j.ajo.2019.06.012

31. Bailey IL, Lovie JE. New design principles for visual acuity letter charts. *Am J Optom Physiol Optic*. (1976) 53:740–5. doi: 10.1097/00006324-197611000-00006

32. Ang M, Mehta JS, Anshu A, Wong HK, Htoon HM, Tan D. Endothelial cell counts after Descemet's stripping automated endothelial keratoplasty versus penetrating keratoplasty in Asian eyes. *Clin Ophthalmol*. (2012) 6:537–44. doi: 10.2147/OPTH.S26343

33. Ang M, Htoon HM, Cajucom-Uy HY, Tan D, Mehta JS. Donor and surgical risk factors for primary graft failure following Descemet's stripping automated endothelial keratoplasty in Asian eyes. *Clin Ophthalmol*. (2011) 5:1503–8. doi: 10.2147/OPTH.S25973

34. Price DA, Kelley M, Price FW, Price MO. Five-year graft survival of Descemet membrane endothelial Keratoplasty (EK) versus Descemet stripping EK and the effect of donor sex matching. *Ophthalmology*. (2018) 125:1508–14. doi: 10.1016/j.ophtha.2018.03.050

35. Birbal RS, Ni Dhubhghaill S, Bourgonje VJA, Hanko J, Ham L, Jager MJ, et al. Five-year graft survival and clinical outcomes of 500 consecutive cases after Descemet membrane endothelial Keratoplasty. *Cornea*. (2020) 39:290–7. doi: 10.1097/ICO.0000000000002120

36. Jung YH, Yoon CH, Kim MK. Clinical outcome of Descemet membrane endothelial keratoplasty (DMEK) with imported donor corneas in eyes of Asian patients; endothelium-in versus endothelium-out method. *PLoS One*. (2022) 17:e0270037. doi: 10.1371/journal.pone.0270037

37. Baydoun L, Ham L, Borderie V, Dapena I, Hou J, Frank LE, et al. Endothelial survival after Descemet membrane endothelial Keratoplasty: effect of surgical indication and graft adherence status. *JAMA Ophthalmol*. (2015) 133:1277–85. doi: 10.1001/jamaophthalmol.2015.3064

38. Peraza-Nieves J, Baydoun L, Dapena I, Ilyas A, Frank LE, Luceri S, et al. Two-year clinical outcome of 500 consecutive cases undergoing Descemet membrane endothelial Keratoplasty. *Cornea*. (2017) 36:655–60. doi: 10.1097/ICO.0000000000001176

39. Mohammed I, Ross AR, Britton JO, Said DG, Dua HS. Elastin content and distribution in endothelial Keratoplasty tissue determines direction of scrolling. *Am J Ophthalmol*. (2018) 194:16–25. doi: 10.1016/j.ajo.2018.07.001

40. Bennett A, Mahmoud S, Drury D, Cavanagh HD, McCulley JP, Petroll WM, et al. Impact of donor age on corneal endothelium-Descemet membrane layer scroll formation. *Eye Contact Lens*. (2015) 41:236–9. doi: 10.1097/ICL.0000000000000108

41. Heinzelmann S, Hüther S, Böhringer D, Eberwein P, Reinhard T, Maier P. Influence of donor characteristics on descemet membrane endothelial keratoplasty. *Cornea*. (2014) 33:644–8. doi: 10.1097/ICO.0000000000000106

42. Maier AK, , Gundlach E, Schroeter J, Klamann MKJ, Gonnermann J, Riechardt AI, et al. Influence of the difficulty of graft unfolding and attachment on the outcome in Descemet membrane endothelial keratoplasty. *Graefes Arch Clin Exp Ophthalmol*. (2015) 253:895–900. doi: 10.1007/s00417-015-2939-9

43. Siggel R, Heindl LM, Cursiefen C. Descemet membrane endothelial keratoplasty (DMEK) in phakic eyes with shallow anterior chamber. *Graefes Arch Clin Exp Ophthalmol*. (2015) 253:817–9. doi: 10.1007/s00417-014-2850-9

44. Ong HS, Ang M, Mehta JS. Evolution of therapies for the corneal endothelium: past, present and future approaches. *Br J Ophthalmol*. (2021) 105:454–67. doi: 10.1136/bjophthalmol-2020-316149

45. Weller JM, Tourtas T, Kruse FE. Feasibility and outcome of Descemet membrane endothelial Keratoplasty in complex anterior segment and vitreous disease. *Cornea*. (2015) 34:1351–7. doi: 10.1097/ICO.0000000000000625

46. Gadhvi KA, Pagano L, Wallace A, Posarelli M, Parekh M, Romano V. New forceps free injection technique for delivering descemet membrane endothelial keratoplasty preloaded endothelium-in grafts. *Eur J Ophthalmol*. (2024) 34:287–91. doi: 10.1177/11206721231208998

47. Jabbour S, Jun AS, Shekhawat NS, Woreta FA, Krick TW, Srikumaran D. Descemet membrane endothelial Keratoplasty using a pull-through technique with novel infusion forceps. *Cornea*. (2021) 40:387–92. doi: 10.1097/ICO.0000000000002558

frontiers | Frontiers in Medicine

TYPE Correction
PUBLISHED 24 June 2025
DOI 10.3389/fmed.2025.1624456

OPEN ACCESS

EDITED AND REVIEWED BY
Massimo Busin,
University of Ferrara, Italy

*CORRESPONDENCE
Marcus Ang
marcus.ang@snec.com.sg

RECEIVED 07 May 2025
ACCEPTED 09 June 2025
PUBLISHED 24 June 2025

CITATION
Cheong EZK, Ng Yin Ling C, Wong QY, Chua CSQ, Htoon HM and Ang M (2025) Corrigendum: Clinical outcomes of DMEK comparing endothelium-out injector and endothelium-in pull-through techniques in Asian eyes. *Front. Med.* 12:1624456. doi: 10.3389/fmed.2025.1624456

Corrigendum: Clinical outcomes of DMEK comparing endothelium-out injector and endothelium-in pull-through techniques in Asian eyes

Ezekiel Ze Ken Cheong[1], Clarissa Ng Yin Ling[2], Qiu Ying Wong[2,3], Chloe Si Qi Chua[2,3], Hla Myint Htoon[1,3] and Marcus Ang[1,2,3]*

[1]Ophthalmology and Visual Sciences Academic Clinical Program, Duke-NUS Medical School, Singapore, Singapore, [2]Singapore National Eye Centre, Singapore, Singapore, [3]Singapore Eye Research Institute, Singapore, Singapore

KEYWORDS

Descemet membrane endothelial keratoplasty (DMEK), clinical outcomes, graft survival, surgical techniques, pull-through, endothelium-in

A Corrigendum on
Clinical outcomes of DMEK comparing endothelium-out injector and endothelium-in pull-through techniques in Asian eyes

by Cheong, E. Z. K., Ng Yin Ling, C., Wong, Q. Y., Chua, C. S. Q., Htoon, H. M., and Ang, M. (2025). *Front. Med.* 12:1555620. doi: 10.3389/fmed.2025.1555620

In the published article, there was an error in Figure 1 as published. Panels C and D of Figure 1 have been erroneously swapped. The corrected Figure 1 with its unchanged caption appear below.

The authors apologize for this error and state that this does not change the scientific conclusions of the article in any way. The original article has been updated.

10.3389/fmed.2025.1624456

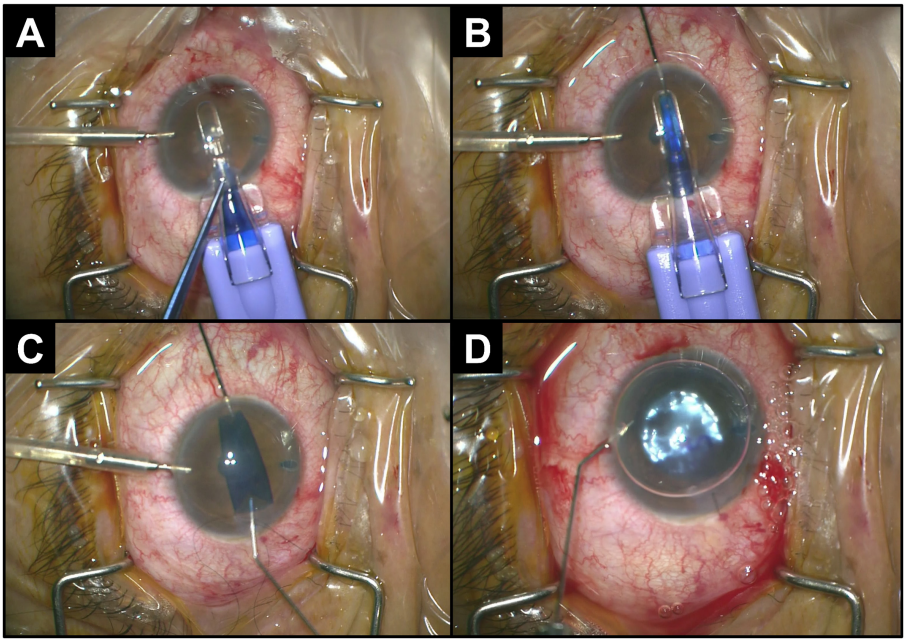

FIGURE 1
Intraoperative procedure for pull-through DMEK. **(A)** Insertion of the cartridge into the anterior chamber through a clear cornea incision. **(B)** Grasping and pulling-through of graft with forceps. **(C)** Natural unfolding of the graft with endothelium-down. **(D)** Injection of gas to tamponade the donor graft to the recipient cornea.

frontiers | Frontiers in Medicine

TYPE Original Research
PUBLISHED 09 May 2025
DOI 10.3389/fmed.2025.1537139

OPEN ACCESS

EDITED BY
Georgios D. Panos,
Aristotle University of Thessaloniki, Greece

REVIEWED BY
Jian Hua Huang,
Hunan University of Chinese Medicine, China
Xue Xiao,
Guangdong Pharmaceutical University, China

*CORRESPONDENCE
Qi Xu
✉ xuqiahtcm@yeah.net
Zhaohui Fang
✉ fangzhaohui1111@163.com

†These authors have contributed equally to this work and share first authorship

RECEIVED 30 November 2024
ACCEPTED 23 April 2025
PUBLISHED 09 May 2025

CITATION
Zhang H, Li Y, Xu Q and Fang Z (2025) Unveiling the molecular mechanisms of stigmasterol on diabetic retinopathy: BNM framework construction and experimental validation.
Front. Med. 12:1537139.
doi: 10.3389/fmed.2025.1537139

Unveiling the molecular mechanisms of stigmasterol on diabetic retinopathy: BNM framework construction and experimental validation

Hongrong Zhang†, Yufan Li†, Qi Xu*† and Zhaohui Fang*

Anhui University of Chinese Medicine, Hefei, China

Background: Diabetic retinopathy (DR), one of the most common complications of diabetes, severely impacts patients' quality of life. The combined use of the traditional Chinese medicines Astragalus, Fructus ligustris, and Cornus officinalis has yielded considerable therapeutic effects in clinical DR treatment.

Methods: In this study, a multimodule framework (BNM) encompassing bioinformatics, network pharmacology, and machine learning (ML) based on molecular fingerprints was innovatively developed to thoroughly investigate the molecular mechanisms of this Chinese medicine in treating DR.

Results: A total of 40 active components and 12 core targets were identified. Enrichment analysis identified key pathways such as VEGF signaling pathway, TNF signaling pathway and HIF-1 signaling pathway. Prediction models using key targets, such as PPARG, were constructed from the GEO database and validated via immune infiltration analysis and molecular docking, revealing that PPARG may be a potential target for DR treatment. Moreover, the core component of this Chinese medicine, stigmasterol, was identified using a ML model based on molecular fingerprints. *In vivo* experiments demonstrated that stigmasterol can regulate glucose and lipid metabolism, improve systemic inflammatory levels, and ameliorate ocular vascular changes in DR by modulating the expression of PPARG.

Conclusion: The BNM framework suggests that PPARG may be an important target for stigmasterol in the treatment of DR, with its mechanism potentially related to the VEGF/VEGFR pathway.

KEYWORDS

herbal medicine, diabetic retinopathy, machine learning, molecular fingerprint, experimental verification

1 Introduction

Diabetic retinopathy (DR) is one of the most common microvascular complications of diabetes. Currently, approximately 103 million people with diabetes worldwide are affected by DR (1). A 2020 study on the causes of blindness and visual impairment revealed that DR is the fifth most common cause of preventable blindness and moderate to severe visual

impairment (2). Currently, DR is commonly treated clinically with intravitreal injections of steroids and anti-vascular endothelial growth factor. However, these treatments can have unstable therapeutic effects and considerable side effects (3). Consequently, it is important to find safe and effective new drugs.

Since traditional Chinese medicines (TCMs) are composed of a variety of herbs with extensive active ingredients and drug targets, they have shown outstanding clinical efficacy in the treatment of DR (4). The triplet medicine composed of *Astragalus-Fructus ligustris-Cornus officinalis*, known as HuangQi (HQ)-NvZhenZi (NZZ)-ShanZhuYv (SZY), has been extensively applied in the clinic to treat DR and serves as the core medicinal component in numerous traditional Chinese medicine prescriptions, as it can effectively ameliorate the clinical symptoms of DR (5). According to TCM theory, vision is closely related to the liver, as well as the contents of Qi and blood in humans. HQ supplements Qi whereas NZZ and SZY supplement the blood in liver, which then sends blood upwards to the eyes to supplement Qi and the blood and improve eyesight. Previous laboratory studies have shown that the astragaloside IV contained in HQ inhibits the expression of miR-138-5p, thereby increasing the activities of Sirt1/Nrf2 and the antioxidant capacity of cells to improve ferroptosis and reduce cell death, ultimately inhibiting the progression of DR (6). Luteolin, an effective component of NZZ, can reduce the expression of NLRP1, NOX4, TXNIP, and NLRP3, thereby increasing inflammation and oxidative stress and inhibiting the retinal cell apoptosis in DR rats (7). The quercetin and saponins extracted from SZY can lower blood glucose and blood lipid levels by protecting islet function, thus improving insulin resistance and regulating glucose and lipid metabolism (8–11). Moreover, SZY extract can improve diabetes-related complications (12). However, the specific effects, targets and mechanisms of the combined use of these three drugs have not been systematically studied.

Fortunately, the development of artificial intelligence (AI) technology has brought new opportunities for research in this field. Owing to its excellent data processing capabilities, AI can reveal the deep connections between the chemical components of TCMs, diseases, and targets, providing a new approach to understand the complex interactions between the components of TCMs and elucidating the mechanisms of diseases. For example, Li et al. combined machine learning (ML) and deep learning models to predict antioxidant activity in gentian (13). Gu et al. developed a heterogeneous graph neural network model to predict the compatibility strength and probability among the herbs within the relevant prescriptions of colorectal adenoma (14). Zhang et al. applied the deep learning graph embedding algorithm framework Node2vec, in combination with Danshen and Chuanxiong, to successfully predict new targets for the treatment of cardiovascular diseases (15). These studies indicate that the application of AI technology in TCM research cannot only promote an understanding of the mechanisms of action of TCMs but also provide new perspectives for explaining the interactions between TCMs and diseases.

In this study, an integrated framework (BNM) encompassing bioinformatics, network pharmacology, and molecular fingerprint ML to assess the potential of the using the triplet medicine HQ, NZZ, and SZY for the treatment of DR was successfully developed and validated. We extracted the active components of these herbs from TCM databases and the literature and performed functional enrichment analysis, constructed a diagnostic model, and carried out immunological analysis and molecular docking by screening core targets and components. Furthermore, we developed a ML model using 990 compounds from the LOPAC-1280 and Prestwick Chemical Library and validated it with the core components of the triplet medicine. We also applied the Breaking of Retrosynthetically Interesting Chemical Substructures (BRICS) and Retrosynthetic Combinatorial Analysis Procedure (RECAP) algorithms for fragment analysis of the core components to evaluate the potential of this model to generate lead components. Finally, these findings were corroborated through animal experiments (Figure 1). In summary, in our research, we evaluated the efficacy of combined DR treatment with the triplet medicine from multiple perspectives, utilized a molecular fingerprint ML model to identify effective TCM components, and provided a novel perspective for drug research and repurposing.

2 Materials and methods

2.1 Construction of the DR drug-associated gene network

All the components in HQ, NZZ, and SZY were collated on the basis of the Traditional Chinese Medicine Systems Pharmacology Database and Analysis Platform (TCMSP). Generally, oral bioavailability (OB) is one of the most crucial absorption, distribution, metabolism and excretion (ADME) pharmacokinetic parameters, whereas drug likeness (DL) indicates the similarity between the physical properties of the component in question and those of known drugs (16). In this study, the criteria for identifying effective components were set to OB $\geq$ 30% and DL $\geq$ 0.18. The relevant targets of the bioactive components were subsequently identified using the SwissTargetPrediction database and standardized using the UniProt database. DR-related genes were obtained from the Comparative Toxicogenomics Database (CTD) and the GeneCards and Disease Gene Network (DisGeNET) databases. The genes associated with diseases and drugs were intersected using the UpSetR package in R software to identify the intersecting genes. Three DR–TCM-related genes were subsequently added to the gene set after review of the literature. A protein–protein interaction (PPI) network was constructed on the basis of the gene sets. The PPI network developed using the STRING platform, an interactive gene database, gave a high confidence interaction score (0.7), indicating a targeted network. All of the database searches were limited the species to *Homo sapiens*.

2.2 Core network cluster mining and functional analysis

To further explore the core network, we employed Cytoscape software (version 3.82) to visualize the target network. Network analysis tools were employed to calculate the key network metrics, including the network diameter, the clustering coefficient, and multiedge node pairs. The MCODE plugin, which employs molecular complex detection, was used for core network mining on

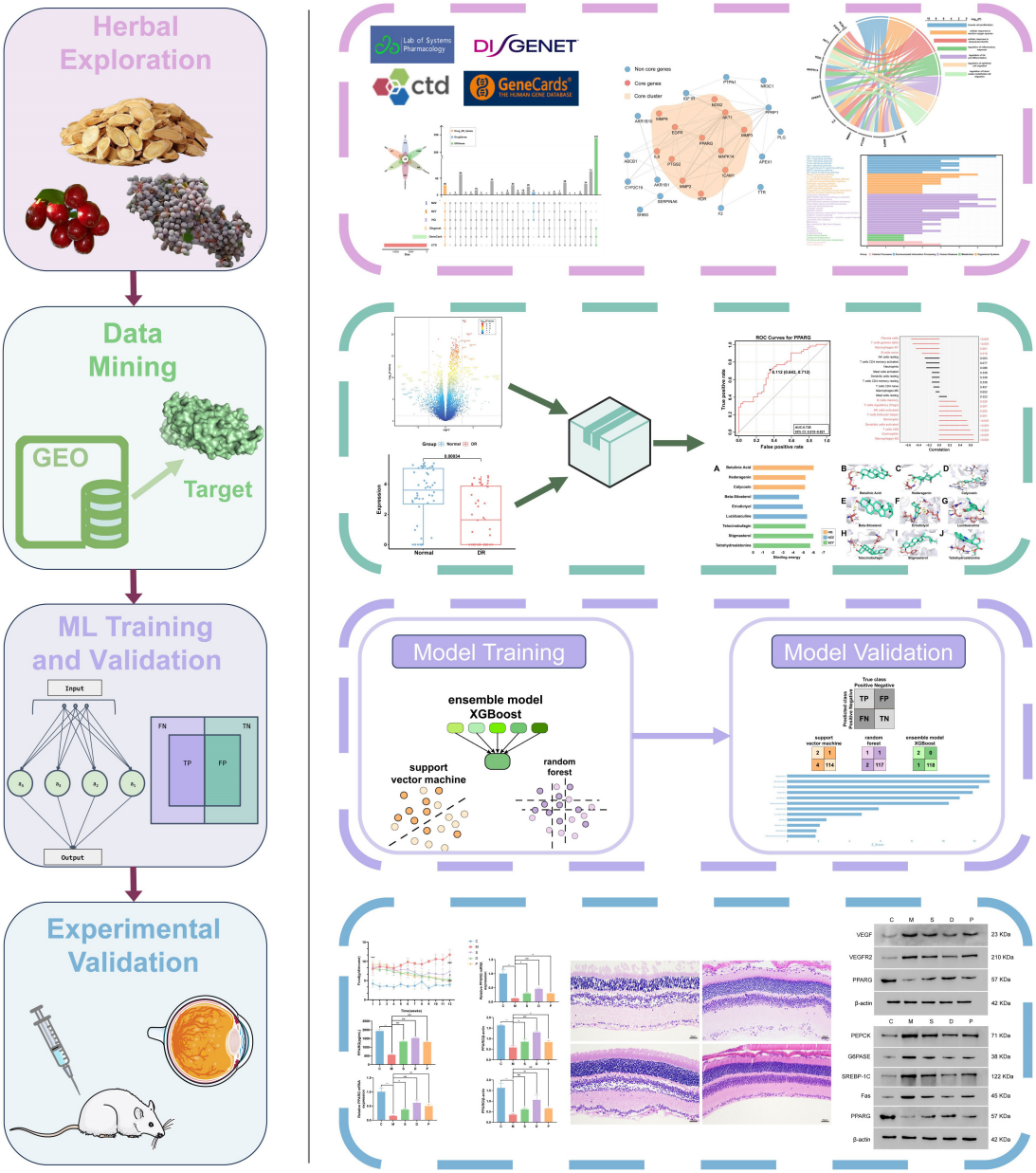

FIGURE 1
Workflow of this study. Different colors denote different modules. The pink color represents the network pharmacology module, the green color represents the bioinformatics module, the purple color represents the molecular fingerprint-based ML module, and the blue color represents the animal experimental validation module.

the target network. The core network group was obtained with the following parameters: degree cut-off = 2, node score cut-off = 0.2, K-core = 2, and max depth = 100.

The clusterProfiler package in R was employed for gene ontology (GO) and Kyoto Encyclopedia of Genes and Genomes (KEGG) analyses of both the target and core networks, and the results were filtered at the level of p-value ≤ 0.05. GO analysis encompasses three domains: biological process (BP), molecular function (MF), and cellular component (CC). The GO results were filtered to exclude the terms significantly unrelated to DR. KEGG analysis revealed the top 40 target networks and the top 30 core networks, as the latter results were weakly correlated with DR. The results were plotted using the R packages ComplexHeatmap, ggplot2, and circlize.

2.3 Identification of differentially expressed genes (DEGs)

Mining of the core network group and functional analysis revealed that 12 core targets were strongly correlated with DR. To further investigate and confirm the biological functions of the core targets in DR, we randomly selected PPARG for subsequent analysis. The Gene Expression Omnibus (GEO) database includes

high-throughput gene expression data, DNA microarray data, and hybridization array data (17). The GSE146615 microarray dataset, including 42 control samples and 52 samples from individuals with DR, was downloaded from the GEO database. Differential expression analysis was performed using the limma package in R. The limma package is renowned for its capabilities in terms of data normalization and precise gene expression data interpretation, and has therefore become the preferred choice for high-throughput and microarray differential analysis (18). The screening criteria were $|\log (FC)| > 1$ and p-value < 0.001. The ggplot2 package was employed to generate a volcano plot, which was used to visualize the top 30 DEGs. A focused analysis of PPARG was subsequently conducted to explore its expression in the normal and DR groups, and the data were plotted with the ggpubr package.

2.4 Diagnostic prediction model establishment and immune analysis

To evaluate the diagnostic and predictive utility of PPARG for DR, a predictive model was developed using microarray datasets. Analysis was conducted using the pROC package in R software. Binary classification models are commonly evaluated using receiver operating characteristic (ROC) curves (19). The position of the ROC curve in relation to the upper left quadrant is indicative of the classification performance of the method in question. The bootstrap algorithm was employed for statistical analysis. Bootstrap, proposed by Efron, is a simulation-based sampling statistical inference algorithm that does not require assumption of a specific theoretical distribution (20). The area under the curve (AUC) can then be used to assess the predictive accuracy of PPARG. A larger AUC indicates greater accuracy of using PPARG for DR diagnosis. The abscissa False Positive Rate (FPR) and ordinate True Positive Rate (TPR) of the ROC curve can be calculated via the following formula.

$$FPR = \frac{FP}{FP+TN} \tag{1}$$

$$TPR = \frac{TP}{TP+FN} \tag{2}$$

Here, TP, TN, FP, and FN represent the numbers of true positive, true negative, false positive, and false negative results, respectively (Equations 1 and 2). TP represents the number of samples correctly predicted as positive by the model. TN represents the number of samples correctly predicted as negative by the model. FP represents the number of samples predicted as positive by the model but that were actually negative. FN represents the number of samples predicted as negative by the model but that were actually positive. FPR is calculated as the proportion of actual negative samples that were incorrectly predicted as positive by the model. TPR is calculated as the proportion of actual positive samples that were correctly predicted as positive by the model.

An investigation was subsequently conducted to determine whether PPARG disrupts normal homeostasis by mediating immune dysregulation, thereby leading to DR. To this end, the CIBERSORT algorithm was employed to assess the correlation between PPARG and 22 immune cell types within the dataset. The CIBERSORT algorithm is a canonical computational method for analyzing immune outcomes. It employs the principles of linear SVM regression to deconvolve the expression profiles of immune cell subtypes and calculate their abundance (21). The statistical threshold was set to $p < 0.05$, and the results were visualized using the ggpubr package in R.

2.5 Binding free energy calculations

To evaluate the functional effects of the active components present in HQ, NZZ, and SZY on PPARG, we employed AutoDock software (version 1.5.6) to compute the binding free energies between PPARG and these components. The structure of PPARG was retrieved from the RCSB Protein Data Bank (PDB) database, and the water molecules present were subsequently removed. The structures of the active components of these three medicinal preparations were sourced from the PubChem database. After processing, a Lamarckian genetic algorithm was used to predict the molecular conformations of the protein receptor and small molecules, and the binding energies of the active ingredients were computed separately. These binding energies indicate the affinity of the small molecule for the protein. The binding energies were also calculated via the following formula:

$$\Delta G_{BIND} = \Delta G_{VDW} + \Delta G_{HBOND} + \Delta G_{ELECT} + \Delta G_{TOR} + \Delta G_{DESOLVA} \tag{3}$$

In Equation 3, ΔGBIND represents the binding free energy, ΔGVDW denotes the van der Waals potential, ΔGHBOND represents the hydrogen bonding potential, ΔGELECT denotes the electrostatic potential, ΔGTOR represents the dihedral angle torsional energy, and ΔGDESOLVA indicates the free energy of solvation; the units are kcal·mol^{-1}. The coordinates of the active cavity center of PPARG were defined as x_center = 3.812, y_center = 49.518, and z_center = 67.059, and the search space box was set to 126*126*126. The time of conformational searches was set to 50. ΔGBIND < -5 kcal·mol^{-1} indicates good binding capacity, while ΔGBIND < -7 kcal·mol^{-1}indicates strong binding capacity.

Additionally, the three highest binding energies of the active components with PPARG were selected. The pyplot module in Python was used to construct a bar chart. Finally, the conformations were visualized with PyMOL software (version 2.1) according to the calculated binding free energies.

2.6 Drug composition model validation

2.6.1 Data assembly and feature determination

To validate the therapeutic efficacy of the aforementioned nine compounds in DR, a diverse array of compounds was gathered to train a ML model. We collected 394 negative compounds from LOPAC-1280, and defined the 9 components of HQ, NZZ, and SZY as positive compounds. Significantly more negative compounds than positive compounds were included to ensure that the model would be able to identify positive compounds with greater accuracy. Although the majority of the compounds were deemed negative, it

is possible that a small proportion of these molecules may have been mislabelled, as there may be undiscovered compounds that could be used to treat DR.

These 403 compounds were converted to SMILES format, and the RDKit package in Python was employed to compute a range of physical and chemical descriptors from 200 unique aspects, including Hybrid Estate-VSA descriptors, topochemical descriptors, and the QED and Lipinski parameters. RDKit is a computational chemistry toolkit that can process molecules, analyze different chemical input formats, filter out unwanted compounds, standardize molecules, and calculate various molecular characteristics (22). The results were plotted using the matplotlib package in Python.

2.6.2 Model training

To increase the computational accuracy and stability of the model, three distinct ML algorithms were employed: XGBoost 2.0.3, random forest (RF), and SVM. Both RF and SVM utilized scikit-learn 1.3.0. The Gini index was used to assess the feature importance of the 200 physicochemical descriptors in the dataset. Feature importance helps to indicate the significance of the physicochemical descriptors, which are believed to be closely linked to classification. When each feature node pertains to the same class, the Gini index is minimal, leading to the highest purity and minimal uncertainty (23).

The acquired feature dataset was subsequently reconstructed and assembled using various models. The dataset containing 403 compounds was split into training and testing sets via stratified random sampling (70% for training and 30% for testing). To ensure fair comparison among the models and robust model performance, the positive samples were fully utilized. Following cross-validation to check for overfitting, model comparisons were assessed via three performance metrics: precision, recall, and F1 score, as follows.

$$Precision = \frac{TP}{TP + FP} \tag{4}$$

$$Recall = \frac{TP}{TP + FN} \tag{5}$$

$$F1\ score = \frac{2}{\frac{1}{Precision} + \frac{1}{Recall}} \tag{6}$$

Precision represents the proportion of samples predicted to be positive by the model that are actually positive, emphasizing the accuracy of the prediction [Equation (4)]. Recall represents the proportion of actual positive samples that were correctly predicted by the model, which emphasizes the coverage of positive samples (Equation 5). F1 score is the harmonic mean of Precision and Recall, which is used to assess the model's performance in a combined manner (Equation 6). F1 score is designed to balance Precision and Recall, thereby mitigating the extremes that may occur when these metrics are used individually. Precision, recall, and F1 score take values between 0 and 1, with higher values indicating better predictive performance of the model.

Moreover, we considered the possibility of optimizing the three models in accordance with the existing predictions. Encouragingly, the class weight parameters for the SVM and RF models were adjusted to the balanced and default values, respectively. Additionally, the maximum depth of the XGBoost model was 10 and the colsample_bytree was 0.5, which were suggested to be the optimal choices. The optimized model was subsequently retrained, and the results of each prediction were evaluated in detail by plotting the mean AUC, which can eliminate the instances of a single prediction being either poor or overly high, facilitating an objective assessment of the performance of the three models on the dataset (24). Three ML models were compared using the Python package numpy, sklearn, and matplotlib for visualization.

2.6.3 Model evaluation

Upon evaluation, the SVM model exhibited the least predictive power, and the XGBoost model was marginally superior to the RF model in terms of predictive ability. XGBoost was selected for evaluation to ascertain its performance in practical applications, and the dataset was augmented by incorporating 596 compounds from LOPAC-1280 and the Prestwick Chemical Library for a total of 999 distinct compounds. The compounds were subsequently no longer categorized as either negative or positive, enabling the model to autonomously interpret and make decisions on the sole basis of the physical and chemical descriptions, thereby completing the identification task. The data were normalized using XGBoost, and z scores and probabilities were calculated. A z_score greater than 1.83 was considered indicative. The z scores were calculated as follows:

$$\tilde{X} = \frac{1}{n}\sum_{i=1}^{n} X_i \tag{7}$$

$$Z\ score = \frac{\tilde{X} - E[X]}{\sigma\ X\ /\sqrt{n}} \tag{8}$$

In Equation (7), $\tilde{X}$ denotes the average value, n represents the number of samples, and X_i represents the observed value of the i-th sample. $\tilde{X}$ is calculated by summing the observed values of all samples and dividing by the number of samples n, thereby reflecting the center of the data set. In Equation (8), E[X] denotes the overall mean. $\sigma\ X$ denotes the standard deviation. The z_score indicates whether the sample mean deviates significantly from the overall mean, which can serve as one indicator among others for assessing the model's performance. The results were plotted using the matplotlib package in Python.

2.6.4 Exploring the possibility of identifying lead compounds

Decomposing drug molecules into fragments and constructing chemically feasible fragment libraries are pivotal stages in the drug discovery process. To explore the nine drug components of HQ, NZZ and SZY for lead compound development on the basis of fragments, the RECAP and BRICS algorithms were employed to extract commonalities from the drug molecular fragments. The RECAP algorithm, which is based on retrosynthetic analysis, manipulates a series of cleavage sites to yield a set of plausible drug molecular fragments that adhere to the fundamental principles of practical cleavage tools (25). In contrast, the BRICS algorithm segments molecules on the basis of bond formation (26). Consequently, fragments similar to those generated by BRICS can be used to reassemble new drug molecules, thereby increasing the probability that these fragments can be used to synthesize new drugs (27). Finally, molecular structures were drawn using the rdkit.Chem.Draw package in Python.

2.7 Experimental verification in an animal model

2.7.1 Animal grouping, modeling, and treatment

The number of experimental animals per group was calculated using the resource-equation method with the following formula:

$$E = K(n-1) \quad (9)$$

In Equation (9), K is the number of treatment groups, n is the number of animals per group, and E is the error degrees of freedom. Setting $E = 20$, the equation yielded $n = 6$ animals per group. To accommodate potential attrition, 10 animals were allocated to each group (28).

Forty 8-week-old SPF male db/db mice and 10 8-week-old SPF male C57BL/6 mice were reared at 22.5°C with 40–50% humidity on a 12/12 h light/dark cycle. The C57BL/6 mice were fed ordinary feed, while the db/db mice were fed a high-fat diet. This study was approved by the Animal Ethics Committee of Anhui University of Chinese Medicine (ethics number: AHUCM-mouse-2024116) and was conducted in strict accordance with the animal experiment guidelines.

After 1 week of adaptive feeding, the db/db mice were randomly divided into a model group (M; 0.2 $mL{\cdot}kg^{-1}{\cdot}d^{-1}$ 0.9% NaCl), a positive control group (P; 10 $mg{\cdot}kg^{-1}{\cdot}d^{-1}$ pioglitazone + 230 $mg{\cdot}kg^{-1}{\cdot}d^{-1}$ calcium oxybenzoate), a Chinese medicine intervention group (D; 910 $mg{\cdot}kg^{-1}{\cdot}d^{-1}$), and a single drug intervention group (S; 100 $mg{\cdot}kg^{-1}{\cdot}d^{-1}$ stigmasterol), with 10 animals in each group. Once a day for 12 weeks, the C57BL/6 mice in the blank control group (C) were given an equal volume of 0.9% NaCl solution. The general conditions of the mice, such as activity, hair color, and water intake, were observed. Body mass was measured every 3 weeks, and blood glucose level, determined from a sample taken from the tip of the tail, was measured before and 12 weeks after treatment.

2.7.2 Haematoxylin and eosin staining

The retinal tissue of the mice was fixed with 4% paraformaldehyde solution for 24 h, dehydrated, embedded in paraffin and made into 5 μm slices. The slices were treated with xylene, anhydrous ethanol and 75% ethanol in sequence, washed, and stained with haematoxylin for 5 min. Following dehydration with gradient ethanol and staining with eosin solution for 20 min, the pathological morphologies of the retinal tissue slices were observed via optical microscopy after dehydration with anhydrous ethanol and sealing and making transparent with xylene and neutral gum.

2.7.3 Detection of biochemical indices

Fasting blood glucose (FBG), total cholesterol (TC), and triglyceride (TG) levels were assessed using a fully automated biochemical analyser. The levels of glycated hemoglobin A1c (HbA1c), low-density lipoprotein cholesterol (LDL-C), high-density lipoprotein cholesterol (HDL-C), PPARG, tumor necrosis factor-α (TNF-α), interleukin-1β (IL-1β), interleukin-6 (IL-6), and interleukin-10 (IL-10) were determined via enzyme-linked immunosorbent assays (ELISAs).

2.7.4 Western blotting (WB)

The tissue blocks were washed with precooled phosphate-buffered saline (PBS) 2–3 times, cut into small pieces and placed in a homogenization tube, and 10 volumes of lysis solution was added. Homogenization was performed on ice for 30 min with shaking every 5 min to ensure complete tissue lysis. Then, the mixture was centrifuged at 12,000 rpm and 4°C for 10 min, and the supernatant, which contained the total protein, was collected. The protein concentration was determined via the BCA method. After performing gel electrophoresis, transferring to a PVDF membrane, and sealing, the PVDF membrane was immersed in 1:1,000 dilutions of the following monoclonal antibody solutions at 4°C with shaking on a bed overnight: vascular endothelial growth factor (VEGF), VEGFR2, PEPCK, G6PASE, SREGBP-1C, Fas, and PPARG. Then, sheep anti-rat HRP-labeled secondary antibody (diluted 1:5,000) was added for incubation at 37°C for 2 h. The samples were washed with Tris-buffered saline containing Tween-20 (TBST) 3 times for 5 min each time. Finally, the samples were analyzed with an enhanced chemiluminescence (ECL) system.

2.7.5 Quantitative polymerase chain reaction (qPCR)

The tissue blocks were ground completely, and an appropriate amount of TRIzol reagent was added to extract total RNA. Reverse transcription was performed according to the kit instructions, followed by gentle mixing and centrifugation The reverse transcription program was as follows: 25°C for 5 min, 42°C for 30 min, and 85°C for 5 min. After reverse transcription, amplification was performed as follows: predenaturation at 95°C for 5 min; followed by 40 thermal cycles of denaturation at 95°C for 10 s, annealing at 60°C for 20 s, and extension at 72°C for 20 s. β-Actin was selected as the internal reference to determine the Ct value of each target. The relative mRNA expression levels were calculated via the $2\text{-}\Delta\Delta Ct$ method. The primers used are shown in Table 1.

2.7.8 Statistical analysis

The BNM framework was developed using R (version 4.3.0) and Python (version 3.8). Data were analyzed using SPSS version 26.0. The Shapiro-Wilk test was employed to assess the normality of the experimental data. Results are presented as mean ± standard deviation. Homogeneity of variances across groups was evaluated using Bartlett's test. Differences among groups were analyzed using one-way ANOVA, followed by Tukey's *post hoc* analysis for multiple comparisons. For comparisons between two groups, an independent samples t-test was conducted. A significance level of $\alpha = 0.05$ was set, and $p < 0.05$ was considered statistically significant. The results of the animal experiments described above were visualized using GraphPad Prism version 9.0.0.

3 Results

3.1 TCM component mining and target acquisition

TCMSP database screening yielded a total of 40 chemical components, of which 17 were from HQ, 9 were from NZZ,

TABLE 1 Primer sequences used for qPCR.

Gene	Primer	Sequence (5′-3′)
VEGF	F	TCTTCCAGGAGTACCCCGAC
	R	GGGATTTCTTGCGCTTTCGT
VEGFR2	F	TCCACATGGGCGAATCACTC
	R	GCAATTCTGTCACCCAGGGA
PEPCK	F	TGCGGATCATGACTCGGATG
	R	AGGCCCAGTTGTTGACCAAA
G6PASE	F	GGGCATCAATCTCCTCTGGG
	R	GTCCAGGACCCACCAATACG
SREBP-1c	F	ACTGGACACAGCGGTTTTGA
	R	CTCAGGAGAGTTGGCACCTG
Fas	F	GTGGATCTGGGCTGTCCTG
	R	AGCAAAATGGGCCTCCTTGA
PPARG	F	ATTGAGTGCCGAGTCTGTGG
	R	GGCATTGTGAGACATCCCCA
β-actin	F	GATATCGCTGCGCTGGTCG
	R	AGGTGTGGTGCCAGATCTTC

and 14 were from SZY. Mining using Swiss Target Prediction yielded a total of 1071 targets, of which 475 were from HQ, 226 were from NZZ, and 370 were from SZY. A total of 4,560 targets, 648 targets, and 13,901 targets related to DR were subsequently identified from the GeneCards, DisGeNET, and CTD databases, respectively. The UpSetR package was used for intersection of the six different target classes, as shown in Figure 2A, and 30 target intersecting genes were obtained. After literature mining, MAPK14, ICAM1, and IL6 were added to the list intersecting genes to form a gene set. High-confidence interaction scores were subsequently generated using the STRING database to obtain target network clusters, which helped us to better understand the interactions between the therapeutic targets.

3.2 Core network construction and functional enrichment analysis

To further explore the interactions in the core network, we analyzed the target network cluster. The target network cluster results were further analyzed using the MCODE plugin in Cytoscape software, and a network cluster consisting of 12 core genes was obtained (Figure 2D), wherein red nodes represent the core network genes and blue nodes represent the noncore network genes. Moreover, we aimed to assess which relevant DR biological processes and pathways might be affected by HQ, NZZ, and SZY. We conducted GO and KEGG analyses on the gene set and the core network cluster. The GO analysis of 33 genes yielded 1,262 entries. After removing the terms clearly unrelated to DR, we found associations with positive regulation of fat cell differentiation, response to insulin, and response to lipopolysaccharide amongst the BPs. The MFs were focused on steroid binding and transmembrane receptor protein tyrosine kinase activity. The CCs were centered on the membrane raft and blood microparticles (Figure 2B). The 12 core network clusters contained a total of 1226 GO entries. Upon comparison, we discovered that the main enriched terms were associated with muscle cell proliferation, the cellular response to reactive oxygen species, and the response to lipopolysaccharide (Figure 2E). Interestingly, both GO analyses included the regulation of fat cell differentiation and the response to lipopolysaccharide, indicating that these two biological processes may be important. Moreover, the KEGG enrichment results for the 33 genes and 12 core network clusters together indicated that the VEGF signaling pathway, TNF signaling pathway and HIF-1 signaling pathway may play key roles in DR therapy, as their degree of enrichment and pathway importance were higher (Figures 2C,F).

3.3 Validation of PPARG in clinical samples

To explore the functions of the core network genes in DR, we selected PPARG from the GSE146615 microarray dataset as the target for further investigation. After filtering and screening, 331 genes were differentially expressed, amongst which 162 were upregulated and 169 were downregulated. The volcano plot displaying the top 30 DEGs (Figure 3A) revealed a significant difference in the expression of PPARG, which was consistent with our previous analysis. Additionally, after performing a separate analysis of the PPARG gene, we found that the expression of PPARG in the DR group was very significantly lower than that in normal tissue ($p < 0.001$) (Figure 3B).

3.4 Analysis of the diagnostic prediction model performance and immune microenvironment analysis

To evaluate the diagnostic value of PPARG for DR, we established a PPARG diagnostic prediction model on the basis of the GSE146615 dataset. The TPR and FPR of PPARG were evaluated via ROC curve analysis, and the results revealed that the AUC value of PPARG was 0.720 (95% CI: 0.615–0.821) (Figure 3C). These findings indicate that PPARG has high diagnostic value for DR. To further explore whether PPARG affects the development of DR through immune cells, we evaluated the relationship between PPARG expression and immune cells in DR using the CIBERSORT algorithm. Considering $p < 0.05$ as a correlation, PPARG was negatively correlated with four immune cells (Figure 3D), namely, plasma cells ($p < 0.001$), gamma delta T cells ($p < 0.001$), M1 macrophages ($p = 0.001$) and naive B cells ($p = 0.018$). PPARG was positively correlated with the infiltration of 9 types of immune cells, namely, M2 macrophages ($p < 0.001$), eosinophils ($p < 0.001$), CD8 T cells ($p < 0.001$), activated dendritic cells ($p < 0.001$), monocytes ($p < 0.001$), follicular helper T cells ($p = 0.001$), activated NK cells ($p = 0.002$), regulatory T cells (Tregs) ($p = 0.007$) and memory B cells ($p = 0.02$). Taken together, these findings suggest that PPARG may play a key role in the progression of DR by regulating immune cells in the body.

FIGURE 2
Drug–disease network mining and functional analysis. **(A)** The drug targets of HQ, NZZ, and SZY were intersected with the acquired DR disease targets. **(B)** GO analysis of target network targets; blue represents BPs, yellow represents MFs, and green represents CCs. The closer the dots are to the periphery, the greater the significance of the GO entry. **(C)** KEGG enrichment analysis of the target network. A larger number of genes is associated with a more significant KEGG enrichment result. **(D)** Core network target mining. **(E,F)** GO and KEGG analyses of the core network targets.

3.5 Analysis of the binding free energies

To identify the ability of the identified components to bind to the target, we calculated the binding free energies between PPARG and selected components. The structures of 40 components were obtained from PubChem, of which 17 were from HQ, 9 were from NZZ and 14 were from SZY. The protein structure of PPARG was obtained from the RCSB PDB database (ID: 8aty). The 40 drugs were docked to PPARG, and the three drugs with the highest binding free energies were selected for visualization (Figure 4A). The results indicated that the three most active components of HQ and their binding free energies with PPARG were −6.01 kcal·mol^{-1} (betulinic acid), −5.17 kcal·mol^{-1} (hederagenin), and −5.12 kcal·mol^{-1} (calycosin). The three most active components of NZZ and their binding free energies with PPARG were −4.54 kcal·mol^{-1} (β-sitosterol), −4.9 kcal·mol^{-1} (eriodictyol), and −5.33 kcal·mol^{-1} (lucidusculine). Finally, the three most active components of SZY and their binding energies with PPARG were −5.18 kcal·mol^{-1} (telocinobufagin), −5.94 kcal·mol^{-1} (stigmasterol), and −5.64 kcal·mol^{-1} (tetrahydroalstonine). Figures 4B–J show that the components adopted different binding modes at the PPARG site, forming hydrogen bonding, H-π bonding and π-π bonding interactions. The above results indicate that these components have good, stable binding to PPARG in terms of binding free energy, verifying the therapeutic effects of HQ, NZZ, and SZY in DR.

3.6 Assessment of feature importance in the ML models

We initially assembled a dataset of 9 DR (positive) and nonDR (negative) compounds identified via TCM mining. The

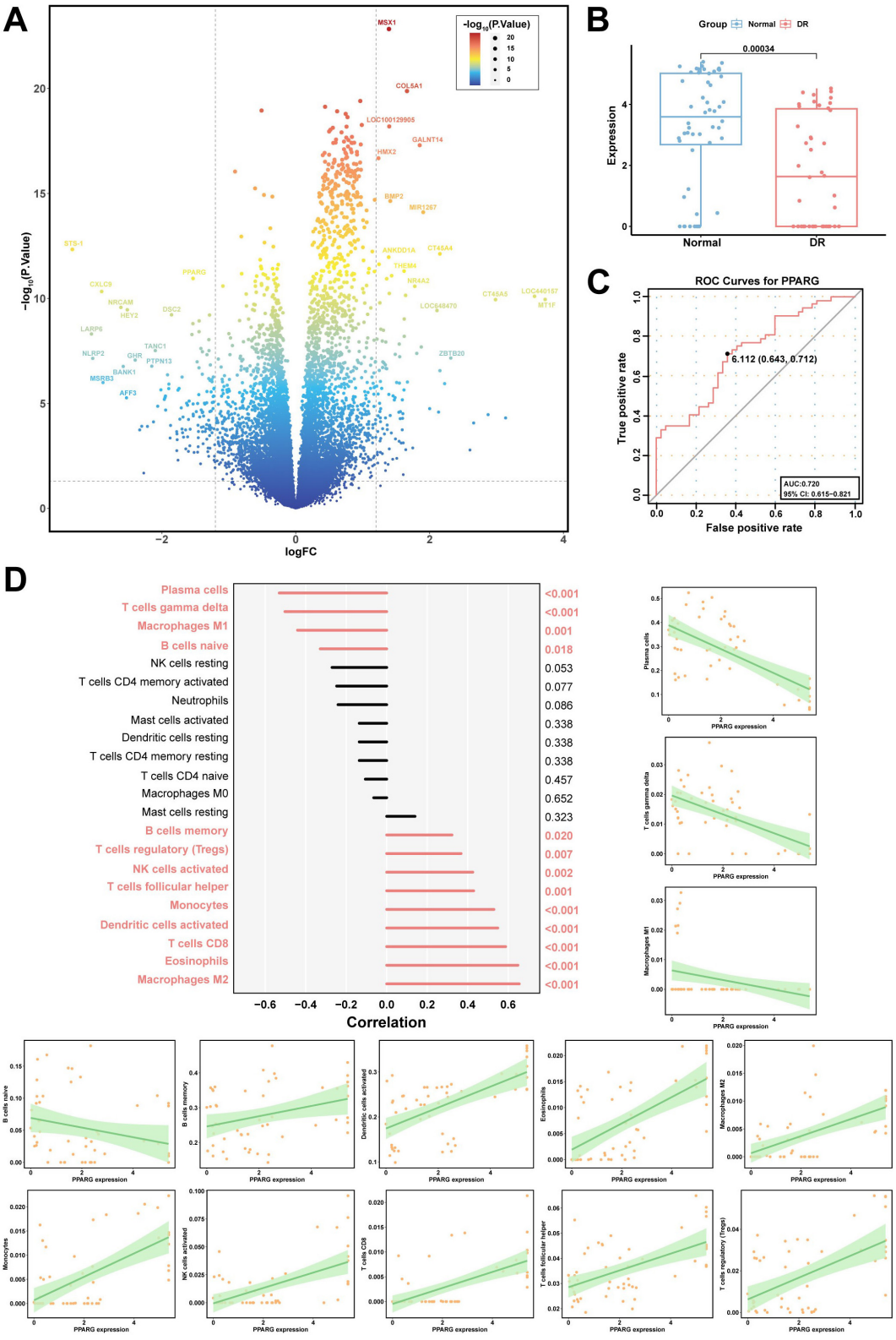

FIGURE 3
Evaluation of the DEGs, diagnostic modeling, and immunoassays. **(A)** Volcano map of the DEGs from the GSE146615 dataset (Significance increases from blue to red, with deeper red indicating higher significance of DEGs). **(B)** Differential expression of PPARG in DR and normal tissues in the GSE146615 dataset. **(C)** ROC curve and AUC of PPARG for DR diagnosis. The ROC curve is depicted as a red line. **(D)** PPARG and immune cells: plasma cells, gamma delta T cells, M1 macrophages, naive B cells, M2 macrophages, eosinophils, CD8 T cells, activated dendritic cells, monocytes, follicular helper T cells, activated NK cells, regulatory T cells (Tregs), and memory B cells. The green shading represents the confidence interval of the fitted curve.

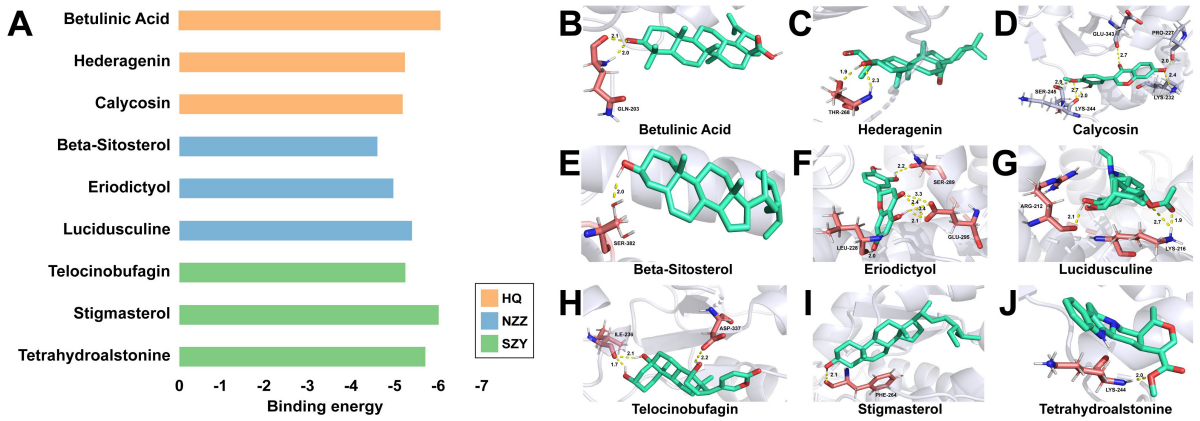

FIGURE 4
Binding free energy calculations. **(A)** Binding free energies of nine herbal components to PPARG. **(B–J)** Betulinic acid, hederagenin, calycosin, β-sitosterol, eriodictyol, lucidusculine, telocinobufagin, stigmasterol, and tetrahydroalstonine bind to PPARG with different binding modes. The green compound structure represents the small-molecule drug, the white indicates the protein, and the red highlights distinct protein residues.

nonDR data include a wide range of FDA-approved or clinical-stage compounds from LOPAC-1280, and 394 compounds were identified as clearly not associated with DR, such as adaphostin, trimipramine maleate, and propionylpromazine hydrochloride, upon analysis of both the LOPAC-1280 database and literature mining. The chemical structures of the compounds in the dataset were then converted into numerical format for model training, with 0 (negative) and 1 (positive), and 200 physicochemical descriptors were calculated using the RDKit package. We subsequently used RF to determine the feature values for model validation on the basis of physicochemical descriptors, performed feature selection on the entire dataset, and filtered out feature-irrelevant physicochemical descriptors to intervene in the impurity metric via the Gini index. After normalization, we obtained 120 feature values (Figure 5A and Supplementary Table 1), which were used in conjunction with a dataset of 403 compounds to train the different models for DR analysis.

3.7 Model validation

We then attempted to train the dataset using three different ML models: SVM, RF and XGBoost. Although the SVM algorithm is usually applied to linearly divisible datasets, the clever feature of SVM is that it can use kernels for classification and is therefore equally balanced when the data are not divisible. The dataset was randomly divided into a training set (split = 0.7) and a test set, with the training set containing 282 samples and the test set containing the remaining 121 samples. A fair comparison of performance between the models was made on the basis of cross-validation of the datasets and full use of the positive samples. After testing (Figure 5B), we found that the TN, TP, FN, and FP values were 114, 2,4 and 1 for the SVM model; 117, 1, 2, and 1 for the RF model; and 118, 2, 1, and 0 for the XGBoost model, respectively. We also used three performance metrics, precision, recall and F1 score, to evaluate the performance of the three models (Figures 5C–E). We believe that false positives are more detrimental than false negatives in early drug development, as they can lead to the mistaken assumption that compounds are effective, thereby increasing the cost of downstream drug development.

We also considered that the precision, recall and F1 scores could be effectively improved by adjusting the SVM and RF class weights as well as increasing the maximum depth of XGBoost. Through cross-validation, we found that the mean AUCs for the SVM, RF and XGBoost models were 0.63 ± 0.28, 0.65 ± 0.16, and 0.68 ± 0.12, respectively (Figures 5F–H). On the basis of the mean AUCs and considering the heterogeneity of the data, we believe that all three models have excellent performance.

3.8 Model prediction

Although all three models all had excellent performance, we focus mainly on the XGBoost model because of its lack of false positives and higher mean AUC, indicating higher accuracy. After adding the compounds from LOPAC-1280 and the Prestwick Chemical Library, we composed a dataset containing a more compounds (999). The abilities of these compounds to treat DR were predicted on the basis of their physicochemical characteristics using the XGBoost model. Figure 5I shows that most of the nine compounds derived from herbs had high z scores, among which stigmasterol ranked the highest, indicating that stigmasterol might be the best drug from HQ, NZZ, and SZY for DR treatment. Interestingly, three compounds, allylestrenol, exifone, and naltrindole hydrochloride, had higher z scores than some of the other compounds. Nevertheless, we believe that this finding is reasonable because there may be some compounds with undiscovered therapeutic effects on DR.

3.9 Fragmentation analysis of nine components

To explore the contributions of the functional groups of the nine components in the triplet medicine and assess whether these components can be modified to become lead components,

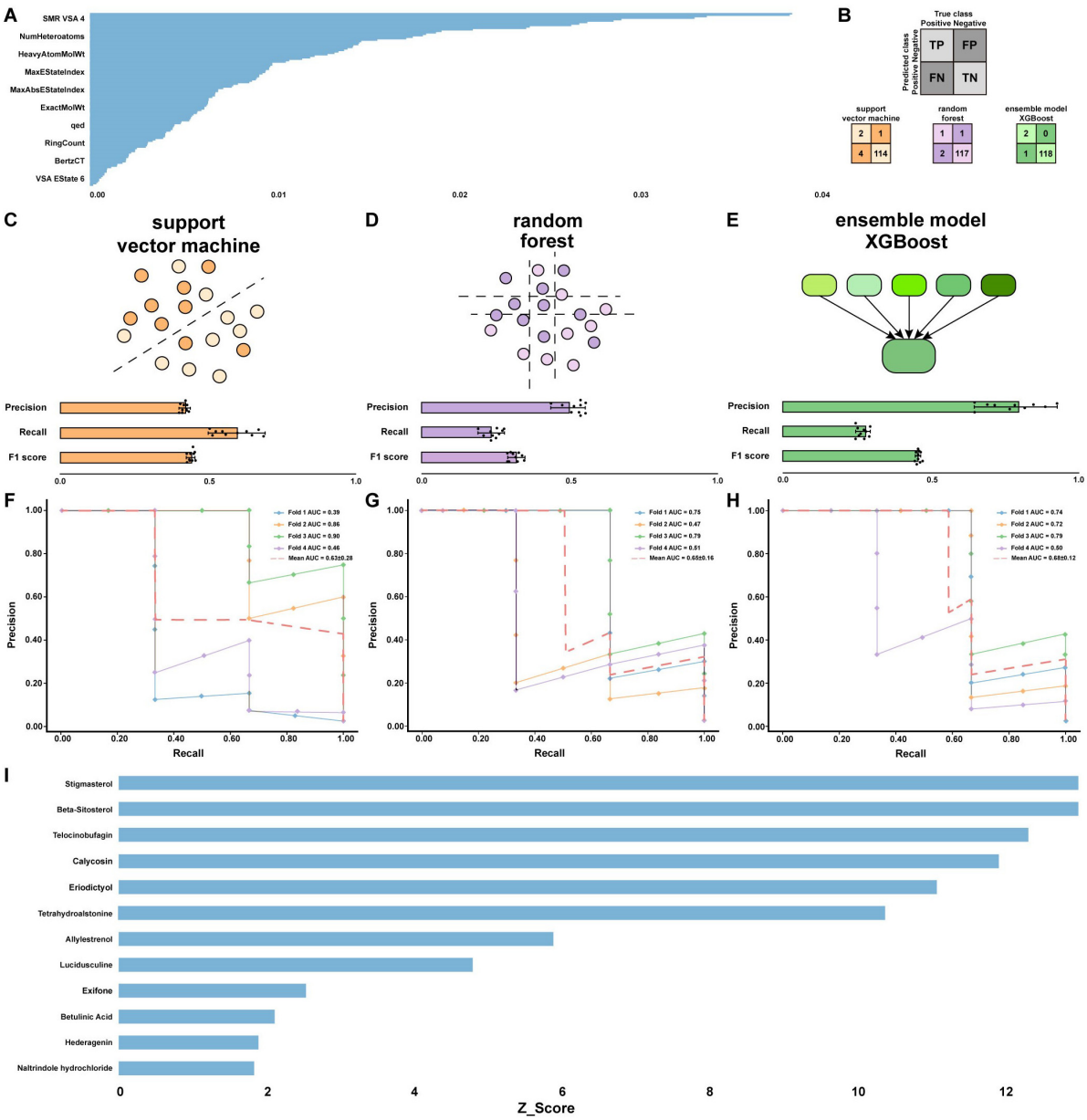

FIGURE 5
Drug composition ML data feature screening and model training, testing and evaluation. **(A)** Feature importance of 200 physicochemical descriptors in the data model using the RDKIT ML model. **(B)** Three ML algorithm models, SVM, RF and XGBoost, were evaluated on the test set to obtain confusion matrices. **(C–E)** The SVM, RF, and XGBoost algorithms were trained for cross-validation to compute three metrics: precision, recall and F1 score. The bar graph represents the average performance, and the error bars represent the standard deviation. **(F–H)** The SVM, RF and XGBoost algorithms were cross-validated 4 times to obtain precision-recall results and mean precision-recall values. **(I)** A dataset of 999 unclassified compounds was subsequently evaluated using the XGBoost ML algorithm and assigned a z score to indicate their potential as a drug to treat DR, with a higher z score representing a greater probability of treating DR.

we performed fragment segmentation of nine components using the RECAP and the BRICS algorithms. Fragment-based drug discovery (FBDD) is a common lead discovery approach that differs from high-throughput screening (HTS) in that early FBDD results may have more applicable physicochemical properties. Upon segmentation by both algorithms, we found that the BRICS algorithm, which is based on bond synthesis, separated β-sitosterol, telocinobufagin, eriodictyol, tetrahydroalstonine, and betulinic acid into two fragments each; stigmasterol, calycosin, and hederagenin into three fragments each; and lucidusculine into four fragments. However, the RECAP algorithm, which differs in that it is based on retrosynthesis, split stigmasterol, calycosin, tetrahydroalstonine, betulinic acid, and hederagenin into 2 fragments each; lucidusculine into 3 fragments; and was unable to fragment β-sitosterol, telocinobufagin or eriodictyol. Interestingly, the segmentation results for tetrahydroalstonine were consistent for both algorithms (Figures 6A–I). In conclusion, these nine components can be further developed into lead components and thus new drugs on the basis of their fragments through the contributions of their respective functional groups.

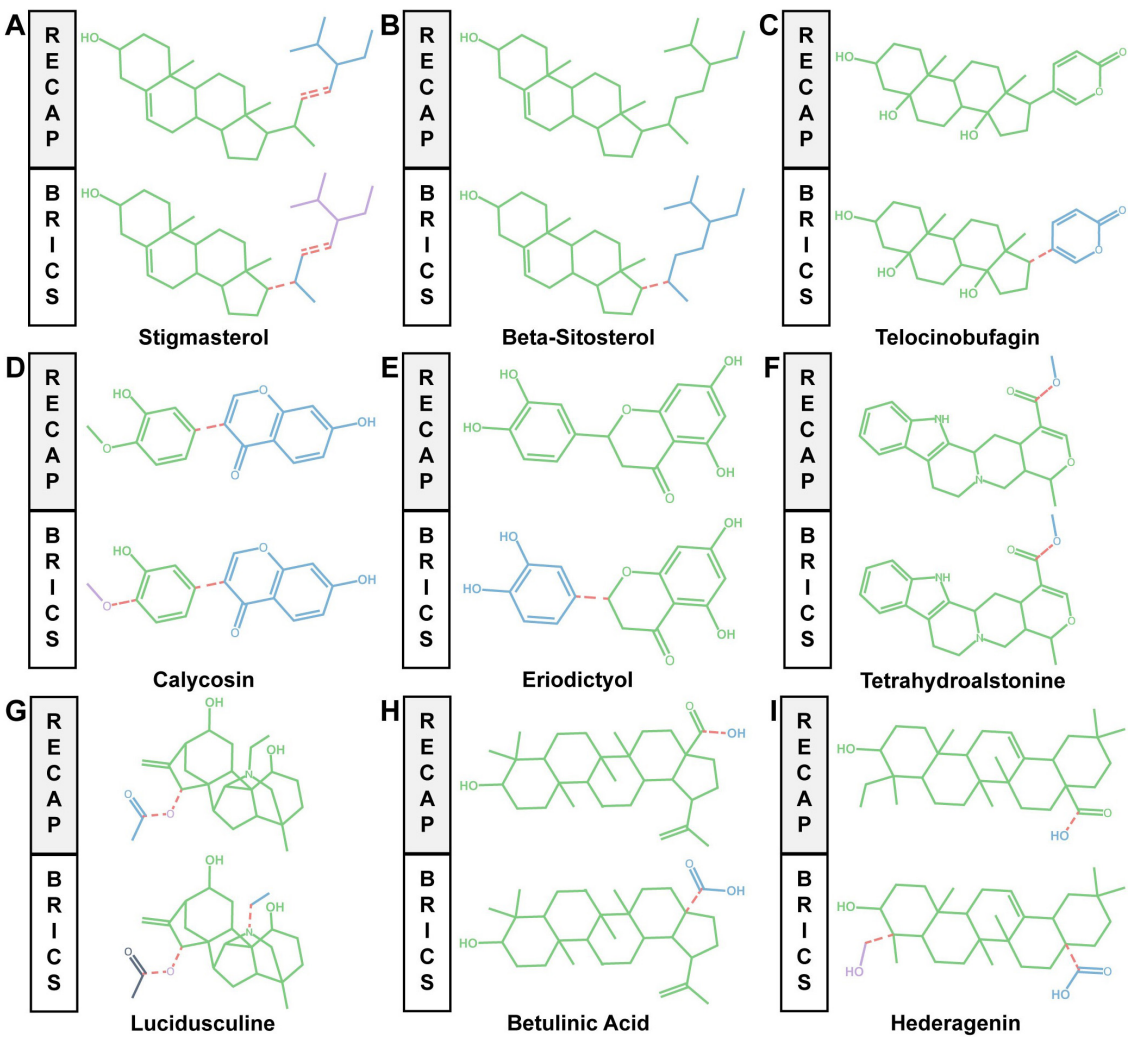

FIGURE 6
Generation of drug molecular fragments. **(A–I)** Molecular fragments of stigmasterol, β-sitosterol, telocinobufagin, calycosin, eriodictyol, tetrahydroalstonine, luciduscline, betulinic acid, and hederagenin obtained using the RECAP and BRICS algorithms. Different molecular fragments are represented using distinct color codes, with red dotted lines indicating the broken bonds.

3.10 The effects of drug intervention on the general condition of DR model mice

Before drug intervention, the mice in group C had neat and shiny fur, were responsive, were agile, and had normal food and water intake as well as body weight. Compared with those in group C, the mice in groups M, D, S, and P had greasy fur, were less responsive, and presented distinct symptoms of diabetes, with increased food and water intake, a significant increase in body weight ($p < 0.05$) (Figures 7A,B), and a marked increase in FBG levels ($p < 0.05$) (Figure 7C). After 12 weeks of drug intervention, compared with the mice in group M, the greasiness of the fur in groups D, S, and P improved, their responsiveness gradually increased, food and water intake decreased ($p < 0.05$), and body weight gradually decreased, although there was no significant difference compared with that in the group M (Figures 7A,B). Compared with group C mice, group M mice had significantly greater FBG, HbA1c, TC, TG, and LDL-C levels after 12 weeks of intervention ($p < 0.05$) and a significantly lower HDL-C level ($p < 0.05$). Compared with the group M mice, the mice in groups D, S, and P had significantly lower FBG, HbA1c, TC, TG, and LDL-C levels ($p < 0.05$) and a significantly higher HDL-C level ($p < 0.05$) (Figures 7C–E).

3.11 The effect of drug intervention on the pathological morphology of the retina in DR model mice

In group C mice, the retinal structure was clear and intact, had neatly arranged cells in each distinct layer, and a complete and continuous inner retinal membrane. Compared with the mice in group C, the mice in group M had obvious vascular dilatation of the retina, visible neovascularisation, unclear hierarchies, loose and irregularly arranged cells in each layer, an obvious reduction in the number of cells, vacuole-like changes in some intercellular spaces, swelling of the inner retinal borders, uneven surfaces, and the local detachment of retinal ganglion cells (RGCs). Compared

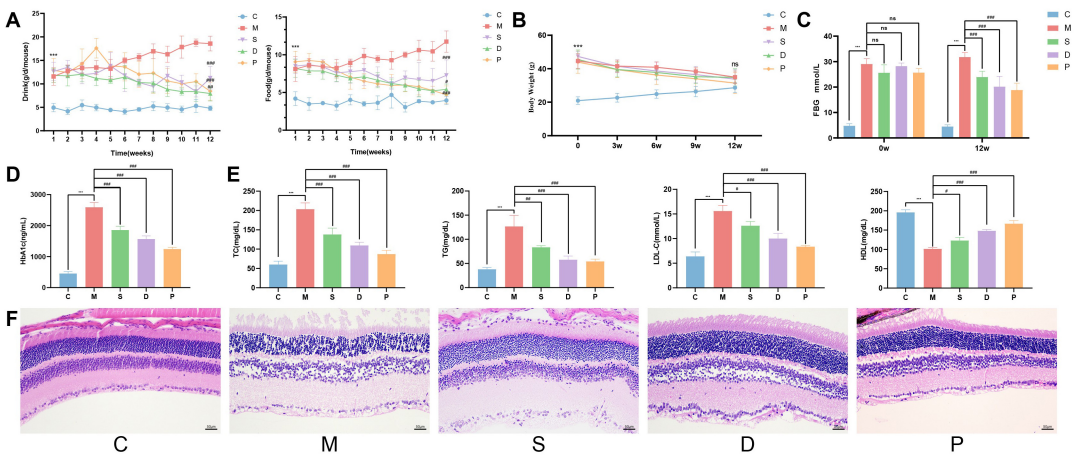

FIGURE 7
The general condition of the mice in each group. **(A)** Consumption of water (left) and food (right). **(B)** Changes in body weight over 12 weeks. **(C)** FBG levels at 0 w and 12 w. **(D)** HbA1c levels at 12 w. **(E)** The levels of lipid-related indices (from left to right: TC, TGs, LDL-C, and HDL-C). **(F)** HE-stained images of retinal tissue. Compared with the C group, $^{*}p < 0.05$, $^{**}p < 0.01$, $^{***}p < 0.001$. Compared with the M group, $^{\#}p < 0.05$, $^{\#\#}p < 0.01$, $^{\#\#\#}p < 0.001$. ns, no significance.

with the mice in group M, the mice in groups D, S, and P showed different degrees of improvement in retinal morphology, with reduced vasodilatation, less neovascularisation, clear layers, significantly more cells in all layers that were more neatly arranged, fewer vacuole-like changes, and less RGC detachment. Among the groups, groups D and P showed more obvious improvements in DR symptoms and more normal retinal morphologies (Figure 7F).

3.12 Effects of drug intervention on the expression of PPARG and inflammatory factors in DR model mice

Determination of the levels of inflammatory factors in different groups of mice via ELISA revealed that serum TNF-α, IL-1β, and IL-6 levels were significantly greater in group M mice than in group C mice ($p < 0.05$). Compared with those of the mice in group M, the serum TNF-α, IL-1β, and IL-6 levels of the mice in groups D, S, and P significantly decreased to different degrees ($p < 0.05$) (Figure 8A). Since PPARG is an important inflammatory regulator (29), we detected the protein and mRNA levels of PPARG in retinal tissues via WB and qPCR and in serum via ELISA and found that the intraretinal expression of PPARG was lower in the mice in group M than in the mice in group C. Moreover, compared with that in the mice in group M, the intraretinal expression levels of PPARG in the mice in groups D, S, and P were significantly elevated (Figures 8A–C).

3.13 Effects of drug intervention on the expression of VEGF and VEGFR2 in the retinal tissue of DR model mice

Angiogenesis is the main pathogenic mechanism of DR, and VEGF is an important marker of angiogenesis. Upon detection of VEGF and VEGFR2 expression in the retinas of the experimental mice via WB and qPCR, we found that VEGF and VEGFR2 were upregulated in the retinas of the mice in group M compared with those of the mice in group C. Compared with those of the mice in group M, the expression levels of VEGF and VEGFR2 in the retinas of the mice in groups D, S, and P were reduced to different degrees (Figures 8B,C).

3.14 Effects of drug intervention on the expression of PPARG and markers of glucose and lipid metabolism in the livers of DR model mice

Since PPARG plays important roles in fatty acid storage and glucose metabolism, on the basis of its upregulation in the retina, we examined the levels of PPARG and glycolipid metabolism-related indices in the liver. The results revealed that PPARG was downregulated in the livers of group M mice compared with those of group C mice and was upregulated in the livers of group D, S, and P mice compared with those of group M mice (Figures 8F,G). The expression levels of PEPCK, G6PASE, SREBP-1c, and Fas were increased in the livers of the mice in group M compared with those in group C but decreased to varying degrees in the livers of the mice in groups D, S, and P compared with those in group M (Figures 8F,G). Similarly, we examined VEGF and VEGFR2 expression in the liver, and the results revealed that VEGF and VEGFR2 were upregulated in the livers of the mice in group M compared with that of the mice in group C and downregulated in the livers of the mice in groups D, S, and P compared with that of the mice in group M (Figures 8D,E).

4 Discussion

DR is a common microvascular complication of diabetes caused by sustained hyperglycaemia that leads to tissue, nerve,

TABLE 2 Research comparison.

Target	Our research	Previous research
PPARG	BNM: Computational analysis shows that PPARG exhibits higher expression levels in the normal group and lower expression levels in the DR group. Experiment: The intraretinal expression of PPARG was lower in mice of group M compared to those in group C, and was significantly elevated in groups D, S, and P.	In STZ-induced SD rat models, PPARG expression is significantly downregulated, while inflammatory factors IL-1β, IL-6, and TNF-α are markedly upregulated (30).
IL-6	BNM: Computational analysis suggests that IL-6 may be a core gene. Experiment: Serum IL-6 levels were significantly higher in group M mice than in group C mice and were significantly reduced in groups D, S, and P compared with those in group M.	The researchers discovered that, in LM rats, retinal damage became evident at 30 weeks, which coincided with a significant elevation in serum IL-6 expression levels (31).
VEGF and VEGFR2	BNM: Computational analysis identifies VEGF signaling pathway as a potential core regulatory pathway. Experiment: VEGF and VEGFR2 were upregulated in the retinas of mice in group M compared with those in group C, and the expression levels of VEGF and VEGFR2 in the retinas of mice in groups D, S, and P were reduced to varying degrees.	The expression levels of VEGF and VEGFR2 were significantly upregulated in the retinal tissue of STZ-induced Lewis mice, whereas anti-VEGF treatment markedly downregulated their expression levels (32).

and microcirculation disorders in the eye, ultimately resulting in damage to or the loss of visual function. HQ, NZZ, and SZY are commonly used Chinese herbs for treating DR. Together, these herbs nourish liver blood to brighten the eyes and have shown significant therapeutic effects in the clinical treatment of DR. The complexity of the diverse components and vast data have led to significant limitations in elucidating the material basis of Chinese herbal components and their specific mechanisms of action in disease treatment. AI technology, with its powerful data processing and pattern recognition capabilities, has shown great potential in analyzing the complex chemical component TCM datasets. In this study, we applied AI technology to explore the therapeutic mechanisms of the herbal trio HQ–NZZ–SZY in detail, aiming to provide more substantial scientific evidence for clinical application.

In this study, the core components of HQ, NZZ, and SZY were mined on the basis of OB ≥ 30% and DL ≥ 0.18. A comprehensive analysis of their predicted target genes was also conducted. The targets of the TCM were merged with genes related to DR from the CTD, GeneCards, and DisGeNET databases to construct a core target network, which led to the identification of 12 core genes, including PPARG (Figure 2D). The differential expression of PPARG in DR and its significant diagnostic and predictive capabilities were validated on public databases (Figures 3A–C). Animal experiments confirmed that the level of PPARG in the retinal tissue of DR model mice was significantly lower than that in the mice in the blank control group (Figures 8B,C). The liver is an important site for glucose and lipid metabolism and can store glucose by synthesizing glycogen and regenerate glucose via gluconeogenesis under fasting conditions. Therefore, the expression of PPARG in the livers of DR model mice was evaluated and it was revealed that, compared with that in the blank control group, the expression of PPARG in the livers of DR model mice also tended to decrease (Figures 8F,G). Some other core genes also play important roles in the development and progression of DR. Studies have shown that increased MAPK14 levels inhibit IGFBP-3 expression, and intravitreal injection of IGFBP-3 can reduce TNF-α levels in the retinal tissue of diabetic rats, thereby potentially mitigating retinal damage caused by inflammatory responses. Elevated proinflammatory factors increase ICAM1 expression, which contributes significantly to microcirculation disorders in diabetic patients, leading to leukocyte adhesion and aggregation in retinal vessel walls, which disrupts the blood-retina barrier and damages retinal nerve cells (33–35).

To study the potential therapeutic effects of the TCM herbal trio HQ, NZZ and SZY on DR, the interactions of their main components with PPARG were explored via molecular docking. It was revealed that the nine components betulinic acid, hederagenin, calycosin, β-sitosterol, eriodictyol, luciduscline, telocinobufagin, stigmasterol, and tetrahydroalstonine strongly bind to PPARG (Figures 4A–J). This implies that this herbal trio may play an important role in the treatment of DR by regulating the expression levels of PPARG. To further explore the therapeutic effects of these nine components on DR, three ML models integrating molecular fingerprint techniques, SVM, RF, and XGBoost, were constructed for their systematic evaluation. Among the evaluated models, the XGBoost model achieved the highest mean AUC and showed better performance in terms of precision, recall, and F1 score, along with improved confusion matrix metrics (TP, TN, FP, and FN), compared with the other two models (Figures 5A–H). Therefore, further data mining was performed using the XGBoost model. The results showed that stigmasterol had the greatest z score, suggesting that stigmasterol may exhibit significant efficacy in the treatment of DR (Figure 5I).

FBDD plays a significant role in drug discovery and development. Structure-based fragmentation is a methodology used in drug design and compound synthesis to decompose compounds into small molecular fragments, thereby identifying and optimizing key structural features and conformational relationships (36). The algorithms used for fragmentation analysis in this study are the BRICS algorithm and the RECAP algorithm. Both algorithms are mainly based on the principle of trans-synthesis, where a set of rules controls the cleavage of chemical bonds, usually emphasizing the selective cleavage of acyclic bonds (37). It was found that stigmasterol yielded different fragmentation patterns when analyzed with the two algorithms; specifically, the BRICS algorithm identified an additional set of carbon chain breaks compared to the RECAP algorithm, suggesting that it may be necessary to evaluate the chemical units synthesized (Figure 6A). The remaining eight drug components are also somewhat amenable to molecular fragmentation segmentation

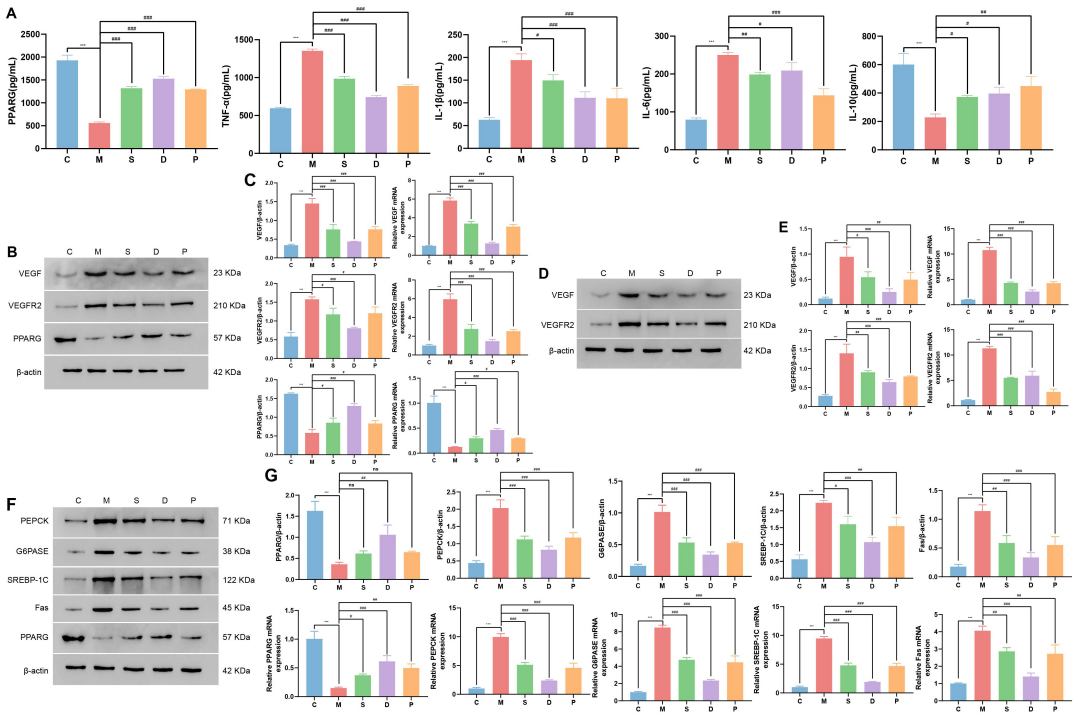

FIGURE 8
Expression of related factors in the liver and retina of each group of mice. **(A)** Detection of serum PPARG and inflammatory factors via ELISA (from left to right: PPARG, TNF-α, IL-1β, IL-6, and IL-10). **(B,C)** Results of WB and qPCR analysis of VEGF, VEGFR2, and PPARG in the retina. **(D,E)** Results of WB and qPCR analysis of VEGF and VEGFR2 in the liver. **(F,G)** Liver glucolipid metabolism-related indices determined via WB and qPCR (from left to right: PPARG, PEPCK, G6PASE, SREBP-1C and Fas). Compared with the C group, $^{*}p < 0.05$, $^{**}p < 0.01$, $^{***}p < 0.001$. Compared with the M group, $^{\#}p < 0.05$, $^{\#\#}p < 0.01$, $^{\#\#\#}p < 0.001$. ns, no significance.

using algorithms, suggesting that they also have potential as lead components (Figures 6B–I).

Stigmasterol is a plant-derived sterol widely present in various plants and foods, such as vegetable oils, nuts, and grains, that has a tricyclic chemical structure similar to that of cholesterol (38, 39). Stigmasterol also has good anti-inflammatory, immunomodulatory, antioxidant, and hypoglycaemic effects (40). Studies have shown that stigmasterol can improve insulin deficiency in patients with diabetes by inhibiting pancreatic cell apoptosis and, in some studies, exhibits activity as an α-glucosidase inhibitor, which is considered to play an important role in lowering blood sugar (41, 42). Furthermore, the efficacy of the TCM herbal trio and stigmasterol were validated in a DR mouse model. Compared with those of the control group mice, the retinal cells of the model group mice presented unclear boundaries, dilated blood vessels, newly formed blood vessels (Figure 7F). Moreover, the FBG, HbA1c, TC, TG, and LDL-C levels significantly increased ($p < 0.001$), whereas the level of HDL-C decreased ($p < 0.001$). Intervention with the TCM herbal trio or stigmasterol significantly reduced the FBG, HbA1c, TC, TG, and LDL-C levels ($p < 0.05$) while increasing the HDL-C level ($p < 0.05$) (Figures 7C–E). Furthermore, in the retinal tissue, blood vessel dilation was alleviated, there were fewer new blood vessels, the cell layers were distinguishable, there were significantly more cells in each layer, the arrangement was more orderly, vacuolar changes were diminished, and there was less shedding of RGCs, collecting approaching normal retinal morphology (Figure 7F). Previous experimental evidence has suggest that stigmasterol can enhance the expression levels of PPARG *in vivo* (43). In the course of our research, intervention with the TCM herbal trio or stigmasterol increased the expression of PPARG ($p < 0.05$) (Table 2), indicating that both the herbal trio and stigmasterol may play a role in lowering blood sugar, regulating lipids, and improving ocular fundus lesions in DR by regulating the expression of PPARG.

Moreover, PPARG is an important regulatory factor in glucose and lipid metabolism that can improve insulin resistance and enhance the sensitivity of target organs to insulin; thus, PPARG has a role in lowering blood sugar (44–48). PEPCK, G6Pase, SREBP-1c and Fas are important indicators reflecting the status of glycolipid metabolism in the liver: PEPCK and G6Pase are the rate-limiting enzymes in glycogenolysis and gluconeogenesis in the liver (49). SREBP-1c regulates the conversion of glucose to lipids in the liver. Inhibiting SREBP-1c expression can effectively reduce fat production and lipid accumulation (50, 51). Fas is a key enzyme in the conversion of glucose to fatty acids (52–54). Fas inhibitors can effectively increase insulin sensitivity and play an important role in maintaining glucose homeostasis in the body (55). Therefore, in this study, the levels of the abovementioned glucose and lipid metabolism-related indicators in the liver were evaluated. Compared with those in group C, the expression levels of PEPCK, G6Pase, SREBP-1c, and Fas were increased in the livers in group M ($p < 0.001$). Furthermore, compared with those in group M, the expression levels of PEPCK, G6Pase, SREBP-1c, and Fas in the livers in groups D, S, and P decreased to varying degrees

($p < 0.05$) (Figures 8F,G). A cohort study shows that improved glucose and lipid metabolism and controlling blood sugar and lipid levels in T2DM can reduce microvascular complications like DR (56). These findings indicate that the TCM herbal trio and stigmasterol can regulate glucose and lipid metabolism possibly through promoting the activity of PPARG, thereby playing a therapeutic role in DR.

On the other hand, PPARG is an important immunomodulator that is closely associated with the expression levels of inflammatory mediators and the inflammasome activation (57). Analysis of the interactions between PPARG and the immunological microenvironment revealed significant correlations between PPARG and 13 different types of immune cells. Specifically, PPARG is negatively correlated with plasma cells, gamma delta T cells, M1 macrophages, and naive B cells, which may suggest that these cells are more active in environments with low PPARG expression or are related to the suppressive effects of PPARG. Conversely, PPARG is positively correlated with nine types of immune cells, including M2 macrophages, which may indicate that these cells play a positive role in microenvironments where PPARG expression is active (Figure 3D). Persistent hyperglycaemia can lead to chronic inflammation within the body, and as the inflammatory response intensifies, inflammatory cells infiltrate and damage retinal tissues, exacerbating retinal vascular permeability, vascular dilation, and retinal thickening (58). The upregulation of PPARG cannot only redirect sugar metabolism but also alleviate the inflammatory response within the body, thereby reducing the damage caused by hyperglycaemia (30). Studies have shown that stigmasterol reduces the expression levels of serum IL-1β, IL-6, TNF-α, and other inflammatory mediators, which may be due to its ability to activate PPARG. This activation can improve the balance between Treg and Th cells and reduce systemic inflammation (59). Moreover, in the serum of the DR model mice, it was found that compared with those in group C, the levels of the proinflammatory factors TNF-α, IL-1β, and IL-6 were significantly increased ($p < 0.001$) and the level of the anti-inflammatory factor IL-10 was decreased ($p < 0.001$) in group M (Table 2). Additionally, compared with group M, the levels of TNF-α, IL-1β and IL-6 were reduced ($p < 0.05$) while IL-10 was increased ($p < 0.05$) in the groups D, S, and P (Figure 8A). These findings indicate that the TCM herbal trio and stigmasterol can reduce the levels of proinflammatory factors and increase the levels of anti-inflammatory factors in the body, thereby improving inflammation in DR.

In this study, in-depth GO and KEGG enrichment analyses of the 12 core targets of the TCM herbal trio were conducted. The analyses revealed that three signaling pathways, including the VEGF signaling pathway, were significantly enriched (Figure 2F). VEGF is an important factor that regulates angiogenesis. In DR, VEGF can bind to its receptor (VEGFR2), which promotes the formation of new blood vessels at the fundus and increases vascular permeability. Compared with normal blood vessels, these pathological new blood vessels lack stable endothelial cells and peripheral supporting cells, making them structurally immature and prone to rupture, which can cause damage to and bleeding in the retina and lead to manifestations such as cystoid macular oedema and optic disc oedema, which are characteristic of DR (32, 58). Studies have shown that increased VEGF expression can activate PPARG phosphorylation, inducing lipid synthesis that promotes T-cell activation, thereby maintaining the activated state of T cells and promoting the occurrence of inflammatory responses (60). Therefore, changes in the expression of the factors in VEGF pathway may initiate the induction of fundus lesions in DR. Consequently, the expression of VEGF and VEGFR2 in retinal and liver tissues was detected. Compared with those in group C, the expression levels of VEGF and VEGFR2 in the retina and liver in group M were increased ($p < 0.001$) (Table 2), but compared with those in group M, the expression levels of VEGF and VEGFR2 in the retina and liver in groups D, S, and P decreased ($p < 0.05$) (Figures 8B–E), indicating that the VEGF/VEGFR2 pathway may be the mechanism by which the TCM herbal trio and stigmasterol exert their therapeutic effects on vascular lesions in the fundus of DR patients.

In summary, in this study, a multimodule framework (BNM) that integrates bioinformatics, network pharmacology, and ML based on molecular fingerprints was developed to thoroughly investigate the potential mechanisms of action of the TCM formula consisting of HQ, NZZ, and SZY on DR, and the mechanisms were validated with animal experiments. This study elucidates the specific molecular mechanisms by which these TCM components treat DR from both theoretical computational and biological experimental perspectives, offering a new perspective for medical research. *In vivo* experiments have demonstrated that the combined HQ-NZZ-SZY formula, along with their key component stigmasterol, can modulate the expression of PPARG. This modulation helps regulate glucose and lipid metabolism while reducing systemic inflammation, thereby inhibiting retinal neovascularization and attenuating the progression of DR. Given that insulin resistance constitutes a critical pathophysiological mechanism in diabetes, based on the aforementioned experimental findings, we tentatively propose that stigmasterol may serve as a potential PPARG modulator for diabetic patients exhibiting significant insulin resistance. This could not only delay DR progression but also ameliorate hyperglycemia and dyslipidemia induced by insulin resistance. However, this study still has some limitations. First, although the molecular mechanism of DR regulation by stigmasterol in this study was investigated by the multimodal BNM framework and verified by animal experiments, the computational results may be biased due to the limited generalization ability of machine learning algorithms and the complexity and diversity of biological systems, and further experiments with human samples are still needed to verify our findings. Secondly, the FBDD-based drug research design in this study is still at a preliminary theoretical stage, necessitating further investigations. Finally, this study shows that upregulation of PPARG inhibits the VEGF/VEGFR2 pathway, thereby attenuating key pathological features of DR. Future in-depth studies are planned to elucidate the precise underlying molecular mechanisms. Therefore, future work will focus on collecting more clinical trial data and animal experimental models for more in-depth research.

Data availability statement

Publicly available datasets were analyzed in this study. The TCM data were retrieved from TCMSP and GSE146615 was retrieved from the GEO database. Further inquiries can be directed to the corresponding authors.

Ethics statement

The animal study was approved by the Animal Ethics Committee of Anhui University of Chinese Medicine. The study was conducted in accordance with the local legislation and institutional requirements.

Author contributions

HZ: Conceptualization, Investigation, Methodology, Validation, Visualization, Writing – original draft. YL: Conceptualization, Investigation, Methodology, Writing – review and editing. QX: Methodology, Project administration, Supervision, Writing – review and editing. ZF: Conceptualization, Funding acquisition, Resources, Writing – review and editing.

Funding

The author(s) declare that financial support was received for the research and/or publication of this article. This work was supported by the National Natural Science Foundation of China (82174153), the Anhui Province Traditional Chinese Medicine Inheritance and Innovation Research Project (2024CCCX253) and the Collaborative Innovation Project for Universities of Anhui Province (GXXT-2020-025).

Conflict of interest

The authors declare that the research was conducted in the absence of any commercial or financial relationships that could be construed as a potential conflict of interest.

Generative AI statement

The authors declare that no Generative AI was used in the creation of this manuscript.

Publisher's note

Supplementary material

The Supplementary Material for this article can be found online at: https://www.frontiersin.org/articles/10.3389/fmed.2025.1537139/full#supplementary-material

References

1. Tan T, Wong T. Diabetic retinopathy: Looking forward to 2030. *Front Endocrinol (Lausanne).* (2022) 13:1077669. doi: 10.3389/fendo.2022.1077669

2. Fung T, Patel B, Wilmot E, Amoaku W. Diabetic retinopathy for the non-ophthalmologist. *Clin Med (Lond).* (2022) 22:112–6. doi: 10.7861/clinmed.2021-0792

3. Kapa M, Koryciarz I, Kustosik N, Jurowski P, Pniakowska Z. Future directions in diabetic retinopathy treatment: Stem cell therapy, nanotechnology, and PPARalpha modulation. *J Clin Med.* (2025) 14:683. doi: 10.3390/jcm14030683

4. Li W, Xing Q, Liu Z, Liu R, Hu Y, Yan Q, et al. The signaling pathways of traditional Chinese medicine in treating diabetic retinopathy. *Front Pharmacol.* (2023) 14:1165649. doi: 10.3389/fphar.2023.1165649

5. Wang Y, Fang Z. Experience of FANG zhaohui in treating early diabetic retinopathy with ligustrum fructus-dogwood astragalus decoction. *Clin J Traditional Chinese Med.* (2022) 34:1431–4. doi: 10.16448/j.cjtcm.2022.0814

6. Tang X, Li X, Zhang D, Han W. Astragaloside-IV alleviates high glucose-induced ferroptosis in retinal pigment epithelial cells by disrupting the expression of miR-138-5p/Sirt1/Nrf2. *Bioengineered.* (2022) 13:8240–54. doi: 10.1080/21655979.2022.2049471

7. Pradhan G, Kulkarni Y. Diabetes and its complications: Role of luteolin, a wonder chemical from the natural source. *Curr Diabetes Rev.* (2024) 21:e1833548591. doi: 10.2174/0115733998285798240217084632

8. Wu H, Liu X, Xie S, Zhou J, Corradini M, Pan Y, et al. Inhibitory effects of phenolic compounds from blueberry leaf on alpha-amylase and alpha-glucosidase: Kinetics, mode of action, and molecular interactions. *J Sci Food Agric.* (2025):doi: 10.1002/jsfa.14187 Online ahead of print.

9. Saikia L, Barbhuiya S, Saikia K, Kalita P, Dutta P. Therapeutic potential of quercetin in diabetic neuropathy and retinopathy: Exploring molecular mechanisms. *Curr Top Med Chem.* (2024) 24:2351–61. doi: 10.2174/0115680266330678240821060623

10. Li X, Guo L, Huang F, Xu W, Peng G. Cornuside inhibits glucose-induced proliferation and inflammatory response of mesangial cells. *Korean J Physiol Pharmacol.* (2023) 27:513–20. doi: 10.4196/kjpp.2023.27.6.513

11. Zhu W, Chen M, Wang Y, Chen Y, Zhang Y, Wang Y, et al. Regulation of renal lipid deposition in diabetic nephropathy on morroniside via inhibition of NF-KB/TNF-a/SREBP1c signaling pathway. *Chem Biol Interact.* (2023) 385:110711. doi: 10.1016/j.cbi.2023.110711

12. Fletcher J, Olsson G, Zhang Y, Burkhardt B. Oral gavage delivery of *Cornus officinalis* extract delays type 1 diabetes onset and hyperglycemia in non-obese diabetic (NOD) mice. *Febs Open Bio.* (2024) 14:434–43. doi: 10.1002/2211-5463.13758

13. Li X, Zeng P, Wu X, Yang X, Lin J, Liu P, et al. ResD-Net: A model for rapid prediction of antioxidant activity in gentian root using FT-IR spectroscopy. *Spectrochim Acta A Mol Biomol Spectrosc.* (2024) 310:123848. doi: 10.1016/j.saa.2024.123848

14. Gu L, Ma Y, Liu S, Zhang Q, Zhang Q, Ma P, et al. Prediction of herbal compatibility for colorectal adenoma treatment based on graph neural networks. *Chin Med.* (2025) 20:31. doi: 10.1186/s13020-025-01082-5

15. Zhang D, Cui W, Hou L, Yang J, Lyu L, Wang Z, et al. Expanding potential targets of herbal chemicals by node2vec based on herb-drug interactions. *Chin Med.* (2023) 18:64. doi: 10.1186/s13020-023-00763-3

16. Huang P, Guo Y, Hu X, Fang X, Xu X, Liu Q. Mechanism of Shenfu injection in suppressing inflammation and preventing sepsis-induced apoptosis in murine cardiomyocytes based on network pharmacology and experimental validation. *J Ethnopharmacol.* (2024) 322:117599. doi: 10.1016/j.jep.2023.117599

17. Hu W, Xu Y. Transcriptomics in idiopathic pulmonary fibrosis unveiled: A new perspective from differentially expressed genes to therapeutic targets. *Front Immunol.* (2024) 15:1375171. doi: 10.3389/fimmu.2024.1375171

18. Li Y, Yu J, Li R, Zhou H, Chang X. New insights into the role of mitochondrial metabolic dysregulation and immune infiltration in septic cardiomyopathy by integrated bioinformatics analysis and experimental validation. *Cell Mol Biol Lett.* (2024) 29:21. doi: 10.1186/s11658-024-00536-2

19. Li J. Area under the ROC Curve has the most consistent evaluation for binary classification. *PLoS One.* (2024) 19:e316019. doi: 10.1371/journal.pone.0316019

20. Roth L, Studer M, Zuercher E, Peytremann-Bridevaux I. Robustness assessment of regressions using cluster analysis typologies: A bootstrap procedure with application in state sequence analysis. *BMC Med Res Methodol.* (2024) 24:303. doi: 10.1186/s12874-024-02435-8

21. Weng J, Zhu X, Ouyang Y, Liu Y, Lu H, Yao J, et al. Identification of Immune-Related biomarkers of schizophrenia in the central nervous system using bioinformatic methods and machine learning algorithms. *Mol Neurobiol.* (2025) 62:3226–43. doi: 10.1007/s12035-024-04461-5

22. Kunnakkattu I, Choudhary P, Pravda L, Nadzirin N, Smart O, Yuan Q, et al. PDBe CCDUtils: An RDKit-based toolkit for handling and analysing small molecules in the Protein Data Bank. *J Cheminform.* (2023) 15:117. doi: 10.1186/s13321-023-00786-w

23. Das S, Biswas S, Chakraborti A, Chakrabarti B. Finding critical points and correlation length exponents using finite size scaling of Gini index. *Phys Rev E.* (2024) 109:24121. doi: 10.1103/PhysRevE.109.024121

24. Welvaars K, van den Bekerom M, Doornberg J, van Haarst E. Evaluating machine learning algorithms to Predict 30-day Unplanned REadmission (PURE) in Urology patients. *BMC Med Inform Decis Mak.* (2023) 23:108. doi: 10.1186/s12911-023-02200-9

25. He J, Sun Y, Ling JA. molecular fragment representation learning framework for Drug-Drug interaction prediction. *Interdiscip Sci.* (2025) 17:42–58. doi: 10.1007/s12539-024-00658-3

26. Wilson J, Sokhansanj B, Chong W, Chandraghatgi R, Rosen G, Ji H. Fragment databases from screened ligands for drug discovery (FDSL-DD). *J Mol Graph Model.* (2024) 127:108669. doi: 10.1016/j.jmgm.2023.108669

27. Banerjee S, Dumawat S, Jha T, Lanka G, Adhikari N, Ghosh B. Fragment-based structural exploration and chemico-biological interaction study of HDAC3 inhibitors through non-linear pattern recognition, chemical space, and binding mode of interaction analysis. *J Biomol Struct Dyn.* (2024) 42:8831–53. doi: 10.1080/07391102.2023.2248509

28. Alka K, Kumar J, Kowluru R. Impaired mitochondrial dynamics and removal of the damaged mitochondria in diabetic retinopathy. *Front Endocrinol (Lausanne).* (2023) 14:1160155. doi: 10.3389/fendo.2023.1160155

29. Geng Q, Xu J, Cao X, Wang Z, Jiao Y, Diao W, et al. PPARG-mediated autophagy activation alleviates inflammation in rheumatoid arthritis. *J Autoimmun.* (2024) 146:103214. doi: 10.1016/j.jaut.2024.103214

30. Yu W, Luo R, He C, Li Z, Yang M, Zhou J, et al. Bergenin mitigates neuroinflammatory damage induced by high glucose: Insights from Zebrafish, murine microbial cell line, and rat models. *Front Pharmacol.* (2024) 15:1339178. doi: 10.3389/fphar.2024.1339178

31. Canz M, Baguña-Torres J, Huerta J, Isla-Magrané H, Zufiaurre-Seijo M, Salas A, et al. Diabetic retinopathy features in lund MetS rats. *Exp Eye Res.* (2025) 252:110274. doi: 10.1016/j.exer.2025.110274

32. Li Q, Onizuka S, Park K, Ma M, Fickweiler W, Park H, et al. Differential effects of retinol-binding protein 3 and Anti-VEGF antibodies on retinal dysfunctions in diabetic retinopathy. *Diabetes.* (2025) 74:787–97. doi: 10.2337/db24-0822

33. Pec M, Jurica J, Bolek T, Skornova I, Pecova M, Cingel M, et al. Endothelial markers in type 2 diabetic patients with acute decompensated heart failure: A pilot study. *Metabolites.* (2025) 15:91. doi: 10.3390/metabo15020091

34. Das U. Lipoxin a4 (LXA4) as a potential drug for diabetic retinopathy. *Medicina (Kaunas).* (2025) 61:177. doi: 10.3390/medicina61020177

35. Zhou L, Xu Z, Lu H, Cho H, Xie Y, Lee G, et al. Suppression of inner blood-retinal barrier breakdown and pathogenic Muller glia activation in ischemia retinopathy by myeloid cell depletion. *J Neuroinflammation.* (2024) 21:210. doi: 10.1186/s12974-024-03190-9

36. Jinsong S, Qifeng J, Xing C, Hao Y, Wang L. Molecular fragmentation as a crucial step in the AI-based drug development pathway. *Commun Chem.* (2024) 7:20. doi: 10.1038/s42004-024-01109-2

37. Yang R, Zhou H, Wang F, Yang G. DigFrag as a digital fragmentation method used for artificial intelligence-based drug design. *Commun Chem.* (2024) 7:258. doi: 10.1038/s42004-024-01346-5

38. Mahawer S, Karakoti H, Kumar R, Prakash O, Kumar S, Rawat S, et al. Assessment of antibacterial, nematicidal and herbicidal activities of Cautleya spicata (Sm.) Baker extracts, with chemical profiling using GC-MS. *Sci Rep.* (2025) 15:7179. doi: 10.1038/s41598-025-91661-1

39. Zhou R, Zhang Y, Xu L, Sun Y. Stigmasterol attenuates triple-negative breast cancer stem cell properties by inhibiting JAK3. *J Cancer.* (2025) 16:1618–30. doi: 10.7150/jca.94822

40. Bakrim S, Benkhaira N, Bourais I, Benali T, Lee L, El O, et al. Health benefits and pharmacological properties of stigmasterol. *Antioxidants (Basel).* (2022) 11:1912. doi: 10.3390/antiox11101912

41. Bhavsar D, Kutre S, Shikhare P, Kumar S, Behera S, Chauthe S. Pharmacoinformatics approach for type 2 diabetes mellitus therapeutics using phytocompounds from Costus genus: An in-silico investigation. *J Biomol Struct Dyn.* (2024):doi: 10.1080/07391102.2024.2330712 Online ahead of print.

42. Cherigo L, Liao-Luo J, Fernandez J, Martinez-Luis S. Isolation of alpha-glucosidase inhibitors from the panamanian mangrove plant mora oleifera (Triana ex Hemsl.) ducke. *Pharmaceuticals (Basel).* (2024) 17:890. doi: 10.3390/ph17070890

43. Zhang S, Yang Y, Zhang R, Gao J, Wu M, Wang J, et al. The potential mechanism of alpiniae oxyphyllae fructus against hyperuricemia: An integration of network pharmacology, molecular docking, molecular dynamics simulation, and in vitro experiments. *Nutrients.* (2024) 17:71. doi: 10.3390/nu17010071

44. Dufour D, Zhao X, Chaleil F, Nothnagel P, Bjoras M, Lefrancois-Martinez A, et al. Pharmacological inhibition of SUMOylation with TAK-981 mimics genetic HypoSUMOylation in murine perigonadal white adipose tissue. *Adipocyte.* (2025) 14:2474107. doi: 10.1080/21623945.2025.2474107

45. Cao J, Su T, Chen S, Du Z, Lai C, Chi K, et al. Evaluating lipid-lowering drug targets for full-course diabetic retinopathy. *Br J Ophthalmol.* (2025):doi: 10.1136/bjo-2024-325771 Online ahead of print.

46. Adeva-Andany M, Adeva-Contreras L, Carneiro-Freire N, Ameneiros-Rodriguez E, Vila-Altesor M, Calvo-Castro I. The impact of high altitude (hypobaric hypoxia) on insulin resistance in humans. *J Physiol Biochem.* (2025) 81:35–55. doi: 10.1007/s13105-025-01069-8

47. Du X, Mendez-Lara K, Hu S, Diao R, Bhavimani G, Hernandez R, et al. An alternatively translated isoform of PPARG proposes AF-1 domain inhibition as an insulin sensitization target. *Diabetes.* (2025) 74:651–63. doi: 10.2337/db24-0497

48. Zhang X, Li R, Chen M, Ye W, Liang J, Yang W, et al. Investigating the potential mechanism of Pioglitazone in Sepsis-Related brain injury through transcriptomics. *Gene.* (2024) 931:148892. doi: 10.1016/j.gene.2024.148892

49. Radhakrishnan S, Mohan K, Natarajan A. Hesperetin-loaded chitosan nanoparticles ameliorate hyperglycemia by regulating key enzymes of carbohydrate metabolism in a diabetic rat model. *J Biochem Mol Toxicol.* (2024) 38:e23805. doi: 10.1002/jbt.23805

50. Deguchi K, Ushiroda C, Kamei Y, Kondo K, Tsuchida H, Seino Y, et al. Glucose and insulin differently regulate gluconeogenic and ureagenic gene expression. *J Nutr Sci Vitaminol (Tokyo).* (2025) 71:46–54. doi: 10.3177/jnsv.71.46

51. Lu H, Yang S, Li W, Zheng B, Zeng S, Chen H. Hericium erinaceus protein alleviates high-fat diet-induced hepatic lipid accumulation and oxidative stress in vivo. *Foods.* (2025) 14:459. doi: 10.3390/foods14030459

52. Matsukawa T, Yagi T, Uchida T, Sakai M, Mitsushima M, Naganuma T, et al. Hepatic FASN deficiency differentially affects nonalcoholic fatty liver disease and diabetes in mouse obesity models. *JCI Insight.* (2023) 8:e161282. doi: 10.1172/jci.insight.161282

53. Pan R, Wang T, Bai J, Zhang J, Gu Y, Zhao Z, et al. Lactobacillus plantarum fermented barley extract attenuates obesity in HFD-induced obese rats by regulating gut microbiota. *Lipids.* (2025):doi: 10.1002/lipd.12435 Online ahead of print.

54. Leite J, Vilas-Boas E, Takahashi H, Munhoz A, Araujo L, Carvalho C, et al. Liver lipid metabolism, oxidative stress, and inflammation in glutamine-supplemented ob/ob mice. *J Nutr Biochem.* (2025) 138:109842. doi: 10.1016/j.jnutbio.2025.109842

55. Hwang J, Jeong H, Baek J, Lee J, Ryu H, Kim J, et al. The inhibitory effects of maclurin on fatty acid synthase and adipocyte differentiation. *Int J Mol Sci.* (2024) 25:8579. doi: 10.3390/ijms25168579

56. Geng T, Zhu K, Lu Q, Wan Z, Chen X, Liu L, et al. Healthy lifestyle behaviors, mediating biomarkers, and risk of microvascular complications among individuals with type 2 diabetes: A cohort study. *PLoS Med.* (2023) 20:e1004135. doi: 10.1371/journal.pmed.1004135

57. Konger R, Xuei X, Derr-Yellin E, Fang F, Gao H, Liu Y. The loss of PPARgamma expression and signaling is a key feature of cutaneous actinic disease and squamous cell carcinoma: Association with tumor stromal inflammation. *Cells-Basel.* (2024) 13:1356. doi: 10.3390/cells13161356

58. Toohey T, Shortt J, John N, Al-Qureshi S, Wickremasinghe S. Intravitreal anti-vascular endothelial growth factor therapy in the treatment of vision loss associated with hematologic malignancy. *Am J Ophthalmol Case Rep.* (2024) 36:102095. doi: 10.1016/j.ajoc.2024.102095

59. Angsusing J, Singh S, Samee W, Tadtong S, Stokes L, O'Connell M, et al. Anti-inflammatory activities of yataprasen thai traditional formulary and its active compounds, Beta-Amyrin and stigmasterol, in RAW264.7 and THP-1 cells. *Pharmaceuticals (Basel).* (2024) 17:1018. doi: 10.3390/ph17081018

60. He J, Chen Y, Ding H, Zhou J, Xing Z, Yang X, et al. Autocrine VEGF-B signaling maintains lipid synthesis and mitochondrial fitness to support T cell immune responses. *J Clin Invest.* (2024) 134:176586. doi: 10.1172/JCI176586

frontiers | Frontiers in Medicine

TYPE Original Research
PUBLISHED 16 June 2025
DOI 10.3389/fmed.2025.1605391

OPEN ACCESS

EDITED BY
Georgios D. Panos,
Aristotle University of Thessaloniki, Greece

REVIEWED BY
Stanislao Rizzo,
Università Cattolica Roma, Italy
Christoph Leisser,
Hanusch Hospital, Austria

*CORRESPONDENCE
Carlo Gesualdo
✉ carlo.gesualdo@unicampania.it

†These authors have contributed equally to this work

RECEIVED 03 April 2025
ACCEPTED 26 May 2025
PUBLISHED 16 June 2025

CITATION
Rossi S, Gesualdo C, Della Corte M, Del Giudice A, Rosolia A, Trotta MC and Simonelli F (2025) Lutein-based dye vitrectomy for idiopathic epiretinal membrane: a pilot study.
Front. Med. 12:1605391.
doi: 10.3389/fmed.2025.1605391

Lutein-based dye vitrectomy for idiopathic epiretinal membrane: a pilot study

Settimio Rossi[1†], Carlo Gesualdo[1*†], Michele Della Corte[1], Antonio Del Giudice[1], Andrea Rosolia[1], Maria Consiglia Trotta[2] and Francesca Simonelli[1]

[1]Eye Clinic, Multidisciplinary Department of Medical, Surgical and Dental Sciences, University of Campania "Luigi Vanvitelli", Naples, Italy, [2]Department of Experimental Medicine, University of Campania "Luigi Vanvitelli", Naples, Italy

Introduction: The use of vital dyes is essential for enhancing visualization of the vitreous and vitreoretinal interface during surgery. In this study, we evaluated the efficacy of a new lutein-based vital dye (LB-VD) for selective staining of the vitreous body and posterior hyaloid in patients undergoing 25 G vitrectomy for idiopathic epiretinal membrane (ERM).

Methods: A total of 18 patients who underwent ERM surgery assisted by LB-VD were retrospectively analyzed. The surgeon completed a postoperative satisfaction questionnaire to evaluate the vitreous staining. Data on best-corrected visual acuity (BCVA), central retinal thickness (CRT), intraocular pressure (IOP), and fixation stability were collected at baseline and at 4 and 6 months post-surgery.

Results: LB-VD effectively stained the vitreous body and posterior hyaloid, facilitating key surgical maneuvers. Significant improvements were observed in BCVA and CRT at both 4 and 6 months post-surgery. Specifically, BCVA improved from 0.60 ± 0.29 LogMAR at baseline to 0.33 ± 0.26 LogMAR at 4 months (p = 0.004) and to 0.32 ± 0.25 LogMAR at 6 months (p = 0.003). CRT decreased significantly from 429 (375–499) μm at baseline to 335 (254–375) μm at 4 months (p = 0.03) and to 323 (240–356) μm at 6 months (p = 0.01). Fixation stability improved in approximately 95% of patients by 6 months. No significant changes in IOP were noted.

Discussion: LB-VD provided clear visualization of the vitreous body and posterior hyaloid, thereby facilitating key vitreoretinal surgical tasks. These findings suggest that LB-VD is an effective and safe alternative to traditional dyes currently used in vitreoretinal surgery.

KEYWORDS

chromovitrectomy, vitreoretinal surgery, vitreous body staining, posterior hyaloid detachment, idiopathic epiretinal membrane

1 Introduction

The ability to visualize tissues and anatomical planes is crucial in vitreoretinal surgery. To improve visualization of the vitreous, internal limiting membrane (ILM), and the epiretinal membrane and to enable delicate maneuvers, vital dyes or crystals are used to stain these intraocular components (1, 2).

Vital dyes are molecules containing chromophores that bind living tissues through chemical reactions, thereby enhancing visualization and their subsequent removal during vitreoretinal surgery (2). The first vital dye introduced for this purpose was indocyanine green (ICG), which was used to improve the visualization of the ILM. However, numerous clinical and experimental studies have revealed retinal toxicity associated with ICG, including changes in the retinal pigment epithelium (RPE), visual field defects, and optic nerve atrophy. These challenges have led to the exploration of alternative dyes, such as Trypan Blue (TB), Patent Blue (PB), and Brilliant Blue G (BBG) (3–6).

In this regard, triamcinolone acetonide (TA) is traditionally used to stain the vitreous, aiding in visualization and delicate surgical maneuvers such as performing posterior vitreous detachment, cutting the vitreous base, and removing the peripheral vitreous cortex. Unlike vital dyes, TA adheres to acellular tissues and consists of water-insoluble synthetic corticosteroid crystals that connect vitreous fibrils, enhancing visualization (7). Two formulations of TA are used in vitreoretinal surgery: non-preservative-free triamcinolone acetonide (non-PFTA) (Kenalog®; Bristol-Myers Squibb, NJ), which contains 0.99% benzyl alcohol as a preservative, and preservative-free triamcinolone acetonide (PFTA; Triesence®; Alcon, Fort Worth, Texas). Initially used as an off-label intravitreal treatment of macular edema, TA has been adopted as a dye in pars plana vitrectomy (PPV) (8). However, studies have shown increased septic risk, higher post-injection intraocular pressure, and toxicity to human neuroretinal and RPE cell cultures, primarily due to the presence of benzyl alcohol (9–14). Therefore, several strategies have been adopted to reduce the potential toxicity of TA, such as dilution with a balanced salt solution. Finally, PFTA formulations were developed and approved for intravitreal use; however, even in these formulations, the results regarding the safety profile remain controversial (15–18). Furthermore, TA is a non-selective dye that stains indiscriminately all tissues at the vitreous–retinal interface, including the vitreous, posterior hyaloid, vitreous cortex residues, ERM, and ILM (2, 7).

The introduction of a lutein-based vitreous dye (LB-VD; Vitreo Lutein) offers a potentially safer alternative to TA-based formulations. LB-VD not only improves visualization of vitreous fibrils but also provides additional benefits related to blue light filtering and the neuroprotective and antioxidant properties of lutein and zeaxanthin (19, 20). *In vitro*, LB-VD demonstrated a superior safety profile over all TA-based formulations in terms of cell vitality, metabolism, and proliferation (15). Moreover, LB-VD selectively stains the vitreous and posterior hyaloid without interacting with the membranes at the vitreous–retinal interface (1, 2).

To date, no clinical studies have evaluated the safety and efficacy of LB-VD. Therefore, this study aims to assess the properties of LB-VD in a cohort of patients with idiopathic ERM undergoing PPV.

2 Materials and methods

A retrospective observational study was conducted at the Eye Clinic of the University of Campania "Luigi Vanvitelli," involving 18 patients who underwent vitrectomy for idiopathic macular pucker. The study adhered to the principles outlined in the Declaration of Helsinki and was approved by the Ethics Committee of the University of Campania "Luigi Vanvitelli" (Protocol 0013692/I, 09 May 2024). All participants were informed about the potential risks and benefits of the surgical procedure, and they consented to participate by signing a written informed consent form.

Patients with idiopathic ERM were included in the study. The exclusion criteria were as follows: refractive error ≥ ± 6.0 diopters, history of ocular trauma or surgery, advanced cataract, glaucoma or other optic neuropathies, secondary epiretinal membrane (ERM), choroidal neovascularization of any origin, diabetic retinopathy, retinal vascular occlusion, central serous chorioretinopathy (CSCR), macular hole, macular telangiectasia, and age-related macular degeneration (AMD).

Baseline data, including gender, age, best-corrected visual acuity (BCVA), central retinal thickness (CRT), intraocular pressure (IOP), microperimetry (MP), and lens status (phakic and pseudophakic), are summarized in Table 1.

All surgeries were performed by the same expert vitreoretinal surgeon (SR), using the vital dye LB-VD (crystallin lutein 2%; 019004 Vitreo Lutein™; VitreoCare – Alfa Instruments, Italy) to visualize the vitreous body during 25G PPV. In phakic patients, vitrectomy was combined with phacoemulsification of the cataract and implantation of an intraocular lens (IOL) to prevent cataract

TABLE 1 Baseline demographic and ocular characteristics.

Total number of patients analyzed, *n*	18
Sex, *n* (%)	
Male	7 (38,8)
Female	11 (61,2)
Age, years	
Mean ± SD	69,77 ± 5,15
BVCA (LogMAR)	
Mean ± SD	0.33 ± 0.26
CRT, μm	
Median (IQR)	429 (375–499)
IOP, mmHg	
Median (IQR)	14 (13–16)
Microperimetry sensitivity, dB	
Median (IQR)	14 (12–16)
Fixation stability, *n* (%)	
Stable	7 (39)
Relatively stable	1 (5)
Unstable	10 (56)
Lens status, *n* (%)	
Phakia	6 (30)
IOL	12 (70)

BCVA: best-corrected visual acuity; CRT: central retinal thickness; IOP: intraocular pressure; MS: macular sensitivity; FS: fixation stability.

formation from affecting the final visual outcome. The surgical procedure included the following steps: performing three sclerotomies via 25G trocars; initial vitrectomy; introduction of LB-VD; core vitrectomy with removal of the posterior hyaloid; introduction of Dual blue dye with a 2 min wait time; epiretinal membrane peeling; inspection of the peripheral retina; air tamponade; and suturing of sclerotomies, if necessary. An intraoperative OCT visualization system (iOCT-ZEISS ARTEVO 800) was employed throughout the procedure to facilitate visualization of the vitreous body and to assess the outcome of epiretinal membrane peeling. All procedures adhered to international standards, and no intraoperative or postoperative complications were reported. Surgical procedures were recorded in MP4 format, enabling frame extraction for the analysis of LB-VD's effectiveness in optimizing vitreous and posterior hyaloid visualization. Additionally, at the end of each vitrectomy, the surgeon completed a satisfaction questionnaire to evaluate LB-VD's ability to distinctly identify the vitreous body and posterior hyaloid.

All patients underwent a comprehensive ophthalmological examination, which included measuring the best-corrected visual acuity (BCVA-LogMAR) using Early Treatment Diabetic Retinopathy Study (ETDRS) charts at 2 m, assessing the anterior segment with slit lamp biomicroscopy, and measuring intraocular pressure with Goldmann applanation tonometry. Fundus examination was conducted using binocular indirect ophthalmoscopy, and spectral domain optical coherence tomography (SD-OCT) was performed using the ZEISS CIRRUS 5000 system (Carl Zeiss, Dublin, CA), using a five-line raster scan and macular cube scan pattern. Additionally, microperimetry was performed with the Nidek MP-3 (Nidek Technologies, Italy) to evaluate the mean sensitivity of the central macular area and fixation stability within central 2 and 4 degrees (FS 2° and FS 4°).

These examinations were repeated at baseline, 4 months, and 6 months after vitrectomy to assess anatomical and functional changes resulting from the surgery.

2.1 Statistical analysis

The Shapiro–Wilk test and Levene's test were employed to assess data distribution and homogeneity. Variables based on repeated observations were analyzed using Friedman's test, followed by Dunn's *post-hoc* test, or using repeated measures analysis of variance (RM-ANOVA), followed by Bonferroni's multiple comparison test. For RM-ANOVA, Mauchly's test was performed to assess sphericity, and if violated, the appropriate correction (Greenhouse–Geisser or Huynh-Feldt) was applied. RM-ANOVA data were reported as mean ± standard deviation (SD), while skewed data were presented as median (interquartile range -IQR). A p-value of <0.05 was considered statistically significant.

3 Results

At the Eye Clinic of the "Luigi Vanvitelli" University of Campania, 18 patients (7 men and 11 women) with a mean age of 69.8 ± 5 years, diagnosed with idiopatic macular pucker and undergoing 25G vitrectomy, were enrolled. A total of 18 eyes (one from each patient) were analyzed. The baseline informations are summarized in Table 1.

All surgical procedures were performed according to international standards, and no intra-operative and/or postoperative complications, inflammation, or adverse events were recorded. After the procedure, the surgeon completed a satisfaction questionnaire and expressed satisfaction with the LB-VD dye's ability to distinctly identify the vitreous body and posterior hyaloid (Figure 1). Additionally, by

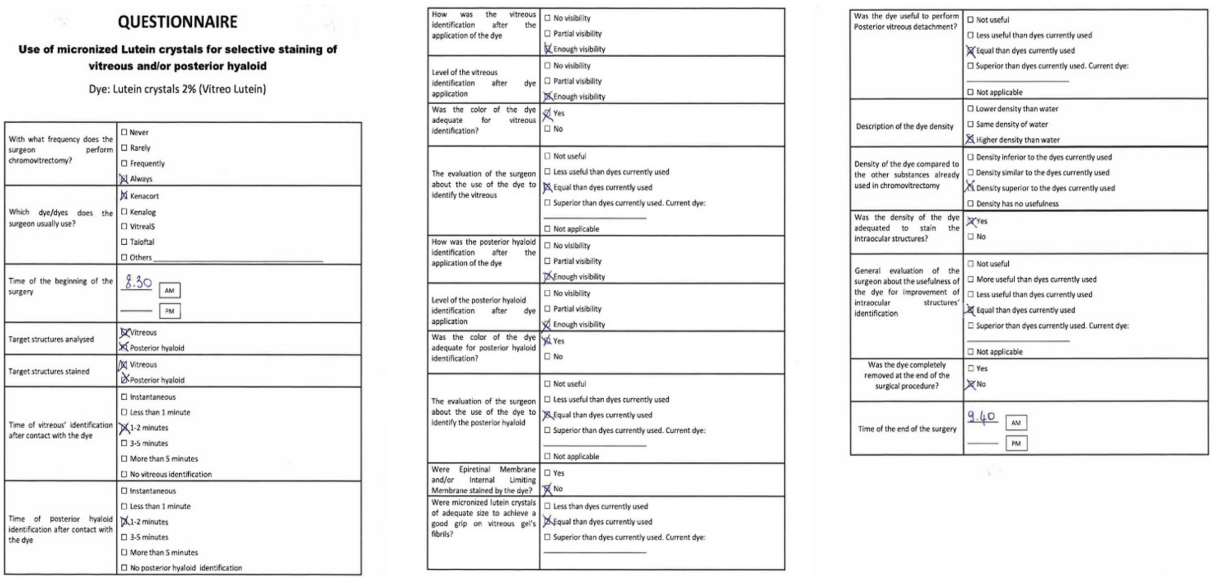

QUESTIONNAIRE

Use of micronized Lutein crystals for selective staining of vitreous and/or posterior hyaloid

Dye: Lutein crystals 2% (Vitreo Lutein)

With what frequency does the surgeon perform chromovitrectomy?	☐ Never ☐ Rarely ☐ Frequently ☒ Always
Which dye/dyes does the surgeon usually use?	☒ Kenacort ☐ Kenalog ☐ Vitreal5 ☐ Taioftal ☐ Others_____
Time of the beginning of the surgery	8.30 AM _____ PM
Target structures analysed	☒ Vitreous ☒ Posterior hyaloid
Target structures stained	☒ Vitreous ☒ Posterior hyaloid
Time of vitreous' identification after contact with the dye	☐ Instantaneous ☐ Less than 1 minute ☒ 1-2 minutes ☐ 3-5 minutes ☐ More than 5 minutes ☐ No vitreous identification
Time of posterior hyaloid identification after contact with the dye	☐ Instantaneous ☐ Less than 1 minute ☒ 1-2 minutes ☐ 3-5 minutes ☐ More than 5 minutes ☐ No posterior hyaloid identification

How was the vitreous identification after the application of the dye	☐ No visibility ☐ Partial visibility ☒ Enough visibility
Level of the vitreous identification after dye application	☐ No visibility ☐ Partial visibility ☒ Enough visibility
Was the color of the dye adequate for vitreous identification?	☒ Yes ☐ No
The evaluation of the surgeon about the use of the dye to identify the vitreous	☐ Not useful ☐ Less useful than dyes currently used ☒ Equal than dyes currently used ☐ Superior than dyes currently used. Current dye: _____ ☐ Not applicable
How was the posterior hyaloid identification after the application of the dye	☐ No visibility ☐ Partial visibility ☒ Enough visibility
Level of the posterior hyaloid identification after dye application	☐ No visibility ☐ Partial visibility ☒ Enough visibility
Was the color of the dye adequate for posterior hyaloid identification?	☒ Yes ☐ No
The evaluation of the surgeon about the use of the dye to identify the posterior hyaloid	☐ Not useful ☐ Less useful than dyes currently used ☒ Equal than dyes currently used ☐ Superior than dyes currently used. Current dye: _____ ☐ Not applicable
Were Epiretinal Membrane and/or Internal Limiting Membrane stained by the dye?	☐ Yes ☒ No
Were micronized lutein crystals of adequate size to achieve a good grip on vitreous gel's fibrils?	☐ Less than dyes currently used ☒ Equal than dyes currently used ☐ Superior than dyes currently used. Current dye: _____

Was the dye useful to perform Posterior vitreous detachment?	☐ Not useful ☐ Less useful than dyes currently used ☒ Equal than dyes currently used ☐ Superior than dyes currently used. Current dye: _____ ☐ Not applicable
Description of the dye density	☐ Lower density than water ☐ Same density of water ☒ Higher density than water
Density of the dye compared to the other substances already used in chromovitrectomy	☐ Density inferior to the dyes currently used ☐ Density similar to the dyes currently used ☒ Density superior to the dyes currently used ☐ Density has no usefulness
Was the density of the dye adequated to stain the intraocular structures?	☒ Yes ☐ No
General evaluation of the surgeon about the usefulness of the dye for improvement of intraocular structures' identification	☐ Not useful ☐ More useful than dyes currently used ☐ Less useful than dyes currently used ☒ Equal than dyes currently used ☐ Superior than dyes currently used. Current dye: _____ ☐ Not applicable
Was the dye completely removed at the end of the surgical procedure?	☐ Yes ☒ No
Time of the end of the surgery	9.40 AM _____ PM

FIGURE 1
Questionnaire on the use of micronized lutein crystals for selective staining of the vitreous and/or posterior hyaloid during PPV. The form includes questions regarding the frequency of dye use, time of surgery, identification of target structures, and the surgeon's evaluation of the dye's usefulness for surgical procedures such as posterior vitreous detachment.

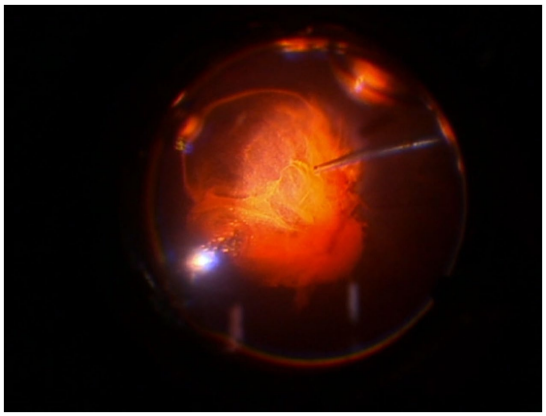

FIGURE 2
Intraoperative image demonstrating successful staining and ability to highlight the vitreous and the posterior hyaloid with LB-VD.

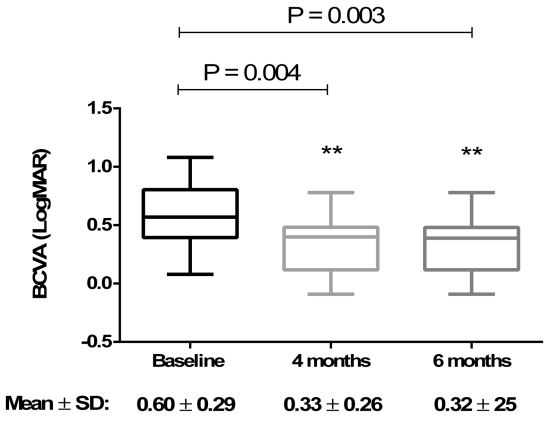

FIGURE 3
Improvement in best-corrected visual acuity (BCVA) at 4 and 6 months compared to baseline. The box plot shows a significant increase ($p < 0.01$) in mean BCVA at 4 months (0.33 ± 0.26 LogMAR) and 6 months (0.32 ± 0.25 LogMAR) compared to baseline (0.60 ± 0.29 LogMAR) (RM-ANOVA followed by Bonferroni's test and Geisser–Greenhouse correction). Data are reported as mean ± standard deviation (SD).

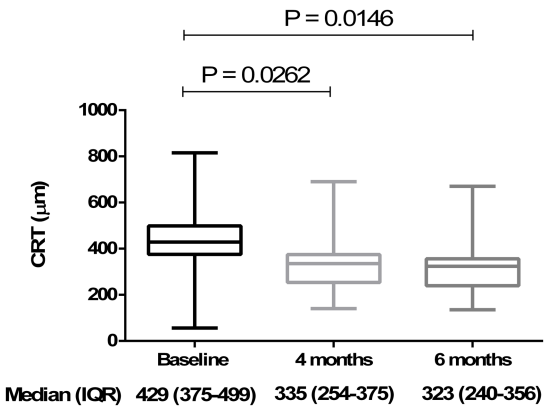

FIGURE 4
Changes in central retinal thickness (CRT) at 4 and 6 months compared to baseline. The box plot shows a significant reduction ($p < 0.05$) in CRT at 4 months [335 (254–375) µm] and 6 months [323 (240–356) µm] compared to baseline [429 (375–499) µm] (Friedman's test, followed by Dunn's test). Data are reported as median and interquartile range (IQR).

extracting frames from the surgical videos, the dye's effective performance was objectively documented. LB-VD was observed to integrate well with the vitreous gel, selectively coloring the posterior hyaloid due to its specific affinity (Figure 2).

Analyzing the functional results after vitrectomy, we observed that all patients exhibited a statistically significant improvement in BCVA at 4- and 6-month follow-ups. At 4 months, the average BCVA improved from 0.60 ± 0.29 LogMAR to 0.33 ± 0.26 LogMAR ($p = 0.004$). At 6 months, it further improved to 0.32 ± 0.25 LogMAR ($p = 0.003$). No significant difference in BCVA was observed between the 4- and 6-month time points ($p > 0.05$) (Figure 3). A significant reduction in mean central retinal thickness (CRT) was observed both at 4- and 6-month post-surgery. At 4 months, the mean CRT decreased from 429 (375–499) µm to 335 (254–375) µm ($p = 0.03$). At 6 months, the CRT was further reduced to 323 (240–356) µm ($p = 0.01$). No significant differences in CRT were noted between the 4-month and 6-month follow-up periods ($p > 0.05$) (Figures 4, 5). Analysis of intraocular pressure (IOP) revealed no significant changes compared to baseline during the follow-up period ($p > 0.05$) (Figure 6). Microperimetry results revealed no significant changes in macular sensitivity compared to baseline at any follow-up time point ($p > 0.05$). However, with regard to fixation stability, the following observations were recorded: (a) 56% of patients ($n = 10$) who had unstable fixation at baseline achieved stable fixation by 6 months after vitrectomy; (b) 39% of patients ($n = 7$) maintained stable fixation throughout the follow-up period; and (c) 5% of patients ($n = 1$) had unstable fixation both at baseline and at all follow-up time points (Figure 7).

4 Discussion

The evaluation of the efficacy and safety of various dyes used in vitreoretinal surgery remains a critical and evolving area of research. In this context, we have conducted an innovative analysis of a new LB-VD designed specifically for selective staining of the vitreous body and posterior hyaloid. This study focused on a cohort of patients with idiopathic ERM who underwent 25G PPV with LB-VD assistance.

Since 2000, chromovitrectomy, the intraocular application of dyes to facilitate visualization of preretinal tissues during vitreoretinal surgery, has become a popular approach to facilitate the performance of key surgical maneuvers, such as ILM and ERM peeling, along with sufficient vitreous removal. The first dye used in chromovitrectomy, ICG, facilitated ILM identification but showed multiple signs of retinal toxicity (5, 6). Subsequently, additional dyes, such as TB and PB, were introduced for the identification of the ERM, and TA for a better vitreous visualization. Finally, more recently, other natural dyes with anti-inflammatory and antioxidant

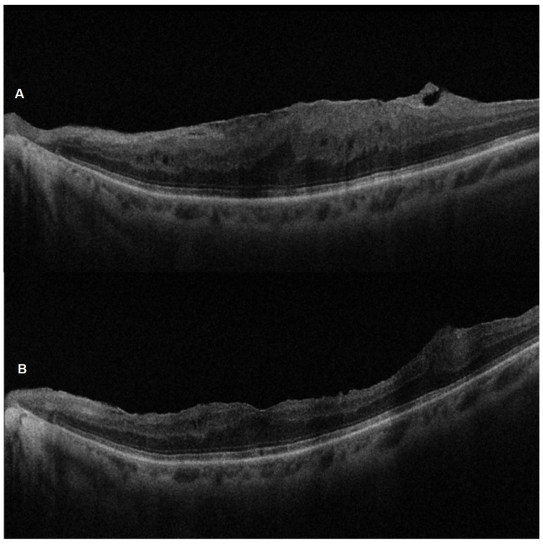

FIGURE 5
SD-OCT pre-operative **(A)** and 6-month post-ERM surgery **(B)** images of the left eye of a 67-year-old woman. Note the successful peeling and the morphological recovery of the foveal profile.

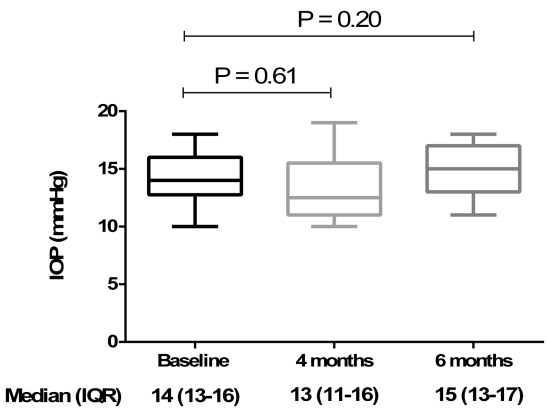

FIGURE 6
Analysis of intraocular pressure (IOP) at baseline, 4 months, and 6 months. The box plot shows stable IOP values across all time points, with no significant differences ($p > 0.05$) at 4 months [13 (11–16) mmHg] and 6 months [15 (13–17) mmHg] compared to baseline [14 (13–16) mmHg] (Friedman's test, followed by Dunn's test). Data are reported as median and interquartile range (IQR).

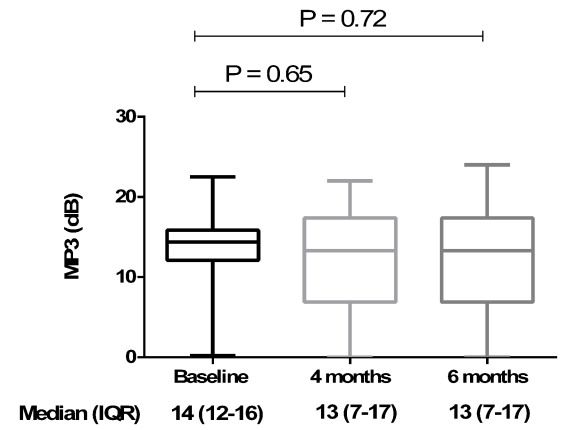

FIGURE 7
Retinal sensitivity measured using microperimetry (MP3) at 4 and 6 months compared to baseline. The box plot shows stable MP3 over the time: 14 (12–16) dB at baseline, 13 (7–17) dB at 4 months, and 13 ± (7–17) dB at 6 months. No statistically significant differences ($p > 0.05$) were observed at 4 and 6 months (compared to baseline) (Friedman's test, followed by Dunn's test). Data are reported as median and interquartile range (IQR).

properties, such as lutein and anthocyanin derived from the açaí fruit, have been proposed (21–24).

TA has traditionally served as the reference dye in vitreoretinal surgery due to its effectiveness in staining the vitreous gel, thereby enhancing visualization and facilitating delicate surgical maneuvers such as posterior vitreous detachment and removal of vitreous cortex remnants (7). Despite the introduction of various formulations of TA, including PFTA versions and injectable suspensions (e.g., Triesence), concerns about its safety persist. Challenges such as cytotoxicity, IOP elevation, cataract development, and risk of sterile endophthalmitis are notable (16, 25–30). Preclinical studies have highlighted that non-PFTA formulations, primarily due to the presence of benzyl alcohol, can lead to reduced cell survival, apoptosis, and subsequent retinal degeneration in human retinal cell cultures (14, 31–34). To address these concerns, several strategies have been employed, including dilution with a balanced salt solution and the development of preservative-free formulations. In recent times, the preservative-free triamcinolone acetonide injectable suspension (TAIS; TRIESENCE; Alcon, Inc., Fort Worth, TX) has been introduced (35); however, even with this latest formulation, questions about retinal cytotoxicity remain. For instance, research by Spitzer et al. has shown that PFTA formulations tend to form larger crystalline aggregates, which can increase contact with retinal tissue and pose a higher risk of cytotoxicity (18).

In recent times, other natural dyes, such as lutein and anthocyanin derived from açaí fruit, have been proposed for intraocular application during vitrectomy. In particular, a new lutein-based vital dye has been introduced as a potentially safer alternative (36). Using *in vitro* models, Lazzara et al. recently demonstrated that LB-VD showed a better safety profile than all TA-based formulations, even when used in combination with perfluorodecalin (PFD), showing the highest levels of cell viability, metabolism, and proliferation (15). Furthermore, LB-VD offers advantages linked to its antioxidant properties, neuroprotective effects, and blue light filtering action. These benefits are attributable to the presence of lipophilic pigments, such as lutein and zeaxanthin, which are physiologically present in the retina.

Furthermore, some authors have highlighted the ability of crystallized lutein-based dyes to improve the visualization of epiretinal membranes using iOCT compared to soluble lutein-based formulations (37). Although lutein-based blue dyes have already been used in vitreoretinal surgery to stain the ILM and/or ERM, demonstrating a good safety profile and effective staining capabilities (36, 38), no clinical studies, to date, have evaluated the properties of crystallin lutein 2% LB-VD. Therefore, we analyzed the effectiveness of LB-VD in staining and improving the visualization of the vitreous body and the posterior hyaloid. We also evaluated the anatomical and functional changes in a cohort of 18 patients with idiopathic macular pucker who underwent

25G PPV assisted by LB-VD. The results were promising: the surgeon reported high levels of satisfaction with LB-VD (as demonstrated by the outcome of the questionnaires), highlighting its excellent ability to visualize the vitreous and the posterior hyaloid, which turned an orange color shortly after dye injection. This facilitated key surgical maneuvers, such as posterior hyaloid detachment and removal of residual peripheral vitreous cortex. Additionally, we observed statistically significant improvements in BCVA and CRT both at 4- and 6-month post-vitrectomy. Fixation stabilization was achieved in approximately 95% of patients by the end of the 6-month follow-up, with no significant changes in intraocular pressure.

5 Conclusion

In conclusion, despite certain study limitations, such as a small sample size, short follow-up, and a collection of questionnaire responses obtained from a single surgeon, our results support the hypothesis that LB-VD is comparable to various vitreous dye formulations, such as TA, in determining effective staining of the vitreous and the posterior hyaloid, further allowing for better ERM visualization through the iOCT. Furthermore, LB-VD shows a specific selectivity for the vitreous body and the posterior hyaloid without any risk of intraoperative or postoperative complications. Overall, these findings suggest that LB-VD may offer a valuable and safer alternative to traditional dyes used in vitreoretinal surgery, with the added benefit of potentially reducing cytotoxic risks while improving surgical outcomes. Further studies are warranted to validate these findings and explore the long-term benefits and safety of LB-VD in a broader patient population.

Data availability statement

The original contributions presented in the study are included in the article/supplementary material, further inquiries can be directed to the corresponding author.

Ethics statement

The studies involving humans were approved by the Ethics Committee of University of Campania "Luigi Vanvitelli," Protocol 0013692/I, 09/05/2024. The study was conducted in accordance with the local legislation and institutional requirements. The participants provided their written informed consent to participate in this study.

Author contributions

SR: Conceptualization, Methodology, Data curation, Writing – original draft. CG: Conceptualization, Data curation, Methodology, Writing – original draft. MDC: Methodology, Data curation, Writing – original draft. ADG: Visualization, Writing – original draft, Data curation. AR: Visualization, Writing – original draft, Data curation. MCT: Data curation, Validation, Writing – original draft. FS: Writing – review & editing, Validation, Supervision.

Funding

The author(s) declare that financial support was received for the research and/or publication of this article. This study was funded by the Italian Ministry of Education, University and Research, grant number PRIN 2020FR7TCL_002.

Conflict of interest

The authors declare that the research was conducted in the absence of any commercial or financial relationships that could be construed as a potential conflict of interest.

Generative AI statement

The authors declare that no Gen AI was used in the creation of this manuscript.

Publisher's note

References

1. Rodrigues EB, Meyer CH, Kroll P. Chromovitrectomy: a new field in vitreoretinal surgery. *Graefes Arch Clin Exp Ophthalmol.* (2005) 243:291–3. doi: 10.1007/s00417-004-0992-x

2. Farah ME, Maia M, Penha FM, Rodrigues EB. The use of vital dyes during vitreoretinal surgery – Chromovitrectomy. In: QD Nguyen, EB Rodrigues, ME Farah, WF Mieler and DV Do, editors. Developments in ophthalmology. Basel, Switzerland: S. Karger AG (2016). 365–75.

3. Weinberger AW, Schlossmacher B, Dahlke C, Hermel M, Kirchhof B, Schrage NF. Indocyanine-green-assisted internal limiting membrane peeling in macular hole surgery – a follow-up study. *Graefes Arch Clin Exp Ophthalmol.* (2002) 240:913–7. doi: 10.1007/s00417-002-0544-1

4. Stanescu-Segall D, Jackson TL. Vital staining with indocyanine green: a review of the clinical and experimental studies relating to safety. *Eye.* (2009) 23:504–18. doi: 10.1038/eye.2008.249

5. Rodrigues EB, Meyer CH, Farah ME, Kroll P. Intravitreal staining of the internal limiting membrane using indocyanine green in the treatment of macular holes. *Ophthalmologica.* (2005) 219:251–62. doi: 10.1159/000086107

6. Narayanan R, Kenney MC, Kamjoo S, Trinh T-HT, Seigel GM, Resende GP, et al. Toxicity of Indocyanine green (ICG) in combination with light on retinal pigment epithelial cells and neurosensory retinal cells. *Curr Eye Res.* (2005) 30:471–8. doi: 10.1080/02713680590959312

7. Couch SM, Bakri SJ. Use of triamcinolone during vitrectomy surgery to visualize membranes and vitreous. *Clin Ophthalmol.* (2008) 2:891–6. doi: 10.2147/opth.s3434

8. Martidis A, Duker JS, Greenberg PB, Rogers AH, Puliafito CA, Reichel E, et al. Intravitreal triamcinolone for refractory diabetic macular edema. *Ophthalmology.* (2002) 109:920–7. doi: 10.1016/s0161-6420(02)00975-2

9. Nelson ML, Tennant MTS, Sivalingam A, Regillo CD, Belmont JB, Martidis A. Infectious and presumed noninfectious endophthalmitis after intravitreal triamcinolone acetonide injection. *Retina*. (2003) 23:686–91. doi: 10.1097/00006982-200310000-00014

10. Yamakiri K, Sakamoto T, Noda Y, Nakahara M, Ogino N, Kubota T, et al. Reduced incidence of intraoperative complications in a multicenter controlled clinical trial of triamcinolone in vitrectomy. *Ophthalmology*. (2007) 114:289–96. doi: 10.1016/j.ophtha.2006.07.044

11. Szurman P, Kaczmarek R, Spitzer MS, Jaissle GB, Decker P, Grisanti S, et al. Differential toxic effect of dissolved triamcinolone and its crystalline deposits on cultured human retinal pigment epithelium (ARPE19) cells. *Exp Eye Res*. (2006) 83:584–92. doi: 10.1016/j.exer.2006.02.012

12. Narayanan R, Mungcal JK, Kenney MC, Seigel GM, Kuppermann BD. Toxicity of triamcinolone acetonide on retinal neurosensory and pigment epithelial cells. *Invest Ophthalmol Vis Sci*. (2006) 47:722–8. doi: 10.1167/iovs.05-0772

13. Chang Y-S, Wu C-L, Tseng S-H, Kuo P-Y, Tseng S-Y. In vitro benzyl alcohol cytotoxicity: implications for intravitreal use of triamcinolone acetonide. *Exp Eye Res*. (2008) 86:942–50. doi: 10.1016/j.exer.2008.03.011

14. Chang Y-S, Lin C-F, Wu C-L, Kuo P-Y, Wu F-S, Shieh C-C, et al. Mechanisms underlying benzyl alcohol cytotoxicity (triamcinolone acetonide preservative) in human retinal pigment epithelial cells. *Invest Ophthalmol Vis Sci*. (2011) 52:4214–22. doi: 10.1167/iovs.10-6058

15. Lazzara F, Conti F, Ferrara M, Lippera M, Coppola M, Rossi S, et al. Safety profile of lutein- versus triamcinolone Acetonide-based vitreous staining. *Transl Vis Sci Technol*. (2023) 12:5. doi: 10.1167/tvst.12.1.5

16. Li Y, Chen H, Hou J, Zhang Y, Li G, Gu X, et al. Further characterization of ocular safety profile of commercially available preserved and preservative-free triamcinolone acetonide. *Retina*. (2012) 32:364–74. doi: 10.1097/IAE.0b013e31821e1f7c

17. Shaikh S, Ho S, Engelmann LA, Klemann SW. Cell viability effects of triamcinolone acetonide and preservative vehicle formulations. *Br J Ophthalmol*. (2006) 90:233–6. doi: 10.1136/bjo.2005.076190

18. Spitzer MS, Mlynczak T, Schultheiss M, Rinker K, Yoeruek E, Petermeier K, et al. Preservative-free triamcinolone acetonide injectable suspension versus "traditional" triamcinolone preparations: impact of aggregate size on retinal biocompatibility. *Retina*. (2011) 31:2050–7. doi: 10.1097/IAE.0b013e318214d076

19. Wilson LM, Tharmarajah S, Jia Y, Semba RD, Schaumberg DA, Robinson KA. The effect of lutein/zeaxanthin intake on human macular pigment optical density: a systematic review and Meta-analysis. *Adv Nutr*. (2021) 12:2244–54. doi: 10.1093/advances/nmab071

20. Sasaki M, Ozawa Y, Kurihara T, Noda K, Imamura Y, Kobayashi S, et al. Neuroprotective effect of an antioxidant, lutein, during retinal inflammation. *Invest Ophthalmol Vis Sci*. (2009) 50:1433–9. doi: 10.1167/iovs.08-2493

21. Feron EJ. Trypan blue staining of Epiretinal membranes in proliferative vitreoretinopathy. *Arch Ophthalmol*. (2002) 120:141. doi: 10.1001/archopht.120.2.141

22. Peyman GA, Cheema R, Conway MD, Fang T. TRIAMCINOLONE ACETONIDE AS AN AID TO VISUALIZATION OF THE VITREOUS AND THE POSTERIOR HYALOID DURING PARS PLANA VITRECTOMY. *Retina*. (2000) 20:554–5. doi: 10.1097/00006982-200005000-00024

23. Mennel S, Meyer CH, Tietjen A, Rodrigues EB, Schmidt JC. Patent blue: a novel vital dye in vitreoretinal surgery. *Ophthalmologica*. (2006) 220:190–3. doi: 10.1159/000091764

24. Peris CS, Badaro E, Ferreira MA, Lima-Filho AAS, Ferreira EL, Maia A, et al. Color variation assay of the anthocyanins from Açai fruit (*Euterpe oleracea*): a potential new dye for vitreoretinal surgery. *J Ocul Pharmacol Ther*. (2013) 29:746–53. doi: 10.1089/jop.2013.0003

25. Januschowski K, Irigoyen C, Pastor JC, Srivastava GK, Romano MR, Heimann H, et al. Retinal toxicity of medical devices used during vitreoretinal surgery: a critical overview. *Ophthalmologica*. (2018) 240:236–43. doi: 10.1159/000488504

26. Gatto C, Romano MR, Giurgola L, Ferrara M, Ragazzi E, D'Amato Tothova J. Ex vivo evaluation of retinal cytotoxicity after the use of multiple medical devices in pars plana vitrectomy in porcine eyes. *Exp Eye Res*. (2021) 213:108837. doi: 10.1016/j.exer.2021.108837

27. Tura A, Alt A, Lüke J, Grisanti S, Haritoglou C, Meyer CH, et al. Biocompatibility of the vital dye acid Violet-17 on retinal pigment epithelial cells. *Clin Ophthalmol*. (2016) 10:1435–45. doi: 10.2147/OPTH.S105695

28. Polski A, Liu KC, Gupta D, Grewal DS, Horns J, Wirostko BM, et al. Incident glaucoma and ocular hypertension after periocular and intravitreal steroid injections: a claims-based analysis. *BMJ Open Ophthalmol*. (2023) 8:e001508. doi: 10.1136/bmjophth-2023-001508

29. Jonas JB, Kreissig I, Degenring RF. Retinal complications of intravitreal injections of triamcinolone acetonide. *Graefes Arch Clin Exp Ophthalmol*. (2004) 242:184–5. doi: 10.1007/s00417-003-0841-3

30. Sampat KM, Garg SJ. Complications of intravitreal injections. *Curr Opin Ophthalmol*. (2010) 21:178–83. doi: 10.1097/ICU.0b013e328338679a

31. Yeung CK, Chan KP, Chiang SWY, Pang CP, Lam DSC. The toxic and stress responses of cultured human retinal pigment epithelium (ARPE19) and human glial cells (SVG) in the presence of triamcinolone. *Invest Ophthalmol Vis Sci*. (2003) 44:5293–300. doi: 10.1167/iovs.03-0490

32. Yeung CK, Chan KP, Chan CKM, Pang CP, Lam DSC. Cytotoxicity of triamcinolone on cultured human retinal pigment epithelial cells: comparison with dexamethasone and hydrocortisone. *Jpn J Ophthalmol*. (2004) 48:236–42. doi: 10.1007/s10384-003-0053-8

33. Morrison VL, Koh HJ, Cheng L, Bessho K, Davidson MC, Freeman WR. Intravitreal toxicity of the kenalog vehicle (benzyl alcohol) in rabbits. *Retina*. (2006) 26:339–44. doi: 10.1097/00006982-200603000-00014

34. Lang Y, Zemel E, Miller B, Perlman I. Retinal toxicity of intravitreal kenalog in albino rabbits. *Retina*. (2007) 27:778–88. doi: 10.1097/IAE.0b013e318030c517

35. Dyer D, Callanan D, Bochow T, Abraham P, Lambert HM, Lee SY, et al. Clinical evaluation of the safety and efficacy of preservative-free triamcinolone (triesence [triamcinolone acetonide injectable suspension] 40 mg/ml) for visualization during pars plana vitrectomy. *Retina*. (2009) 29:38–45. doi: 10.1097/IAE.0b013e318188c6e2

36. Maia M, Furlani BA, Souza-Lima AA, Martins DS, Navarro RM, Belfort R. Lutein: a new dye for chromovitrectomy. *Retina*. (2014) 34:262–72. doi: 10.1097/IAE.0b013e3182a0b7f4

37. Leisser C, Kronschläger M, Findl O. Effekt von Chromovitrektomiefarbstoffen mit Lutein auf die verbesserte Darstellung von epiretinalen Pathologien im intraoperativen OCT. *Klin Monatsbl Augenheilkd*. (2020) 237:1230–4. doi: 10.1055/a-1023-4369

38. Badaro E, Furlani B, Prazeres J, Maia M, Lima AAS, Souza-Martins D, et al. Soluble lutein in combination with brilliant blue as a new dye for chromovitrectomy. *Graefes Arch Clin Exp Ophthalmol*. (2014) 252:1071–8. doi: 10.1007/s00417-013-2539-5

Frontiers in Medicine

Translating medical research and innovation into improved patient care

A multidisciplinary journal which advances our medical knowledge. It supports the translation of scientific advances into new therapies and diagnostic tools that will improve patient care.

Discover the latest Research Topics

See more →

Frontiers

Avenue du Tribunal-Fédéral 34
1005 Lausanne, Switzerland
frontiersin.org

Contact us

+41 (0)21 510 17 00
frontiersin.org/about/contact